Inclusive J/ψ production at mid-rapidity in p–Pb collisions at $\sqrt{s_{\mathrm{NN}}} = 5.02$ TeV

Michael Winn
Physikalisches Institut,
University of Heidelberg

A thesis submitted to the degree
Doctor of Natural Sciences
Heidelberg 2016

Dissertation
submitted to the
Combined Faculties for Natural Sciences and Mathematics
of the Ruperto-Carola University of Heidelberg, Germany
for the degree of
Doctor of Natural Science

put forward by
Michael Winn (M.Sc. Physics)
born in Saarbrücken, Germany

Oral examination on April 28, 2016

Inclusive J/ψ production at mid-rapidity in p–Pb collisions at $\sqrt{s_{\mathrm{NN}}} = 5.02$ TeV

Referees: Prof. Dr. Johanna Stachel

Prof. Dr. Hans-Christian Schultz-Coulon

Abstract

Charmonia are a key observable for deconfinement in nucleus–nucleus (A–A) collisions at the LHC. Measurements in proton–nucleus (p–A) collisions and their comparison with proton–proton (pp) collision results provide complementary information on nuclear effects that are present in the absence of the Quark–Gluon Plasma (QGP). In addition, the calculation of the production of charmonia in p–A collisions presents a challenging test of perturbative QCD at low scales Q^2 and low fractional momentum of the involved partons. The inclusive J/ψ production in proton–lead collisions at $\sqrt{s_{\rm NN}} = 5.02$ TeV has been measured with ALICE in the $\rm e^+e^-$-decay channel at mid-rapidity down to vanishing transverse momentum ($p_{\rm T}$): integrated, as a function of $p_{\rm T}$, centrality and charged-particle multiplicity. The nuclear modification factor of J/ψ indicates a strong suppression of charmonium production integrated, at low $p_{\rm T}$ and as function of centrality. The dependence of the normalised J/ψ yield as a function of the normalised charged particle multiplicity is consistent with the measurement in pp collisions and in the open heavy-flavour sector. It provides information on the correlation of soft and hard particle production.

An extrapolation of the expected J/ψ production behaviour in A–A collisions based on the p–A measurement assuming the factorisation of the nuclear modification strengthens the evidence for an additional J/ψ production component at low $p_{\rm T}$ in A–A collisions. This component is expected from J/ψ production from unbound charm quarks within the QGP or at the phase boundary.

Kurzzusammenfassung

Charmonia sind eine Schlüsselobservable für 'Deconfinement' in Kern-Kern-Kollisionen (A–A-Kollisionen) am LHC. Messungen in Proton–Nukleus Stößen (p–A-Stößen) und deren Vergleich mit denen in Proton–Proton Kollisionen (pp-Kollisionen) bieten komplementäre Informationen über Effekte in Kern-Kollisionen, die auch in der Absenz von 'Deconfinement' wirksam sind. Zudem stellt die Berechnung der Produktion von Charmonia in p–A-Kollisionen eine Herausforderung für perturbative QCD bei niedrigen Skalen Q^2 und kleinem fraktionalem Impuls der beteiligten Partonen dar.

Die inklusive J/ψ-Produktion bei $\sqrt{s_{\rm NN}} = 5.02$ TeV wurde mit ALICE in Proton-Blei-Kollisionen im Dielektronenzerfallskanal bis zu verschwindendem Transversalimpuls ($p_{\rm T}$) bei zentraler Rapidität integriert, als Funktion von $p_{\rm T}$, der Zentralität und der Multiplizität geladener Teilchen gemessen. Der integrierte nukleare Modifikationsfaktor als auch der zentralitätsabhängige und der $p_{\rm T}$-abhängige bei niedrigen $p_{\rm T}$ deuten auf eine starke Unterdrückung der J/ψ-Produktion hin. Die Abhängigkeit der normierten J/ψ-Produktionsrate als Funktion der normierten Multiplizität geladener Teilchen ist konsistent mit der Messung in pp-Kollisionen und im 'Open-heavy-Flavour'-Sektor. Sie liefert Informationen über die Korrelation von harter und weicher Teilchenproduktion.

Eine Extrapolation des erwarteten J/ψ-Produktionsverhaltens in A–A-Kollisionen, basierend auf der Messung in p–A-Kollisionen unter der Annahme von Faktorisierung der Modifikation in p–A-Kollisionen, stärkt die Evidenz für eine zusätzliche J/ψ-Produktionskomponente bei niedrigen $p_{\rm T}$. Diese Komponente wird von J/ψ-Produktion von ungebundenen Charm-Quarks im Quark-Gluon-Plasma oder an der Phasengrenze erwartet.

Contributions to physics analyses with ALICE

1. J. Adam et al. (ALICE Collaboration), *Rapidity and transverse momentum dependence of the inclusive* J/ψ *nuclear modification factor in p–Pb collisions at* $\sqrt{s_{NN}} = 5.02$ *TeV*, published in JHEP 1506 (2015) 055.

   Paper committee member representing the J/$\psi \rightarrow e^+e^-$ analysis at mid-rapidity

2. J. Adam et al. (ALICE Collaboration), *Centrality dependence of inclusive* J/ψ *production in p–Pb collisions at* $\sqrt{s_{NN}} = 5.02$ *TeV*, published in JHEP 1511 (2015) 127.

   Paper committee member representing the J/$\psi \rightarrow e^+e^-$ analysis at mid-rapidity

3. J. Adam et al. (ALICE Collaboration), *Multiplicity dependence of inclusive* J/ψ *production in p–Pb collisions at* $\sqrt{s_{NN}} = 5.02$ *TeV*, in preparation.

   Paper committee member representing the J/$\psi \rightarrow e^+e^-$ analysis at mid-rapidity

4. J. Adam et al. (ALICE Collaboration), *Centrality dependence of inclusive* ψ*(2S) production in p–Pb collisions at* $\sqrt{s_{NN}} = 5.02$ *TeV*, in preparation.

   Internal review committee member

Contributions to the installation and the operation of ALICE

Gas system of the ALICE Transition Radiation Detector.

Maintenance of the gas system 2013–2015 and testing as well as installation of new detector components 2013–2014.

Contents

1. Introduction

The understanding of the structure of matter and its interactions down to the smallest accessible length scales has been an important goal of scientific research since the beginning of the 20th century when the atomic hypothesis was commonly accepted. The scattering experiments by H. Geiger and E. Marsden [1] revealed the substructure of atoms. Rutherford realised that the main contribution to the mass of the atom was concentrated in a dense core, the nucleus [2].
After the discovery of the neutron by Chadwick in 1932 [3], it was clear that the nucleus composed of nucleons is held together by a short-ranged force, called the strong nuclear force. After first ideas of the nucleon-nucleon interaction by Heisenberg, further developed by Fermi, Yukawa [4] found a description of the attractive part of the interaction by introducing a new massive field, later called the pion. The pion was indeed discovered in 1947 [5, 6], and subsequently in the coming years, a full 'zoo' of particles was found experimentally. The breakthrough in the understanding of this large number of strongly interacting particles, later called hadrons, was the 'eightfold way' proposed in 1961 independently by Gell-Mann [7] and Ne'eman [8]: the observed hadrons were ordered and additional states were predicted by postulating constituents of the hadrons with fractional electromagnetic charges of 1/3 and 2/3, called quarks.
The structure functions measured in deep inelastic electron-proton (ep) collisions by the SLAC-MIT experiment [9, 10] at the Stanford Linear Accelerator Center, operational between 1967 and 1973, showed a scaling behaviour, which was introduced by Bjorken [11] as a signature for point-like constituents of the proton. These constituents were called partons by Feynman [12] and after further experimental support finally identified in the beginning of the seventies as quarks, the fundamental degrees of freedom of the strong interaction[1]. This association implied

[1] Later on, since the 'notion' partons was attributed to all proton constituents, the gluons were also called partons.

that quarks are not only a formal mathematical construction, but physical degrees of freedom.

Although the eightfold way and the subsequently developed quark model by Gell-Mann[13] and Zweig [14] was successful in describing the mass spectrum of the hadrons with the help of quarks, it did not provide a satisfactory description of the strong interaction. Quantum ElectroDynamics (QED) was at that time the established quantum field theory of the electromagnetic interaction based on a $U(1)$ gauge symmetry. After many struggles, a quantum field theory for the strong interaction, Quantum ChromoDynamics (QCD), was proposed in 1973 [15, 16] with $SU(3)$ as gauge group. The 3 charges and 3 anti-charges occurring in the gauge theory of the strong interaction are referred to as colours, which constitute an additional degree of freedom. Since the $SU(3)$ group is non-commutative, the massless gauge field degrees of freedom of QCD, the gluons, can interact with themselves in contrast to photons in QED.

The discovery of the so-called asymptotic freedom for specific quantum field theories including QCD in 1973 by D. J. Gross, F. Wilczek [17] and H.D. Politzer [18] paved the road to reliable perturbative treatment for theories like QCD, which have large coupling constants at low energy transfer: the coupling strength of the interaction decreases with increasing momentum transfer and the theory becomes non-interacting in the ultraviolet limit in contrast to QED, which has a very weak dependence of the energy transfer and becomes stronger interacting at larger momentum transfer. After this breakthrough, QCD became within a short time scale the accepted theory of the strong interaction: the turning point was the discovery of the J/ψ particle in November 1974 [19, 20], also known as the November revolution, which will be discussed in Section 2.1. QCD has successfully passed a large number of experimental tests in the perturbative regime. The strong nuclear force is nowadays understood as a residual force of QCD between the nucleons in the nucleus.

An impressive illustration of the success of QCD is the experimental confirmation of the running of the strong coupling constant α_S as predicted by asymptotic freedom, which is shown in Fig. 1.1.

Although quarks and gluons are the fundamental degrees of freedom of QCD, only colour-neutral objects, hadrons, have been observed in nature travelling distances for longer than a typical time scale of strong interactions, which amounts to about 1 fm/c = 0.3 $\cdot 10^{-23}$ s. This central property of the strong interaction is called

'confinement'. It has not been proven based on QCD and remains one of the most outstanding mathematical quests in physics.

QCD constitutes today, together with Quantum Flavour Dynamics describing the electro-weak dynamics, the Standard Model of particle physics, which describes all building blocks of ordinary matter, i.e., excluding dark matter, and matter interactions apart from gravitation.

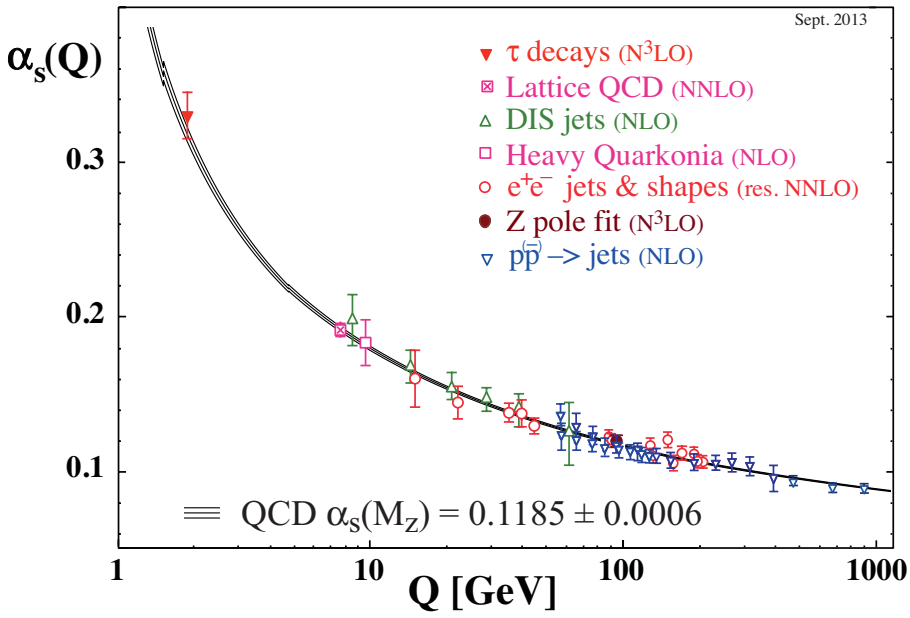

Figure 1.1.: Running of the strong coupling constant α_s as a function of the energy scale Q. The value of the running coupling evaluated at the mass of the Z boson $\alpha_s(M_Z)$ is also indicated. The figure is taken from the PDG 2014 QCD review by S. Bethke, G. Dissertori and G. Salam [21].

The QCD Lagrangian density is composed of a classical, a gauge-fixing and a ghost part depending on the gauge. In addition, one can add a CP-symmetry violating term to the QCD Lagrangian, which has not been confirmed experimentally. The classical part of the Lagrangian is discussed following the notation of Ref. [22][2]:

$$L = \frac{1}{4} F^A_{\alpha\beta} F_A^{\alpha\beta} + \sum_{flavours} \bar{q}_a (i \not{D} - m)_{ab} q_b \tag{1.1}$$

The first term $F^A_{\alpha\beta} F_A^{\alpha\beta}$ describes the pure gluon dynamics of gluon field propagation and inter-gluon interaction, i.e., it represents the Yang-Mills part of the Lagrangian

[2]The gauge fixing term, the auxiliary ghost fields appearing depending on the gauge and the potentially CP-violating term are detailed in Ref. [22].

density. $F^A_{\alpha\beta}$ is the field strength tensor, which can be expressed in terms of the gluon field A^A_α:

$$F^A_{\alpha\beta} = [\partial_\alpha A^A_\beta - \partial_\beta A^A_\alpha - g f^{ABC} A^B_\alpha A^C_\beta] \tag{1.2}$$

The Greek letters α, β represent the Lorentz indices. The Roman letters A, B represent the 8 colour indices in the adjoint representation of $SU(3)$. The first two terms have the same structure as in Abelian QED, whereas the last term encodes the non-Abelian characteristics and hence the gluon-gluon interaction: g is the coupling constant and f^{ABC} are the structure constants of $SU(3)$. The latter part of the Lagrangian density is responsible for the presence of triple and quartic gluon vertices in QCD. The second part of the classical Lagrangian in Equation (1.1) corresponds to the Lagrangian density of the Dirac equation for the quarks with mass m. The interaction of the gluon field with the fermionic fields is included in the covariant derivative $(D_\alpha)_{ab} = \partial_\alpha \delta_{ab} + ig(t^C A^C_\alpha)_{ab}$, where t^C are matrices in the fundamental representation of $SU(3)$. The spinor indices are suppressed in Equation (1.2). The indices for the six different flavours are only indicated by the sum. The Roman letters a, b denote the colour indices in the triplet, i.e., the fundamental representation.

There are seven parameters of the quantum theory, which have to be determined experimentally: the running coupling constant α_s at a reference scale in the perturbative regime and the mass matrix for the six different flavours, which is diagonal in QCD. The running of the coupling constant and the quark masses are determined by the theory itself. As an alternative parameter to α_s, the energy scale Λ_{QCD} at which the running coupling α_s diverges in perturbation theory can be taken as input. Λ_{QCD} is in the neighbourhood of 200 MeV and indicates the order of magnitude of the energy scale at which perturbative calculations break down. The precise value of Λ_{QCD} depends on the renormalisation scheme, the order of the perturbative expansion, which was used to extract Λ_{QCD} from the experimentally determined α_s, and the number of active quark flavours.

Although the underlying theory is known and the parameters of QCD are experimentally constrained, the understanding of the strong interaction is not complete as it is most notably illustrated by the lack of the full understanding of confinement. In particular, the investigation of thermodynamic systems of strongly interacting matter and, more generally, of multi-body systems governed by QCD is the subject of intense research on the theoretical as well as on the experimental side. In this context, relativistic heavy-ion collisions research aims at creating QCD matter in

the laboratory and at extracting its properties. In particular, the creation and investigation of a phase of strongly interacting matter, where the confinement of colour charges is absent at high temperatures, the so-called Quark-Gluon Plasma (QGP), is the prime goal of this effort.
Among other observables, the modification of the J/ψ meson production in nucleus–nucleus (A–A) collisions compared to the production in absence of a deconfined phase was put forward in 1986 [23] and is still recognised as one of the most intriguing signatures of the QGP. Furthermore, the production of J/ψ mesons in proton–proton and proton–nucleus collisions provides an interesting testing ground for the application of perturbation theory and factorisation down to comparatively low energy scales and in interplay with non-relativistic bound state physics.
The measurement of inclusive J/ψ production in proton–lead collisions presented in this thesis provides important information for the interpretation of lead–lead (Pb–Pb) collision results from the LHC in view of an interpretation as a sign of deconfinement. In addition, the measurement contributes to the understanding of charmonium production in proton–nucleus collisions. A short overview of the research field of QGP relevant for the subject of this thesis will be given in the following.

1.1. The phase diagram of strongly interacting matter and heavy-ion collisions

1.1.1. The phase diagram of QCD

The first ideas about the phase diagram of strongly interacting matter are older than QCD. First insights were gained by Pomerantchuk in 1951 [24], who found a limiting temperature for hadronic matter due to the finite size of hadrons. The bootstrap model formulated in 1965 by Hagedorn [25, 26] lead to the conjecture of a maximum temperature for hadronic matter.
A system of strongly interacting matter in equilibrium can be characterised by the temperature and the baryochemical potential or the net baryon density. The baryochemical potential μ_B is the chemical potential related to the net baryon density. The first phase diagram of strongly interacting matter was conjectured

by N. Cabibbo and G. Parisi in 1975 [27] as shown in Fig. 1.2. They found a second-order phase transition between hadronic matter and a deconfined state in quark 'containment' models like the MIT-bag model [28]. A phase transition to a deconfined state of matter at high quark density was also conjectured in 1975 by J.C. Collins and M.J. Perry [29]. The qualitative features such as the transition towards deconfinement discussed by Cabbibo and Parisi remain valid until today.

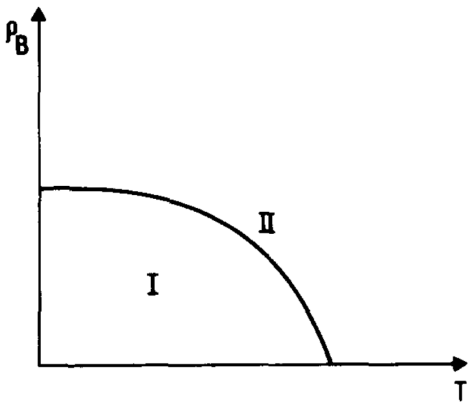

Figure 1.2.: '75: Cabibbo & Parisi

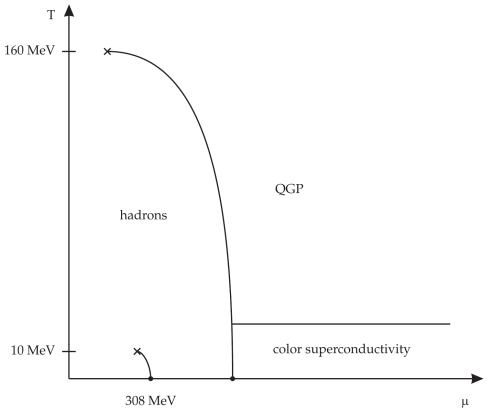

Figure 1.3.: '08: Rischke

Schematic phase diagram of strongly interacting matter by N. Cabibbo and G. Parisi [27] from 1975 on the left hand side and by D. Rischke [30] from 2008 on the right hand side. The variable on the vertical axis of the phase diagram by Cabibbo and Parisi is the baryon density, whereas the temperature axis is horizontal. Phase I denotes hadronic matter, phase II a deconfined state. In the phase diagram by Rischke, the solid line between the deconfined phase (QGP) and the hadronic phase indicates a first order phase transition with a critical endpoint at finite baryochemical potential. The presence of this first order phase transition and its critical endpoint is not confirmed based on the QCD Lagrangian. The precise phase structure at high baryochemical potential with different colour-superconductive phases is conjectured based on QCD-inspired models, whereas the rapid cross-over transition between hadronic matter and the QGP close to the temperature axis [30] is established based on lattice QCD as discussed below. The first order nuclear gas-liquid phase transition and its endpoint are shown as well.

The present knowledge about the phase diagram is schematically shown in Fig. 1.3. At low temperatures and baryochemical potential, the system can be described by a gas of hadrons. In this phase, color charges are confined in colour neutral objects. At high temperatures, the system must be a gas of non-interacting gluons and quarks due to asymptotic freedom. In order to discuss the established phase transition between the hadronic world and the deconfined phase at high temperature and low baryochemical potential, it is necessary to introduce the relevant order

parameters.

For the deconfinement transition, the thermal expectation value of the renormalised Polyakov loop $L = \exp(-F_\infty/(2T))$ can be used as the order parameter in pure gauge theory for the deconfinement phase transition. F_∞ denotes the free energy of two static colour charges at an infinite distance. This energy diverges in the confined phase and it remains finite in the deconfined phase. L is therefore zero in the confined state and finite in the deconfined phase. However, this order parameter indicates only a true first-order phase transition in a pure gauge theory or a gauge theory with fermionic sector with sufficiently heavy fermion masses, i.e, heavy quark masses. It remains finite for physical quark mass values at low temperatures. Furthermore, the approximate global chiral $SU(2)$ symmetry of up and down quarks in the QCD Lagrangian is broken spontaneously. It is responsible for the dynamical generation of the dominant part of hadron masses [31] built from up and down quarks. The order parameter for this phase transition in the chiral limit of massless up and down quarks is the chiral condensate. As in the case of the Polyakov loop, this phase transition is not a first-order phase transition at vanishing baryochemical potential for physical parameter choices [32, 33].

Our knowledge of the nature of the QCD phase diagram as a function of the quark masses is summarised in the 'Columbia plot' shown in Fig. 1.4. It was conjectured that a first order phase transition at finite baryochemical potential can be observed and hence a critical endpoint is present in the μ_B-T phase diagram [34]. The experimental search for the critical point is a major goal of heavy-ion collision research at low beam energies at the Relativistic Heavy Ion Collider (RHIC) and future facilities.

The behaviour of basic thermodynamic properties at vanishing baryochemical potential in the phase diagram is nowadays well established with the use of lattice gauge theory, which was pioneered by K. Wilson [36]. At $T = 154 \pm 9$ MeV, a rapid cross-over to a chirally restored and deconfined state of matter is observed in lattice QCD calculations with realistic quark masses using two different discretisation schemes [32, 33]. Figure 1.5 shows the pressure, the energy and entropy density from Ref. [33] and the comparison between the two groups on the right hand side.

The deconfined phase at high temperature was coined Quark-Gluon Plasma (QGP) by E. Shuryak [37] in 1977, who proposed the creation of a QGP in hadronic collisions [38] in 1978.

Only slightly above the transition temperature, the deconfined system is still charac-

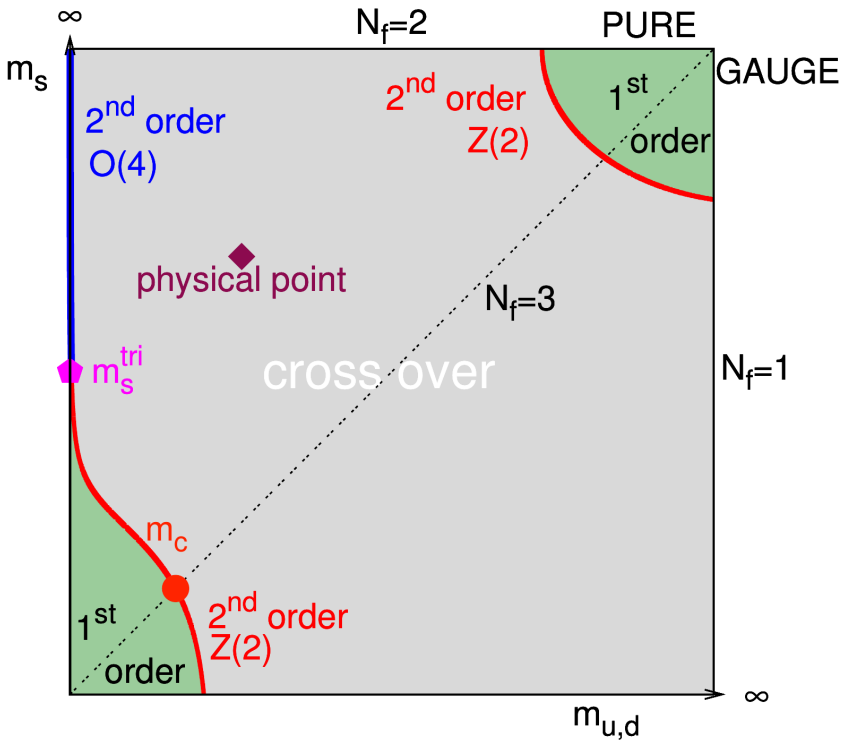

Figure 1.4.: The Columbia plot shows the nature of the QCD phase transition as a function of the masses of u, d and s quarks. This recent version of the diagram for vanishing baryochemical potential is taken from a review by Ding et al. [35]. The point corresponding to the parameters of QCD in nature is also indicated.

terised by strong interactions as it can be expected naively, since the strong coupling diverges in perturbation theory at $Q = \Lambda_{QCD}$, which is a scale close to the phase transition temperature. Therefore, the system cannot be described as a gas consisting of weakly interacting quarks and gluons as at asymptotically high temperatures. The strong deviation from the Stefan-Boltzmann limit in the energy density and the pressure observed in the results of the lattice simulations depicted in Fig. 1.5 is interpreted as sign of these strong interactions. Substantiated by experimental findings, the deconfined phase close to the pseudocritical temperature was baptised strongly coupled QGP, sQGP. It is expected that the early universe has passed through the transition from Quark-Gluon Plasma to ordinary hadronic matter after its creation in the big bang [39].

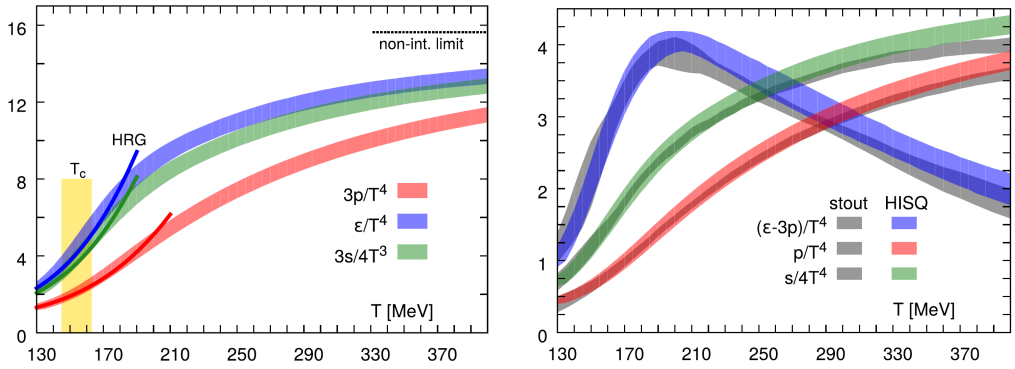

Figure 1.5.: The energy density, pressure and entropy density are shown on the left hand side suitably normalised by powers of temperature T calculated in lattice QCD by the HotQCD collaboration [33]. The corresponding quantities are as well indicated for the Hadron Resonance Gas (HRG), which provides a good description of QCD matter below the transition temperature. The pseudo-critical temperature T_c and the non-interacting high-T limit for an ideal, non-interacting gas of quarks and gluons are indicated. The figure on the right hand side shows the comparison of the trace anomaly of the energy-momentum tensor as well as of pressure and entropy density between the HotQCD collaboration and Budapest-Wuppertal collaboration [32].

1.1.2. Heavy-ion collisions as a laboratory of QCD matter

The idea to experimentally explore the QGP is only little younger than the establishment of QCD as the correct theory of strong interaction and dates back to the late seventies and early eighties. In fact, this conjecture is the culmination of the application of concepts of statistical mechanics to hadronic collisions including the assumption of statistical equilibrium to calculate particle production in hadronic collisions, which was pioneered by E. Fermi in 1950 [40]. Attempts to apply statistical physics concepts to hadronic collisions went on after this initial idea by Fermi and were also the starting point for the bootstrap model by Hagedorn [25, 26]. The application of statistical mechanics to hadronic collisions has been an active field of research at the dawn of the QCD era as documented by the review of Feinberg [41] from 1971.

It was conjectured early on [42] that the collision of relativistic nuclei will provide the critical energy density needed in a sufficiently large volume in order to reach deconfinement and that thermalisation towards a local equilibrium can be achieved rapidly enough. A first sketch of the time evolution of a relativistic hadronic collision was given by Shuryak, see Fig. 1.6, and the picture was further developed in a seminal contribution by Bjorken [43] for the central rapidity region in 1982, Fig. 1.7. Bjorken assumed the applicability of hydrodynamics in heavy-ion collisions. He proposed a simple model for the time evolution of the collision close to mid-rapidity at asymptotically large collision energies, which proved to be applicable to first approximation at very high collision energies of heavy nuclei achieved at the Relativistic Heavy-Ion Collider (RHIC) and at the LHC (Large Hadron Collider) at central rapidities.

The first relativistic heavy-ion collisions were analysed at the Lawrence Berkeley National Laboratory in Berkeley in the Bevalac accelerator with nuclear beams with energies of $\approx$ 2 GeV/nucleon, which were collided on fixed targets. An overview of accelerator facilities colliding heavy-ions in the past and presently is shown in Tab. 1.1.

The observation and characterisation of the created strongly interacting matter is in the centre of heavy-ion research. At the highest accessible collision energies, at the LHC and at top RHIC energies, the phase diagram is probed very close to vanishing baryochemical potential, since the deposited net baryon number around mid-rapidity in the centre-of-mass frame is very small. The reached energy densities

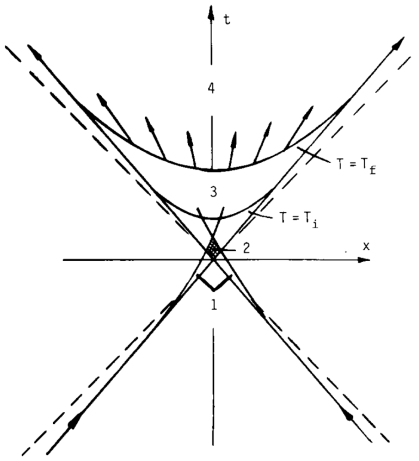

Figure 1.6.: '78: Shuryak

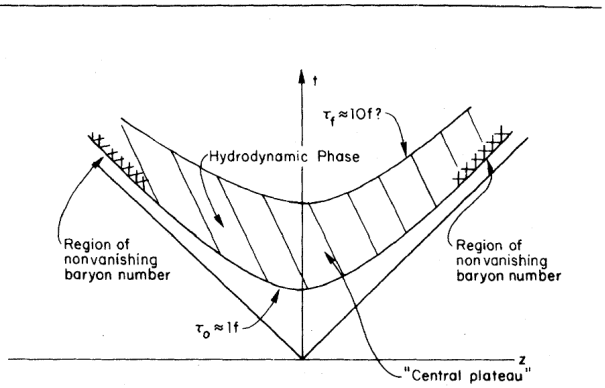

Figure 1.7.: '82: Bjorken

Minkowski diagram of a relativistic hadronic collision by Shuryak from 1978 [38] on the left hand side and the picture of a relativistic heavy-ion collision by Bjorken from 1982 [43] on the right hand side: the ordinate indicates the time in the centre-of-mass frame of the collision, the abscissa the beam direction of the colliding nuclei. Both diagrams show curves for constant eigentime in the moving fluid cells for the thermalisation time or temperature (temperature T_i for Shuryak, time τ_0 for Bjorken) and for the freeze-out time or temperature. Bjorken states estimates for both values, which are not exceedingly far away from values used in nowadays hydrodynamic simulations of heavy-ion collisions of, e.g., 0.2 fm/c [44] for the thermalisation and 5-10 fm/c for the freeze-out depending on collision system and geometry [45]. The hydrodynamic phase is indicated in Bjorken's scenario. In case of Shuryak, the final state interaction phase corresponding to the hydrodynamic phase in Bjorken's picture is denoted by Phase 3.

based on the Bjorken estimate for the LHC [46] correspond to temperatures well above the critical temperature of the cross-over between hadronic and quark-gluon matter.

The collisions of heavy-ions at LHC energies can be illustrated with the diagram by Bjorken in Fig. 1.7: two strongly Lorentz-contracted nuclei with a relativistic γ-factor of over 1000 in the centre-of-mass frame collide and cross each other within about 10^{-2} fm/c. A large amount of energy is deposited by the collision in the central rapidity region. The system at the collision time is characterised by strong colour fields, which build locally thermalised strongly interacting matter within a short time scale between 0.1-1 fm/c. The typical initial temperature for the onset of the hydrodynamic evolution in simulations amounts to about 500 MeV at the LHC, see, e.g., in Ref. [47].

The subsequent evolution of the thermalised medium is described by nearly ideal hydrodynamics [48]. This behaviour follows the paradigm of the sQGP. The ex-

accelerator	lab	mode	largest system $\sqrt{s_{\mathrm{NN}}}$	operation time
Bevalac	LBNL	fixed target	Au–Au 2.4 GeV	1974–1993
AGS	BNL	fixed target	Au–Au 2.7-4.8 GeV	1987–2000
SPS	CERN	fixed target	Pb–Pb 7.3-17.3 GeV	1987–2000
SIS	GSI	fixed target	Au–Au 2.4 GeV	1990–today
RHIC	BNL	collider	Au–Au 7.7-200 GeV	2000–today
LHC	CERN	collider	Pb–Pb 2.76-5.0 TeV	2010–today

Table 1.1.: Past and present accelerator facilities colliding heavy-ions at relativistic energies. AGS and SPS are still in use as preaccelerators of RHIC and LHC. At CERN, there currently remains one fixed-target experiment, NA61, taking data using the heavy-ion beams from SPS. At RHIC, at most collision energies, the focus is on Au–Au collisions, although U–U collisions took also place at the top energy corresponding to $\sqrt{s_{\mathrm{NN}}}$=192.8 GeV.

panding fluid cools down during its close to isentropic expansion and eventually cannot maintain equilibrium any longer due to dilution. Finally, hadrons are released and stream freely. In heavy-ion physics, the transition from a local thermal equilibrium description to free streaming hadrons is further subdivided into two steps: first, no chemical equilibrium can be maintained between the created hadrons after the so-called chemical freeze-out, but the system may stay longer in thermal equilibrium due to elastic collisions until the kinetic freeze-out marks the transition to free streaming particles. Information about the temporal and spatial extension of the system can be inferred from femtoscopic measurements; an introduction to the methodology is given in Ref. [49]. The 'region of homogeneity' at the last interaction between the measured particles amounts to 4800 ± 580 fm^3 based on 2-pion interferometry in the largest produced systems at the LHC [50] at $\sqrt{s_{\mathrm{NN}}} = 2.76$ TeV. This volume is not the total source size and its relation to the system extension at the decoupling is model-dependent. According to Ref. [51] and references therein, it exceeds the system volume per unit of rapidity for a thermal freeze-out at $T = 120(150)$ MeV by a factor 1.47(1.28).

The chemical freeze-out parameters temperature and baryochemical potential can be determined experimentally by the thermal model, which uses a grand-canonical ensemble of a hadron resonance gas to describe the particle yields produced in heavy-ion collisions [52] from SIS up to LHC collision energies. It is hence a unique access to a point on the trajectory of the system through the phase diagram. It has been used as the first tool to position experimental points on the phase diagram of strongly interacting matter. The freeze-out parameters of the thermal model are

argued to be close to the phase boundary to hadronic matter at high collision energies [53] as at RHIC and the LHC, since the chemical equilibration of multi-strange baryons is only reachable at the phase boundary. The argumentation is based on the observation that only in the temperature regime of the phase transition as seen from the hadronic side hadron densities as given by the hadron resonance gas are large enough for the occurrence of processes including more than 2 particles in the incoming and outgoing state, since $2 \rightarrow 2$ processes are clearly insufficient to drive the system into equilibrium at the time scales of the system lifetime. Following this argument, the applicability of the thermal model is an indirect indication for the creation of a deconfined medium in relativistic heavy-ion collisions. Until now, the existence and the duration of an extended hadronic phase between the chemical and the kinetic freeze-out could not be shown experimentally [54] and is disfavoured by the abundance of loosely bound objects as the deuteron, which is measured as predicted by the thermal model [55] with the freeze-out temperature as for the other hadrons and behaving hydrodynamically [56]. However, after the transition from the continuum hydrodynamic description, so-called 'hadronic afterburners' generally improve the description of experimental data by modern hydrodynamic simulations [57]. The switching between the fluid to the hadronic transport description is done at a stage when the system is thought to be in a regime in which both descriptions are applicable. The use of hadronic afterburners in the described way hence implies the presence of a stage where the system is best described by hadronic degrees of freedom, but not yet free-streaming. In summary, the quest is open for the full understanding of the description of the system hadronisation. Nevertheless, it is remarkable and important to note for a further understanding of the microscopic picture that the macroscopic thermal model is able to explain the abundance of a variety of hadrons and nuclei.

The hydrodynamic picture is based on the agreement of hydrodynamical simulations with experimentally measurable particle spectra and correlation observables. They are sensitive not only to the system extension as measured by the already mentioned femtoscopic methods, but also to details of the expansion, the equation of state, the initial conditions and the freeze-out properties. The vast amount of experimental precision spectra and correlation measurements, in particular higher-order anisotropies and their event-by-event distributions, with the dawn of the LHC heavy-ion program and parallel results from RHIC have in recent years solidified the picture of nearly ideal hydrodynamics and of an early thermalisation of the

medium [48]. This is remarkable due to the non-negligible amount of parameters and assumptions involved in the modelling of the initial state, the equation of state, dissipative corrections to the ideal hydrodynamics and the freeze-out conditions. The description of the experimental data requires the use of a very small viscosity over entropy density ratio between 0.07 and 0.43 [48] in natural units ($\hbar = c = k_{\mathrm{B}} = 1$).

The exact mechanism of thermalisation and the matching from the initial state to the hydrodynamic phase is not yet understood and subject of intense theoretical investigations. Efforts are ongoing to improve the expansion strategy of viscous corrections in hydrodynamics and to stretch its applicability to situations where the longitudinal and transverse pressure are different in order to relax the stringent criterion of very early isotropisation to slightly later stages of the system evolution. An overview of this rapidly evolving field is given in Ref. [58]. Furthermore, theory tries to bridge the gap in the description between the initial conditions and the use of hydrodynamics in a theoretical sound way based on the insights gained recently for the prethermalisation stage [59]. The road towards a smooth matching of the different system phases is described in Ref. [60].

The findings of long-range correlations in rapidity in small collision systems indicating an early creation of the correlation, and their incomplete theoretical understanding, first in pp collisions by CMS [61] and later in p–Pb collisions by ALICE [62], ATLAS [63] and CMS [64] were widely unexpected. The experimental measurements can be also modelled by hydrodynamic calculations [65], although one of the most successful models in A–A collisions is not able to reproduce the data [66]. In fact, it was previously assumed that the energy density gradients occuring in these collisions are too large to establish local thermodynamic equilibrium and to have a basis for the applicability of hydrodynamics at any stage of the collision. The arguments put forward are still valid and question a hydrodynamic description of part of the time evolution on conceptual grounds [67].

Therefore, it is important to understand the size and nature of correlations, which originate from the collision of the two complicated, colliding wave functions in the nuclei and discriminate between their signature and the signature of a thermalised fluid. So far, the colour glass condensate effective theory is one framework where calculations were pursued and which promises to explain at least part of the experimental findings. This recent controversy has also an impact on the understanding of the behaviour of charmonium production in small systems and will be discussed

in Section 2.5.5. In summary, the investigations on the experimental and theoretical side in small systems are important to better understand the situation in A–A collisions: it is important to judge the uniqueness of a given description given the experimental measurements and to understand the applicability regime of hydrodynamic descriptions implying the creation of locally thermalised or nearly locally thermalised matter.

In order to classify the character of the phase transition, the measurement of fluctuations of conserved quantum numbers like charge, strangeness and net baryon numbers are discussed in detail in the literature also at LHC energies[3]. There is the hope to map directly the experimental results to quantities extractable from already available lattice QCD simulations. The comparison between experimental data on fluctuations and lattice QCD simulations was already used as an alternative approach to the thermal model to determine the freeze-out parameters of the created matter [51]. Furthermore, the investigation of the net charge fluctuations might enable to measure the universality class of the chiral phase transition by measuring higher cumulants of the event-by-event net charge distributions and hence higher derivatives of the partition function. This might be possible despite the cross-over character of the transition at vanishing baryochemical potential. However, modelling of critical phenomena in a dynamical way accounting for the relevant differences between the situation in LQCD simulations and experimental data is just about to start. An overview of the challenges related to the analysis of these correlations in experimental data and their theoretical interpretation is given in Ref. [45].

Besides the thermal model description of the bulk particle production and the emission pattern described by models based on hydrodynamic evolution and the fluctuations sector, electromagnetic, weak and hard probes provide a tool to test the properties of the created matter in the laboratory.

The suppression of high-p_{T} hadrons and jets, called jet quenching, first proposed as a signature of the QGP by J.D. Bjorken in 1982 [68], and the modification of the jet fragmentation caused by the propagation of partons through the deconfined medium represents a key sector to characterise the quark-gluon plasma. The suppression of high-p_{T} hadron production compared to pp collision expectations in

[3] At lower beam energies, there might be a sensitivity to a critical end point and the first-order phase transition by remaining signatures of the singular behaviour of higher derivatives of the partition function in the thermodynamic limit.

A–A collisions was first observed at RHIC [69] and was the starting point of the experimental investigation of the phenomenon. Today, a wealth of experimental data including measurements of high-p_{T} hadron suppression of different flavours, fully reconstructed jet suppression, jet asymmetry and jet fragmentation and more sophisticated observables are investigated especially at the LHC thanks to higher production rates and larger available phase space than at lower beam energies and more suitably instrumented detectors. Theoretical insights into the topic are progressing and the full exploitation of the vast experimental material of recent years is just at the beginning [70].

The investigation of electromagnetic probes is of particular interest, since the strongly interacting matter is practically transparent for the emitted radiation and the coupling of the matter to the electromagnetic current contains precious information. At low momentum transfers, direct information from all stages of the system evolution is available. The production of real and virtual photons[4] includes the production of thermal radiation of the created matter. Hence, it provides information about the temperature evolution of the produced medium. At high beam energies, virtual direct photons were measured at RHIC [71] in A–A collisions and real photons both at RHIC [72] and at the LHC [73]. Measurements of anisotropic flow were also undertaken at RHIC [74] and at the LHC [75]. The data indicates that there is indeed a thermal high-temperature photon source at low transverse momentum. The quantitative description of the set of available data, both the yield as well as the anisotropic flow constitutes a large theoretical effort. In the dilepton mass spectrum, the vector states, in particular the modification of the spectral shape of the ρ meson conveys information of chiral restoration. A breakthrough was achieved at the SPS [76, 77, 78], which concluded in the observation of the melting of the ρ meson due to chiral symmetry restoration according to the Rapp-Wambach model, see Ref. [79] for a summary of the comparison with SPS data. RHIC results at different collision energies confirmed this observation in recent years [80, 81].

Furthermore, the dilepton continuum between the ϕ resonance and the J/ψ resonance provides more direct information about the temperature of the system than real photons. After subtraction of other sources like the production from charmed hadrons, the Lorentz-invariant mass of the dilepton enables access to the thermal radiation temperature of the QGP phase. Unlike real photons, the dileptons are not affected by the blue shift created by the radial velocities of the fluid cells from

[4] In this context, we refer to small virtualities, but with values larger than the pion mass.

which they originate.

At large four-momentum transfer, electroweak probes produced in hard partonic encounters serve as candles for the behaviour in absence of strong interaction matter effects as the production of very high-p_{T} photons not originating from hadron decays and of electro-weak gauge bosons.

Finally, quarkonium production is the central observable sensitive to the deconfinement phase transition as conjectured in the seminal contribution of Matsui and Satz [23]. The measurement in p–Pb collisions at the LHC presented in this thesis provides crucial information in this context.

1.2. Outline

The next section of the thesis is devoted to a short introduction into the field of charmonium production at TeV-scale hadronic collisions. After a general introduction, the main concepts for the description of charmonium in pp collisions are presented. The role of charmonium as states sensitive to deconfinement in A–A collisions is explained. Finally, the models describing the modification of charmonium production in p–A collisions are introduced.
Section 3 presents the capabilities of the different LHC experiments for charmonium detection. The ALICE capabilities at mid-rapidity are described in detail. Section 4 describes the data sample characteristics and the methods employed for the event characterisation for the centrality and multiplicity dependent measurements.
The measurement of inclusive J/ψ production at mid-rapidity is presented in Section 5. The measured observables, the selection criteria on pair and track level are introduced first. It follows a description of the $Acc. \times eff.$ corrections, the signal extraction, the pp reference for the determination of the nuclear modification factors and the uncertainties of the measurement.
The results of this thesis are presented in Section 6. Comparisons with other available experimental data and with model calculations are given and discussed in detail. The conclusions and the outlook are given in Section 7.
The appendices present, besides further details on the theory of charmonium production and the analysis, an extended section on the gas system of the ALICE Transition Radiation Detector in Appendix A and of projections for charmonium measurements with ALICE at the LHC in pp and in p–Pb collisions in the data taking period 2015–2018 in Appendix B.

2. Charmonium production in hadronic collisions

2.1. The charmonium family

The investigation of charmonium dates back to the November revolution of particle physics in 1974, when the J/ψ was discovered simultaneously in p–Be collisions at the Brookhaven National Lab [19] and in e^+e^- collisions at the Stanford Linear Accelerator Center [20]. The narrow resonance was soon interpreted as a bound state of a charm and an anticharm quark [82, 83], the first observation of the charm quark. The detection of the J/ψ and the first excited state $\psi(2S)$ found shortly later [84] were crucial to accept QCD as the theory of the strong interaction: the small widths and the emerging spectrum of states could be explained as the property of two bound heavy colour charge carriers interacting with a weak coupling at short distances as predicted by asymptotic freedom.
The mass spectrum of the charmonium states shown in Fig. 2.1 can be derived with percent accuracy from a non-relativistic Schrödinger equation in analogy to positronium in quantum electrodynamics by using a Cornell-type potential, which was first introduced in 1975 [85]:

$$V(r) = -\frac{4}{3}\frac{\alpha_s}{r} + k \cdot r \tag{2.1}$$

The variable r denotes the radial distance between the two colour charges, α_s the running coupling constant of QCD and the string tension k parametrising the non-perturbative long-distance behaviour, which prohibits the release of a free colour charge out of the potential. The factor 4/3 is the Casimir factor of $SU(3)$. A typical value of k is about 0.2 GeV^2 [86]. The long-range limit of this QCD interaction has hence a similarity to 1+1 dimensional QED, i.e., the field lines are getting closer

and closer and forming a flux tube.

The charmonium states below the open-charm threshold cannot decay to non-charmonium states without annihilation of the $c\bar{c}$-quark pair. Therefore, the decay of the charmonium ground states to hadrons by the strong interaction has to proceed via 2 (η_c, para-charmonium) or 3 (J/ψ, ortho-charmonium) hard gluons implying a suppression of the decay width by 2 or 3 orders in α_s. In case of the J/ψ, the decay width via a virtual photon contributes to about 25% [21] to the total decay width being of the same order of magnitude as the decay via 3 gluons. This fact causes the narrow width of 93 keV [21] and consequently long life-time of the J/ψ state.

The form of the potential between two static colour charges can be nowadays derived from lattice QCD studies and follows approximately the phenomenological Cornell-potential shape. Systematic corrections using effective field theory taking into account the non-static character of the charm quarks can be used to calculate the mass spectrum of charmonium from the QCD Lagrangian directly up to high precision [87].

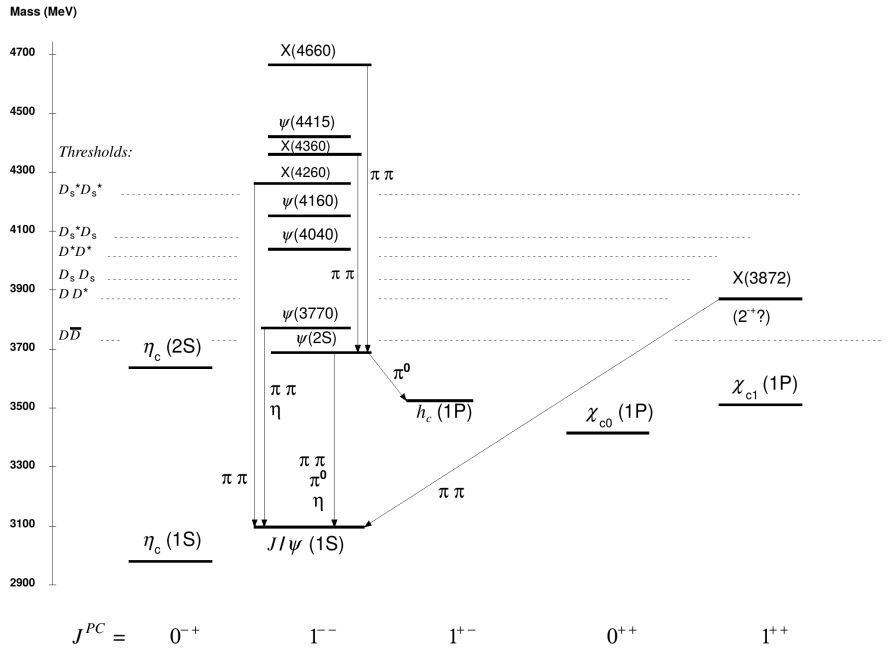

Figure 2.1.: The level scheme of the $c\bar{c}$-bound-states showing experimentally established states with solid lines taken from Ref. [21]. Singlet states are called η_c and h_c, triplet states ψ and χ_{cJ}, and non-conventional charmonium states X. Only observed hadronic transitions are shown; the single photon transitions are omitted for clarity.

Since 1986 [23], charmonium is seen as the most striking probe of deconfinement in heavy-ion collisions. Substantial theoretical and experimental progress has been made since then. Unfortunately, the importance of different mechanisms for charmonium production in proton-(anti)proton (pp/p$\overline{\text{p}}$) and even more in proton-nucleus (p–A) collisions, which is often used as baseline for nucleus-nucleus (A–A) collision results, is not quantitatively understood. The concepts used to describe charmonium production in pp/p$\overline{\text{p}}$, p–A and A–A collisions at the TeV-scale are summarised in the following. Although we restrict the discussion to the charmonium system, the description of bottomonium production is based on the same ideas and concepts with different relative importance of the considered phenomena.

2.2. Charmonium production in hadronic collisions

The inclusive production of charmonium in hadronic collisions is classified by:

1. direct production: production of the $c\overline{c}$-pair by the strong interaction and hadronisation directly to the state measured in the final state.

2. prompt production: direct production and feed-down from other directly produced charmonium states. The decay products of prompt production originate from the primary vertex within the experimental resolutions at experimentally accessible momenta.

3. non-prompt production: production of charmonium states in the decay chain of weak decays of hadrons containing a b valence quark (B-hadron). This component can be separated from the prompt production component of a given state at finite momenta of the B-hadron by the virtue of modern silicon vertex detectors. The first fully experimental separation of the non-prompt component in hadronic collisions was achieved by CDF in 1993 [88]. The method was used for cross section measurements shortly later [89, 90, 91][1].

The prompt J/ψ production, the most commonly measured charmonium state, differential and integrated as a function of transverse momentum, has been measured by all LHC experiments in pp collisions in different kinematic regimes [96, 97, 98, 99,

[1] Earlier methods to deduce the non-prompt component suffered from either model [92, 93, 94] or resolution limitations [95] at hadron colliders.

100, 101, 102, 103, 104, 105, 106] at collision energies 2.76, 7, 8 and 13 TeV. There also exists a high-precision measurement by CDF in $p\bar{p}$ collisions at 1.96 TeV [107]. A selection of results of the ratio of non-prompt over inclusive production with emphasis on low-p_T at mid-rapidity is given in Fig. 2.2.

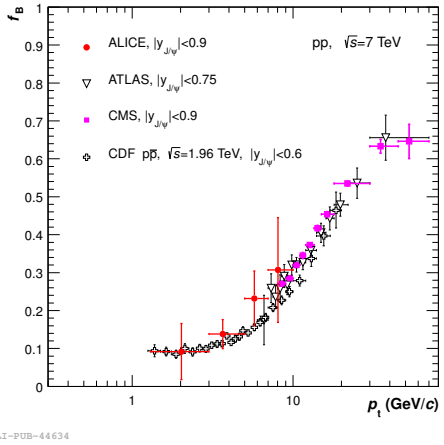

Figure 2.2.: Non-prompt fraction of J/ψ production

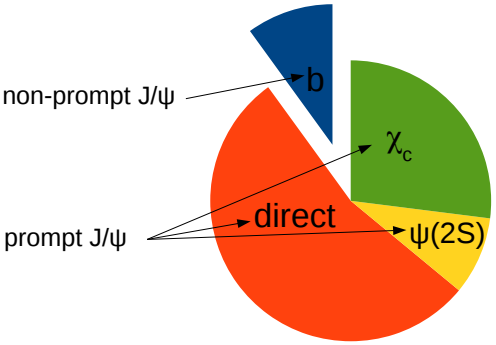

Figure 2.3.: Inclusive J/ψ production integrated over p_T at around $y \approx 0$.

The non-prompt fraction of J/ψ production as a function of transverse momentum at mid-rapidity measured by ALICE [99], ATLAS [96] and CMS [101] at 7 TeV in pp collisions and by CDF [107] at 1.96 TeV in $p\bar{p}$ collisions is shown on the left hand side. At low transverse momentum, the prompt component amounts to about 90%, the feed-down from B-hadrons grows up to 30 % at a transverse momentum of 10 GeV/c and increases further. On the right hand side, the approximate contributions to the inclusive J/ψ production integrated over transverse momentum around mid-rapidity in pp collisions at LHC collision energies are shown.

The b feed-down fraction as a function of transverse momentum does not change beyond the experimental uncertainties between Tevatron at $\sqrt{s} = 1.96$ TeV and LHC at $\sqrt{s} = 7$ TeV for the measurements shown in Fig. 2.2. The rapidity dependence is weak within the rapidity region exploited by the LHC experiments $|y| < 4.5$ in pp collisions[2], although LHCb measured a small, but significant change of the b feed-down as a function of rapidity [105, 106] within their acceptance. The fraction of the J/ψ produced from B-hadron decays amounts to about 10% at low transverse momentum and increases monotonically as a function of p_T as shown in Fig. 2.2. The χ_c feed-down to the prompt J/ψ cross section at low transverse momenta has been measured by CDF [108] ($p_T > 4$ GeV/c) and LHCb [109] ($p_T > 2$ GeV/c) and amounts to about 12%-30% in the measurement acceptance. The contribution of

[2]The rapidity is defined in Section 3.3.

direct $\psi(2S)$ production to prompt J/ψ production can be estimated from prompt ψ(2S) production data and branching ratio measurements. It amounts to about 10% at $p_{\mathrm{T}} \approx 0$ GeV/c transverse momentum rising up to about 30% at around p_{T}=10 GeV/c [110, 111, 112]. Figure 2.3 shows the resulting approximate contributions to inclusive J/ψ production in pp/p$\overline{\mathrm{p}}$ collisions at TeV-scale collision energy integrated over transverse momentum.

2.3. Charmonium production in pp collisions

Since the mass of the $c\bar{c}$-quark pair of about 3 GeV/c^2 is significantly larger than the mass scale given by Λ_{QCD}, perturbative QCD combined with factorisation theorems can be used to calculate prompt charmonium production. All discussed calculations for pp collisions as well as the vast majority of approaches for p–A collisions are based on perturbative QCD. Differences are introduced by the consideration or by neglecting of different diagrams or resummations in different operator-product expansions and the source and extraction strategy of the required non-perturbative factors.

At TeV-scale collision energies, charmonium production at experimentally accessed rapidities ($|y_{\mathrm{lab}}| < 4.5$[3]) and transverse momenta ($p_{\mathrm{T}} < 120$ GeV/c) is dominated by gluon fusion due to the dominance of gluons in the probed Bjorken-x range of about 10^{-2}-10^{-4}. The parton distribution functions of the different partons inside the proton at a factorisation scale of $Q^2 = 10$ GeV^2 as a function of Bjorken-x, which is the relevant scale for the production of charmonium at about $p_{\mathrm{T}} = 0$ GeV/c, are shown in Fig. 2.4. A comparison of the Bjorken-x values probed by the relevant experiments measuring in pp, p$\overline{\mathrm{p}}$ and ep collisions is given in Fig. 2.5.

In a perturbative QCD framework, the production of charmonium is separated in the collision of the partons, which emerge from a non-perturbative state, collide and produce a $c\bar{c}$-quark pair. The partonic production cross section (short distance matrix elements) can be calculated with perturbative QCD. A non-perturbative transition of the $c\bar{c}$-quark pair to the corresponding charmonium bound state follows.

In the case of charmonium production at low transverse momentum, we are facing two challenges:

[3]The rapidity is defined in Section 3.3.

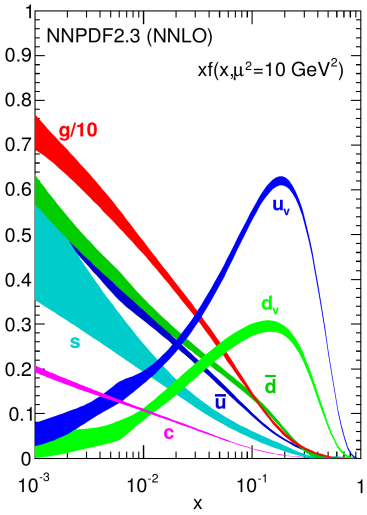

Figure 2.4.: proton PDFs

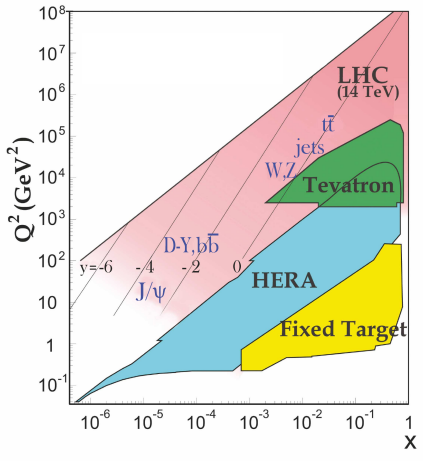

Figure 2.5.: Experimental phase space

Left hand side: The parton distribution functions in the collinear-factorisation scheme for the different parton species based on [113] taken from Ref. [21] for a factorisation scale of about 3 GeV. Right hand side: The accessible values of Bjorken-x as a function of Q^2 for LHC (pp collider), Tevatron ($\mathrm{p\overline{p}}$ collider), HERA (ep collider) and for pp fixed-target experiments taken from Ref. [21]. Typical observables for a given Q^2 are indicated and the corresponding rapidities are given for $\sqrt{s} = 14$ TeV.

1. The collinear-factorisation formalism, widely and successfully used in high-energy physics to calculate production cross sections of jets, weak-gauge bosons and the Higgs particle, is derived in the Bjorken limit: $Q^2, s \to \infty, x_{Bj} \approx Q^2/s = \text{const}$. Charm production including charmonium production at low p_{T} is among the first perturbatively calculable observables at hadron colliders which witness the failure of low-order calculations in this framework, since it is among the final states in hadronic collisions with the lowest still experimentally accessible scale. It is therefore probing the lowest Bjorken-x. Due to the hard scale in the process, charmonium is be still amenable to perturbative QCD, but other factorisation approaches, which are less theoretically developed may give a better convergence behaviour already at lower order by employing a different operator product expansion and different resummation strategies than in the collinear framework.

2. The factorisation with respect to the final state, i.e., the factorisation of the hadronisation of a $c\bar{c}$-pair to quarkonium with respect to the hard interaction, is not settled and different approaches are used for calculations of $c\bar{c}$-

boundstate production in general, not only at low p_{T}.

All perturbative models can be hence classified depending on how they treat the incoming gluon flux and how they handle the transition from the $c\bar{c}$-quark pair to the bound state.
Besides the collinear framework, J/ψ production has been calculated at LHC energies within the k_{T}-factorisation approach and within the colour glass condensate effective field theory ansatz to describe the incoming gluon flux.
The k_{T}-factorisation approach employs the non-perturbative 'unintegrated' parton distribution functions for the description of the initial state. It is designed for low-Bjorken-x, where a large phase space for gluon radiation is available between beam rapidity and the partons participating in the hard interaction. The approach incorporates a finite k_{T} of the incoming gluons, which is not present in the collinear framework introduced above by construction. Nevertheless, the type of diagrams considered in the k_{T}-factorisation appear also in the collinear framework. They are however not absorbed as part of the non-perturbative initial state parton distributions, but have to be computed order-by-order in the hard-scale matrix elements. The k_{T}-factorisation approach attaches a single gluon from each hadron to a charm quark line in the diagrams as in the collinear-factorisation approach. No calculations have been published for p–A collisions. A more detailed introduction to the differences of the different factorisation schemes is given in Appendix C.1 and a short discussion of calculations for charmonium production in pp collisions at the LHC within the k_{T}-factorisation approach is given in Appendix C.1.2.
However, it is possible that more than two gluons from the initial state are attached to the quark line. This type of diagrams naturally violates factorisation in the collinear- and the k_{T}-factorisation scheme and is power suppressed by $1/Q^n$. These terms are beyond the 'leading-twist' approximation which is used in collinear factorisation. In principle, a large number of gluons can be attached to the quark line. It is in particular expected in the Regge limit of QCD of $x \to 0$, where the hadron becomes a densely-packed object, that these diagrams become important. This kind of diagrams might already be parametrically non-negligible for charmonium production due to the very high gluon densities probed at the Bjorken-x by low-p_{T} charmonium. One possibility to deal with this dense regime of QCD, allowing for multiple gluon radiation both in the initial state as well as multiple attachments of gluons to the quark-line in the concerned diagrams is the effective field theory

Colour Glass Condensate (CGC), for a review see [114], which treats the valence quarks as static colour sources on the light cone. This ansatz enables a separation of the gluon dynamics at low-x, which turn out to be describable by classical field theory for leading-order calculations. The framework has been also applied to charmonium production in pp collisions by assuming the dense state only for one hadron and a dilute prescription for the other hadron. The set-up is particularly well suited for forward rapidity production in pp collisions. In this framework, calculations could be done at LO and are described in detail in Appendix C.1 and in Section 2.5.2 for the p–Pb collision system.

In summary, the described approaches make different bets on the importance of the contributing diagrams either starting from the Regge limit or in the Bjorken-limit of QCD. However, both limits are not well fulfilled by charmonium production at the LHC, since Bjorken-x is neither in the optimal applicability range of collinear factorisation of about 0.1, nor is it expected that the saturation scale is reached already at the scale of charmonium production at the LHC in pp collisions.

Depending on the non-perturbative transition to the bound state, different hard partonic cross sections (short distance matrix elements) or different weights of them enter the calculation. The assumption on the transition also changes the kinematics due to different gluon phase-space in the final state and hence the probed kinematic regions of the gluon distribution functions. In addition, the polarisation of the most commonly measured charmonium vector states depends strongly on the weight of the short-distance matrix elements to the total production. The polarisation presents the largest systematic uncertainty on the production cross section for most kinematic regions, if not measured experimentally. Fortunately, when measured, the polarisation in quarkonium production turned out to be rather weak. The standard approach of isotropic decay in the resonance rest frame for the correction of acceptances hence appears to be a good approximation.

Concerning the transition between the $c\bar{c}$-pair and the bound states, the Colour Singlet Model (CSM), Non-Relativistic QCD (NRQCD) approaches and the Colour Evaporation Model (CEM) are used for calculations. A fragmentation function approach has been discussed in the literature, but this is particularly designed for high-p_{T} production. It is mappable to NRQCD by a reordering of the contributions and is hence not further discussed here. A short explanation of its relation to the NRQCD approach and further references can be found in Ref. [115].

The CSM assumes that the $c\bar{c}$-pair is produced with the proper quantum num-

bers including colour of the bound state that it is projected to[4]. For direct orthocharmonium production as J/ψ, the non-perturbative transition probability can be extracted from the electromagnetic decay width. The model has therefore high predictive power and was put forward in the collinear framework up to NLO and even parts of the NNLO corrections. A more detailed introduction is given in Appendix C.2.2.

The NRQCD approach [116] uses effective field theory exploiting the scale hierarchy given in the non-relativistic bound state to evaluate by power counting in the relative quark velocity v which Fock state configurations contribute to the bound state production. The collision-system independent, non-perturbative factors called Long Distance Matrix Elements (LDME) needed for the projection are typically extracted by fits to experimental data in absence of precise non-perturbative theoretical calculations from, e.g., lattice QCD. The NRQCD approach has been put forward up to NLO for the p_{T}-differential cross sections in α_s and $O(v^4)$ in the collinear framework and up to leading order in k_{T}-factorisation as well as in the CGC framework. NRQCD factorisation has been proven for high-p_{T} charmonium production [117]. It naturally includes the CSM contributions, which are of $O(v^0)$ for direct orthocharmonium production. This approach is in principle the theoretically most sound approach. However, no conclusion based on data comparisons could be so far achieved due to considerable number of parameters and different opinions on the range of applicability of the NRQCD collinear framework at low p_{T}. A recent overview is given in Ref. [118]. A more detailed account with references to different calculations employing NRQCD factorisation is given in Appendix C.2.3. A hybrid approach [119] employing NLO collinear factorisation at high p_{T} and LO CGC calculations at low p_{T} promises to resolve the discrepancies between data and theory in the NRQCD calculations mentioned before. However, calculations have been only undertaken for a subsample of the available experimental data on quarkonium. In particular, polarisation calculations proved to provide stringent model tests in the past and have not been provided yet in the novel approach. For a conclusive picture, calculations need to be carried out consistently for the whole available data set. In addition, the resummation of logarithms of the type $log(p_{\mathrm{T}}/M_{c\overline{c}})$, instrumental for the precise Higgs particle production cross sections at the LHC, are not yet taken

[4]The wave function of the bound state can be decomposed in a Fock state representation of which the components are identified with the outgoing state of the hard partonic interaction. Hence, the transition from the outgoing state of the hard partonic interaction to the bound state can be quantified by a quantum mechanical projection.

into account for any calculations although they may play a role for the description at low p_{T} [120].

The Colour Evaporation Model (CEM) assumes that the $c\bar{c}$-pair production below the open-charm threshold is distributed among the different charmonium states without precise tracing of the quantum numbers at the time of the projection to the bound state. Every direct charmonium-state production contribution receives one non-perturbative factor independent of the collision system. The CEM therefore provides strong predictive power. However, no polarisation calculations have been undertaken and the model is often regarded rather as an estimate than a precise calculation of the cross section. NLO calculations are available in the collinear-factorisation framework. A more detailed description of the CEM can be found in Appendix C.2.1.

To date, no comprehensive theoretical description of cross section and polarisation data of prompt charmonium production down to low p_{T} at hadron colliders exists [118]. In particular, the lack of understanding of the transition to the non-perturbative final state is the main physics motivation for precision cross section and polarisation measurements in pp collisions at hadron colliders. In addition, pp data are reference measurements for heavy-ion collision data. The struggles to describe the transition from the $c\bar{c}$-pair to the bound state prominently reflect that the dynamics of hadronisation and thus confinement are still far from being quantitatively understood for two colour charge carriers moving at non-relativistic relative velocities in the environment of high-energy hadronic collisions. Eventually, non-perturbative calculations for the transition to the bound state and advances in the factorisation tools should provide a fully consistent and quantitative picture based directly on QCD.

The production of charmonium in pp collisions is hence an excellent laboratory to test the applicability of state-of-the-art perturbative QCD methods and its interplay with non-perturbative QCD in difficult territories.

2.4. Charmonium production as messenger of deconfinement in heavy-ion collisions

In heavy-ion collisions, the suppression of J/ψ production has been proposed as a signature of deconfinement in 1986. The understanding of charmonium production in nucleus-nucleus (A–A) collisions has been since then a major goal of heavy-ion research on the experimental and on the theoretical side.
Given the fact that the hadronic production of charmonium in pp collisions is only qualitatively understood, it is a priori not evident how to define a baseline expectation for heavy-ion collisions. In addition, the interaction of a $c\bar{c}$-quark pair with the soft degrees of freedom produced in the collision is in principle sensitive to quantum effects in QCD and out-of-equilibrium physics, which are difficult to address quantitatively. The application of concepts and findings in systems in thermal equilibrium up to different degrees and/or classical pictures is based on assumptions which are difficult to test experimentally or difficult to deduce directly from QCD. Despite these complications, it is possible to give predictions for certain underlying physical pictures. They can be tested experimentally. The collisions at the LHC are in this respect more straightforward to treat than collisions at lower centre-of-mass energies thanks to a better separation of scales.

2.4.1. The initial idea

The early conjecture of Matsui and Satz [23] is based on the analogy of the screening in a plasma of colour charges with the screening of electrical charges in an electromagnetic plasma. The phenomenologically known non-relativistic potential in Equation (2.1) of two static colour charges is screened in this picture and the following colour screened Coulomb-like potential arises:

$$V(r) = -(\alpha_{eff}/r)\exp(-r/r_D(T)) \tag{2.2}$$

where α_{eff} denotes the effective coupling for the Coulombic term and r_D the screening length. When the screening length is larger than[5] the classical bound-state ra-

[5] In the classical calculation by Matsui and Satz, the bound states do not disappear exactly for radii larger than the screening length. A factor of O(1) appears for this condition.

dius, the corresponding bound state will disappear at the given temperature. The screening length scales with $1/T$ in the weak coupling limit of a gas of quarks and gluons [121][6].

After this initial idea, a lot of effort was invested to derive the exact temperature dependence of the bound-state behaviour with increasing sophistication based on QCD. Although the exact behaviour relevant for the states occurring in nature are still not fully settled, it became evident from effective field theory approaches [122] that not only the real part of the potential in the Schrödinger equation is relevant, but also the imaginary part. The imaginary part corresponds to a decay width representing a dissolution of the charmonium state in addition to the bound-state spectrum modification due to the change of the real part of the potential. The gain in understanding of the static behaviour in a thermal heat bath of charmonium can be expected to approach maturity in the coming years. In fact, spectacular progress has been made recently [123]. Unfortunately, a dynamical description of a moving $c\bar{c}$-quark pair in a non-static medium remains already conceptually a challenge and ab-initio theory just started to address these questions, see, e.g., Ref. [124].

All phenomenological ansätze described in the following are hence based on assumptions of the bound-state behaviour in the QGP, which are not rigorously shown based on the QCD Lagrangian. In addition, all currently discussed models rely on the assumption that the number of charm and anticharm quarks is approximately conserved throughout the evolution of the system after the creation of the charm quarks at a time scale of $t \approx \frac{1}{2 \cdot m_c}$ in the restframe of the $c\bar{c}$-quark pair. This assumption is justified, since the mass scale of the $c\bar{c}$-quark pair in the medium is much larger than the expected temperatures, i.e., thermal production contribution is small at LHC collision energies. This naive expectation is confirmed by numerical estimates [125, 126]. Furthermore, the rate of charm-annihilation has been estimated as well and is found to be negligible [127] at the relevant charm-quark densities.

Due to charm conservation, the ideal observable to test modifications of charmonium production is the comparison of charmonium to the inclusive charm production, which is dominated by open-charm hadrons. Charmonium production contributes only with about 0.7% to the total charm production cross section at 7 TeV in pp collisions in the LHCb acceptance [104, 128].

[6] As explained in Ref. [121], this is only the case for ultra-relativistic charge carriers in a plasma. In the non-relativistic case, the screening length actually increases as a function of T.

However, due to restricted experimental accessibility to the open-charm cross section, the production rate of J/ψ in A–A collisions has been compared to the production in pp collisions scaled with appropriate factors in the so-called nuclear modification factor R_{AA}[7]:

$$R_{\mathrm{AA}} = \frac{\mathrm{d}N/\mathrm{d}y^{\text{A-A}}_{\mathrm{J}/\psi}}{<N_{\mathrm{coll}}> \cdot \mathrm{d}N/\mathrm{d}y^{\mathrm{pp}}_{\mathrm{J}/\psi}} = \frac{\mathrm{d}N/\mathrm{d}y^{\text{A-A}}_{\mathrm{J}/\psi}}{<T_{\mathrm{AA}}> \cdot \mathrm{d}\sigma/\mathrm{d}y^{\mathrm{pp}}_{\mathrm{J}/\psi}}, \tag{2.3}$$

where $\mathrm{d}N/\mathrm{d}y_{\mathrm{J}/\psi}$ denotes the yield in a rapidity range in the corresponding collision system, $<N_{\mathrm{coll}}>$ the mean number of binary nucleon-nucleon collisions extracted from a Glauber model and $<T_{\mathrm{AA}}>$ the mean nuclear overlap function from a Glauber model. $\mathrm{d}\sigma/\mathrm{d}y_{\mathrm{J}/\psi}$ is the corresponding J/ψ cross section. The phenomenological and experimental foundations of the Glauber model, the concept of centrality and its application are explained in detail in Reference [129]. The Glauber model aspects relevant for the centrality determination in p–A collisions are introduced in Section 4.3.1.

The formula is given for the production in a given rapidity window integrated as a function of transverse momentum. In absence of any nuclear effects, the nuclear modification factor R_{AA} equals unity. The original idea of Matsui and Satz of suppression of charmonium production in A–A collisions by deconfinement is an idealisation and requires that the creation process of the charmonium states is not different compared to properly scaled pp collision expectations and that they are in thermal equilibrium with the medium after their creation. The original proposal of Matsui and Satz was based hence on an instantaneous thermalisation. The underlying picture consists of having formed the J/ψ bound state before the QGP formation. The J/ψ meson and not a preresonant state experiences the effect of colour screening [86] as it is also the case in equilibrium lattice QCD calculations. In Ref. [130],the simplification was used that all $c\bar{c}$-quark pairs for which the resonance formation time exceeds the flight time in the QGP are not modified at all, whereas all other $c\bar{c}$-quark pairs are fully affected by colour screening. The idea was further developed by using the indications from lattice QCD of different dissolving temperatures of the quarkonium states as a thermometer for the QGP [130]. This behaviour would be visible also in the inclusive J/ψ cross section due to the feed-

[7] The original proposal was a comparison with Drell-Yan production, which was done at SPS energies, but which is not achieveable at LHC and RHIC energies due to the increasing dileptons from charm production. In addition, the comparison is always limited by the statistics of Drell-Yan pairs.

down contributions from χ_c and ψ(2S) to the J/ψ production.
It is clear that this picture presents a simplification of the actual situation, since the formation process itself is influenced by the presence of colour-charge carriers. In addition, thermalisation takes time and does not happen instantaneously, i.e., the wave function of the bound state needs time to 'feel' its environment.

2.4.2. Time scales at the LHC

For the description of charmonium in A–A collisions, the following time scales are relevant: the crossing time of the two nuclei, the formation time of the $c\bar{c}$-quark pair, the time until the light-flavour quarks and gluons thermalise, the time until the c-quarks and/or a $c\bar{c}$-quark pair is thermalised, the time scale for the lifetime of the deconfined medium, the time scale for the colour neutralisation of the $c\bar{c}$-quark pair, the hadronisation time scale between the creation of the $c\bar{c}$-quark pair and the formation of the given bound state in vacuum as well as in a QGP. Some calculations also introduce an influence due to the presence and lifetime of a hadronic phase after the phase transition in particular in case of the loosely bound $\psi(2S)$, e.g., in Ref. [131]. It is important to note that the mentioned numbers are time scales, not durations: they describe ensemble averages and are locally varying within the system created within a collision. This implies that a 'factorisation' of the different processes based on their characteristic time is only justified when the process time scales are different by sufficiently large factors. Otherwise fully dynamical pictures need to be applied describing the processes in overlapping time regimes, which are considered yet to be out of scope of present modelling.
At the LHC, it is usually assumed that a quark-gluon plasma state in local thermal equilibrium is created even before the hadronisation of charmonium would be finished in vacuum: the description of bulk properties with hydrodynamic simulations requires the assumption of thermalisation between 0.1-1 fm/c and the hadronisation time of J/ψ τ_ψ can be estimated with different ansätze and amounts to about $0.3 - 1.0$ fm/c [132, 133, 130, 134, 135] in the $c\bar{c}$-quark pair restframe. The fluid life-time is about 5-10 fm/c at the LHC [45], which gives roughly the scale for the QGP lifetime τ_{QGP}. The duration of the colour neutralisation process of the $c\bar{c}$-quark pair might also depend on the dominant production mechanism: rather short

in case of the colour singlet model or coinciding with the time of the hadronisation in case of a soft colour neutralisation as suggested by a dominance of the colour octet mechanism [136].

The energy loss of a colour charge carrier has been estimated early on based on theoretical considerations [137]. It amounts to about $\Delta E \approx 30$ GeV for a very highly energetic quark traversing a medium of 10 fm neglecting differences between quarks of different flavours due to the dead-cone effect causing weaker gluon emissions for heavy quarks as explained in Ref. [22]. Results from comparisons with experimental data still lead to similar estimates [138][8]. One could also roughly estimate the charm thermalisation time $\tau_{\text{c-therm}}$ by considering the involved scales in the system $\tau_{\text{c-therm}} \approx \frac{M_c}{T} \cdot \tau_{\text{therm}}$. With typical numbers from hydrodynamical simulations, this estimate of $\tau_{c-therm}$ is indeed smaller than τ_{QGP}. Hence, a (partial) thermalisation of the bulk of the 'hot'[9] initially produced charm quarks seems possible at the LHC. In summary, the following ordering of time scales at the LHC is expected:

$$\begin{aligned} \tau_{\text{crossing}} << \tau_{\text{therm}} < \tau_{\text{c-therm}} < \tau_{\text{QGP}} \\ \text{In addition: } \tau_{\text{QGP}} >> \tau_{\psi} >> \tau_{\text{therm}} \end{aligned} \tag{2.4}$$

Therefore, it seems natural to either expect $c\bar{c}$-bound-state formation within the QGP lifetime, if they can exist in the QGP, or at the hadronisation stage for the bulk of the $c\bar{c}$-quark pair production at low p_{T}, but no existence of charmonium states prior to QGP formation at the LHC. In addition, thermal concepts should be at least partially applicable for the produced $c\bar{c}$-quark pairs.

2.4.3. Late stage production via (re)combination

In 2000, two groups proposed two distinct mechanisms for charmonium production at late stages. They predicted an enhancement with respect to a melting scenario at large beam energies and possibly an enhancement with respect to expectations based on pp collisions without a consideration of deconfinement [139, 140].

[8] The energy loss is of course also dependent on the energy of the parton itself and on the path length, but we only want to indicate the rough scale of the phenomenon.

[9] The p_{T} spectrum is harder than thermal, the $\langle p_{\text{T}} \rangle$ of J/ψ production in pp collisions at the LHC is about 3 GeV/c at mid-rapidity. Open-charm measurements at the LHC at mid-rapidity do not reach sufficiently low p_{T} to determine $\langle p_{\text{T}} \rangle$ reliably.

In the first model, it is assumed that there are no bound states formed before or during the lifetime of the deconfined medium. They are all produced at the chemical freeze-out from initially produced $c\bar{c}$-quark pairs with thermal statistical weights between the different charmed hadronic states. This scenario is illustrated in Fig. 2.6. More details are given in Refs. [141, 127, 142].

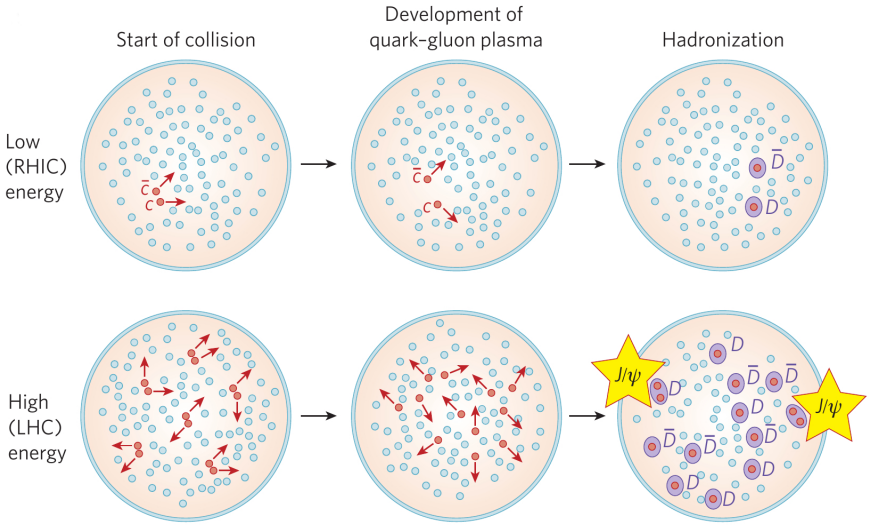

Figure 2.6.: Illustration of the statistical model [139] assuming the production of J/ψ at the phase boundary between the QGP and ordinary hadronic matter taken from [46].

In the second scenario, the J/ψ production occurs via destruction and formation of the bound states in the QGP implemented within a transport approach. It is the solution of the Boltzmann equation for charm quarks considering $c\bar{c}$-bound-state formation or simplifications of it by ignoring the spatial dependencies. This approach has been followed up in various incarnations and with different input assumptions for the involved cross sections and different type and levels of sophistication for the description of the bulk matter [143, 144, 145, 146, 147, 148, 149].

In the limit of large formation cross sections or long QGP lifetimes, the transport approaches lead to the same result as the statistical model, if the freeze-out temperature and the relevant volume are taken to be the same. The statistical model result for charm production hence represents the equilibrium limit of the transport model approach: if the system is completely thermalised at the end of the time evolution, it has no memory of its past and the result becomes independent of interaction cross sections used in the transport approach and the solution of the calculation

will be the equilibrium limit. In the statistical hadronisation model, it is assumed that the cross sections for resonance formation are large at the phase boundary and the hadronic abundances hence reflect the equilibrium weights between the open- and hidden-charm particles due to the non-perturbative process of hadronisation. Both types of models are able to describe the global features of the observations at RHIC and at the LHC in A–A collisions [150]. However, the input charm cross section, which is the most important parameter in the calculation, varies by about a factor two, see Ref. [150] and references therein. Furthermore, the transport models differ in the underlying assumptions and results used for the resonance formation and destruction cross sections. The unknown initial charm production cross section is the main motivation for the investigation of charmonium production in p–A collisions from the QGP physics perspective.

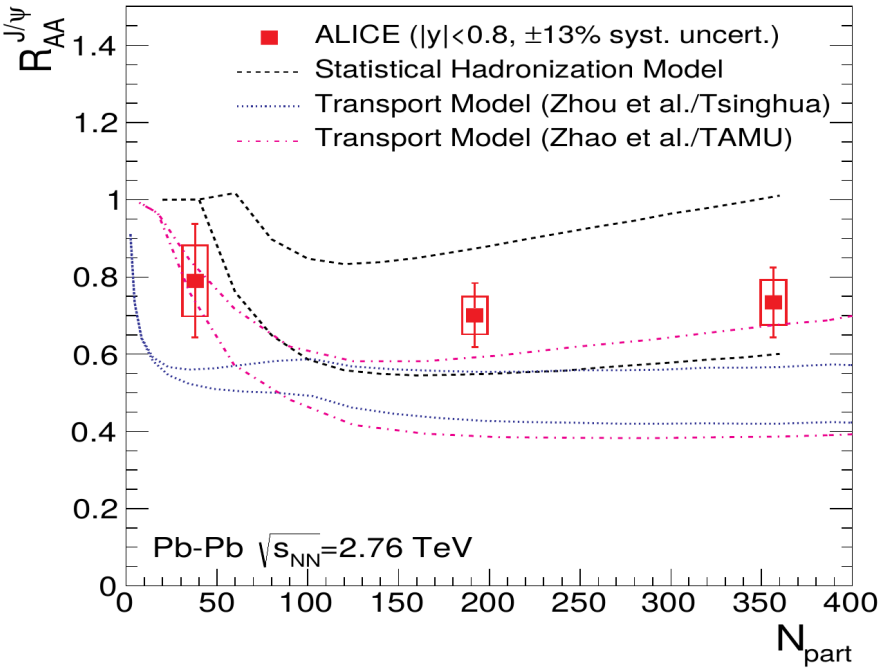

Figure 2.7.: The nuclear modification factor of inclusive J/ψ production at mid-rapidity as a function of centrality at the LHC [150]. The data [151] is compared to the statistical hadronisation model [142] and the transport model by the TAMU [146, 145] and the Tsinghua groups [152, 153, 143, 144]. The bands denote the uncertainties due to the imprecise knowledge of the charm cross section assumed in the different approaches.

2.5. Charmonium production in proton(deuteron)-nucleus collisions

In addition to deconfinement, it is necessary to consider the effects which are present in nucleus-nucleus collisions in the absence of deconfinement. A nucleus-nucleus collision cannot be reduced to an incoherent superposition of nucleon-nucleon collisions in this gedankenexperiment. Hence, it is important to quantify these phenomena for the determination of deconfinement effects on charmonium production in nucleus-nucleus collisions. Traditionally, they are studied in proton(deuteron[10])-nucleus collisions. We will introduce the main concepts for the discussion of the results of this thesis in Section 6.

In the literature, these effects are often summarised as 'cold nuclear matter' (CNM) effects. We will avoid this term, since it does not appear very instructive to talk about CNM in the context of modification of J/ψ production at LHC collision energies. The term is contrasted to 'hot' nuclear matter with which the creation of a deconfined thermodynamic system is meant. However, the notion 'matter' is not used here in the sense of an equilibrium ensemble and 'cold' is not corresponding to a temperature in the absence of equilibrium. Furthermore, most of the discussed modifications of J/ψ production in p–A with respect to pp collisions are effects which are also present in pp collisions and which are only parametrically enhanced: most of the discussed effects are related to multiple scattering or multiple gluon radiation which also occur in pp collisions despite a smaller relative importance for the same kinematic regime. This fact is naively expected, since the crossing time of the proton through the nucleus is the shortest time scale in the process and the transverse size of the spot resolved by the production of a $c\bar{c}$-quark pair is much smaller than the size of an individual nucleon inside the nucleus.

2.5.1. Nuclear absorption

This mechanism describes the interaction of the not yet fully formed J/ψ resonance with the nucleons in the colliding nuclei. It has been considered as the main effect

[10] At RHIC, only deuteron-nucleus collisions were recorded until 2014.

of nuclear modification in p–A collisions at SPS energies up to $\sqrt{s_{\mathrm{NN}}} = 29$ GeV. Parameterisations were extracted from p–A collisions by experimental collaborations and applied to A–A collisions, see, e.g., in Refs. [154, 155]. The term 'anomalous' suppression was coined, i.e., suppression in A–A collision beyond the suppression based on the extrapolation from p–A data. The implied parametrical dependence of the correction of the nuclear absorption was criticised in Ref. [156, 157] and in earlier publications referenced therein.

At the LHC, however, the crossing time of the proton through the nucleus of about 10^{-2} fm/c is much shorter than the formation time of the J/ψ and other charmonium states and of the order of the formation time of the $c\bar{c}$-quark pair. It is therefore expected that the nuclear absorption plays no role at LHC energies. Indeed, the vanishing importance of the nuclear absorption can be shown theoretically based on Glauber-Gribov scattering theory [158, 159].

2.5.2. Gluon shadowing, multiple scattering and saturation physics

It is known via measurements of deep inelastic scattering and Drell-Yan production in p–A collisions that the parton distribution functions extracted from data in the collinear-factorisation framework are modified in the nucleus compared to the free proton. Parton distribution function modifications were derived for valence and sea-quarks. The modification of the gluon distribution functions is assumed to behave similarly in most models [160]. As physical origins of this modification, multiple scattering of the colour dipole originating from the probing virtual photon with the nucleus is mainly discussed. However, an overall consistent theoretical description of the experimental facts is missing [160]. The different regimes in Bjorken-x of the nuclear modification of the structure function F_2 are shown in Fig. 2.8.

Of course, this modification does not exclusively influence Drell-Yan production in p–A collisions, but also observables with hadronic final states and hence charmonium production.

Nowadays, the effect is mostly treated by a DGLAP evolution of the Parton Distribution Function (PDF) modification as a function of Q^2 at Next-Leading-Order (NLO) in collinear factorisation [161, 162, 163, 164, 165, 166]. The nuclear PDFs at low Bjorken-x suffer from large uncertainties due to insufficient experimental con-

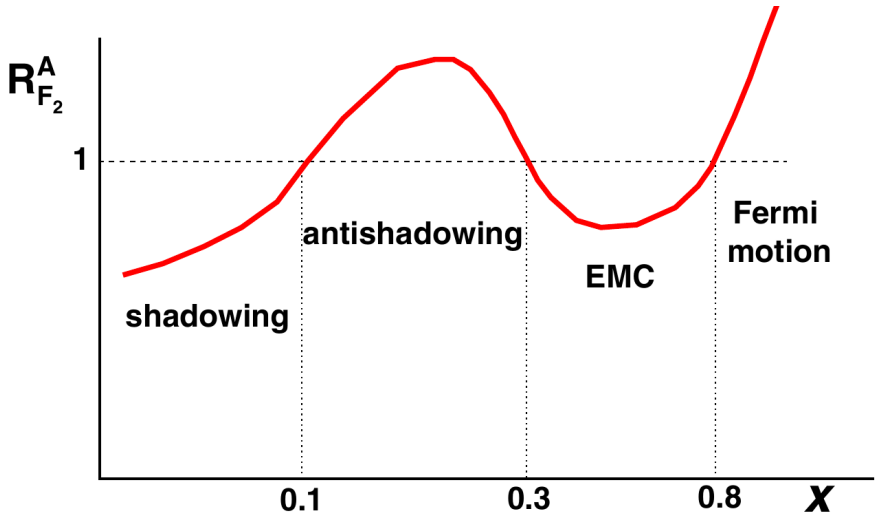

Figure 2.8.: Different regimes of nuclear modification of the parton distribution function expressed by the ratio between the structure functions in the nucleon and in the nucleus with atomic mass number A: $R^A_{F2} = F_2^A/(A \cdot F_2^{\text{nucleon}})$. The figure is taken from Ref. [160].

straints. The resulting distributions therefore strongly depend on the input parameterisation at the starting scale for the DGLAP evolution equation and the selection of the input data for the fits [166]. Either only Deep Inelastic Scattering (DIS) in e–A collisions and Drell-Yan (DY) or also hadronic final state results from p–A(d–A) collisions are taken into account. The usage of hadronic final state results from p–A (d–A) collisions for the PDF-fits requires the assumption that the hadron production is only or at least dominantly modified by this specific type of shadowing and not by other effects. A summary of the experimental data considered for the parameterisation of the nuclear parton distribution functions in the Q^2-x plane is shown in Fig. 2.9. In addition, a treatment of shadowing in the PDFs implies that it is indeed a so-called leading-twist effect, i.e., that it is not produced by power-suppressed contributions and neglected in the operator product expansion underlying the collinear-factorisation framework. Since it is conceptually not settled, how to compute the shadowing corrections explicitly, it is not clear whether this assumption holds. It has been argued in Ref. [167] that leading-twist shadowing is negligible even at the LHC despite the low Bjorken-x values probed.

The parameterisation EPS09 [163] for the nuclear modification is most popular. It shows a sizeable shadowing in the gluon distribution functions. It will be shown and discussed combined with various models calculating J/ψ production. However,

it is not clear that hadronic final states in p–A collisions can be used to provide evidence for a sizeable effect of leading-twist shadowing in this parameterisation.

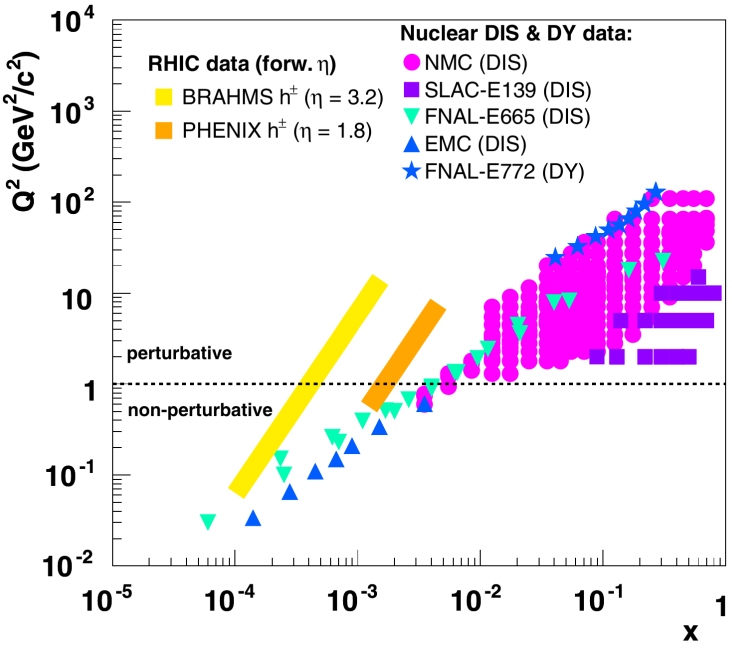

Figure 2.9.: Q^2 and Bjorken-x of experimental data used for the extraction of the shadowing parameterisations. The graph is taken from Ref. [160].

Quarkonium production in Ultra-Peripheral nuclear Collisions (UPCs) can constrain the nuclear parton distribution functions [168]. Figure 2.10 shows the leading-order process for this production mechanism involving the virtual-photon cloud of one nucleus. The corresponding cross section is proportional to the square of the gluon parton distribution function of the nucleus at leading order. The measurement of the coherent production of J/ψ compared to models illustrates this discrimination power prominently in Fig. 2.11. However, the level of model uncertainties due to approximations in the calculations is presently too large to exploit the power of the already available data [169, 118].

Alternatively to the collinear treatment, the calculation of charmonium production in A–A collisions probes a low enough Bjorken-x range that a treatment in the CGC ansatz may become even more appropriate than in pp collisions, since the saturation scale is proportional to $A^{1/3}$, where A denotes the atomic mass number of the nucleus. The theoretical framework is introduced in depth in Ref. [171]. Calculations for charmonium production within the Color Glass Condensate (CGC) have

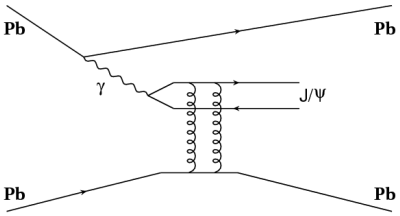

Figure 2.10.:
Vector meson production in UPC at leading-order from Ref. [170].

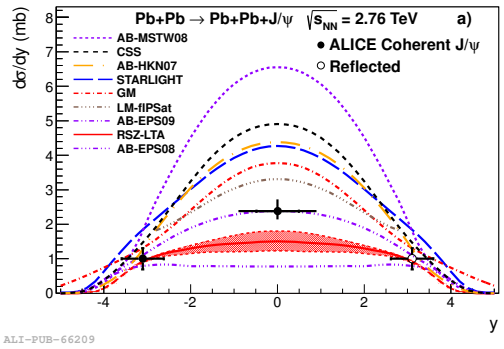

Figure 2.11.:
Coherent J/ψ production in UPC by ALICE compared to models [169].

been combined with the Colour Evaporation Model (CEM) and the Non-Relativistic QCD (NRQCD) and will be shown in the discussion of the results of this thesis in Section 6.

The approach in the framework of colour-dipole phenomenology presented in Ref. [156] is in spirit related to a CGC approach. The coherent gluon emission causing higher-twist 'charm' shadowing identified as dominant modification in the lead-ion rest frame can be qualitatively matched to effects also present in the CGC approach in the infinite momentum frame. However, a first calculation presented in Ref. [172] was off by a factor between 2 and 3 from the LHC data. We will hence not discuss this specific approach more in detail.

In summary, the experimental data sample in theoretically clean cases such as deep inelastic scattering in e–A collisions and Drell-Yan in p–A and the theoretical understanding of ultra-peripheral A–A collisions is not yet sufficient to discriminate between different phenomenological approaches or to independently constrain the precise magnitude of gluon shadowing in the parton distribution functions in the kinematic range relevant for inclusive J/ψ production at the LHC.

2.5.3. Coherent energy loss

Arleo and Peigné argued that the formalism used for the energy loss of partons in a nucleus and in hot QCD matter is applicable to a $c\bar{c}$-colour dipole. They used hence their coherent-energy-loss model based on small-angle gluon radiation to J/ψ production in p–A collisions. The effect might represent the main nuclear effect in

proton-nucleus data [136]. The main point of their argumentation is that the interference of gluon emissions from initial and final state radiation is important in contrast to another approach considering parton energy loss for the modification of J/ψ production at TeV-scale energies [173]. The latter approach was only applied to high-p_{T} charmonium production and is not further considered in this thesis for comparison. A short explanation about the differences of the used approaches is given in Ref. [174]. A pictorial view of the process is shown in Fig. 2.12.
The effect is a higher-twist effect, i.e., it is by construction not included in a pure collinear-factorisation approach. It was pointed out in Ref. [175] that the approach relies on the separation of time scales between the $c\bar{c}$-quark production and the gluon radiation from the $c\bar{c}$-quark pair, which is not justified at the LHC in particular at forward rapidities. The latter requirement for the calculation is not present in the CGC calculations as the one in Ref. [175].

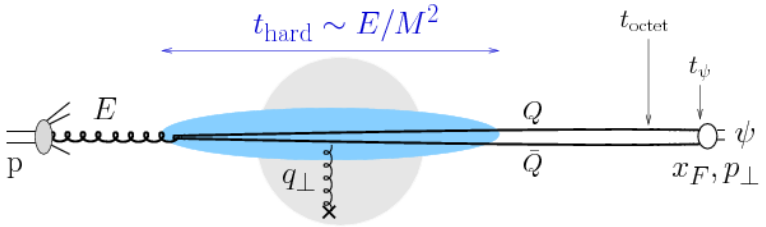

Figure 2.12.: Illustration of the coherent energy loss of the colour dipole in the nucleus before forming the charmonium resonance. The picture is taken from Ref. [136].

In addition, it is assumed that the colour dipole is in a colour octet state for a significant time fraction of its travel through the nucleus and is therefore radiating off gluons. The ansatz crucially depends on a long duration of the colour neutralisation process and favours therefore the dominance of a contribution of colour octet amplitudes to the total cross section due to its applicability at low Feynman-x according to the authors [136]. The only free parameter of this scenario is the energy transfer, which is fixed from fixed-target data. Detailed comparison of the coherent-energy-loss model with the experimental data will be shown and discussed in Section 6.

2.5.4. Cronin effect and p_t broadening

Comparing the production of hadrons in p–A collisions to pp collisions, an enhancement of hadron production at a transverse momentum of a few GeV/c has been found by Cronin et al. [176], the so-called Cronin-effect. This observation was confirmed in many other cases and is usually interpreted as a sign of multiple scattering of the partons in the nucleus prior to the hard scattering, for a review see [177]. This effect was proposed early on to be relevant for J/ψ production [178]. It increases the average transverse momentum squared of J/ψ production. It is hence called p_{T} broadening.

The effect is sometimes incorporated in phenomenological models for J/ψ production in p–A collisions [179, 173]. However, the particular mechanism proposed in Ref. [178] stems from gluons from different nucleons which is not the proper description at LHC energies, since coherence between the gluon scattering sets in as argued in Ref. [180]. The scattering centres are not resolved any more. This fact leads in this picture to a reduction of the effect at larger collision energies. This was observed in experimental hadron p_{T} spectra at the LHC, where only a hint of the Cronin peak can be observed [181]. In Ref. [182], it was argued that only the consideration of both the multiple scattering before and after the hard interaction can account for hadronic final states. These two contributions were added in Ref. [182] without consideration of coherence between the two contributions. The latter approach produces naturally a sizeable difference between the p_{T} broadening of Drell-Yan and the one of charmonium production. It well describes the centrality-differential p_{T} broadening of J/ψ production measured by ALICE at forward and backward rapidity [183]. In the coherent-energy-loss approach, the p_{T} broadening is attributed to the mentioned small-angle gluon radiation [174]. The ALICE data on centrality-dependent broadening is qualitatively described by the approach, but not quantitatively at forward rapidity. Calculations exist which associate the Cronin peak with the modification of the nuclear PDFs at intermediate Bjorken-x, the 'antishadowing' region shown in Fig. 2.8. A short discussion of different models for the description of the Cronin effect can be found in Ref. [177]. Furthermore, the appearance of the peak at RHIC and LHC energies in hadron p_{T} spectra is claimed to appear already within the CGC framework without the consideration of additional effects [184].

Finally, the dependence of the peak on the particle species in the inclusive hadron

data at the LHC is appreciable [185]. The effect is dominantly present for protons. This behaviour was also interpreted as radial flow due to a collective expansion. Alternatively, it could indicate that effects from the hadronisation of the colour tubes like colour reconnections [186] are responsible for the particle-species dependence, since they can produce similar effects as the conjectured collective expansion in pp collisions. A discussion is given in Ref. [185].
Similarly to the single-hadron observables, the p_{T} broadening of heavy-quark production is claimed to be already fully included in the CGC approach [171]. In summary, it remains unclear how the effect needs to be incorporated at the LHC in addition to the effects discussed in Section 2.5.2.

2.5.5. Quark-Gluon Plasma and late stage hadronic interaction in p–Pb collisions?

In the light of the findings with particle correlations, where collective motion of particles in high-multiplicity p–A collisions [62, 63, 64] and in very high-multiplicity proton-proton collisions [61] was observed and discussed in the context of hydrodynamical descriptions, there have been speculations about the potential onset of deconfinement in p–A collisions as shortly discussed in Section 1.1.2. However, even under the assumption that a deconfined medium is created which features a situation close to local thermodynamic equilibrium, it is questionable whether processes with heavy quarks can be influenced due to the short time scales, length scales and the rareness of sufficiently high-multiplicity events as discussed with example calculations for Pb–Pb and p–Pb collisions at the LHC in Ref. [67][11]. Lifetimes and radial extensions are about a factor 2 to 3 smaller in p–A collisions compared to A–A collisions in the same set-up when comparing a system in A–A collisions at a centrality of 20-30% ($\mathrm{d}N/\mathrm{d}\eta = 430$ at mid-rapidity [187]) with a p–A collision primary charged particle density of $\mathrm{d}N/\mathrm{d}\eta = 270$ at mid-rapidity corresponding to more than 10 times the mean multiplicity of p–Pb collisions. A multiplicity range with a mean of about 3.5 times the mean multiplicity corresponds to only 1% of the inelastic p–A cross section and contains less than 10% of the J/ψ yield. Even if the time and space extensions are sufficient to affect heavy-flavour production, it

[11] The model uncertainties are very large and large difference are expected in different approaches. This reference was chosen as illustration based on the detailed description and discussion of the involved scales.

is difficult to imagine that they will be visible in multiplicity-integrated results due to the rareness of events with sufficiently large multiplicities.

In the heavy-flavour sector and more generally in observables involving a hard scale, there was no specific observation which points unambiguously towards an interpretation in this direction. In fact, the near-side ridge known from $\eta-\phi$ hadron-hadron correlations in high-multiplicity pp and in p–Pb collisions was also seen in preliminary data from ALICE on heavy-flavour electron-hadron correlations [188] at high multiplicities. However, if there exists an explanation for the ridge-like structure which is not caused by the formation of a matter close to thermal equilibrium but from the collision of the complicated proton 'wave-functions'[12], it is likely that this explanation will equally apply both to heavy-flavour correlations and to di-hadron correlations.

Nevertheless, QGP formation [189], extended hadronic interactions as in the comover model [190] or both [131] are popular to explain the observed ψ(2S) behaviour measured by ALICE [191, 192] and confirmed by LHCb [193] in p–Pb collisions. The impact on the J/ψ nuclear modification in p–Pb collisions due to these late stage interactions is not expected to be the dominating effect in all of these approaches. The ψ(2S) results and their impact on the interpretation of charmonium production will be discussed in Section 6.5.1.

[12]Wave-function is strictly speaking a non-relativistic term.

3. Experimental access to charmonium at the LHC

3.1. The Large Hadron Collider

The Large Hadron Collider (LHC) is the most powerful hadron collider ever built in terms of collision energy, stored energy and luminosity. The LHC provides proton–proton (pp), proton–lead (p–Pb) and lead-lead (Pb–Pb) collisions to the four large experiments ALICE, ATLAS, CMS, LHCb and in pp collisions to the three smaller experiments TOTEM, LHCf and MoEDAL. Figure 3.1 shows the LHC and its preaccelerator chains. A detailed description can be found in Ref. [194].
ATLAS and CMS are high-energy physics multi-purpose with large phase space coverage and the capability to inspect the full delivered luminosity to search for rare events as Higgs-particle production or signatures from particles beyond the standard model with high precision in particular at high momentum transfer. Design details of the two detectors can be found in Refs. [195, 196].
LHCb is a fully instrumented forward spectrometer focusing on electro-weak precision studies and indirect searches beyond the standard model involving hadrons containing beauty and charm quarks as valence quarks [197].
ALICE is the dedicated heavy-ion experiment specialised in the analysis of A–A collisions at the LHC [198]. Its capabilities and the ones of the central barrel in view of charmonium detection are detailed in the context of the detection capabilities for charmonium of the four large LHC experiments in the following.

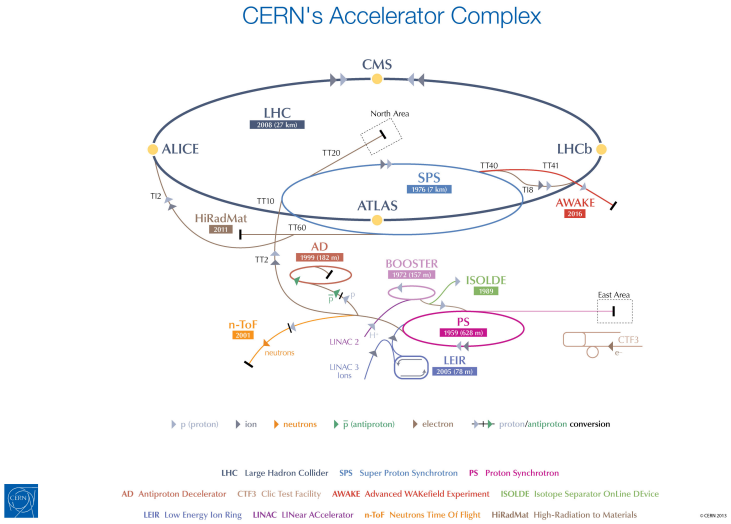

Figure 3.1.: The LHC, its preaccelerators and the position of the experiments are shown. The graphic is taken from Ref. [199].

3.2. Charmonium detection at the LHC

The detection of charmonium in hadronic interactions is mostly restricted to channels, which involve either J/ψ or ψ(2S) in the final state using their decay to dimuons or dielectrons. The corresponding branching ratios are the largest two-body decays to 'stable'[1] particles in the charmonium family as a consequence of their properties outlined in Section 2.1. In addition, the background is strongly reduced in case of a good lepton identification compared to decays involving hadrons, since pions, kaons and protons are more abundantly produced. The inclusive J/ψ production cross section is hence typically the cross section measurement in the charmonium system, which requires the lowest integrated luminosity. ψ(2S) requires higher event statistics, since its direct production rate is smaller, it has less feed-down contributions and its branching to dileptons is reduced compared to J/ψ by about a factor 7.6 [21]. The measurement of J/ψ production is pursued by all four large LHC collaborations. An overview of the acceptances for J/ψ cross section measurements published and preliminary data by the LHC experiments in p–Pb collisions can be found in Fig. 3.2. The instrumentational reasons are explained in the following.

ATLAS and CMS have both large acceptance muon systems and electromagnetic

[1]Stable particle include weakly decaying light flavour hadrons and muons in this context.

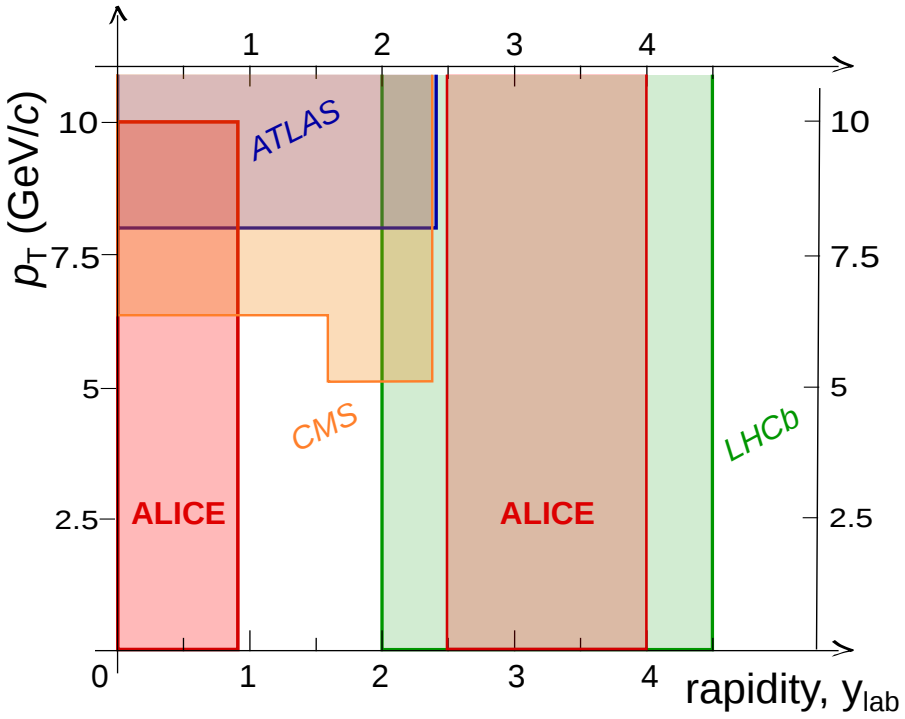

Figure 3.2.: Acceptance in rapidity and transverse momentum of J/ψ measurements for published and preliminary p–Pb data from ALICE [200, 201], LHCb [202],ATLAS [203] and CMS [204] in p–Pb collisions.

calorimetry enabling them to detect and trigger efficiently on J/ψ and ψ(2S) directly or with the latter states in the decay chain as, e.g., the radiative decay channels of χ_c states. For all published results on charmonium, the muon systems were used for production publications in case of both detectors. The J/ψ state is copiously recorded at the luminosities exploited by ATLAS and CMS. It is a candle for the calibration of the efficiency and energy scales of calorimeters and muon systems by tag-and-probe methods at comparatively 'low' track transverse momentum for ATLAS/CMS scales as needed for example in the Higgs analysis in the four lepton channel.

In p–Pb and Pb–Pb collisions, the trigger systems allow them to sample in their kinematical accessible range the full delivered luminosity with dimuon triggers. Since the systems are optimised for high-p_T reach, the dimuon triggers are only efficient at mid-rapidity down to about 7 GeV/c in transverse momentum of the dilepton pair. The latter limitation is mainly caused by the large solenoidal magnetic fields, about 2 T for ATLAS and 3.8 T for CMS, and the large radial distance of the muon system at mid-rapidity, which sets an intrinsic cut-off at large track

curvature, i.e. small muon p_{T} of around 3-4 GeV/c. At forward rapidity, the acceptance can be exploited further down in transverse momentum of the pair, since the muon systems are closer to the beam pipe. CMS measured with early data down to zero transverse momentum [100] of the J/ψ particle at forward rapidity, ATLAS down to p_{T}=1 GeV/c [96]. ATLAS and CMS are equipped with extended silicon vertex detectors allowing them to separate experimentally prompt and non-prompt J/ψ production in their exploited regions of phase space.
LHCb has extended particle identification capabilities both in the hadronic as well as in the leptonic sector and trigger capabilities for muons. It took data from 2010–2013 both in pp as well as in p–Pb collisions, but not in Pb–Pb collisions. The detector is able to detect charmonium via the leptonic decay channels down to zero p_{T}. Purely hadronic decay channels were also exploited as the η_c and J/ψ decaying to p$\overline{\mathrm{p}}$ [205]. As in the case of ATLAS and CMS, measurements of χ_c states reconstructing radiative decays with photons and J/ψ were also performed in pp collisions. LHCb has excellent secondary vertexing capabilities down to zero p_{T} due to the silicon vertex detector and the longitudinal boost at forward rapidity allowing to separate the non-prompt and the prompt component of J/ψ production. As for the multi-purpose detectors, J/ψ is an important calibration candle, in particular for the different b-hadron decays involving J/ψ, and is copiously recorded by the experiment.
A Large Ion Collider Experiment (ALICE) is the dedicated heavy-ion experiment at the LHC. It measures charmonium both at forward rapidity as well as at mid-rapidity in all collision systems.

3.3. Charmonium detection with ALICE

Overview

ALICE is subdivided in the central barrel detectors measuring around mid-rapidity and the muon forward arm. Figure 3.3 shows the ALICE set-up. The forward arm of ALICE is designed to detect muons up to event multiplicities of $\frac{\mathrm{d}N_{\mathrm{ch}}}{\mathrm{d}\eta}|_{y\approx 0} = 8000$. The spectrometer uses a dipole magnet with a field integral of 3 Tm. It was built for the measurement of inclusive J/ψ and ψ(2S), Υ(1S), Υ(2S) and Υ(3S) in the dimuon

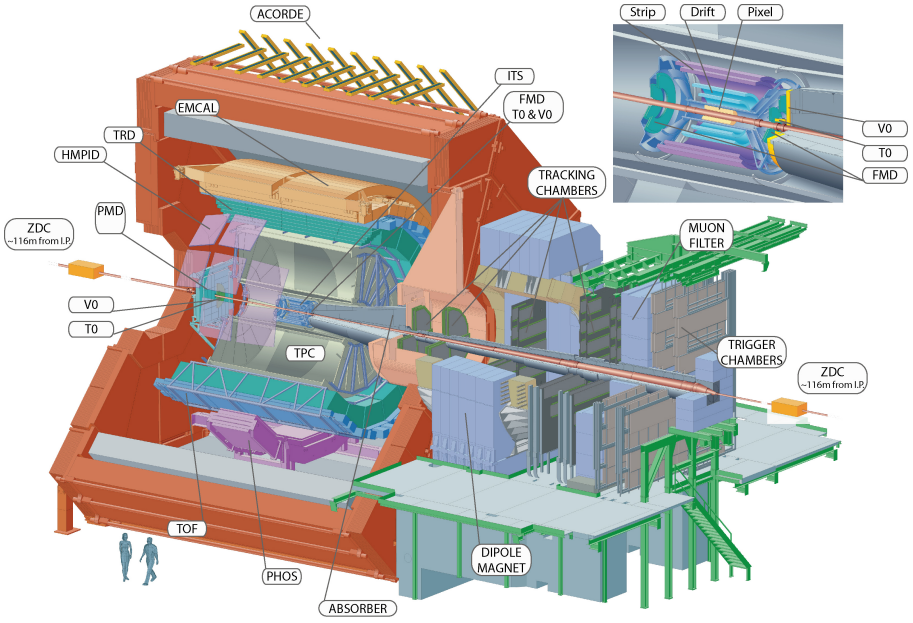

Figure 3.3.: A Large Ion Collider Experiment. The subsystems are indicated with their abbreviations. The graphic is taken from Ref. [206], where a description of all subdetectors can be found.

decay channel and of single muons from weak decays of heavy flavour hadrons employing single and dimuon triggers. It can also detect vector mesons decaying to dileptons at lower masses than the charmonium family. Further details on the muon arm instrumentation and its performance can be found in Refs. [198, 206].

The central barrel features a highly granular tracking system placed in a solenoidal magnetic field of 0.5 T able to measure events with multiplicities corresponding to $\left.\frac{\mathrm{d}N_{\mathrm{ch}}}{\mathrm{d}\eta}\right|_{y\approx 0} = 8000$ [198]. It employs a variety of particle identification methods enabling hadron and electron particle identification over a large range of momenta around mid-rapidity. In inelastic hadronic collisions, the separation of muons from pions is not possible for the relevant phase space of J/ψ and ψ(2S) decays. Hence, the detection of leptonic decay channels is based on the separation of electrons and positron from hadrons. An exception is the investigation of exclusive production as measured in ultra-peripheral Pb–Pb collisions [169], where the measurement is quasi background free and the decay to dimuons can be also used.

Figure 3.4 shows the detailed installation status of the mid-rapidity detectors during the p–Pb data taking in 2013 used for the physics results presented in this thesis. The tracking system with full azimuthal coverage will be introduced with more details in the following. In addition to these subdetectors, the two electromagnetic

calorimeters PHOS and EMCal provide photon detection, electron identification and neutral energy jet component detection (only EMCAL) capabilities in part of the central barrel acceptance. The High Momentum Particle Identification Detector (HMPID) extends the momentum reach of the hadron-PID capabilities to higher momenta than the Time Of Flight (TOF) detector in a fraction of the acceptance. The central barrel detectors are complimented by a number of detectors covering more forward rapidities for either triggering as VZERO, TZERO and ZDC, and event characterisation purposes, VZERO and ZDC, as well as extensions of the charged particle multiplicity, FMD, and photon multiplicity measurements, PMD. The VZERO detector and the ZDC will be shortly introduced since they play a crucial role in this analysis for triggering as well as event characterisation.

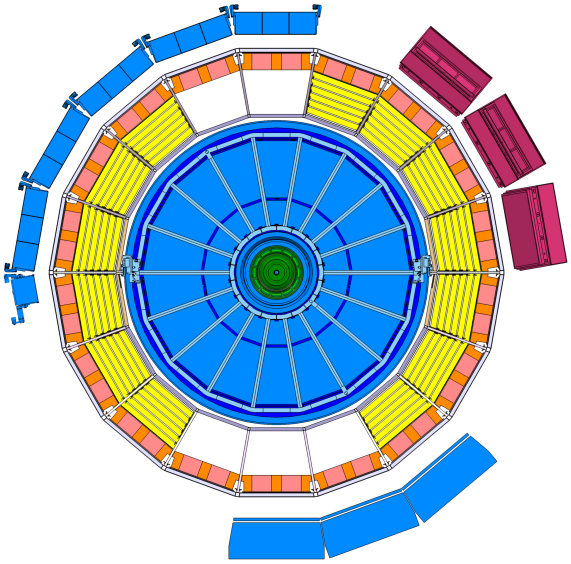

Figure 3.4.: The schematic cross section through the ALICE central barrel during 2013 p–Pb data taking is shown. The Inner Tracking System is indicated in green, which is enclosed by the TPC. The 13 installed sectors of the TRD are indicated in yellow. the most outer detector covering the full azimuth is the TOF. The calorimeters are shown in blue, the HMPID in purple.

The highly granular detector layout at mid-rapidity for robust tracking up to very high multiplicities combined with particle identification over a large range of momentum comes at the price of a slow read-out compared to the other LHC experiments at mid-rapidity, which base their hadronic and electron tracking capabilities mainly on silicon detectors or gaseous detectors with faster readout and smaller drift times. However, the ratio between read-out rate, about 600 Hz in 2011 for minimum-bias hadronic collisions in Pb–Pb collisions [207], and the corresponding

design collision rate, about 8 kHz[194], is small. Hence, the system is able to record a considerable fraction of the delivered luminosity without rare trigger selection. Therefore, most of the central barrel analyses are carried out in minimum-bias collisions or in centrality[2] or charged particle multiplicity triggered events. However, ALICE is able to trigger on rare probes by the TRD, in particular on electrons as well as on jets, as well as by the electromagnetic calorimetry on electrons (EMCal, PHOS), photons (PHOS, EMCal) and jets (EMCal) in particular in p–Pb and pp collisions, but also in Pb–Pb collisions. An assessment of the TRD trigger opportunities for J/ψ measurements for the data taking in 2015-2017 is presented in Appendix B.

Coordinate system

The global ALICE coordinate system is a right-handed orthogonal Cartesian system [208]. Its origin is placed at the second interaction point of the LHC. The z-axis is parallel to the LHC beam axis and is pointing away from the muon arm. The horizontal x-axis approximately points to the centre of the LHC. The y-axis is approximately vertical and pointing upwards. The coordinate system is illustrated in Fig. 3.5.

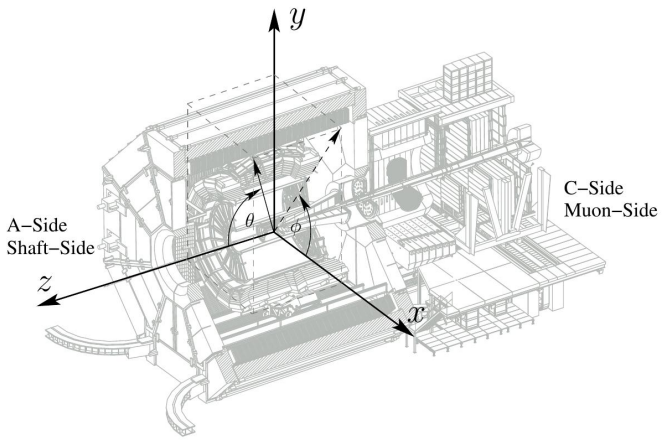

Figure 3.5.: ALICE global coordinate system. The graphic is taken from Ref. [209].

[2]The technical term centrality will be explained in Section 4.3.1.

Acceptance definition

The acceptance of single tracks in this analysis is defined as follows:

$$|\eta| < 0.9$$
$$p_{\mathrm{T}} > 1.0 \text{ GeV}/c$$

with the pseudorapidity $\eta = -\ln[\tan(\theta/2)]$. θ is the polar angle of the track 3-momentum in the lab-frame. The transverse momentum of the track is abbreviated with p_{T}. Tracking and particle identification efficiencies on single track level will be given with respect to this fiducial phase space, if it is not otherwise specified. The $\mathrm{e}^+\mathrm{e}^-$ pair acceptance is defined as $|y_{\mathrm{lab}}| < 0.9$, where the rapidity is defined as $y_{\mathrm{lab}} = 0.5 \cdot \ln[(E_{\mathrm{lab}} + p_{\mathrm{z,lab}})/(E_{\mathrm{lab}} - p_{\mathrm{z,lab}})]$, where E_{lab} is the $\mathrm{e}^+\mathrm{e}^-$ pair energy and $p_{\mathrm{z,lab}}$ the component of the 3-momentum parallel to the beam axis in the laboratory reference frame. The pair acceptance correction includes the vertex correction due to NLO QED modelled via the EvtGen package [210], which models the radiative corrections using PHOTOS [211, 212].

The Inner Tracking System

The Inner Tracking System (ITS) provides the six tracking layers closest to the interaction point. It features three different technologies and represents the silicon detector with the lowest material budget at the LHC with 0.83 and 1.26% of a radiation length per layer excluding thermal shield and support structure [198]. The total material budget between the interaction point and the middle of the TPC amounts to about 10% [73]. This design feature is of major importance for purely tracker based electron analyses as in case of the J/ψ measurements in the dielectron channel: the probability to emit a bremsstrahlung photon with $E > 10$ MeV, corresponding approximately to the achieved momentum resolution in ALICE, from an electron with a momentum of 2 GeV/c amounts only to about 30% and the probability of a photon originating dominantly from decays of abundantly produced π^0s with an energy of 4 GeV to convert in an $\mathrm{e}^+\mathrm{e}^-$ pair in the material is $\approx 10\%$. The two innermost layers are digitally read-out pixel chips, called Silicon Pixel Detector (SPD), positioned at radii of 3.9 and 7.6 cm [198]. It is also able to

provide a fast trigger signal which is particularly useful for trigger purposes in low-multiplicity pp collisions. The signal integration time amounts to typically 300 ns. The pixels have a size of 50 μm in $r\phi$ direction and 425 μm in longitudinal direction. The high granularity of the SPD and its proximity to the interaction point dominate the precision of the distance of closest approach measurement and the secondary vertex resolution capabilities for hadrons with charm or bottom valence quarks at mid-rapidity.
The third and the fourth layer at radii of 15.0 cm and 23.9 cm constitute the Silicon Drift Detector (SDD), the only one of its kind installed at the LHC. It provides an analogue signal and highly granular tracking information both in the bending plane as well as in the direction parallel to the beam axis.
The Silicon Strip Detector (SSD) constitutes the fifth and sixth layer of the ITS. It also measures an analogue signal per measured space point. The energy depositions measured in the SSD and the SDD are used to provide an energy loss signal, which can be used for particle identification. It enables the access to identified particle spectra below the momentum threshold necessary for primary tracks to reach the TPC with high probability, which is about 150 MeV/c for pions [213].
For the detection of charmonium, the requirement of track points from the ITS is important to suppress background from photon conversions created in the ITS material and in the support structures between the ITS and the TPC. Furthermore, its secondary vertex resolution is necessary to separate prompt from non-prompt J/ψ production.

The Time Projection Chamber

The Time Projection Chamber (TPC) is the main tracking device of ALICE and is the largest of its kind ever built. A detailed description of the design details and the performance can be found in Ref. [214]. Its active gas volume in radial direction ranges from $r = 86$ cm to $r = 2.4$ m. The drift field of 400 V/cm is created by a central electrode at a negative voltage of 100 kV and the end caps of the field cage kept at 0 V. Electrons from primary ionisation of charged particles have a maximal drift length of about 2.5 m in either directions away from the central electrode at $z = 0$ cm corresponding to a drift time of around 100 μs. The read-out planes at the two endcaps are equipped with Multi-Wire Proportional Chambers, which are

arranged in 18 sectors in azimuthal direction. Each sector on both sides is equipped with 2 read-out chambers ordered in radial direction. The TPC provides full track length information in $|\eta| < 0.9$ for primary tracks originating from the nominal interaction point position by providing 557 million voxels in space. In addition, it can identify the particle species via the simultaneous measurement of specific energy loss and rigidity in the counting gas for every charged particle traversing the active detector volume. A schematical view of a charged particle trajectory seen in a TPC sector is given in Fig. 3.6. It will be used in this analysis both for tracking as well as for electron identification.

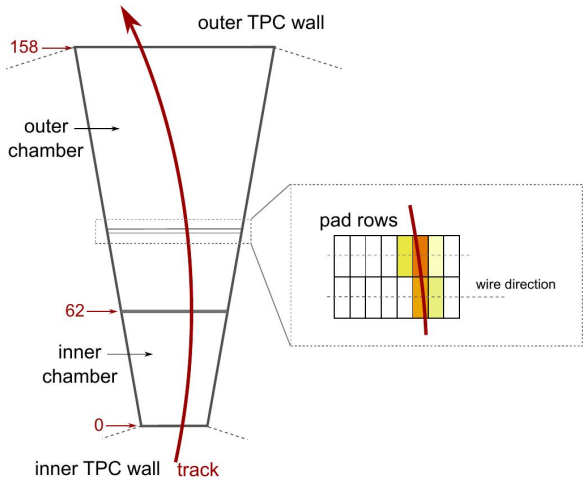

Figure 3.6.: Schematical view of the charged particle trajectory projected to the read-out chambers in a TPC sector. The two read-out chambers are shown. The inlay shows the pads rows in $r\phi$ direction as well as the wire direction. The graphic is taken from Ref. [215].

The Transition Radiation Detector

The Transition Radiation Detector (TRD) is designed to improve the electron identification capabilities of the central barrel, to provide electron and jet triggers as well as to improve the momentum resolution of the combined tracking system at high transverse momentum. The TRD was not fully installed during the p–Pb data taking campaign in 2013 and therefore not yet used for the J/ψ analysis as details in Section 3.3. Details on the detector can be found in Ref. [216]. It was used for triggering during pp collision data taking in pp in 2012 as well as in 2013 p–Pb collision

data taking. The prospects of triggering with the TRD in view of J/ψ production are discussed in Appendix B.

The Time of Flight detector

The Time-Of-Flight (TOF) detector enables to separate electrons from Kaons, protons and deuterons in the crossing region of the respective Bethe-Bloch curves, where the TPC PID cannot disentangle those particle species. The performance of the TOF detector is detailed in Ref. [217].

The VZERO detector

The VZERO detector consists of two scintillator arrays on either side of the interaction point covering a pseudorapidity of $2.8 < \eta < 5.1$ and $-3.7 < \eta < -1.7$ for the nominal vertex position at $z = 0$ cm. The VZERO detector was used as minimum-bias trigger detector in the data taking period analysed in this thesis. The trigger required a coincidence of signals in both scintillator arrays. A detailed description of its design details and the performance can be found in Ref. [218].

The Zero Degree Calorimeter

The hadronic part of the Zero Degree Calorimeter (ZDC) consists of two neutron (ZN) and proton (ZP) calorimeters positioned at a distance of 112.5 m from either sides of the interaction point. They are placed at the splitting point of the common part of both LHC beam pipes. Both systems are complemented with electromagnetic calorimeters with a nominal pseudorapidity coverage of $4.8 < \eta < 5.7$. These sampling calorimeters use quartz as active detector material employing the Cherenkov effect for the signal creation. A short overview of the design is given in Ref. [198]. Its usage during beam data taking is detailed in Ref. [206].
Thanks to its good timing resolution, the ZDC signals provided a rejection of events

in the p–Pb data taking after the reconstruction, where two consecutive beam crossing lead to inelastic collisions reducing the amount of out-of-bunch pile-up. Furthermore, the ZN calorimeter on the lead fragmentation side was used for the centrality estimation in p–A collision as detailed in Section 4.3.1.

ALICE central barrel tracking

Prior to the track finding, potential track space points, so called clusters, are searched for in all subdetectors and located in the corresponding detector.
The track reconstruction in an event in the central barrel for global tracks is subdivided in the following steps:

1. A first vertex is reconstructed based on SPD information. The vertex is reconstructed using track fragments, so called SPD 'tracklets', built from 2 hits in the two SPD layers.

2. Tracks are seeded at the outer TPC radius, where the occupancy is lowest within the TPC-ITS tracking system with the SPD vertex as propagation constraint.

3. The track reconstruction is reconstruction via a Kalman filter running inwards in radial direction through the TPC and the ITS.

4. The Kalman filter is propagated outwards starting at the innermost ITS layer to the outer TPC radius. This step uses the tracks from the previous iteration as seeds.

5. The track is propagated further from the outer TPC radius to the TRD, TOF and EMCal.

6. A final inwards propagation from the outer radii to the interaction point is performed. If a track is confirmed at the TPC inner radius in this last step, it is labelled with TPC-refit. If the global track is found in the ITS with at least two hits, it is labelled ITS-refit.

Detailed information on the tracking algorithm of ALICE can be found in Ref. [219]. We will give a few details on the TPC tracking relevant for this thesis. A more detailed description is given in Ref. [213]. The TPC read-out planes are segmented

in radially ordered 159 pad-rows as shown in Fig. 3.6. A cluster finding algorithm merges signals above noise threshold in subsequent pads in $r\phi$ direction and in time to clusters. Only clusters with more than one contributing pad and several time bins are used for the determination of the track parameters. The number of TPC clusters associated to a track for the tracking information is called $N_{\text{TPC-cluster}}$ in the following. However, the single-pad clusters are still used for track seeding and for particle identification information.

Electron identification choices

The ALICE detectors provide a variety of electron[3] identification methods. Most importantly is the separation from primary charged pions, kaons, and (anti)protons, which are much more abundant around 1 GeV/c than primary electrons[4]. The J/ψ production represents the smallest resonance cross section measured with the central barrel of ALICE in p–Pb collisions [201]. In total, the recorded statistics lead to a number of e^+e^- pair candidates of a few hundreds. The analysis is not feasible without stringent particle identification in contrast to $\phi \to K^+K^-$ or to $D^0 \to K^-\pi^+$ starting at a certain minimum p_{T}.

The detectors and their properties with electron PID capabilities are listed in Table 3.1. The HMPID and PHOS are not considered due to their small acceptances. The matching efficiency for the propagation of TPC-ITS track to the TRD or TOF is about 60-80% depending on detector and p_{T} in the nominal acceptance due to the detector segmentation in z direction and differences in the losses due the azimuthal gaps between sector boundaries in the different detectors at finite track curvature.

In order to keep the single track efficiency as large as possible[5], it was decided to choose the TPC as the only electron identification device in this analysis and to exploit the full accessible pseudorapidity coverage of $|\eta| < 0.9$ with a requirement $p_{\text{T}} > 1$ GeV/c as in J/ψ analyses in pp collisions [151, 220, 99, 221, 222].

[3] Electron will be used in the following as synonym for electron and positron, if not otherwise specified.

[4] Primary particles include in this context decay particles except of particles originating from weak decays of light flavoured hadrons and muons as well as particles produced in the interaction with the detector material.

[5] Of course, the usage of TOF and TRD in if-available mode could have been done, but was not envisaged due to the only moderate gain and the further complication of the analysis procedure.

Detectors	TPC	TRD	TOF	EMCal	ITS
Acceptance					
$\|\eta\|$	< 0.9	< 0.9	< 0.9	< 0.7	< 0.9
ϕ	2π	$0.72 \cdot 2\pi$	2π	$0.3 \cdot 2\pi$	2π
eff. w.r.t ITS-TPC for					
$p_{\mathrm{T}} \in [1.0, 3.0]$ GeV/c	100%	$\approx 80\%$	70-80%*	$\approx 100\%$**	100%

Table 3.1.: Acceptance and matching efficiencies of central barrel detectors with electron PID capabilities in the 2013 p–Pb data sample. These factors do not take into account the efficiency loss required for a separation from hadrons, which is very different between detectors and as a function of momentum. The acceptances are reported in [206]. The precise values for the matching efficiencies for unidentified tracks can be found in [216] for the TRD and [206] for the TOF. (*) for $|\eta| < 0.8$, (**) for $|\eta| < 0.6$.

The TPC particle identification

The Particle IDentification (PID) of the TPC exploits the specific energy loss of charged particles in the counting gas of the TPC. In this context, the mean energy loss of a moderately relativistic charged particle ($0.1 \lesssim \beta\gamma \lesssim 1000$) is described by the Bethe-Bloch formula [21]:

$$\langle -\mathrm{d}E/\mathrm{d}x \rangle = Kz^2 \frac{Z}{A} \frac{1}{\beta^2} \left[\frac{1}{2} \ln \frac{2m_e c^2 \beta^2 \gamma^2 T_{max}}{I^2} - \beta^2 - \frac{\delta(\beta\gamma)}{2} \right] \tag{3.1}$$

where the velocity of the moving charged particle $\beta = v/c$ and the corresponding factor $\gamma = 1/\sqrt{1-\beta^2}$, the electron mass m_e, the charge number Z and T_{max} the maximum kinetic energy transferable to a free electron in a single collision and further factors explained in Ref. [21] are appearing. For a given material, the Bethe-Bloch curve is only depending on β. The energy loss by ionisation offers therefore an opportunity for particle identification, when the rigidity $p/z = m \cdot \beta\gamma/z$, the momentum over the charge number of the charged particle is measured at the same time. The logarithmic rise of the mean energy loss at high $\beta\gamma$ is tamed by the polarisation of the medium traversed by the charged particle. This phenomenon, also called density effect, is encoded in the δ-term of the equation. The polarisation leads to a truncation of the relativistic growth of the electromagnetic field extension [21]. The distribution of the energy deposition of a charged track in thin layers can be described by a Landau-distribution [21].

The TPC-PID signal is calculated with the charge information associated to the TPC clusters of a track. The PID signal of the TPC associated to a track is re-

trieved from a truncated mean of the distribution of the maximal or the total charge associated to the clusters of a given track. For the p–Pb data taking period relevant for this analysis, the maximal charge among all digits within a cluster was used. The gain calibration as well further corrections and the truncation procedure influencing the PID signal of the TPC are explained in Ref. [213]. The average

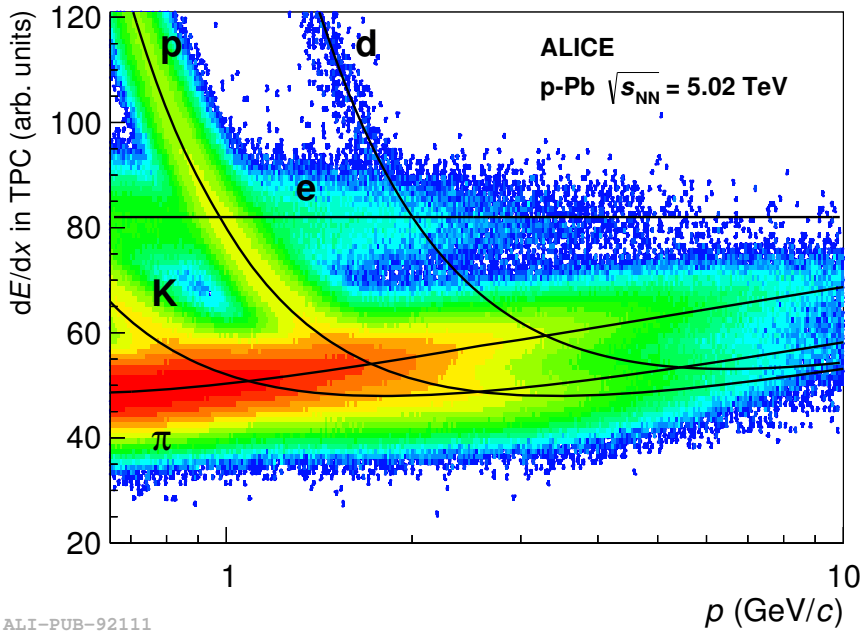

Figure 3.7.: TPC-PID signal as a function of momentum in the p–Pb data taking period used for this analysis as published in Ref. [201]. The expected energy loss of electrons, pions, kaons, protons and deuterons is indicated.

truncated PID signal of the TPC for a given $\beta\gamma$ can be described approximately by the Bethe-Bloch curve and the distribution retrieved after the truncation is Gaussian to first approximation. Although the mean energy loss formula for electrons is different than Equation (3.1), the restricted energy loss of hadrons and electrons measured in particle detectors as the ALICE TPC can be described with the same formula [223]. A restriction of the energy loss measurement in the TPC is already introduced at the level of the cluster finder since the energy deposition of high-energetic δ-electrons above a certain threshold is not attributed to the cluster. The most relevant difference of the mean energy loss described by the Bethe-Bloch formula and the mean of the TPC-PID signal at a given $\beta\gamma$ is found at high $\beta\gamma$. The mean energy loss described by the Bethe-Bloch formula still rises also after the inclusion of the density effects [21, 223]. Since the remaining rise of the mean energy

loss originates from the tail of the energy loss distribution, the restricted energy loss saturates in the so called Fermi-Plateau [223], i.e., the restricted mean energy loss stops to rise further towards higher $\beta\gamma$. The TPC signal of primary electrons is hence to first approximation independent of momentum in the momentum range relevant for this analysis. Fig. 3.7 shows the TPC-PID signal in the p–Pb data sample used for this thesis.

In contrast to the tracking, the PID signal also considers single-pad clusters associated to the corresponding track. However, since the amplification at the chamber borders is not perfectly calibrated due to non-linearities in the response, the clusters in the vicinity of the edges of the wire chambers are not used for PID information. For the vast majority of tracks, the number of PID clusters $N_{\mathrm{PIDcluster}}$ is hence smaller than the number of tracking clusters in the p–Pb data sample.

4. Data sample, event selection and classification

In the following section, the data sample and the used simulations are presented. In addition, the event selection, the luminosity determination and the classification of the events in centrality ranges and in charged-particle multiplicity ranges are explained.

4.1. Data sample

The analysed event sample was recorded during the p–Pb data taking period of the LHC in 2013. It consists of a large sample of minimum-bias triggered events, which was taken at a levelled interaction rate of about 10 kHz.

Each beam of the LHC is partitioned in bunches, which are grouped together in bunch trains [194]. During the p–Pb collision period, the bunch spacing within a bunch train was 200 ns and both beams consisted of maximally 338 proton and 228 lead-ion bunches[1].

With the interaction rate f_{int}, the revolution frequency of the LHC f_{rev} and the number of colliding bunch pairs N_{cb} in ALICE, the mean μ of the Poissonian distribution of occurring inelastic collisions within one bunch crossing can be determined as:

$$\mu = \frac{f_{\mathrm{int}}}{f_{\mathrm{rev}} \cdot N_{\mathrm{cb}}} \tag{4.1}$$

[1] In an initial phase during intensity ramp-up, only 8 bunch pairs were circulated and collided in ALICE. These events correspond to 1.4% of the total analysed statistics.

The value integrated over the full data sample amounts to 0.46%. Hence, the fraction of the number of bunch crossings with more than one inelastic p–Pb collision, so-called same bunch pile-up events, amounts to 0.23%.
Since the signal integration time of the TPC is about 100 μs and large compared to the bunch spacing of 200 ns, pile-up from events not originating from the trigger bunch crossing has to be considered. For all tracks used in this analysis, associated track points in the fast and highly granular silicon pixel detector with signal integration time of 300 ns were used. Hence, the effect is restricted for the J/ψ daughter candidate tracks to signals from two subsequent bunch crossings, which could be still matched between the SPD and the TPC within the resolution of the TPC. This pile-up contribution was efficiently rejected offline by means of the timing information of the Zero Degree Calorimeters. In addition to this method, the timing information of the VZERO detectors was used to reject beam-induced background and out-of-bunch pile-up [218].

Besides the large minimum-bias data sample taken at an interaction rate of 10 kHz, ALICE took also data at higher interaction rates for rare triggering. The interaction rate ranged between about 100 and 200 kHz. This data sample was used for the charmonium results by the ALICE muon arm. The central barrel was triggered by TRD and EMCal single electron triggers. A first study based on the TRD triggered events was conducted in the p–Pb data sample [224, 225]. The TRD trigger opportunities for the data taking in 2015–2018 are discussed in Appendix B.
The EMCal electron triggers were not considered for J/ψ analyses. The lowest electron energy threshold was set to 8 GeV, and this setting was strongly downscaled. There is no low J/ψ p_{T} reach of these triggers. At high J/ψ p_{T}, this trigger is not competitive with ATLAS and CMS due to the reduced acceptance of the EMCal ($\Delta\phi = 107°$, $|\eta_{\mathrm{lab}}| < 0.7$) and the applied prescaling of the trigger.
The twin design of the LHC dipole magnets [194] imposes the same rigidity (p/Z) for both beams. Since the charge over mass ratio is not the same for protons ($A_{\mathrm{p}} = 1$, $Z_{\mathrm{p}} = 1$) and for a lead nucleus ($A_{\mathrm{Pb}} = 208$, $Z_{\mathrm{Pb}} = 82$), the centre-of-mass system of a nucleon–nucleon collision in the asymmetric p–Pb collision system is boosted

with respect to the lab frame:

$$\Delta y = -0.5 \cdot \ln\left(\frac{E_{\mathrm{p}} + E_{\mathrm{Pb}}/A_{\mathrm{Pb}} + (|p_{\mathrm{z,p}}| - |p_{\mathrm{z,Pb}}|/A_{\mathrm{Pb}})}{E_{\mathrm{p}} + E_{\mathrm{Pb}}/A_{\mathrm{Pb}} - (|p_{\mathrm{z,p}}| - |p_{\mathrm{z,Pb}}|/A_{\mathrm{Pb}})}\right) \underset{m_{\mathrm{p}}/E_{\mathrm{p}}\to 0, m_{\mathrm{Pb}}/E_{\mathrm{Pb}}\to 0}{\longrightarrow} -0.5 \cdot \ln(A_{\mathrm{Pb}}/Z_{\mathrm{Pb}}) = -0.465 \tag{4.2}$$

This shift causes the asymmetric centre-of-mass rapidity coverage of the J/ψ measurements despite of the symmetric acceptance of the central barrel detectors in the laboratory frame. Usually, the momentum of the incoming proton(nucleus) beam is chosen such that the z-axis (anti)parallel for the description of p–A collision data. The proton(lead) beam fragmentation side is therefore found at positive (negative) rapidities. In this convention, the rapidity coverage is shifted towards negative or backward rapidities. This sign convention is opposite to the one of the global ALICE coordinate system for the considered data sample, since it was taken with the proton beam pointing towards the muon arm of ALICE. In the following, quantities related to the analysis are quoted in the laboratory frame using the ALICE coordinate system convention whereas the final results in the centre-of-mass system are reported using the standard convention.

The detector conditions of TPC and ITS, which are used for tracking and particle identification in the J/ψ measurement were very stable during the data taking. The data sample is the best recorded data sample in terms of TPC-PID performance due to highest gain operation compared to other data taking periods in 2009–2013[2] and due to the very stable conditions. The only considerable variation as a function of time relevant for this analysis found in the detector QA is a slight decrease of the active area of the first SPD-layer, which is properly modelled in the Monte Carlo (MC) event simulation.

4.2. Simulation data

In order to derive acceptance and efficiency correction factors for the J/ψ measurement, a dedicated simulation is used taking into account the data taking conditions. The standard minimum-bias collision simulation does not provide sufficient J/ψ candidate statistics. The simulation consists of four million events generated with the

[2] In 2009-2013, the main gas component was Neon. In 2015-2017, the TPC is operated with Argon which allows for a further improvement of the PID performance.

HIJING event generator [226]. Half of the events contain one prompt J/ψ decaying to an e^+e^- pair. The other half of the events contain a $b\bar{b}$ pair simulated by PYTHIA 6.4.12 [227] forced to decay with a J/ψ in the final state in the e^+e^- decay mode. The non-prompt component is required for the extraction of the non-prompt fraction of the inclusive J/ψ production that is currently worked on [228].
The J/ψ *to*e^+e^- decay channel was simulating using the EvtGen package [210] employing PHOTOS [211, 212] for the description of the final state radiation in QED. For the prompt J/ψ simulation, the rapidity and p_{T} simulation distribution was taken from an EPS09 leading order colour evaporation model calculation. The spectral shape of the injected J/ψ signal corresponds to the expectation of the model in the forward rapidity acceptance of the ALICE muon arm $3.53 > y_{\mathrm{cms}} > 2.03$. However, the differences between forward and mid-rapidity expectations are smaller than the uncertainties in the calculations.
The produced particles are propagated through a realistic simulation of the ALICE detector system via GEANT3 [229] taking into account the temporal dependence of the detector performance.
For systematic studies of the tracking and particle identification efficiency with e^+e^- pair creation in the detector material, a large minimum-bias collision simulation using the DPMJET [230] generator with a similar number of reconstructed events as the analysed data sample was used.

4.3. Event selection and characterisation

The concept of event centrality and its relation to a multiplicity dependent measurement are explained in this section. It follows a description of the event selection, the luminosity determination, the multiplicity and centrality estimation procedure.

4.3.1. Centrality concept in p–A collisions

In A–A collisions, the collision geometry dependence of observables is of major interest. Mainly the impact parameter dependence is studied in this context.

The measured charged-particle multiplicity or the energy deposition in a given kinematic region not too far away from mid-rapidity can be correlated with the number of nucleons N_{part}, which participate in the collision. N_{part} is strongly correlated with the impact parameter. In addition, it is possible to estimate the number of inelastic binary nucleon–nucleon collisions N_{coll} in an A–A collision. These numbers can be reasonably well defined, since the de-Broglie wave-length of the nucleon is small compared to its transverse size at ultra-relativistic energies. In order to extract the experimental dependence on geometry, the events are classified in intervals of the multiplicity or energy deposition in a detector. These intervals are expressed as percentages of the total inelastic hadronic cross section called centrality percentiles. Collisions with close to 0% centrality produce high charged-particle multiplicities corresponding to a close to full overlap of the colliding nuclei. Collisions with close to 100% centrality producing low multiplicities and exhibit an impact-parameter close to $r_1 + r_2$, where r_1 and r_2 denote the radii of the two nuclei. An average number of participating nucleons and hence an average impact parameter can be deduced from a 'Glauber' fit and assigned to the given centrality quantile. Details about the ALICE centrality estimation in Pb–Pb collisions and the Glauber fit of ALICE can be found in Ref. [231].

Alternatively, the energy deposition from nuclear fragments at around 0 degree with respect to the beam trajectory can be related to the number of nucleons, which are not participating in the A–A collisions, the so-called spectator nucleons $N_{\mathrm{spec}} = 2A - N_{\mathrm{part}}$. The spectators are emitted as free neutrons and protons and as nuclear fragments with higher mass number. The neutrons can be separated in a circular collider from the beam and detected in the neutron zero degree (ZN) calorimeters, since their trajectories are not bent by the magnetic field of the accelerator. The protons exhibit a different rigidity than the beam and are also deflected from the beam allowing their detection in a calorimeter. The ambiguity between most central collisions, very few spectators, and very peripheral collisions, large fragmentation with fragments with $A > 1$ can be resolved by the usage of an electromagnetic calorimeter closer to mid-rapidity as detailed in Section 3.3 for the ALICE set-up. A detailed review about Glauber modelling and centrality estimation in general is given in Ref. [129].

In p–A collisions, the investigation of impact parameter dependences would also provide precious information. The experimental access is more difficult than in A–A collisions, since the scale of the charged-particle multiplicity variations in

nucleon–nucleon collisions and in p–A collisions are not separated. This is already plausible due to the fact that the average number of charged-particles produced in p–Pb collisions around mid-rapidity is only about a factor 4 larger than the mean charged-particle multiplicity in pp collisions at the same collision energy [232]. This fact complicates any attempt to address impact parameter dependencies in p–A collisions treating the nucleons as the smallest entities to be considered. This is illustrated by a standard Glauber model approach comparison between Pb–Pb and p–Pb collisions shown in Fig. 4.1. The resolution of geometry related quantities compared to the full dynamic range of the observable are of similar magnitude. Consequently, quantitatively non-understood correlations of the observable with the centrality estimator variable can influence an attempt of a centrality dependent nuclear modification factor in p–A collisions. In particular, J/ψ production provides a hard-scale in the event. It is expected that the produced multiplicity in the event is larger than in an event with no hard scale involved at the same 'impact' parameter, but there is no recipe, how this correlation is exactly to be quantified and corrected for without interference with the desired quantification of the impact parameter dependence. In addition, resolution effects become important in any case, when one tries to derive the impact parameter dependence of observables from the experimentally measured quantities in p–A collisions.

The ALICE Collaboration suggested in Ref. [233] an approach, which minimises the effects related to the correlation of hard particle production to be investigated and soft particle production used for the centrality estimation. As basis for the centrality estimation, the neutral energy deposition on the lead fragmentation side in the ZN calorimeter is used. This choice guarantees the maximal distance in units of rapidity to the observables in question reducing correlations. As already mentioned in the context of A–A collisions, the number of spectator neutrons is probed by this approach. Since there is no reliable model for the emission pattern of neutrons in forward direction of p–A collisions at ultra-relativistic collision energies, the number of participating nucleons is extracted based on data and additional scaling assumptions. The underlying rationale is introduced in the following. Detailed information can be found in Ref. [233].

The particle production in p–A collisions at mid-rapidity in the acceptance of the central barrel is expected to scale with the number of participating nucleons. Furthermore, the production of particles on the lead fragmentation side as experimen-

tally measured by one of VZERO detectors in the acceptance $2.0 < \eta_{\rm lab} < 5.1$[3] is expected to scale with $N_{\rm part} - 1$, which is equal to $N_{\rm coll}$ in the case of p–A collisions. The production of high-$p_{\rm T}$ particles at mid-rapidity is expected to be proportional with $N_{\rm coll}$. All three assumptions can be used to calculate $\langle N_{\rm part}\rangle, \langle N_{\rm coll}\rangle$ values for a given interval of energy deposition in the ZN detector from data by imposing that the experimentally known $\langle N_{\rm part}\rangle$ for the multiplicity integrated case from the Glauber fit to the VZERO amplitude is reproduced.

The inclusive J/ψ production measurement at mid-rapidity presented in this thesis published together with the corresponding J/ψ result in the muon arm acceptance were the first measurements in ALICE, which used this approach [183] after its introduction in Ref. [233]. The described approach does not extract an experimental resolution for the extracted geometry related observables. An extension of the approach allowing to provide centrality resolution parameters is in work [234].

The measurement of the J/ψ production rate as a function of charged-particle multiplicity addresses the correlation of soft particle production and hard particle production without an attempt to separate geometric and other effects leading to multiplicity variations by a suited definition of the observable.

A multiplicity differential measurement profits from a cleaner experimental definition than the event centrality dependence in p–A collisions, which involves a non-negligible amount of modelling. In addition, since the proposed centrality measure starts to break down within the rarest 20% of the inelastic cross section[4], there is no conceptual problem to extent a multiplicity dependent measurement to the largest available multiplicities measured in the experiment. The measurement can be performed in p–A collisions, pp collisions as well as in Pb–Pb collisions and hence allows a comparison across collision systems. In this analysis, a multiplicity estimator covering approximately the same acceptance as the J/ψ daughters was chosen. The approach is introduced in Section 4.3.5.

However, in several phenomenological calculations, the impact parameter is directly available, whereas the correlation between the soft and the hard particle production is often not provided and even more model dependent as we will discuss in Section 6.4.

[3] This is the acceptance covered on the lead fragmentation side for the beam configuration analysed in this thesis.

[4] In Ref. [183], the 2-10% and the 10-20% centrality classes used for the J/ψ analysis at forward and backward rapidity are already probing $\langle N_{\rm coll}\rangle$ values, which agree within their systematic uncertainties.

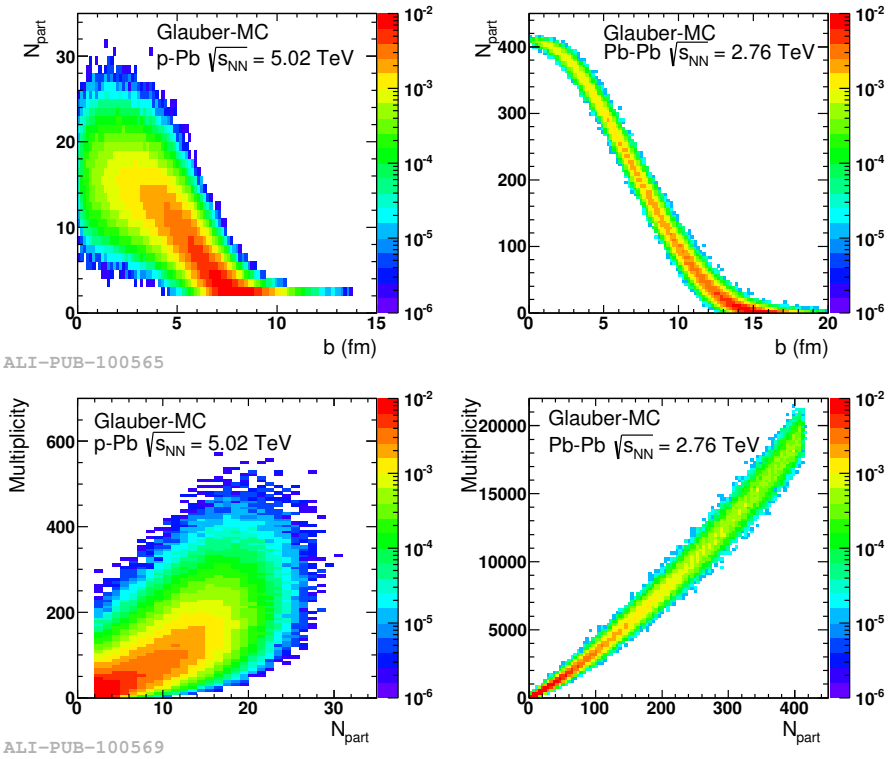

Figure 4.1.: The upper panels show the correlation of the number of participating nucleons with the impact parameter within the ALICE Glauber model for p–Pb collisions on the left hand side and for Pb–Pb collisions on the right hand side. The lower panel shows the correlation between the multiplicity on the lead fragmentation side as measured by the VZERO scintillator array with the number of participating nucleons as extracted from a Glauber fit to the detector amplitude. The figure is taken from Ref. [233].

4.3.2. Event selection, event normalisation and luminosity

Luminosity measurement

The minimum-bias trigger condition cross section for the determination of the integrated luminosity is based on a van der Meer scan analysis [235]. The cross section amounts to $\sigma_{\mathrm{V0AND}} = 2.09 \pm 0.077$ barn. The uncertainty includes a difference found with respect to the independent luminosity measurement via the TZERO detectors of 1%.

Event selection and normalisation for the integrated and p_{t}-differential J/ψ analyses

In this analysis, events being triggered by coincident signals from both VZERO scintillator arrays on either sides of the interaction point are used. The offline rejection of pile-up from subsequent bunch crossings is explained in Section 4.1.
In addition, the event is required to have a reconstructed primary vertex based on global tracks with at least one track contributing to the vertex. The event is selected, if the z coordinate of the reconstructed vertex lies within $[-10, 10]$ cm of the nominal interaction point.
The luminosity is evaluated via:

$$L_{\mathrm{int}} = \frac{N^{\mathrm{corr}}_{\mathrm{V0AND}}}{\sigma_{\mathrm{V0AND}}} \tag{4.3}$$
$$N^{\mathrm{corr}}_{\mathrm{V0AND}} = N^{\mathrm{sel}}_{\mathrm{V0AND}} \cdot \frac{N^{|\mathrm{zvtx}|<10\mathrm{cm}}_{\mathrm{VOAND}}}{N^{int}_{\mathrm{VOAND\text{-}gauss\text{-}fit}}},$$

where $N^{\mathrm{corr}}_{\mathrm{V0AND}}$ is defined as the equivalent number of minimum-bias trigger events, which enter the luminosity calculation. $N^{\mathrm{sel}}_{\mathrm{V0AND}}$ is the number of minimum-bias triggered events passing out-of-bunch pile-up and beam-gas rejection explained in Section 4.1, $N^{|\mathrm{zvtx}|<10\mathrm{cm}}_{\mathrm{VOAND}}$ the subsample of $N^{\mathrm{sel}}_{\mathrm{V0AND}}$ events satisfying the selection on the vertex and its z coordinate, $N^{\mathrm{int}}_{\mathrm{V0AND\text{-}gauss\text{-}fit}}$ the integral of Gauss distribution fitted to z-coordinate distribution of the distribution of the $N^{|\mathrm{zvtx}|<10\mathrm{cm}}_{\mathrm{VOAND}}$ events.
Fig. 4.2 shows the z coordinate distribution of the track vertices with the Gaussian fit. The procedure assumes that all inelastic p–Pb collisions containing a J/ψ in the acceptance for the J/ψ measurement are triggered by the minimum-bias trigger and that every event containing a J/ψ, reconstructed as well as non-reconstructed J/ψ, in the considered rapidity range has a track vertex with at least one contributing track. In addition, it is assumed that all minimum-bias triggered events without a reconstructed vertex follow the same vertex distribution as the events with vertex. Furthermore, the beam-gas and out-of-bunch pile-up rejection is assumed to introduce no biases. Finally, the non-Gaussianity of the z_{vtx} distribution is neglected. In view of the high-efficiency for inelastic collisions and the small size of the additional requirements, no uncertainty is assigned for these assumptions in view of the size total uncertainties of the measured cross sections of at least 12%.
The observables of the multiplicity dependence require the measurement of the

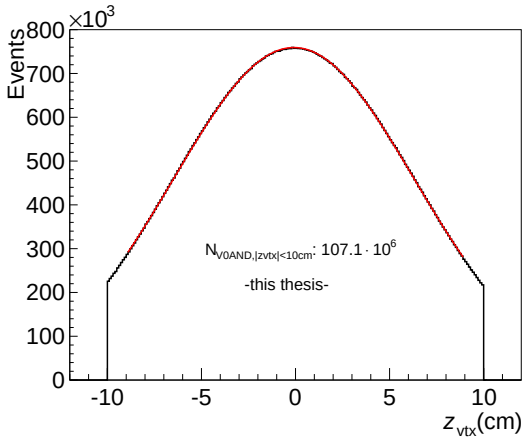

Figure 4.2.: z coordinate distribution of the reconstructed vertices with the Gaussian fit.

event class	$N^{\mathrm{sel}}_{\mathrm{V0AND}}$	$N_{\mathrm{V0AND},\lvert\mathrm{zvtx}\rvert<10cm}$	$N^{\mathrm{corr}}_{\mathrm{V0AND}}$	$N^{\mathrm{corr}}_{\mathrm{NSD}}$
# events/10^6	121.67	107.12	107.39	109.64

Table 4.1.: Event statistics for integrated and p_{T} differential analysis.

J/ψ yield per event. In ALICE, the notion of non-single diffractive (NSD) events was introduced. This event class refers in a Glauber model picture to events, where at least one nucleon–nucleon interaction in the p–Pb interaction is non-single diffractive. It is hence necessary to correct $N^{\mathrm{corr}}_{\mathrm{V0AND}}$ to $N^{\mathrm{corr}}_{\mathrm{NSD}}$. The standard DPMJET event generator response proved to be unreliable [232]. A partially data driven approach was hence applied, which is explained in Ref. [232]. It leads to the correction: $N^{\mathrm{corr}}_{\mathrm{NSD}} = 1.021 \cdot N^{\mathrm{corr}}_{\mathrm{V0AND}}$. This factor is not easily determinable and the related uncertainty amounts to 3.1%, which is larger than the correction itself. All event class numbers mentioned in the description are summarised in Tab. 4.1.

Event selection and normalisation for centrality and multiplicity dependent measurements

For the centrality and the multiplicity dependent analysis, two additional event selection criteria are applied to enable the use of the centrally provided efficiency of the vertex constraints differential in centrality classes. In particular, it is required that the z coordinates of the vertex estimated by the SPD in the first reconstruction

iteration $z_{\mathrm{vtx,SPD}}$ and the final z coordinate estimated by the fully reconstructed tracks $z_{\mathrm{vtx,tracks}}$ do not differ by more than 0.5 cm. In addition, the estimated resolution of the $z_{\mathrm{vtx,SPD}}$ must be less than 0.25 cm. These additional criteria reject 0.33% of the selected events.

4.3.3. Centrality classification

For the J/ψ analysis as a function of centrality, the slicing in event classes is limited by the centrality resolution and by the J/ψ statistics. We consider 4 centrality ranges: 0-20%, 20-40%, 40-60%, 60-100%. The event normalisation for the centrality differential result is by convention within ALICE relative to the number of events triggered by the minimum-bias trigger condition. However, it is necessary to account for the centrality dependence of the vertex finding efficiency. These numbers are summarised in Table 4.2. In the multiplicity dependent analysis, there is no correc-

centrality percentile	0–20%	20–40%	40–60%	60–100%
vertex finding efficiency	100%	100%	99.5%	97.25%

Table 4.2.: Vertex finding efficiency for the centrality differential analysis used for the normalisation to the minimum-bas trigger event class. No uncertainty is considered for these efficiencies.

tion for events without vertex, since events without vertex are explicitly not considered in the multiplicity range down to the lowest multiplicities.

4.3.4. Nuclear overlap functions $\langle T_{\mathrm{pA}} \rangle$

The average nuclear overlap function $\langle T_{\mathrm{pA}} \rangle$ can be used as an alternative method for the calculation of the nuclear modification R_{pA} not relying on a luminosity measurement as shown in Equation (5.4). The value based on the ALICE Glauber model fit to the VZERO signal amplitude on the lead fragmentation side amounts to $\langle T_{\mathrm{pA}} \rangle = (0.0983 \pm 0.0034)$ mb^{-1} [233]. The R_{pA} of J/ψ production based on this $\langle T_{\mathrm{pA}} \rangle$ is consistent with the determination based on the luminosity measurement within the respective uncertainties. The method based on the luminosity was finally used for the determination of the nuclear modification factors.
For the centrality dependent studies, the average values of nuclear overlap function

$\langle T_{\mathrm{pA}}^{\mathrm{mult}} \rangle$ and the number of binary inelastic nucleon–nucleon collisions $\langle N_{\mathrm{coll}}^{\mathrm{mult}} \rangle$ in centrality intervals were determined with the three scaling assumptions mentioned in Section 4.3.1 reproducing the average value integrated over centrality. The largest difference between the methods in the centrality intervals was attached as systematic uncertainty of the quantities without further specification of the uncertainty correlation to the centrality differential J/ψ measurement in this analysis [183] as suggested in Ref. [233]. The uncertainty of $\langle T_{\mathrm{pA}}^{\mathrm{mult}} \rangle$ is fully correlated with respect to the one of $\langle N_{\mathrm{coll}}^{\mathrm{mult}} \rangle$ in the same centrality range. The index 'mult' refers to the fact that for the calculation of $\langle T_{\mathrm{pA}} \rangle$ the particle multiplicity at mid-rapidity estimated with the number of measured clusters in the second layer of the SPD is used, whereas the two other scaling assumptions were used for the uncertainty estimation. The numerical values of the nuclear overlap functions and the number of binary collisions can be found in Tab. 4.3.

ZN class	$\langle N_{\mathrm{coll}}^{\mathrm{mult}} \rangle$	$\langle T_{\mathrm{pA}}^{\mathrm{mult}} \rangle$
0–20%	$11.4 \pm 0.6 \pm 0.9$	$0.164 \pm 0.009 \pm 0.006$
20–40%	$9.6 \pm 0.2 \pm 0.8$	$0.136 \pm 0.003 \pm 0.005$
40–60%	$7.1 \pm 0.3 \pm 0.6$	$0.101 \pm 0.005 \pm 0.003$
60–100%	$3.2 \pm 0.2 \pm 0.3$	$0.046 \pm 0.002 \pm 0.002$

Table 4.3.: The average number of binary nucleon-nucleon collisions $\langle N_{\mathrm{coll}}^{\mathrm{mult}} \rangle$ and the average values of the nuclear overlap function $\langle T_{\mathrm{pA}}^{\mathrm{mult}} \rangle$ with their uncorrelated and global systematic uncertainties for the used centrality classes are shown. The centrality intervals are expressed as percentages of the minimum-bias trigger cross section. ZN refers to the zero degree neutron energy deposition on the lead fragmentation side, which is used for the event classification.

4.3.5. Multiplicity classification

The charged-particle multiplicity is estimated in this analysis by the number of SPD tracklets[5]. They are counted in the pseudorapidity range $|\eta_{\mathrm{lab}}| < 1.0$. Further details about this charged-particle multiplicity estimator can be found in Ref. [232]. Deviations from the charged-track multiplicity[6] with respect to the measured number of SPD-tracklets can arise from inactive pixel chips and incomplete acceptance for event vertices at the extremity of the measurement interval $z_{\mathrm{vtx}} \in [-10, 10]$ cm.

[5] The notion SPD tracklets is introduced in Section 3.3.

[6] The charged-particle multiplicity includes in this context all prompt particles including decay particles except of the decay products from weak decays of light flavour hadrons and of muons.

In addition, the tracklets are only sensitive to tracks with p_{T} larger than about 50 MeV/c in case of charged pions. Furthermore, tracklets can be reconstructed from non-related clusters induced by noise or high occupancy of true tracks. In minimum-bias p–Pb collisions, this contribution is estimated to be a 1% effect [232]. Finally, non-perfect hit detection efficiency could have an impact. However, this is a small correction as well thanks to a single hit detection efficiency above 99% [198].

Since the fraction of active channels of the first (second) SPD layer is about 90% (92.5%) in the respective data sample and since the acceptance coverage is incomplete for vertices with large distance to the nominal vertex position, but still with $z_{\mathrm{vtx}} \in [-10, 10]$ cm, corrections are also required for a relative and not absolute multiplicity measurement aimed for in this analysis.

The chosen approach, which was already employed in pp collisions [221, 222], corrects for the unphysical dependence of the counted tracklets as a function of the z coordinate of the vertex z_{vtz}. For the procedure, the data sample was split in two subsamples to take into account a slight variation of the number of active channels in the first SPD layer. Figure 4.3 shows the $N_{\mathrm{tracklets}}$ distribution as a function of z_{vtx} for the larger of the two subsamples.

For the correction, the average number of SPD tracklets $\langle N_{\mathrm{tracklets}} \rangle$ as a function of the z_{vtx} as shown in Fig. 4.4 is first determined from the histogram in Fig. 4.3. The Figure shows clearly the dependence of the measured number of tracklets on z_{vtx} caused by acceptance edges as well as by inactive SPD channels. The information contained in Fig. 4.4 is used to correct the SPD tracklet number by the following formula:

$$N^{\mathrm{corr}}_{\mathrm{tracklets}}(z_{\mathrm{vtx}}) = N_{\mathrm{tracklets}}(z_{\mathrm{vtx}}) + \Delta N_{\mathrm{pois}} \tag{4.4}$$

where ΔN_{pois} is sampled from a Poissonian probability distribution with the mean $\Delta\lambda_{\mathrm{pois}}$:

$$\Delta\lambda_{\mathrm{pois}} = N_{\mathrm{tracklets}}(z_{\mathrm{vtx}}) \frac{\langle N_{\mathrm{tracklets}} \rangle (z_{\mathrm{vtx}}) - N_{\mathrm{ref}}}{\langle N_{\mathrm{tracklets}} \rangle (z_{\mathrm{vtx}})} \tag{4.5}$$

The corrected $N^{\mathrm{corr}}_{\mathrm{tracklets}}$ distributions have an average value of $\langle N^{\mathrm{corr}}_{\mathrm{tracklets}} \rangle = N_{\mathrm{ref}}$ independent of the z coordinate of the vertex. Hence, this correction removes the detector induced z_{vtx} dependence of $\langle N_{\mathrm{tracklets}} \rangle$. For the J/$\psi$ analysis, the signal is extracted in four slices in the corrected number of tracklets. The tracklet ranges

and the corresponding fractions of the measured minimum-bias cross section are listed in Table 4.4.

The addition of the Poissonian smearing leads to a degradation of the multiplic-

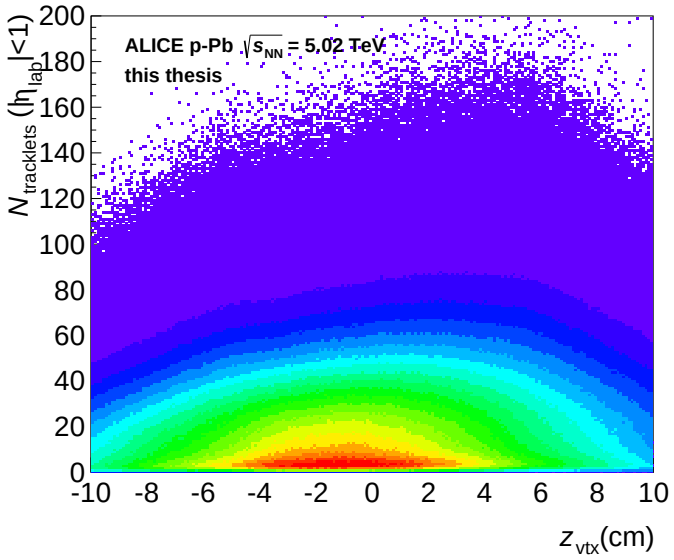

Figure 4.3.: The SPD-tracklets distribution as a function of the z coordinate of the vertex for the larger of the two subsamples considered in this analysis.

ity measurement resolution. Since the smearing is not added deterministically, it induces additional fluctuations on the extracted J/ψ yield from bin flow effects. When the correction procedures is repeated, one receives different invariant mass distributions for a given multiplicity range used for the signal extraction due to a different contribution from $N_{\mathrm{tracklets}}$ values to the considered $N^{\mathrm{corr}}_{\mathrm{tracklets}}$ range. This 'bin-flow' effect induces significant additional fluctuations on the extracted result due to the small available J/ψ statistics per bin. An illustration of the variations at the level of the raw invariant mass distribution is shown in Fig. 4.5. Two invariant mass distributions are shown for the bin corresponding to the largest average multiplicity with the largest fluctuations. The first invariant mass distribution uses the minimal occuring $\langle N_{\mathrm{tracklets}} \rangle$ value as reference value, whereas the second invariant mass distribution uses the maximum of the distribution $N_{\mathrm{ref}} = 31.75$ as reference[7]. It is evident that the usage of the minimum as reference induces a stronger smearing and hence larger fluctuations, since the width of the Poissonian distribution is

[7]Since the ranges are built in the corrected quantities, the two histograms are not a one-to-one comparison. The slicing was done such that the fraction of the total cross section is the same for both cases.

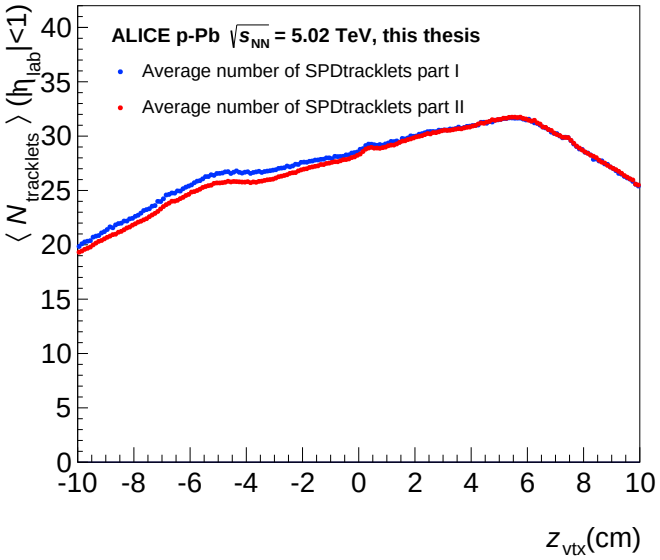

Figure 4.4.: The average number of SPD-tracklets as a function of the z coordinate of the reconstructed vertex for the two sub-samples considered in this analysis corresponding to a different SPD configuration. The observed structure is detector related: the decrease for $|z_{\mathrm{vtx}}| \gtrsim 6$ cm is caused by an incomplete acceptance coverage. The dead-channels are concentrated on the side of the detector towards the muon arm at negative z_{vtx} causing the asymmetry with respect to $z_{\mathrm{vtx}} = 0$ cm.

larger for the vast majority of bins as a function of z_{vtx}. An overview plot for the relative size of the introduced fluctuations at the level of the extracted J/ψ counts is given for the bin with the largest average multiplicity in Fig. 4.6. The figure illustrates the size of the variations of the fluctuations as a function of different z_{vtx} cuts in the event selection and for different choices of N_{ref}. The size of the effect is estimated by the root mean square of the distribution of the retrieved J/ψ counts with the signal extraction procedure described in Section 5.5 divided by the mean of the distribution. Supplementary material for all multiplicity ranges can be found in Appendix D. It can be observed that the correction to the minimum as reference value leads in most cases to the largest fluctuations as expected. The choice of the average value gives similar or better results as the choice of the maximum as reference. Finally, the maximum of the average SPD tracklet numbers as a function of z_{vtx} is taken as reference value to take the same choice as in previous pp analyses and to limit the bin migration fluctuations introduced by the correction. In the event selection, the same cut as in the standard analysis, $|z_{\mathrm{vtx}}| < 10$ cm, was chosen, since the statistical uncertainties on the extracted J/ψ signal counts are the

dominant source of uncertainty and are minimised for this choice with the largest number of contributing events.

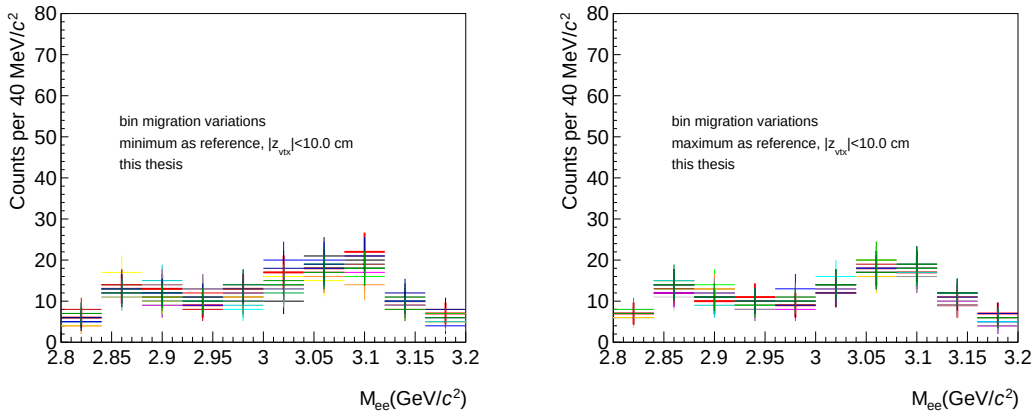

Figure 4.5.: Opposite sign dielectron candidates as a function of invariant mass repeating the multiplicity correction method 20 times with the minimum average SPD tracklet value as reference on the left hand side and with the maximum as reference on the right hand side.

The correction to the maximum leads to a difference in the resolution of the multiplicity estimation as a function of z_{vtx}. This can yield to the selection of significantly different charged-particle multiplicity ranges as a function of z_{vtx} via the selection in the $N^{corr}_{\mathrm{tracklets}}$ variable. The lowest multiplicity range is most problematic in this respect. However, the size of the selected multiplicity range at low multiplicity for the J/ψ measurement is already corresponding to about half of the total inelastic cross section. It was found that the problem is not a concern for this analysis for the given bin choice. A detailed view of the mean charged-particle multiplicity as a function of z_{vtx} for the chosen estimator ranges in simulations can be found in Appendix D.

Finally, it is necessary to translate the number of corrected SPD tracklets $N^{corr}_{\mathrm{tracklets}}$ in a multiple of the mean charged-particle multiplicity. If the detector response was completely linear, the normalised multiplicity variable given in Section 5.7 could be computed solely based on data driven information neglecting folding effects. However, event simulations show that the response is not perfectly linear as shown in Fig. 4.7. The non-linearity of the relationsship between the charged-particle multiplicity and the multiplicity estimator are caused by changes of the event topology and its interplay with the dead areas of the detector as a function of event multiplicity, i.e., by the non-accurateness of the average correction by the employed

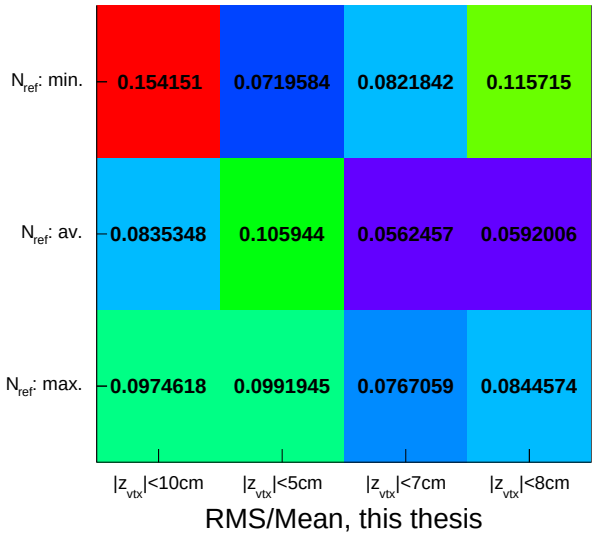

Figure 4.6.: The root mean square of the extracted J/ψ signal from 20 repetitions of the Poissonian smearing divided by the corresponding average for different choices of the reference SPD tracklet number $N_{\text{reference}}$ and z_{vtx} selections is shown for the $N_{\text{tracklets}}$ bin with the largest average multiplicity. This bin shows the largest fluctuations introduced by the correction.

procedure for acceptance holes and the vertex requirement at low multiplicity[8]. In order to take into account this non-linearity, we use the event simulation of minimum-bias collisions with DPMJET to derive linear proportionality factors separately for every multiplicity bin, i.e., we fit the distribution in Fig. 4.7 several times with a function $N_{ch}^{sim} = \alpha_i \cdot \langle N_{\text{tracklets}}^{corr,sim} \rangle$ restricting the fit range every time to the multiplicity range in question. This procedure assumes that the detector response is approximately locally linear within the considered multiplicity range. The correction was checked in simulation by a closure test. The differences between true averages of the charged-particle number in the considered multiplicity range and the value from the explained method can be found in Table 4.4. The differences are small. The largest one amounts to 0.3% in the lowest considered multiplicity range. The values of the slope parameter α_i are listed in Table 4.4.

To get to the relative multiplicity, we correct the mean of $N_{\text{tracklets}}^{corr}$ of a given multiplicity bin with the slope parameters α_i to a simulation based number of average charged-particle multiplicity $\langle N_{ch} \rangle$ for all considered multiplicity ranges.

[8] Events exhibiting a large, but non-zero fraction of tracks out of the SPD acceptance have a larger probability to be not reconstructed with a proper vertex position.

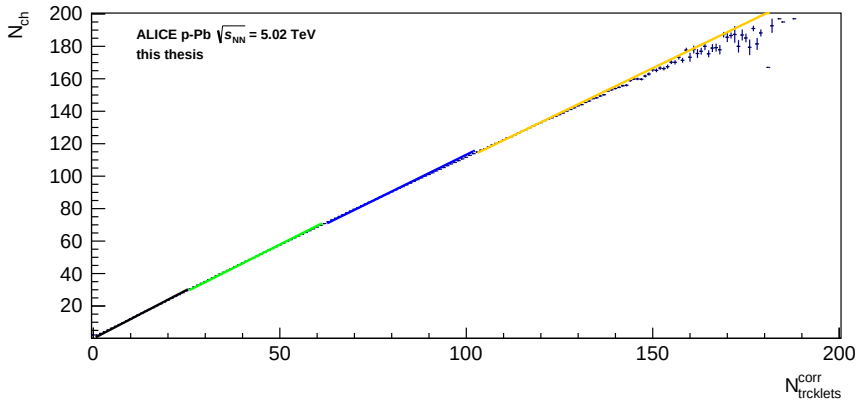

Figure 4.7.: The mean charged-particle multiplicity N_{ch} as a function of the $N^{\mathrm{corr}}_{\mathrm{tracklets}}$ value is shown. The linear fits for the derivation of the α_i factors are shown. The non-linearity of the relation between the two quantities is visible.

Since we are interested in the relative multiplicity, we divide the result by the measurement of the charged-particle density in $|\eta| < 1.0$ from Ref. [232] and multiply by $2(\Delta\eta = 2)$. The used charged-particle density amounts to $\frac{\mathrm{d}N_{ch}}{\mathrm{d}\eta_{\mathrm{lab}}}|_{|\eta|<1.0} = 17.64 \pm 0.01(\mathrm{stat.}) \pm 0.15(\mathrm{syst.})$.

$N^{\mathrm{corr}}_{\mathrm{tracklets}}$ range	fraction of minimum-bias cross section	α_i	$\frac{\langle N_{\mathrm{tracklets}}(\mathrm{sim.})\rangle}{\langle N_{\mathrm{tracklets}}(\alpha_i)\rangle}$
1-25	0.473	0.8372	1.0032
26-61	0.398	0.8641	1.0002
62-102	0.109	0.8835	1.0000
103-200	0.010	0.9007	1.0000

Table 4.4.: Proportionality factors for the correction from the corrected number of SPD tracklets to the charged-particle multiplicity derived from DPMJET minimum-bias collision event simulations. The last column shows the closure test for the multiplicity determination via the α-factors.

The non-linearity correction and the normalisation to the measured absolute quantity introduces a dependence on the event simulation both by the detector simulation and by the physics of the event generator. Detailed studies were done within the $\mu^+\mu^-$ analysis [236, 237] and were used also for the uncertainty estimation in the dielectron analysis presented in Section 5.7.7.

The procedure does not correct for multiplicity-resolution effects, i.e., it does not unfold the bin migrations of the J/ψ signal. The correlation matrix between the estimator and the charged-particle multiplicity in simulations, which can be used for the folding of theory calculations, is shown in Fig. E.1 in Appendix E.

5. Measurement of inclusive J/ψ production in p–Pb collisions at mid-rapidity

In the following section, the measurement of the J/ψ cross sections, yields and nuclear modification factors are detailed. First, the observables are introduced. The track and the pair selection are described. The $Acc. \times eff.$ correction of the raw yield, the signal extraction and the pp reference cross section determinations are detailed. Finally, the systematic uncertainty estimation is summarised.

5.1. Observables

The p_{T}-integrated inclusive J/ψ cross section is defined as follows:

$$\mathrm{d}\sigma/\mathrm{d}y^{\mathrm{p–Pb}}_{\mathrm{J}/\psi} = \frac{N^{\mathrm{J}/\psi}_{\mathrm{raw}}}{Acc. \times eff. \cdot \mathrm{BR} \cdot \Delta y \cdot L_{\mathrm{int}}} \tag{5.1}$$

The p_{T}-differential inclusive J/ψ cross section is given in analogy by:

$$\mathrm{d}^2\sigma/\mathrm{d}y\mathrm{d}p_{\mathrm{T}}{}^{\mathrm{p–Pb}}_{\mathrm{J}/\psi} = \frac{N^{\mathrm{J}/\psi}_{\mathrm{raw}}(p_{\mathrm{T}})}{Acc. \times eff.(p_{\mathrm{T}}) \cdot \mathrm{BR} \cdot \Delta y \cdot \Delta p_{\mathrm{T}} \cdot L_{\mathrm{int}}}, \tag{5.2}$$

where $N^{\mathrm{J}/\psi}_{\mathrm{raw}}$ denotes the raw J/ψ-yield, $Acc. \times eff.$ the acceptance times efficiency factor, Δy the rapidity window of the measurement, L_{int} the integrated luminosity and $\mathrm{BR} = (5.971 \pm 0.032)\%$ the branching ratio of the decay $J/\psi \rightarrow \mathrm{e}^+\mathrm{e}^-$ [21]. In this analysis, the p_{T}-integrated cross section is based on a p_{T}-integrated signal extraction and not on the addition of the p_{T}-differential quantities.

The mean transverse momentum of the measured inclusive J/ψ $\langle p_{\mathrm{T}} \rangle$ in the transverse momentum range $[0, p_{\mathrm{T,max}}]$ was determined by:

$$\langle p_{\mathrm{T}} \rangle = \frac{\int_0^{p_{\mathrm{T,max}}} f(p_{\mathrm{T}}) \cdot p_{\mathrm{T}} \mathrm{d}p_{\mathrm{T}}}{\int_0^{p_{\mathrm{T,max}}} f(p_{\mathrm{T}}) \mathrm{d}p_{\mathrm{T}}} \tag{5.3}$$

$f(p_{\mathrm{T}})$ is a function describing the p_{T} differential J/ψ cross sections. The procedure is explained in detail in Appendix I.

Due to the theoretical uncertainties in the determination of the cross section of J/ψ production in pp collisions illustrated in Section 6.1, the experimental results are mainly compared with theory in terms of a nuclear modification factor, which is given here in two alternative definitions:

$$\begin{aligned} R_{\mathrm{pPb}}(\mathrm{J}/\psi) = & \\ & \frac{N_{\mathrm{raw}}^{\mathrm{J}/\psi}}{(Acc. \times eff.) \cdot N_{\mathrm{NSD\text{-}events}}^{corr} \cdot \Delta y} \cdot \frac{1}{\langle T_{\mathrm{pA}} \rangle \cdot \left(\mathrm{BR} \cdot \mathrm{d}\sigma/\mathrm{d}y_{\mathrm{J}/\psi}^{\mathrm{pp}} \right)} \\ & = \mathrm{d}\sigma/\mathrm{d}y_{\mathrm{J}/\psi \to \mathrm{e}^+\mathrm{e}^-}^{\mathrm{p\text{–}Pb}} \cdot \frac{1}{A_{\mathrm{Pb}} \cdot \left(\mathrm{BR} \cdot \mathrm{d}\sigma/\mathrm{d}y_{\mathrm{J}/\psi}^{\mathrm{pp}} \right)} \end{aligned} \tag{5.4}$$

with the reference cross section in pp collisions $\mathrm{d}\sigma/\mathrm{d}y_{\mathrm{J}/\psi,\mathrm{pp}}$, the atomic mass number of lead $A_{\mathrm{Pb}} = 208$, the number of non-single-diffractive events $N_{\mathrm{NSD\text{-}events}}^{corr}$ used for the normalisation of the J/ψ yield[1], the nuclear overlap function $\langle T_{\mathrm{pA}} \rangle$ detailed in Section 4.3.2. For the p_{T}-differential and the p_{T}-integrated results, the formulation of R_{pA} via the cross section and the atomic number was used.

There was no data sample recorded at the same collision energy in pp collisions as in p–Pb collisions until Decembre 2015. The pp reference cross section is therefore based on an interpolation procedure of experimental results at different collision energies. The procedure is outlined in Section 5.6.

The centrality dependent nuclear modification is called Q_{pPb} instead of R_{pPb} in

[1]The underlying assumptions and the determination of the corresponding value can be found in Section 4.3.2. The normalisation to the non-single diffractive (NSD) event class for nuclear modification factors in p–Pb collisions instead of inelastic collisions was introduced in Ref. [181].

order to indicate the caveats in its determination:

$$Q_{\mathrm{pPb}}(\mathrm{J}/\psi) = \frac{N^{\mathrm{J}/\psi}_{\mathrm{raw,cent}}}{Acc. \times eff._{\mathrm{cent}} \cdot N_{\mathrm{V0AND,cent}} \cdot \Delta y} \cdot \frac{1}{\langle T^{\mathrm{cent}}_{\mathrm{pA}} \rangle \cdot \left(\mathrm{BR} \cdot \mathrm{d}\sigma/\mathrm{d}y^{\mathrm{pp}}_{\mathrm{J}/\psi} \right)}. \quad (5.5)$$

The indices 'cent' denote the quantities in a given range of the multiplicity estimator or of the energy deposition amplitude of a given detector (event class). For comparison purposes, also other selections than the slicing in ZN energy deposition on the lead fragmentation side will be used to illustrate effects due to the correlation of soft and hard particle production and discussed in Section 6.3. For the yield normalisation in a given event class, the number of events fulfilling the minimum-bias trigger condition $N_{\mathrm{V0AND,cent}}$ is used.
In this thesis, in analogy to the corresponding analysis in the pp collision system, the following J/ψ rate observable was used for the quantification of the multiplicity dependence:

$$\frac{\mathrm{d}N^{\mathrm{J}/\psi}_{\mathrm{M}}/\mathrm{d}y}{\langle \mathrm{d}N^{\mathrm{J}/\psi}/\mathrm{d}y \rangle} = \frac{N^{\mathrm{J}/\psi}_{\mathrm{raw,M}}}{N^{\mathrm{J}/\psi}_{\mathrm{raw,NSD}}} \cdot \frac{Acc. \times eff.}{Acc \times eff._{\mathrm{M}}} \cdot \frac{N_{\mathrm{NSD}}}{N_{\mathrm{M}}}. \quad (5.6)$$

This observable was measured as a function of the relative charged particle multiplicity in $|\eta_{\mathrm{lab}}| < 1.0$ defined as:

$$\frac{\mathrm{d}N_{\mathrm{ch,M}}/\mathrm{d}\eta}{\langle \mathrm{d}N_{\mathrm{ch}}/\mathrm{d}\eta \rangle}. \quad (5.7)$$

$N^{\mathrm{J}/\psi}_{\mathrm{raw,M}}$ ($N^{\mathrm{J}/\psi}_{\mathrm{raw,NSD}}$) denotes the raw J/$\psi$ yield in the considered multiplicity range (the integrated raw J/ψ yield normalised to the NSD event class), $Acc. \times eff._{\mathrm{M}}$ the $Acc. \times eff.$ in the considered multiplicity range potentially different with respect to the multiplicity integrated one, $\mathrm{d}N_{\mathrm{ch,M}}/\mathrm{d}\eta$ ($\langle \mathrm{d}N_{\mathrm{ch}}/\mathrm{d}\eta \rangle$) the charged particle density in the considered multiplicity range (in the NSD event sample). The definitions of these 'self-normalised' quantities allows for a partial cancellation of uncertainties in the ratios.

5.2. Track selection

In the following, the track selection including the tracking quality selection criteria and the particle identification for the J/ψ daughter candidate tracks is summarised.

5.2.1. Tracking

All J/ψ daughter candidate tracks have to fulfill the following quality criteria:

- TPC, ITS refit as explained in Section 3.3,
- rejection of kink daughters and kink mother found by the kink finder [206] for the identification of weak decays of charged pions and kaons,
- $N_{\text{TPC-cluster}} > 70$,
- $\chi^2/N_{\text{TPC-cluster}} < 4.0$,
- a hit in one of the two layers of the SPD for the p_{T}-integrated signal and for $p_{\text{T}} > 5$ GeV/c of the e^+e^--pair in the p_{T}-differential analysis; a hit in the first layer for $p_{\text{T}} < 5.0$ GeV/c in the p_{T}-differential analysis, for the centrality and the multiplicity dependent analysis,
- distance of closest approach (DCA) of the track to the primary vertex smaller than 3 cm in z direction and smaller than 2 cm in the transverse plane.

These selection criteria guarantee a large efficiency within the acceptance.
More details on the matching between simulation and data are provided in Section 5.4.3.
The requirements on the ITS, and in particular on the SPD do not only improve the p_{T} resolution, but they also reject out-of-bunch pile-up within the integration time of the TPC, since not all TPC-only tracks from out-of-bunch collisions can be rejected by the criteria explained in Section 4.1. In addition, the requirement on the SPD rejects tracks from photon conversions with production radii larger than that of the first pixel layer, which are the main source of background for analyses without these criteria. For the p_{T}-integrated analysis and the p_{T}-differential analysis for

$p_{\mathrm{T}} > 5.0$ GeV/c, only a hit in either of the first two pixel layers was required to profit from the about 20% larger $Acc. \times eff.$. For the other cases, a hit in the first layer of the SPD was required to increase the S/B by about 60-70% at low p_{T} and high multiplicities. The η and the p_{T} single selection introduced in Section 3.3 was varied as cross check. No dependence of the efficiency corrected result on the J/ψ yields could be found within the statistically allowed deviations.

5.2.2. Momentum resolution, bremsstrahlung and unfolding

The ALICE central barrel tracking system provides an excellent momentum resolution for hadronic tracks as shown in Fig. 5.1, which is confirmed for electron tracks by the Gaussian part of the J/ψ mass distribution in data and in simulation, which shows a resolution of about 20 MeV/c corresponding to a p_{T} resolution of about 0.9% without considering any p_{T} dependence of the resolution and neglecting angular resolutions. Nevertheless, there could be significant bin migration effects due to bremsstrahlung despite the low material budget (see Section 3.3), which would need to be corrected by an unfolding procedure. However, the J/ψ signal is only counted in a restricted invariant mass range down to 2.92 GeV/c^2, which limits the maximally allowed amount of energy lost by bremsstrahlung. The $Acc. \times eff.$ correction in this analysis is applied with by a bin-by-bin correction using an efficiency ratio with the reconstructed properties in the numerator and the generated properties in the denominator. This procedure is already an unfolding correction relying on an input distribution of the signal in the simulation, which is comparable with the data. The necessity of more advanced unfolding techniques with the propagation of the uncertainty correlations between the p_{T} bins was investigated in the course of the pp analysis [151, 99] at $\sqrt{s} = 7$ TeV with the same binning as a function of transverse momentum as in this analysis. The deviations with respect to the current procedure were found to be negligible compared to the uncertainties, which are very similar to the ones in the p–Pb analysis. There is hence no further consideration of unfolding beyond the bin-by-bin correction in this analysis.

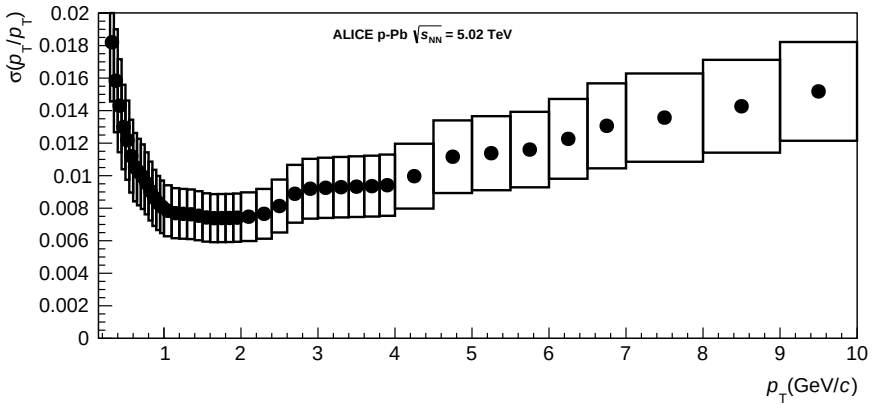

Figure 5.1.: p_{T} resolution for charged tracks optimised for long tracks for the charged particle nuclear modification factor in the same data sample as the presented J/ψ analysis derived from the covariance matrix provided by the Kalman filter algorithm [238]. The track sample is strongly dominated by pions in most kinematic ranges. The mass resolution of the Gaussian part of the J/ψ mass distribution is compatible with the p_{T} resolution between 1 and 4 GeV/c shown here. The figure is taken from Ref. [239].

5.2.3. Particle identification

The Particle Identification (PID) is the most important and critical selection step of this analysis. The TPC PID, which is used in this analysis, cannot separate unambiguously pions and protons[2] from electrons in the relevant phase space for J/ψ decays to electrons. Therefore, a very clean primary electron sample as used in other ALICE analyses [240] and small hadron contamination is always accompanied by a severe decrease in overall raw signal counts in this two-track analysis. Moreover, strong PID selections rejecting pions and protons require a precise calibration of the TPC PID, since the impact of the uncertainty of the electron distribution description on the precision of the efficiency determination is growing with increasing hadron rejection.

The truncated dE/dx signal is calibrated for various detector and geometry related effects on cluster level. These corrections and the truncation are described in Ref. [213]. The expected dE/dx signal for a given species i is extracted from identified particle samples and is parameterised as a function of the following parameters: $\beta\gamma$ at the inner TPC-wall, the momentum at the inner TPC-wall $p^{TPC}_{\text{inner wall}}$ for low momentum tracks, the number of PID-clusters $N_{\text{PIDcluster}}$, the tangent of

[2]Kaons are automatically rejected by rejecting pions and protons via dE/dx for momenta larger than about 1.0 GeV/c.

the polar angle of the track $\tan(\theta)$[3] and the TPC occupancy as estimated by the number of tracks in an event including TPC stand-alone tracks N_{tracks}. The employed procedure is described in detail in Ref. [241]. The deviation of the measured '$\mathrm{d}E/\mathrm{d}x$' signal from a given particle identification assumption is parameterised in this approach as follows:

$$n\sigma_{\text{i,TPC}} = \frac{\mathrm{d}E/\mathrm{d}x_{\text{TPC-track}} - \langle \mathrm{d}E/\mathrm{d}x_i(\beta\gamma, p_{\text{in}}, \tan(\theta), N_{\text{PIDcluster}})\rangle}{\sigma_{\text{exp}}(N_{\text{PIDcluster}}, \tan(\theta), 1/\mathrm{d}E/\mathrm{d}x)} \tag{5.8}$$

The behaviour of the $n\sigma_{\text{i,TPC}}$ is approximately Gaussian around the mean; however, a non-Gaussian tail is present [241]. The multiplicity dependent parameterisation of the TPC PID signal in p–Pb collisions was first tested within this analysis.

In data, it is required that the daughter candidate track has a $\mathrm{d}E/\mathrm{d}x$ signal not deviating more than 3 standard deviations from the expected $\mathrm{d}E/\mathrm{d}x$ for electrons ($|n\sigma_{\text{electron,TPC}}| < 3$). In addition, protons and pions are rejected by requiring a $\mathrm{d}E/\mathrm{d}x$ signal that is larger than 3.5 standard deviations from the proton and the pion expectation ($n\sigma_{\text{proton,TPC}}, n\sigma_{\text{pion,TPC}} > 3.5$). This requirement is loosened for the p_{T}-differential analysis for $\mathrm{e}^+\mathrm{e}^-$-pair p_{T} larger than 5 GeV/c to increase the signal statistics.

The effect of the selection as a function of $\mathrm{d}E/\mathrm{d}x$ and momentum at the inner TPC wall is displayed in Fig. 5.2, which can be compared with the distributions before any PID selection in Fig. 3.7. Due to the multidimensional parameterisation of the $\mathrm{d}E/\mathrm{d}x$ width for a given species, the selection criteria represent not a sharp line in the $\mathrm{d}E/\mathrm{d}x$-momentum space.

Since the TPC-PID response is not sufficiently well modelled in simulation in order to use it for efficiency corrections in the demanding J/ψ measurement at low p_{T}, the parameterisation of the TPC-PID response in data for a given species is attached to a track according to the particle identity known from the simulation. The $n\sigma$ distribution is assumed to be Gaussian. This procedure is used to derive PID efficiencies in simulations. This method can only be used without further adjustments, if the parameterisation in data is sufficiently precise as a function of the observables and if there are no important dependencies on other observables relevant for the final observables as well as if simulation and data do not exhibit very different distributions of, e.g., TPC PID clusters. In general, the agreement between simulation and data is reasonably good. The distribution of PID-clusters of electrons is shown in

[3] effectively the pseudorapidity η

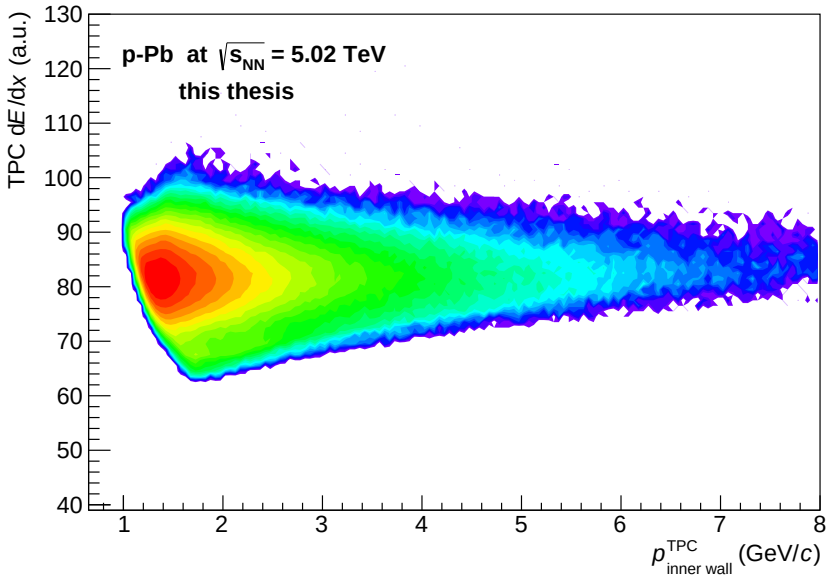

Figure 5.2.: The effect of requiring $|n\sigma_{\text{electron,TPC}}| < 3.0$ $n\sigma_{pion,\text{TPC}} > 3.5$ and $n\sigma_{\text{proton,TPC}} > 3.5$ hadron rejection as a function of the dE/dx signal and the momentum at the inner TPC wall.

data and in simulations in Fig. 5.3 (data) and Fig. 5.4 (simulation).
The residual deviations of the PID-parameterisation and the true distributions as a function of momentum p_{in}, η and azimuthal angle ϕ and PID-cluster number enter into the systematic uncertainty. More details concerning the determination can be found in Section 5.4.4 on efficiency and Section 5.7.2 on uncertainty determination. In addition, an alternative approach for the hadron rejection was followed and is explained in Appendix G.2.

5.2.4. Rejection of electrons and positrons from photon conversions

Tracks originating from e^+e^--pair creation in the detector material represent a significant background. These tracks are vetoed, if they are reconstructed with the V0-finder algorithm [206] and fulfill the criteria listed in Appendix K. The J/ψ efficiency is not affected by this rejection cut as studied for the pp analysis and the Pb–Pb analyses [151, 242].

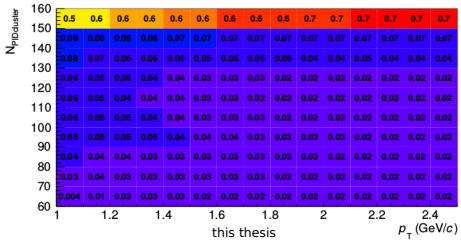

Figure 5.3.: Data

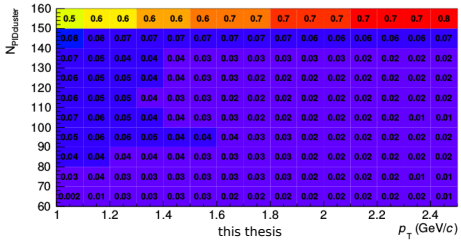

Figure 5.4.: Simulation

Distribution of $N_{\mathrm{PIDcluster}}$ as a function of track-p_{T} in the data from electrons from photon conversions on the left hand side and in the simulation used for the efficiency correction on the right hand side. The fractions of the track distribution in a given p_{T} range among the $N_{\mathrm{PIDcluster}}$-ranges are indicated by the colour code and the provided numbers. The conversion tracks are selected according to the selection criteria listed in Appendix K.

5.3. e^+e^--pair selection

From the candidate tracks, the invariant mass is calculated based on the track parameter at the distance of the closest approach to the primary vertex. The maximal possible rapidity for an e^+e^--pair with the single track pseudorapidity acceptance is $y_{\mathrm{lab}} = 0.9$. Since the analysis is statistically limited, the pair acceptance is taken to be $|y_{\mathrm{lab}}| < 0.9$.

The track acceptance choice results in a triangular shaped acceptance in the di-electron pair rapidity for low-p_{T} J/ψ candidates as shown in Section 5.4.2 due to the large opening angle between the decay daughters. When correcting the raw J/ψ number to the nominal acceptance of $|y_{\mathrm{lab}}| < 0.9$ by a factor from simulations, the input of the simulation for the rapidity dependence of J/ψ production influences the retrieved result. However, the rapidity dependence of particle production around mid-rapidity is weak. The related impact on the $Acc. \times eff.$ evaluation will be discussed in Section 5.4.2.

5.4. Acceptance and efficiency

5.4.1. Overview

In this analysis, the raw J/ψ yield was directly retrieved prior to the $Acc. \times eff.$ correction, i.e., no weighting on track level or pair level was done before the signal extraction:

$$N_{\mathrm{J}/\psi,corr} = \frac{N_{\mathrm{J}/\psi,raw}}{Acc. \times eff.} \tag{5.9}$$

The $Acc. \times eff.$ factor applied in this particular way is sensitive to the repartition of the signal density in the dimensions integrated over in the simulation used for its determination. However, the signal density of an $\mathrm{e}^+\mathrm{e}^-$-pair decay of a J/ψ meson can dependent on 5 variables. The assumption of isotropic decay in the J/ψ rest frame detailed shortly later and the azimuthal symmetry reduce the dependence to only p_{T} and y of the $\mathrm{e}^+\mathrm{e}^-$-pair. The $Acc. \times eff.$ itself might naturally depend on more variables related to the detector. However, these dependencies only enter on average as long as they do not introduce a weight as a function of p_{T} or y.
The $Acc. \times eff.$ used to correct the measured raw yield is retrieved from the simulation by counting the generated J/ψ candidates in the pair acceptance and the $\mathrm{e}^+\mathrm{e}^-$-pairs passing all selection criteria as follows in p_{T} ranges Δp_{T} and y ranges Δy:

$$Acc. \times eff.(\Delta p_{\mathrm{T}}, \Delta y) = \frac{N_{\mathrm{J}/\psi,\mathrm{rec.sim}}\left(\Delta p_{\mathrm{T}}(\mathrm{rec}), \Delta y_{\mathrm{rec}}\right)}{N_{\mathrm{J}/\psi,\mathrm{gen.sim}}\left(\Delta p_{\mathrm{T}}(\mathrm{gen.sim}), \Delta y(\mathrm{gen.sim})\right)} \tag{5.10}$$

The correction has to be weighted as a function of p_{T} and rapidity y, if the signal is retrieved in a range in rapidity or p_{T}, in which the signal density is not independent of p_{T} or y and the $Acc. \times eff.$ is not independent of p_{T} and y at the same time. Assuming that the signal density is independent of rapidity in the considered rapidity range, which is a good approximation as explained in Section 5.3, one gets the following expression for the p_{T}-'differential' $Acc. \times eff.$ evaluated in p_{T} ranges

Δp_{T}:

$$Acc. \times eff.(\mathrm{J}/\psi, p_{\mathrm{T}})|_{y\mathrm{lab}\in[-0.9,0.9]} = \frac{N_{\mathrm{rec.sim}} \in \Delta p_{\mathrm{T}}(\mathrm{rec})}{N_{\mathrm{gen.sim}} \in \Delta p_{\mathrm{T}}(\mathrm{gen})} \tag{5.11}$$

This $Acc. \times eff.$ as a function of p_{T} can be used as input for reweighting in order to correct for the potentially inaccurate input simulation distribution as explained in Section 5.4.2. This correction does not take care of bin migration effects due to finite p_{T} resolution caused by the division neglecting the difference between reconstructed and generated p_{T}. Bin migration effects are negligible considering the size of the simulation $Acc. \times eff.$ reweighting correction of 2% compared to its uncertainty of 3% and are not considered as explained in Section 5.2.2.

In the following the $Acc. \times eff.$ is subdivided for better visualisation of the different components:

$$\begin{aligned} Acc. \times eff. =& \frac{N_{\mathrm{J}/\psi,\mathrm{rec.sim}}}{N_{\mathrm{J}/\psi,\mathrm{gen.sim}}} \\ =& \frac{N_{\mathrm{J}/\psi,\mathrm{rec.sim}}}{N_{\mathrm{J}/\psi,\mathrm{rec.nomass}}} \cdot \frac{N_{\mathrm{J}/\psi,\mathrm{rec.nomass}}}{N_{\mathrm{J}/\psi,\mathrm{rec.nomass,noPID}}} \\ & \cdot \frac{N_{\mathrm{J}/\psi,\mathrm{rec.nomass,noPID}}}{N_{\mathrm{J}/\psi,\mathrm{rec.nomass,noPID,notrack}}} \cdot \frac{N_{\mathrm{J}/\psi,\mathrm{rec.nomass,noPID,notrack}}}{N_{\mathrm{J}/\psi,\mathrm{gen,acceptance}}} \\ & \cdot \frac{N_{\mathrm{J}/\psi,\mathrm{gen,acceptance}}}{N_{\mathrm{J}/\psi,\mathrm{gen.sim}}} = \varepsilon^{\mathrm{ee}}_{\mathrm{mass}} \cdot \varepsilon^{\mathrm{ee}}_{\mathrm{PID}} \cdot \varepsilon^{\mathrm{ee}}_{\mathrm{tracking}} \cdot Acc.^{\mathrm{ee}} \end{aligned} \tag{5.12}$$

where the indices 'nomass', 'noPID', 'notrack' indicate the number of reconstructed J/ψ without the invariant mass selection detailed in Section 5.5, without particle identification, without any track quality selection. The $N_{\mathrm{J}/\psi,\mathrm{gen.sim}}$ denotes the number of generated J/ψ with both daughter tracks satisfying the single track acceptance conditions. p_{T} and y dependencies have been suppressed as indices.

For J/ψ with $p_{\mathrm{T}} < 10$ GeV/c, the opening angle of the dielectron pair is always larger than 24° within the acceptance. Therefore, there is no efficiency or resolution deterioration from two track effects in the J/ψ decay. The tracking and particle identification factorise in single track efficiencies giving the terms in Equation (5.12)

an intuitive meaning as in the case of the PID step:

$$\varepsilon_{\mathrm{PID}}^{\mathrm{ee}} = \frac{\int \varepsilon_{\mathrm{PID}}(\vec{p}_{e+}) \cdot \varepsilon_{\mathrm{PID}}(\vec{p}_{e-}) Acc. \times eff.(\vec{p}_{\mathrm{e+}}, \vec{p}_{\mathrm{e\text{-}}})_{\mathrm{noPID}} \mathrm{d}^3 p_{e+} \mathrm{d}^3 p_{e-}}{\int Acc. \times eff.(\vec{p}_{\mathrm{e+}}, \vec{p}_{\mathrm{e\text{-}}})_{\mathrm{noPID}} \mathrm{d}^3 p_{e+} \mathrm{d}^3 p_{e-}}$$

$$\approx \frac{\int \varepsilon_{\mathrm{PID}}(|\vec{p}|_{e+}) \varepsilon_{\mathrm{PID}}(|\vec{p}|_{e-}) Acc. \times eff.(|\vec{p}|_{e+}, |\vec{p}|_{e-}) \mathrm{d}|p|_{e+} \mathrm{d}|p|_{e-}}{\int Acc. \times eff._{\mathrm{noPID}} \mathrm{d}|\vec{p}|_{e+} \mathrm{d}|\vec{p}|_{e-}} \tag{5.13}$$

The last equality is only approximate due to the η dependence of the PID separation power and φ dependence induced by the sector boundaries of the TPC parameterised by the PID cluster dependence of the PID resolution.

The $Acc. \times eff.$ correction relies on the simulation data introduced in Section 4.2. The injected prompt J/ψ signal is used by default for the efficiency correction, since there is no measurable difference in efficiency between prompt and non-prompt J/ψ with the very wide distance of closest approach selection criteria used in this analysis for a given rapidity y and transverse momentum p_{T} of the $\mathrm{e^+e^-}$-pair. This was explicitly verified by a double-differential comparison of $Acc. \times eff.$ in $y^{\mathrm{e^+e^-}}$ and $p_{\mathrm{T}}^{\mathrm{e^+e^-}}$. The latter test shows that the resolution effects can be neglected for the variations of the input shapes between the two simulation cases supporting the statement that bin migration effects are not important. The correction by the reweighting of the p_{T}-differential $Acc. \times eff.$ shape on the input distributions is discussed in Section 5.4.2.

In electroweak, Υ and top analyses at the LHC, for example in this ATLAS publication [243] or in a more recent Υ measurement by CMS [244], the dependence on the phase space extrapolation relying on simulation assumptions is avoided by quoting cross sections in fiducial phase space. In the inclusive J/ψ analysis with ALICE at mid-rapidity, the cross section under the condition of the given p_{T} and η cut on the daughter tracks could be determined as well. However, the related uncertainty on the J/ψ cross section due to the mentioned phase space extrapolation is negligible compared to other systematic effects relying on the assumption of unpolarised production discussed in Section 5.4.2. In addition, the PID criteria on track level are not independent of p_{T} and η. Hence, a complete decoupling from the acceptance would require an extended acceptance definition or to apply weights on track level. Since the latter steps are not followed, no fiducial cross sections are determined in this analysis. In absence of statistical limitations, one could remove

the y-shape dependence largely[4] by weighting the pair candidates as a function of rapidity. However, this would require very large candidate statistics.
The $Acc. \times eff.$ from simulations is shown in Fig. 5.5 regrouped in the two time intervals with different SPD active channel maps.

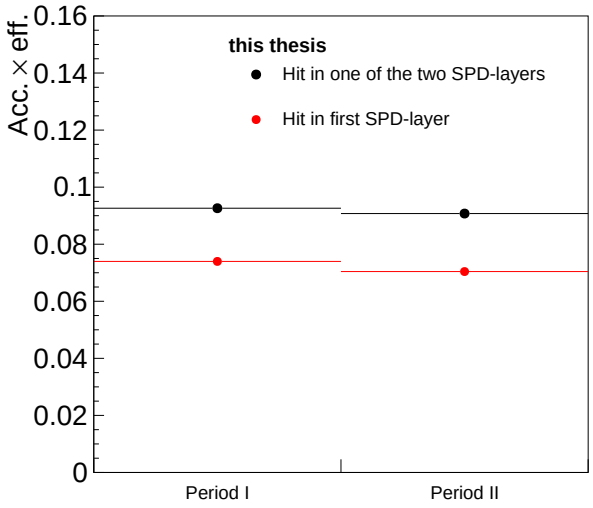

Figure 5.5.: $Acc. \times eff.$ for the injected prompt J/ψ in the simulations using the default selection criteria for the p_{T}-integrated analysis in black and for the multiplicity and centrality differential analyses in red for the two subsamples with different SPD active channel map. The shown $Acc. \times eff.$ is not yet reweighted for the differences in the p_{T}-differential behaviour in simulation and in data as explained in Section 5.4.2.

The steps of the $Acc. \times eff.$ determination introduced in Equation (5.12) are depicted in Fig. 5.6 as a function of p_{T} for the selection criteria in the p_{T}-integrated analysis. The p_{T} shape of the acceptance is explained in details in the following section. The shape of the tracking efficiency part is caused by the single track efficiency shape as a function of p_{T}, which is created mainly by the TPC geometry. An example can be seen in Fig. 19 of Ref. [206]. The dip in the PID efficiency is explained in detail in Section 5.4.4 and is a similar effect as the minimum of the acceptance curve. The slow decrease of efficiency towards higher $\mathrm{e^+e^-}$-pair p_{T} is caused by the approaching of the pion and electron $\mathrm{d}E/\mathrm{d}x$ bands, since the pion rejection is kept at a constant distance to the pion expectation. The shape of the invariant mass window ($\mathrm{m_{ee}} \in [2.92, 3.16]$ GeV/c^2) efficiency originates from the fact that the track cuts acting on momentum or p_{T} already reject the NLO QED

[4] Apart from resolution effects.

contribution at the vertex and the bremsstrahlung to different degrees at different e^+e^--pair p_T.

Figure 5.7 shows the $Acc. \times eff.$ steps as a function of of the e^+e^--pair rapidity y. The reason for the triangular shape of the acceptance is explained in Section 5.3. The rapidity dependence of the tracking requirement is caused primarily by edge effects for candidate events with vertices at large z_{vtx}, where not the complete pseudorapidity range is covered by all ITS layers. The slight asymmetry around mid-rapidity is caused by the concentration of the non-active SPD channels at negative z values. Asymmetries in the other steps arise from from the non-symmetric rapidity input distribution due to the boost between the lab and the nucleon-nucleon collision system introducing different weights within a given bin. The shape of the PID contribution is caused by a better separation power between different species at large moduli of track pseudorapidity. The reduction of the efficiency of the invariant mass selection is caused by different amounts of crossed material at large track pseudorapidity for large z_{vtx} values. Supplementary figures for other selection criteria are shown in Appendix G.5. The steps will be explained in more details in the following.

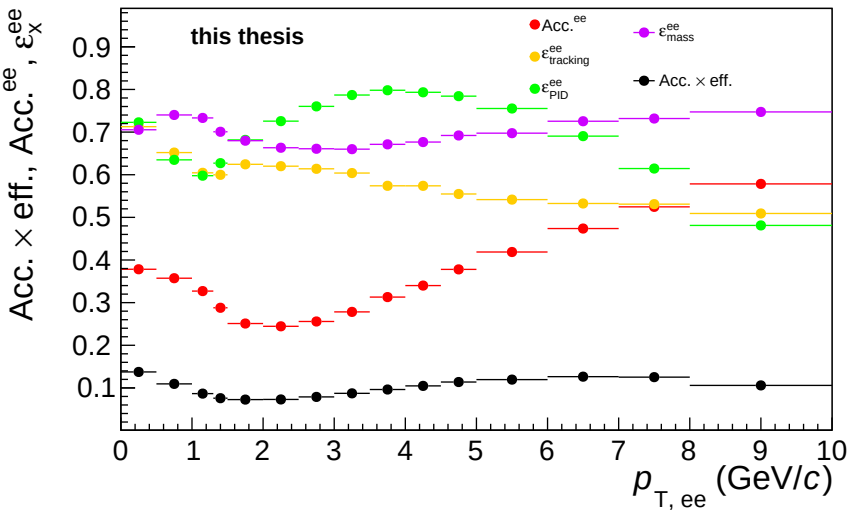

Figure 5.6.: The transverse momentum dependence of the $Acc. \times eff.$-factor separated in several steps for the selection criteria in the integrated analysis. The invariant mass window for the signal extraction is $[2.92, 3.16]$ GeV/c^2.

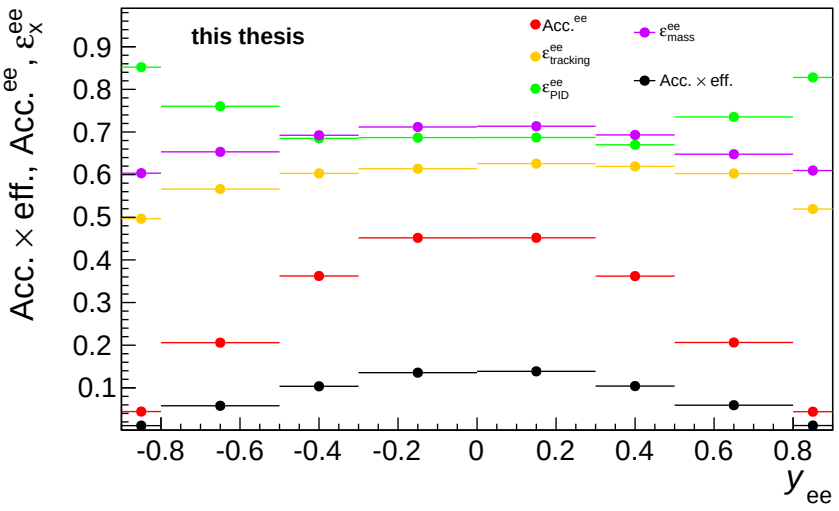

Figure 5.7.: The rapidity dependence of the $Acc. \times eff.$-factor separated in several steps for the selection criteria in the integrated analysis. The invariant mass window for the signal extraction is $[2.92, 3.16]$ GeV/c^2.

5.4.2. Acceptance

Figure 5.6 displays the $Acc.^{ee}$ defined in Equation 5.12. The characteristic non-monotonic p_T pair shape is introduced by the daughter track acceptance selection in p_T. It can be explained by the fact that at vanishing e^+e^--pair p_T and after the pseudorapidity cuts on the daughter tracks, no daughter track p_T below 1 GeV/c is kinematically possible for a mother particle with the J/ψ mass. However, at finite e^+e^--pair p_T, the p_T cut on the daughter tracks, the acceptance is reduced. This is caused by the boost of the J/ψ particle, which leads to a significant fraction of e^+e^--pairs, which have one track which has a p_T below the p_T acceptance cut value. The effect is most extreme for e^+e^--pair p_T of about 2 GeV/c and decreases with increasing higher e^+e^--pair p_T, since the fraction of concerned pairs decreases. The increase of the acceptance at high p_T is explained by the decrease of the opening angle leading to an acceptance of 100% within $|y_{J/\psi}| < 0.9$ for $p_T \to \infty$.
The acceptance behaviour of J/ψ in the central barrel of ALICE with a track-p_T cut at 1 GeV/c is similar to the measurement of Υ with ATLAS [245] or CMS [246]. The ratio of the minimum single track p_T over the resonance mass is in ALICE and the CMS/ATLAS cases about 1/3. A comparison of the acceptances between this

ALICE J/ψ measurement and a CMS Υ measurement in pp collisions is shown in Appendix G.1. The p_{T} acceptance of the daughter tracks is also inducing strong variations of angular differential $Acc. \times eff.$ factors for quarkonia measurements and can be the reason for the limitation of polarisation measurements to high p_{T} [247, 248] or the restriction to single lepton trigger data [249]. The rapidity shape of the acceptance factor analogously defined as for the p_{T}-differential case is shown in Fig. 5.7. It exhibits a triangular shape due to the large opening angle of most J/ψ candidates in the acceptance as explained in Section 5.3.

As mentioned in Section 2.3, the polarisation of the produced J/ψ influences strongly the $Acc. \times eff.$ factors in particular at low and most strikingly at intermediate p_{T} (1 GeV/c < p_{T} < 5 GeV/c) of the produced J/ψ for typical p_{T} selections of the daughter tracks, where the $Acc. \times eff.$ changes by up to 44% for extreme polarisation assumptions for the ALICE acceptance [151]. However, a constraining polarisation measurement is out of reach in p–A collisions with the accumulated statistics in 2013 in the central barrel of ALICE.

In recent years, the analysis of prompt J/ψ production in pp collisions has shown small polarisations at Tevatron measured by CDF [250, 251][5] at mid-rapidity at transverse momenta down to 4 or 5 GeV/c and at the LHC [249, 252][6] at forward rapidities for transverse momenta down to 2 GeV/c. At mid-rapidity, the polarisation was also measured well above 10 GeV/c [250, 251, 248] showing a sizeable polarisation. There is to date no measurement of the J/ψ polarisation in p–A or A–A collisions. Although there are differences in the contributions of the different short-distance matrix elements implying differences between the polarisation in pp and in p–A collisions in some calculations [253], it is not expected that the polarisation in p–A collisions will differ very strongly from the one in pp collisions. Conventionally, J/ψ hadronic production cross sections are given under the assumption of unpolarised production in absence of polarisation measurements. This is also done in this analysis and no uncertainty for the latter assumption is given. The cross section variations related to extreme polarisation assumptions are close to identical to the analogue cross section measurements in pp collisions, which uses the same track acceptance choices and J/ψ p_{T} ranges as in this analysis [151, 99]. For the main result of this thesis in view of theory comparisons, the nuclear modification

[5] The two results from CDF are inconsistent with each other, but both results are consistent with no polarisations at the lowest measured J/ψ p_{T}, which is most relevant for this analysis.

[6] In the ALICE publication, inclusive J/ψ polarisation is measured.

factors, the related uncertainty partially cancels, since the reference cross section is constructed from pp collision results reconstructed under the assumption of no polarisation in case of ALICE [151] and PHENIX [254]. The CDF result used for the interpolation [107] assumes the small measured, but finite polarisation at Tevatron and no polarisation at the lowest p_{T}, where no measurement is available.
Since the $Acc. \times eff.$ factor is not a constant as a function of p_{T} and rapidity due to the acceptance and the electron identification selection criteria, it is necessary to investigate and to correct for the discrepancy between the simulation input and the corresponding data shapes as explained in Section 5.4.1. First, the dependence on the p_{T} shape of the input simulation is discussed.
As a first step, the p_{T}-differential result corrected with bin-by-bin correction factors as explained in Section 5.4.1 was fitted with the following function:

$$f(p_{\mathrm{T}}) = C_0 \cdot \frac{p_{\mathrm{T}}}{(1 + (p_{\mathrm{T}}/p_0)^2)^n} \tag{5.14}$$

The fit parameters are the normalisation C_0 and the constants p_0 and n. The fit takes into account the statistical and systematic uncertainties except of the luminosity uncertainty. Secondly, the $Acc. \times eff.$ as a function of p_{T} was fitted with a polynomial. Both functions were folded to derive a 'fully differential' $Acc. \times eff.$ The $Acc. \times eff.$ resulting from this procedure and the one directly from the input simulation in the p_{T} ranges used for the final p_{T}-differential result were determined and compared. The derived discrepancy is below 1% for all considered bins. This discrepancy has to be compared with statistical uncertainties of at least 12% and different systematic uncertainties of similar size. It was hence not further considered as source of uncertainty. The p_{T}-integrated yield was determined with a signal extraction integrating over the full phase space and not as a sum of the p_{T}-differential contribution. Therefore, the $Acc. \times eff.$ in the p_{T} ranges as in Fig. 5.6 as a function of transverse momentum had to be reweighted according to the fit to the experimental p_{T}-differential result. The deviation of the reweighted $Acc. \times eff.$ and the one directly from the simulation amounts to about 2.0% and was applied as a correction. The systematic uncertainty of this procedure due to the experimental uncertainty on the p_{T}-differential result is explained in Section 5.7.4.
Secondly, the rapidity shape has to be varied, since the $Acc. \times eff.$ is not flat as a function of the rapidity and there might be a significant impact due the not exactly known true distribution as a function of rapidity. The rapidity distribu-

tions of the simulated prompt and non-prompt J/ψ samples are different, since the simulated prompt J/ψ are boosted according to the expected rapidity shift of the centre-of-mass system, whereas the non-prompt J/ψ are simulated with the pp rapidity shape, which is centred at mid-rapidity. We reweight the simulation for non-prompt J/ψ with the same p_{T}-distribution as the prompt J/ψ simulation sample and extract the p_{T}-integrated $Acc. \times eff.$ and compare the residual discrepancy in the p_{T}-integrated $Acc. \times eff.$ caused by the rapidity shift. The underlying rapidity shape of the non-prompt J/ψ corresponds to a smooth variation of R_{pA} by 8% with a lower value at forward rapidity and higher value at backward rapidity as expected by theory within the rapidity range of the measurement. The observed difference of the two p_{T}-integrated $Acc. \times eff.$ factors amounts to 0.32%. The statistical uncertainties between the two simulation samples are fully uncorrelated. The relative statistical uncertainty on the ratio is about 0.4%. In view of the small size of the deviations compatible with the statistical uncertainty of the simulated sample, no systematic uncertainty is assigned due to the imprecise knowledge of the rapidity distribution knowing that available phenomenological calculations expect a weaker variation of the rapidity dependence than the tested one.

5.4.3. Tracking efficiency

Within the fiducial acceptance defined in Section 3.3, the combined ITS-TPC tracking of ALICE is not 100% efficient, although no electron or positron track is stopped for $p_{\mathrm{T}} > 1.0$ GeV/c in the small amount of material budget throughout the combined ITS-TPC system described in the Sections 3.3 and 3.3.
The inefficiencies occur during the track finding procedure described in Section 3.3 by tracks that are not found during the seeding or rejected due to bad quality, since their projection to the read-out plane of the TPC falls completely or partially in the dead-areas between the multi-wire proportional chambers. A few tracks are also lost at the central electrode. In addition, a fraction of the stand-alone TPC tracks are not matched to at least 2 corresponding hits in the inner tracking system during the final step of the track reconstruction. The associated inefficiency amounts to about 1.0-4.5% for electrons as a function of p_{T} according to simulation. Furthermore, the track can have no associated hit of the combined ITS-TPC track in either of the two SPD layers, in simulation, the efficiency loss on the $\mathrm{e}^{+}\mathrm{e}^{-}$-pair level by this requirement is found to be about 5%. Inefficiencies are also introduced by the

requirement of a hit in the first layer of the ITS. The inefficiency with respect to a hit requirement in either of the two first layers amounts to about 78% on pair level according to simulations as depicted as a function of rapidity in Section 5.8, which reflects roughly the squared fraction of active channels of the first ITS layer of about 90% on average. Finally, tracks are rejected by further quality requirements listed in Section 5.2.1. The associated efficiency loss is smaller than the one from all other considered sources. Occupancy effects can be safely neglected in the multiplicity environment of minimum bias p–Pb collisions at low interaction rate, since the tracking efficiency performance of the ALICE central barrel is not different in pp collisions and in central Pb–Pb collisions [206]. Since the $Acc. \times eff.$ determination is based on the description of the ALICE set-up in simulations, the MC simulation validation for the J/ψ measurement is discussed in the following. Since it represents the largest efficiency loss, the first mentioned effect related to

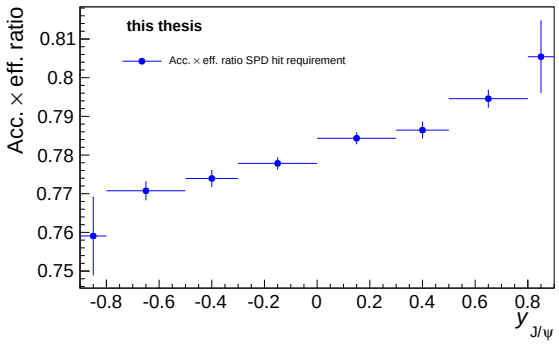

Figure 5.8.: The ratio of the $Acc. \times eff.$ of J/ψ between the requirement of a hit in the first layer of the SPD and a requirement of a hit in either of the two layers on both daughter tracks as a function of rapidity as seen in simulation.

the wire chamber borders was investigated. In order to probe the description, the efficiency of the default track choice was determined relative to an additional fiducial phase space requirement, called 'in-active-volume cut' in the following, where it is assumed that the TPC stand-alone tracking efficiency is close to 100% in case of nominal TPC gain and where the tracking performance is very well described in simulation [255]: a track passes the selection, if it exhibits at least 120 crossed TPC pad rows, for which the crossing track trajectory has 1.5 cm distance from the multi-wire proportional chamber borders and less than 220 cm from the central electrode in electron drift direction. The ratio of the efficiency for this fiducial cut criterion in data and in simulation for non-identified tracks is shown in Fig. 5.9 and

Fig. 5.10 for both charges separately. The corresponding double ratio are shown in Appendix G.3. The structure of the simple ratio is expected, since the track curvature of a 1 GeV/c track corresponds approximately to the $\Delta\varphi$ spanned by a TPC sector. The deviations from unity in the double ratio are below 1%.
The same quantities are derived for the default PID criteria within the TPC applied in data and depicted in Fig. 5.11 and Fig. 5.12. The double ratios are shown in Appendix G.3. The minimum of the simple ratio is significantly larger than the corresponding quantity for non-identified tracks. This observation implies that the hadron rejection criterion acts partially as an acceptance selection at the border of the multi-wire proportional chambers, where more tracks are rejected due to a smaller number of PID-clusters per track and hence worse dE/dx-signal resolution. The deviations between data and simulation are larger for the electrons and positrons than for non-identified tracks and exhibit mostly different signs at a given p_{T} than for the corresponding quantities for non-identified tracks. The observed larger deviations for electrons and positrons than for non-identified tracks are therefore attributed to the systematic mismatch of the particle-identification efficiency in data and in simulations. The effects observed in the data driven cross checks of the particle identification cross checks are discussed in Section 5.4.4.
The 'in-active-volume-cut' employed for this cross check is not applied in the J/ψ analysis due to the substantial loss of tracks as it is visible in Fig. 5.11. Within ALICE,

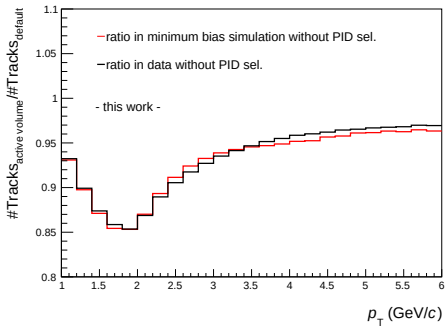

Figure 5.9.: negatively charged

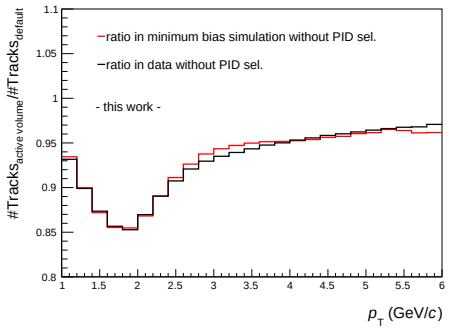

Figure 5.10.: positively charged

The ratio of the reconstructed tracks selected in this analysis with the additional 'in-active-volume-cut' and without the additional requirement for negatively charged tracks on the left hand side and positively charged tracks on the right hand side. No particle identification is applied.

as for example in Ref. [181], the track prolongation efficiency from the ITS to the TPC is probed in a data-driven approach by comparing the number of ITS-TPC and

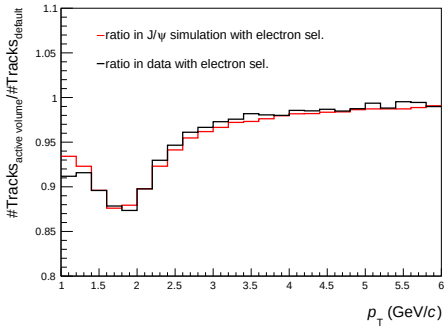

Figure 5.11.: negatively charged

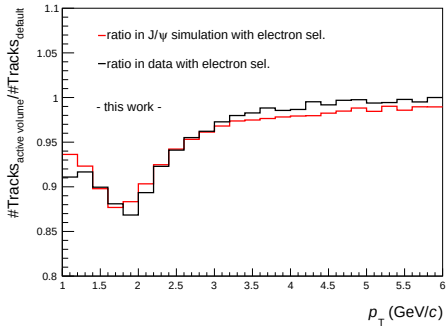

Figure 5.12.: positively charged

The ratio of the reconstructed tracks selected in this analysis with the additional 'in-active-volume-cut' and the track selection without the additional requirement for negatively charged tracks on the left hand side and positively charged tracks on the right hand side. The standard particle identification of this analysis is applied.

TPC stand-alone non-identified tracks with the number of detected non-identified TPC-ITS tracks as a function of p_{T}, η and φ:

$$\varepsilon_{\text{prol prox}} = \frac{N_{\text{tracks, TPC-ITS}}}{N_{\text{tracks,TPC-ITS and TPC standalone}}} \tag{5.15}$$

This proxy cannot be identified directly with the prolongation efficiency. The comparison of this ratio between simulation and data is also sensitive to pile-up in the TPC not accounted for in the simulation, the amount of strange particles and secondaries from material interaction entering the number of TPC stand-alone tracks, which cannot have a match in the ITS. In addition, different spectral shapes in simulation and data can modify the ratio. Finally, different p_{T} resolutions in TPC stand-alone tracking or combined tracking in simulation and in data can influence this ratio as well. The latter two effects are mostly relevant for p_{T}-differential determination at higher p_{T} than relevant for this analysis.

In the low pile-up environment of the p–Pb data sample, the effect caused by out-of-bunch pile-up can be largely eliminated by exploiting the TPC stand-alone distance of closest approach of tracks with a resolution of better than 1 cm and the offline out-of-bunch pile-up rejection explained in Section 4.1.

A data driven check for electrons would be desirable, since electrons suffer from bremsstrahlung and differences between electrons and hadrons are expected. For primary electrons with a transverse momentum larger than 1.0 GeV/c as used in this analysis, there is presently no possibility to select them track-by-track based on

TPC-only information with high purity and with sufficient statistics in data due to the large background from e^+e^--pair creation at the beam-pipe and within the ITS. Since there is no resonance decaying at the primary vertex to electrons/positrons in large amounts with the available statistics, no tag-and-probe procedure can be easily adopted. The J/ψ meson itself would be actually the first obvious candidate in the e^+e^- mass spectrum.

Investigations with non-identified tracks with close to identical tracking selection criteria as in this analysis indicate deviations of $\varepsilon_{\text{prol prox}}$ between data and simulations in p–Pb collisions below 1% on track level. In addition, studies were carried out with charged kaons, which are practically not contaminated from weak decays of light-flavour hadrons[7]. They support the findings based on non-identified tracks. It was checked in simulation that the prolongation efficiency for primary electrons from J/ψ-decays without specific requirements on SPD hits ranges between 95.5%-99% depending on p_{T} for $|\eta| < 0.9$. The prolongation efficiency is depicted in Fig. 5.13, where it is compared to the one of charged kaons. The differences amount to 0-1.5%. For the p_{T}-integrated J/ψ yield the $Acc. \times eff.$ is reduced by about 4% by the ITS refit requirement for both decay daughters without consideration of the additional SPD requirements.

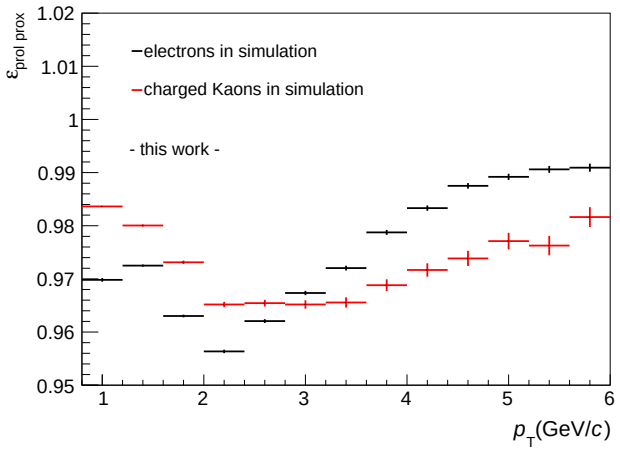

Figure 5.13.: The prolongation efficiency proxy is compared between primary electrons identifed based on simulation information and passing standard electron selection and charged kaons identifed based on simulation information. Only the ITS refit criterion implying two associated track points in any of the 6 ITS layers is required for the numerator of the ratio.

[7] In fact, the largest contribution stems from Ω decays ($\Omega^- \rightarrow K^-\Lambda$). The number of charged kaons from this decays are suppressed by a factor O(1000) compared to the total amount of primary kaons as measured in Refs. [256, 257].

Due to the high gain of the TPC in the p–Pb data sample, the uncertainties on the track efficiency due the selection criteria in the distributions of $\chi^2/N_{\text{cluster}}$, DCA, N_{cluster} are negligible. This can be seen from the corresponding distributions in simulation and in data for electrons shown in Appendix G.3. The distributions are not identical, but the selection acts where the introduced inefficiency is below 1% or maximally about 1% for the N_{cluster} requirement.

5.4.4. Particle identification efficiency

The particle identification is related to the largest efficiency reduction in the track selection for a large fraction of measured phase space. Figure 5.6 shows the dependence of $\varepsilon^{\text{ee}}_{\text{PID}}$ on e^+e^--pair p_{T} for standard criteria ($|n\sigma_{\text{electron}}| < 3.0$, $n\sigma_{\text{proton}}$, $n\sigma_{\text{pion}} > 3.5$). The distributions for the other particle identification criteria used in this thesis are shown in Appendix G.5. The shape of $\varepsilon^{\text{ee}}_{\text{PID}}$ as a function of p_{T} is caused by the interplay of proton and pion exclusion via the TPC PID. At low pair-p_{T}, the pion rejection has practically no influence and electrons with $p_{\text{T}} > 1$ GeV/c are not rejected by the proton exclusion for a large fraction of the phase space at $p_{\text{T}} = 0$ GeV/c of the e^+e^--pair. The dip in the $Acc. \times eff.$ at $p_{\text{T}} \approx 1$GeV/c of the pair is caused by the proton rejection: the proton rejection acts effectively as a $|\vec{p}|$ selection[8] on the daughter tracks due to the crossing of the proton and electron line in the two dimensional $\text{d}E/\text{d}x$-momentum space. Hence, there is an interplay between the acceptance daughter-p_{T} cut and with the proton rejection: with no p_{T}-acceptance selection on the daughter tracks, the proton rejection has a much stronger impact, since the p_{T} and the $|\vec{p}|$ can only deviate by about a factor 1.4 in the track acceptance $|\eta| < 0.9$. This is illustrated by the $Acc. \times eff.$ and efficiency factors shown in Fig. 5.14. The same selection criteria are applied as in Fig. 5.6 except of a change of the track-p_{T} acceptance selection to $p_{\text{T}} > 0.8$ GeV/c. The higher tracking efficiency at very low p_{T} compared to Fig. 5.6 for the pair is related to geometry and can be seen on single track level in Fig. 19 of Ref. [206][9].

Due to the interplay between acceptance and particle identification and the related uncertainties, the analysis for the p_{T}- and multiplicity-integrated and the p_{T}-

[8] This selection is slightly η and $N_{\text{PIDcluster}}$-dependent.

[9] The total inefficiency of about 15-20% shown in Ref. [206] for primary charged particles is partially induced by the inclusion of multi-strange baryons in the definition of primary charged particles which are not reconstructed in the TPC due to their decay. In addition, there are also inefficiencies for hadrons due to hadronic interactions in the material.

differential quantities was also performed with a variation of the minimum track p_{T} between $0.8, 1.0, 1.1$ GeV/c and the proton and the pion rejection between $3.0, 3.5, 4.0$ $n\sigma$ varying the criteria independently with respect to each other. Details of these cross checks are given in Appendix F. At higher pair-p_{T}, the efficiency loss related to the electron identification increases smoothly due to the relativistic rise of the pion dE/dx expectation towards the electrons. Due to the smaller background, the pion rejection was attenuated to 3.0σ at pair $p_{\mathrm{T}} > 5.0$ GeV/c in the p_{T}-differential analysis. The corresponding $Acc. \times eff.$ as a function of pair p_{T} is shown in Appendix G.5.

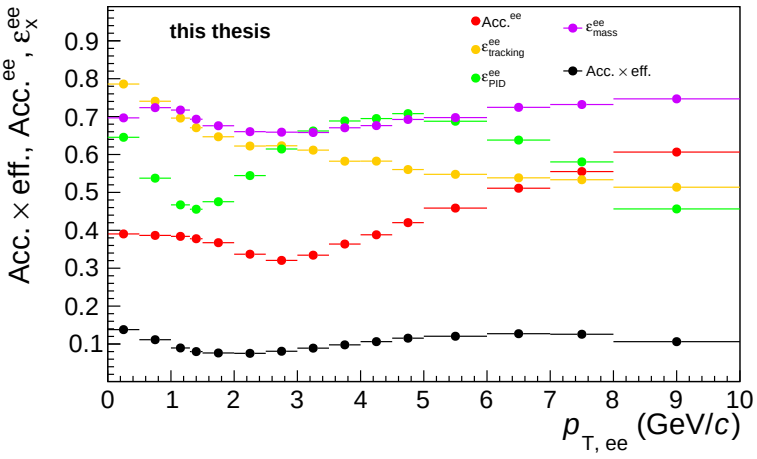

Figure 5.14.: The transverse momentum dependence of the $Acc. \times eff.$-factor separated in several steps chosing a daughter-$p_{\mathrm{T}} > 0.8$ GeV/c and otherwise the same selection criteria as in Fig. 5.6.

The dE/dx-measurement-based PID selection is the most delicate step of the efficiency determination. As explained in Section 5.2.3, the description relies on a 4 dimensional parameterisation ($\beta\gamma$, tan(θ), $N_{\mathrm{PIDcluster}}$, multiplicity) of the TPC-PID response in data. The data parameterisation is superimposed to the simulation as detailed in Section 5.2.3.

The usage of identified electrons by other means than the TPC PID for a fully data-driven efficiency determination would be the best solution. As in the case of the tracking efficiency determination, the selection of primary[10] electrons in this context is difficult as the J/ψ itself as first candidate is already statistically limited.

[10] In this context, tracks originating not from interaction with the material and not from decays of weakly decaying light-flavour hadrons are meant.

Tag-and-probe methods with primary tracks as employed in ATLAS and CMS for high-p_{T} leptons for the performance determination of calorimeters and muon systems in data are not available. A second choice is the electron identification with another detector than the TPC. The candidate detectors are the EMCal and the TRD.

The EMCal has no sufficient stand-alone hadron suppression to get pure electron samples in the momentum range 1-5 GeV/c, since hadron tracks have a non-negligible probability to have a hadronic shower in the calorimeter material. EMCal electron analyses in ALICE rely always on the TPC-PID information in the relevant momentum range for this analysis as for example the analysis in the p–Pb data sample [240]. In addition, the EMCal has no full phase space coverage as detailed in Table 3.1. Whereas the azimuthal restriction can be dealt with, the EMCal covers several of the 18 sectors of the TPC, the pseudorapidity restriction prevents a validation of the TPC PID performance without delicate extrapolations.

In principle the very good TRD electron identification [206] could be used to define pure electron samples for TPC-PID performance evaluation. Since it was not fully installed, the fraction of TRD-PID was only available for about 50% of the TPC-ITS tracks. In addition, the most critical phase space regions at the TPC sector boundaries have the lowest matching efficiency to the TRD and the TRD performance is similarly affected at those boundaries due to less track points [216].

Therefore, non-primary tracks originating from $\mathrm{e}^+\mathrm{e}^-$-pair creation from photons, dominantly originating from electromagnetic $\pi^0 \rightarrow \gamma\gamma$ decays are used for data-driven cross checks. In order to guarantee a similar PID-response of tracks from γ-conversions and primary tracks, it is necessary to require a small radial distance of the conversion vertex to the primary vertex [241]. In practice, this was done by requiring at least 2 hits in the ITS. The particle identification efficiency was derived in data and in simulations with conversions and compared with the efficiency seen with true primary electrons from J/ψ decays in the the dedicated simulation data. The number of selected conversion tracks is not sufficient to derive efficiencies multi-dimensionally with sufficient accuracy. It is therefore not suited in this data sample for a fully data-driven particle identification efficiency determination. Nevertheless, one dimensional comparisons provide a very good data-driven test of the efficiency determination precision achieved in simulation.

The electrons and positrons were selected by an algorithm finding oppositely charged tracks from non-primary vertices [206], and additional criteria listed in Appendix K.

Nevertheless, there is still a non-negligible fraction of pions in the track sample, which can be seen in Fig. 5.15, dominantly from K^0_S decays. This background source is increasingly distorting the derived efficiencies for increasing momentum. Therefore, the exclusion cut efficiency was compared with respect to the electrons in $-2.0 < n\sigma_{\text{electron}} < 3.0$[11] and not to $-3.0 < n\sigma_{TPC,electron} < 3.0$, i.e., we define in the case of Fig. 5.16:

$$\varepsilon_{\text{PID}} = \frac{N_{\text{electrons}}(-2.0 < n\sigma_{\text{electron}} < 3.0 \& n\sigma_{\text{pion}} > 3.5 \& n\sigma_{\text{proton}} > 3.5)}{N_{\text{electrons}}(-2.0 < n\sigma_{\text{electron}} < 3.0)} \tag{5.16}$$

The residual contamination is then negligible. This was checked by fits of the conversion electron $n\sigma$ distributions.

Figure 5.16 shows an one-dimensional efficiency determination with electrons and positrons from conversion processes in data and in simulation compared to the efficiency seen with the J/ψ decay electrons in simulation. The statistical uncertainties are clearly visible for the conversion data samples. The conversions from simulation were taken from the large minimum bias production, since the four million events in the dedicated production for the determination of the J/ψ acceptance and efficiency corrections do not contain a sufficient number of conversions. The overall agreement is reasonable and the differences do not exceed 2.0% except of the lowest momentum bins below 1.3 GeV/c as it can be seen more clearly in the corresponding ratios shown in Fig. 5.17,5.18 and 5.19. The same figures for the particle identification criteria used at pair-p_{T} larger 5 GeV/c are shown in Appendix G.2. The situation is very similar in the latter case.

The best test of the simulation description is the direct comparison of the conversion efficiencies in data and in simulations shown in Fig. 5.19, since this comparison is not sensitive to differences in the phase space occupation in the integrated dimensions φ and η between primary and tracks from γ-conversions and potential differences in the PID response caused for example by different incident angles of the tracks with respect to the pad-row at the same track p_{T}. However, the other two ratios show that the tracks from γ-conversions behave in simulation very similar compared to primary tracks from J/ψ decays (Fig. 5.18) and that the agreement with

[11] Assuming that the differences of the true electron distribution and the MC simulation electron distribution is negligible in the rejected phase space below -2.0 $n\sigma_{\text{electron}}$, since this part of the distribution contributes only to about 2% of the integral. This assumption was checked by the inspection of the corresponding distributions.

respect to conversion tracks from data and J/ψ decay electrons from simulations is similar than the direct comparison between data and simulation with tracks from γ-conversions (Fig. 5.17). Hence, the conversion sample can be directly used for the estimation of deviations for tracks from J/ψ decays. The large discrepancies below 1.3 GeV/c, most prominently in the direct conversion comparison, are not critical for the acceptance choices for this J/ψ analysis for the assumption of isotropic decays. Although the deviation amounts to 16% for the conversion comparison as it can be already seen in Fig. 5.16, only one track[12] of about 25% of e^+e^--pairs in the first two p_T bins of this analysis has a momentum below 1.3 GeV/c. This fact is illustrated by Fig. 5.20, where the normalised distribution of the momenta of both decay daughters from a fast simulation of the decay kinematics after the daughter acceptance selection in the e^+e^--pair p_T bins considered in this analysis is shown. In addition, no dependence of the result on the variation of the proton rejection is found in the selection variations explained in Appendix F. However, for future polarisation measurements, these discrepancies have to be controlled much better.

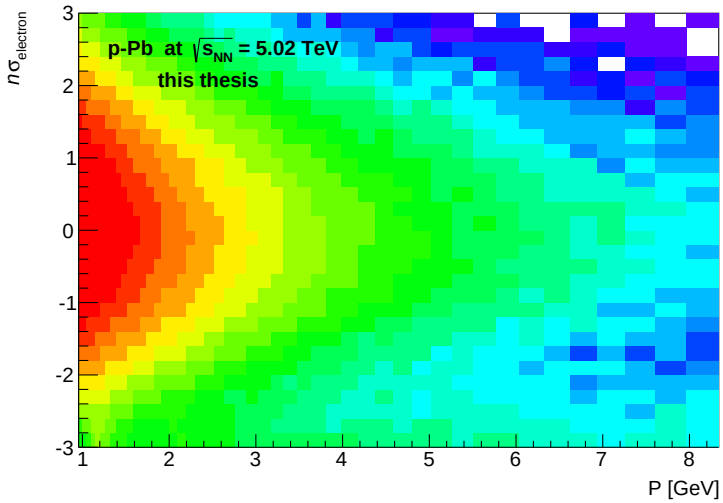

Figure 5.15.: The $n\sigma_{\mathrm{TPC,electron}}$ distribution as a function of the track momentum at the inner TPC-wall is shown for tracks from γ-conversions. A non-negligible contamination from hadrons can be seen at low values of $n\sigma_{\mathrm{TPC,electron}}$.

[12] Only one of the decay tracks of a J/ψ at finite momentum can fall in this momentum region. The momentum of one of the two decay decay daughters must have a momentum larger than the one in the rest frame of the J/ψ, i.e., it must be larger than 1.5 GeV/c.

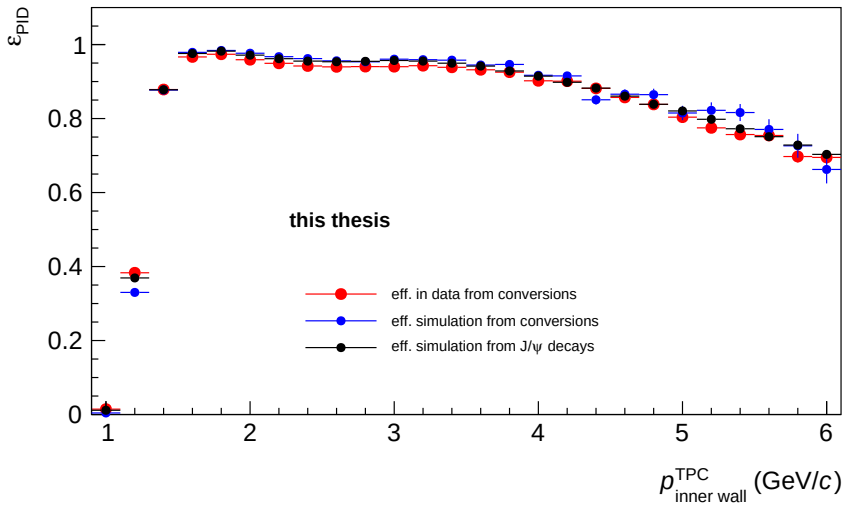

Figure 5.16.: The single track PID-efficiency for electrons and positrons derived from conversions in data and in simulations and from J/ψ decays in simulation as defined in Equation (5.16). Further details are explained in Section 5.4.4.

5.4.5. Acceptance and efficiency as a function of multiplicity/centrality

The potential variation of the $Acc. \times eff.$ as a function of multiplicity needs to be investigated in particular in view of multiplicity or centrality differential measurements. Since the ALICE set-up is designed for the high multiplicities in central Pb–Pb collisions, only two effects are considered.

The $Acc. \times eff.$ can be distorted at very low multiplicities due to the contribution

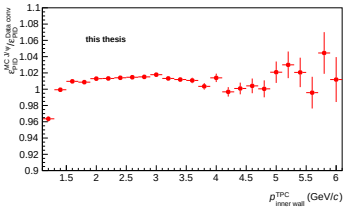

Figure 5.17.: J/ψ simulation vs. conversion data

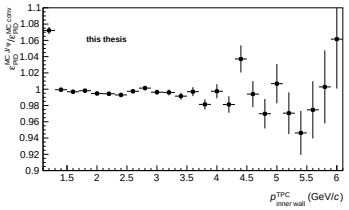

Figure 5.18.: J/ψ simulation vs. conversion simulation

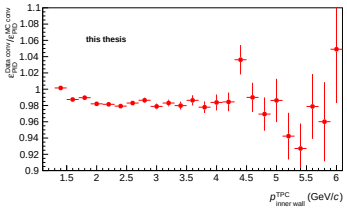

Figure 5.19.: conversions data vs. simulation

The ratio of single track PID-efficiencies as defined in Equation (5.16) derived from conversions, from simulation of J/ψ decay daughters and from conversions in simulations. Further details are explained in Section 5.4.4.

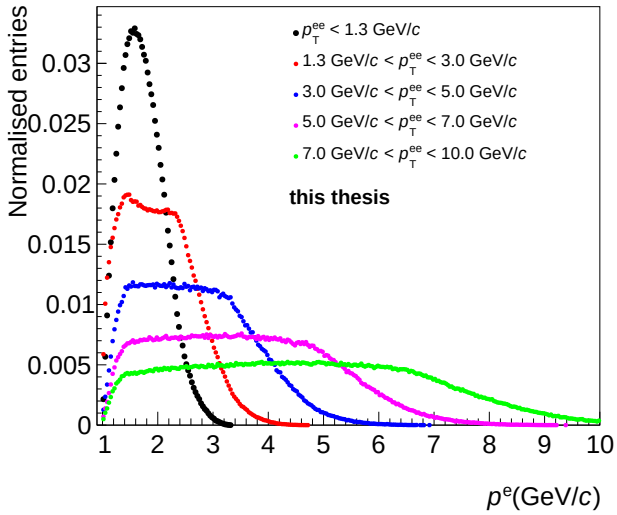

Figure 5.20.: Normalised distribution of momenta of both decay tracks after the track-acceptance cuts in fast simulation for the different p_{T} ranges considered in the p_{T}-differential analysis.

of J/ψ daughter tracks to the multiplicity estimation itself. Furthermore, the PID efficiency could show a dependence on the charged particle multiplicity.

First, we consider a perfect multiplicity measurement and perfect measurement of J/ψ within the defined acceptance within the given cuts of pseudorapidity and p_{T}. We hence only consider an acceptance correction of the J/ψ counts.

At very low multiplicities, the daughter tracks of the J/ψ meson will contribute significantly to the overall charged-particle multiplicity of the event in the acceptance. For an ideal detector, the acceptance correction factor, which extrapolates from the fiducial cross section with given η and p_{T} track cuts to the cross section in the defined phase space $|y_{\mathrm{J}/\psi}| < 0.9$, will vary, if the multiplicity definition includes the tracks of the J/ψ as done in this analysis[13]: the multiplicity binning acts as a J/ψ veto at very low multiplicities. If the multiplicity dependence in the simulation is different from the real dependence, this effect will result in a biased $Acc. \times eff.$ determination. As for the ideal detector case, an analogue effect arises from inefficiencies of the detector.

This effect was studied in simulation and is visible for very small multiplicity ranges both on acceptance as well as on SPD requirement level. The acceptance and the tracking efficiency was found to be constant as a function of multiplicity for the

[13]They are not excluded for simplicity, since there is no direct correspondence between SPD-tracklets and reconstructed tracks.

chosen bin choices. Hence, the effect is negligible for the large first considered multiplicity range including events with up to about 30 tracks.

The parameters describing the expected dE/dx signal position of a given particle species and the expected resolution of the TPC depend on multiplicity. The dependence of the expected energy loss do not introduce a dependence of the efficiency on multiplicity, when the effect is corrected for.

The TPC-PID resolution variation is also parametrised as a function of charged-particle multiplicity and can introduce a variation of $Acc. \times eff.$ for J/ψ as a function of multiplicity. This effect is negligible for the applied PID selection in the p_{T}-integrated J/ψ yield determination. This is demonstrated in Fig. 5.21, where the multiplicity dependence of the PID parameters derived from data was taken into account in the simulation.

In summary, the impact of both effects is found to be negligible. No reweighting of the signal counts as a function of multiplicity/centrality for the efficiency determination was necessary despite the unrealistic multiplicity/centrality dependence in the simulation.

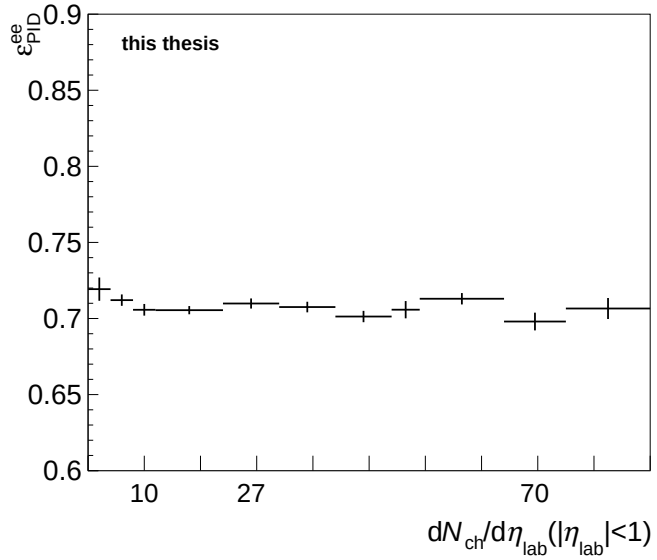

Figure 5.21.: The particle identification efficiency for the J/ψ candidates defined as in Section 5.4.1 as a function of the multiplicity estimator in simulation taking into account the multiplicity dependent PID parameterisation is shown. The uncertainty bars indicate the statistical precision of the simulations.

5.5. Signal extraction

In the following section, the extraction the raw J/ψ signal counts in this analysis is explained.

5.5.1. Signal shape

The extraction of the signal counts in case of a e^+e^--analysis of J/ψ is complicated by the significant tail of the signal towards lower masses. This tail is due to the impact of the NLO QED-process J/$\psi \rightarrow e^+e^- + \gamma$ and the bremsstrahlung of the electrons/positrons emitted in the crossed material budget between the TPC and the vertex. The signal extraction is based on bin counting in the mass range $[2.92, 3.16]$ GeV/c^2 after the subtraction of the background as in all inclusive J/ψ analyses with ALICE at mid-rapidity [151, 220, 221, 258, 242].
Due to the tail, a signal extraction window for a bin counting based raw yield determination always excludes a significant fraction of the signal. The limited statistics enforce to deduce this fraction of the signal within the considered invariant mass range for the bin counting based on the dedicated detector simulation, which also includes the impact of the radiative NLO-order process.

5.5.2. Background composition and description

The background composition was investigated in a PYTHIA 6.4 Perugia Tune [259] pp minimum-bias collision simulation at $\sqrt{s} = 7$ TeV for the analysis in Ref. [151] with very similar selection criteria. The main background sources are:

- a combination of 2 secondary electrons from 2 different e^+e^- pair conversion processes,
- a combination of a secondary and a primary electron (Dalitz-decay electrons or an electrons from a semileptonic decay of a heavy-flavour hadron) ,
- primary electron pairs originating from a $c\bar{c}$-pair, where both c-hadrons decay semileptonically (HFE-HFE-bkg.),

- primary electron pairs originating from a $b\bar{b}$-pair, where both b-hadrons decay semileptonically (HFE-HFE-bkg.),
- a combination of primary electrons from different sources (for example from π^0-Dalitz and semileptonic decays of D- or B-mesons),
- a pion/proton/deuteron combined with electrons from all quoted sources,
- and a pion/proton/deuteron combined with another pion/proton.

In p–Pb collisions, the main background sources are the same as in pp collisions. Except of the hadron-hadron contribution, each of the background sources contribute with at least 5% in the pp simulation. This simulation already suffers from the unprecise knowledge of the background composition. The situation is even more unclear in p–Pb collisions. In particular, the knowledge of the charm and beauty quark production at mid-rapidity in p–Pb collisions is limited. The estimate used in model calculations for the Pb–Pb collision system vary by a factor two for $c\bar{c}$ pair production as mentioned in Section 2.5. Analyses sensitive to the total $c\bar{c}$ cross section both in the e^+e^- channel as well as the measurements of open charm hadrons are still ongoing within the ALICE collaboration in p–Pb and in pp collisions[14]. In addition, the angular distribution of the e^+e^--pair emission from $c\bar{c}$-pair and $b\bar{b}$-pair creation varies depending on the relative contribution of different Feynman diagrams and the considered order in perturbation theory. Hence, the invariant mass shape varies, which is one large contribution to the uncertainty in the $c\bar{c}$-pair cross section determination via dilepton pairs. In future, angular measurements of D-mesons as in Ref. [260] by LHCb should be used to constrain the $c\bar{c}$ pair production in MC event generators. Furthermore, the phenomenological knowledge on the correlation between charm production and light flavour hadron production also influences the background and is not well known due to the lack of a quantitative understanding of the correlation between soft and hard particle production. Constraining measurements of correlations between D-mesons and charged tracks only started in pp and in p–Pb collisions within ALICE and suffer from statistical limitations and do not cover the complete phase space, which is relevant for the J/ψ background due to the limitation of topological selections at low p_{T}.

Hence, a precise estimate of the background composition cannot be given at the

[14] In principle, the background shape of this measurement could be also exploited, but the selection criteria are not optimised for that purpose in order to preserve large J/ψ statistics.

present stage and template fits commonly used in high-energy physics employing shapes from simulation data with scaling factors from cross section measurements or other data driven sources are not expected to provide reliable shapes. In addition, the purity of the electron sample may be different in the full detector simulation and experiment due to imperfect modelling of the PID-selection purity and of the photon conversion background due to imprecisions in the simulation of the mother particle spectra and their correlation with other tracks in the event.

In fact, the background shape is dominated by the kinematical constraints set by the acceptance and the TPC-PID selection creating a smooth elevation of the background at lower masses m_{ee} than the J/ψ peak for the p_{T}-integrated signal extraction and the first two p_{T} ranges considered in the analysis $p_{\mathrm{T}} \in [0, 1.3]$, $[1.3, 3.0]$ GeV/c. This behaviour is shown in Fig. 5.23 for the p_{T}-integrated analysis and in Fig. 5.24 for the p_{T} differential case. Variations of the track-p_{T} acceptance selection or the proton rejection move the maximum of this bump further to lower masses or larger masses towards the J/ψ peak. Different signal yield extraction approaches and ad-hoc fit assumptions were investigated and are detailed in Appendix F. Finally, a mixed-event signal approach was followed.

For the mixed-event signal extraction, opposite sign pairs are built from electrons and positrons from different collisions. This approach does not take into account correlations in the particle emission due to the physical processes as long as they cannot be characterised by a event specific variable, but it models the detector-related phase space effects appropriately.

The mixed-event background was scaled to match the total integral of the invariant mass dielectron entries in two predefined scaling mass ranges. The default scaling window choice is $m \in [2.0, 2.5]$ GeV/c^2 and $[3.2, 3.7]$ GeV/c^2. The impact of the ψ(2S) can be safely neglected, since it is expected that the number of $\mathrm{e^+e^-}$-pairs from ψ(2S) compared to J/ψ is reduced by a factor 30 to 100. This can be derived in the p–Pb collision system from the ALICE muon-arm results [191]. The statistical uncertainty of the scaling factor was taken into account in the statistical uncertainty of the retrieved signal counts. The signal counts were extracted in the mass range $[2.92, 3.16]$ GeV/c^2 by bin counting taking the fraction of the signal into account in this mass range, which are not counted (about 31%) based on the simulation introduced in Section 4.2.

Due to the correlated heavy-flavour background and also possible correlations in the hadron-electron pair background, it is not a priori clear that a mixed event

is able to describe the observed shape. Conceptually, the applicability of this approach is therefore not immanent as in a Pb–Pb analysis, i.e. especially due to the HFE-HFE background: the emission directions of the heavy-flavour hadron pair are not uncorrelated. A combinatorial background shape can be nevertheless a good approximation: the smaller mass of the electrons/positrons compared to the mass of the decay particle at small mother particle boosts already leads to a considerable decorrelation between the emission directions. The agreement between the mixed-event shape and the opposite sign background and the reached consistency with other signal extraction methods justifies this approach a posteriori at the present stage of statistical precision.

The possible impact of the spectral behaviour of the background particles, changes in p_{T} and η densities, as a function of event-related observables requires the test of mixing in event categories, since otherwise the same-event pair characteristics are statistically not properly represented in the mixed-event sample. Evident variables for forming those categories are the z-coordinate of the vertex and the multiplicity observed within the acceptance, which is used for the analysis. Different from the analysis in semicentral Pb–Pb-collisions, there is no easily identifiable event topology observable as the event-plane, which causes correlations and influences the background shape. An example ratio of the normalised invariant mass distributions for the p_{T}-integrated case for different event mixing categories are shown in Fig. 5.22. Further supplementary material can be found in Appendix F.4. The difference for the extracted signal yield between different event-mixing categories choices is about (for the first two p_{T}-bins) or less (p_{T}-integrated and and third p_{T}-bin) than 1%[15]. The default analysis was carried out not taking into account different mixing categories except of the z-vertex coordinate. We do not consider those deviations as source of systematic uncertainty because the signal extraction uncertainty estimated differently is larger by a factor 5 to 13 for the absolute yield measurements.

The signal extraction is shown in Fig. 5.23 for the p_{T}-integrated case. The upper panels shows the raw mass spectrum and the background shape. The lower panel shows the background subtracted invariant mass distribution. In the background subtracted mass distribution, the signal shape from simulations is drawn in order to illustrate the signal shape with the significant tail towards lower masses. Al-

[15] For the two highest p_{T}-bins, larger deviations appear in some cases, but there are only 1-2 counts in absolute terms.

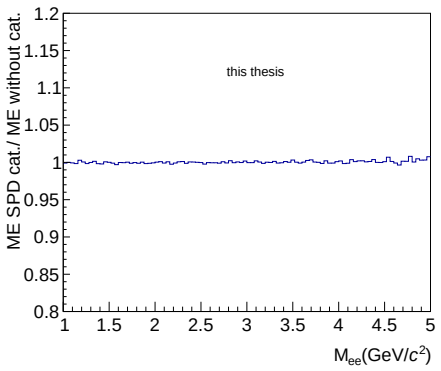

Figure 5.22.: Ratio of the p_{T}-integrated normalised mass distribution. The numerator is based on event mixing in categories of SPD-tracklets distribution, the denominator on event mixing without mixing categories.

though the χ^2/NDF of the background subtracted distribution and a scaled signal shape from simulations amounts to 1.3 in the mass range $[1.4, 5.0]$ GeV/c^2, the background description tends to an underprediction of the invariant mass distribution in the invariant mass range around 2.5 GeV/c^2 and to an overshoot for masses above 3.3 GeV/c^2. These indications of the deviations enter the systematic uncertainty, which is explained in Section 5.7.1 by variations of the scaling regions for the background description. The relative deviations between like-sign approaches used as cross check detailed in Appendix F and mixed-event signal extraction for the signal p_{T} and multiplicity integrated yield are non-negligible. They amount to 10.5% for the standard selections and scaling regions. However, the additional statistical uncertainty contained in the like-sign signal extraction has to be taken into account as well. The difference in terms of this non-shared statistical uncertainty amounts to 1.3 σ_{ind}. Details can be found in Appendix F including cross checks with the different signal extraction methods varying the background composition and the signal over background ratio by more than a factor two by variations of the ITS requirements, the single track p_{T} acceptance cut and the particle identification requirements.

The signal extractions for the p_{T}-differential case are shown in Fig. 5.24. The lowest p_{T} bin is shown on the left hand side, the bin with the largest p_{T} on the right hand side. It is clearly visible that the signal over background increases from about 0.5 in the lowest p_{T} bin to about 4 in the largest p_{T} bin. Similar conclusions for the p_{T}-dependent analysis as for the p_{T}-integrated are valid for the comparison with the like-sign signal extraction. The deviations are sizeable in relative terms, but they

do not exceed 1.5 σ_{ind}.

For the multiplicity as well as the centrality dependence, also the event mixing technique was adapted. Fig. 5.26 shows the signal extraction for the default signal extraction window $[2.92, 3.16]$ GeV/c^2 and the default scaling windows: $[3.2, 3.7]$ GeV/c^2 and $[2.0, 2.5]$ GeV/c^2. The corresponding signal extractions for the multiplicity dependence are shown in Fig. 5.25. The background shape is similar as for the integrated signal extraction in both cases. However, the signal over background decreases from the lower to larger charged-particle multiplicities from 4 to 0.7. A similar, but milder dependence of the signal over background is observed for the centrality differential measurement, which is expected due to the correlation between the centrality estimation and the charged-particle multiplicity at mid-rapidity.

For the estimation of the systematic uncertainties, the scaling mass windows for the mixed-event background and the signal extraction window were varied. The central result points correspond to an average over signal extractions with different choices. The procedure is detailed in Section 5.7.1.

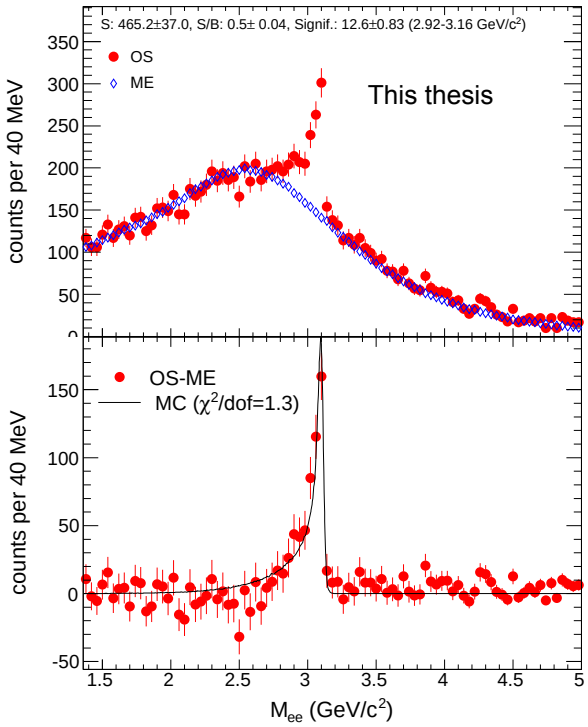

Figure 5.23.: The mixed-event signal extraction for the integrated signal extraction is shown. The lower plot shows the comparison of the scaled mixed-event subtracted invariant mass distribution compared with the signal shape derived from the full detector simulation.label this thesis

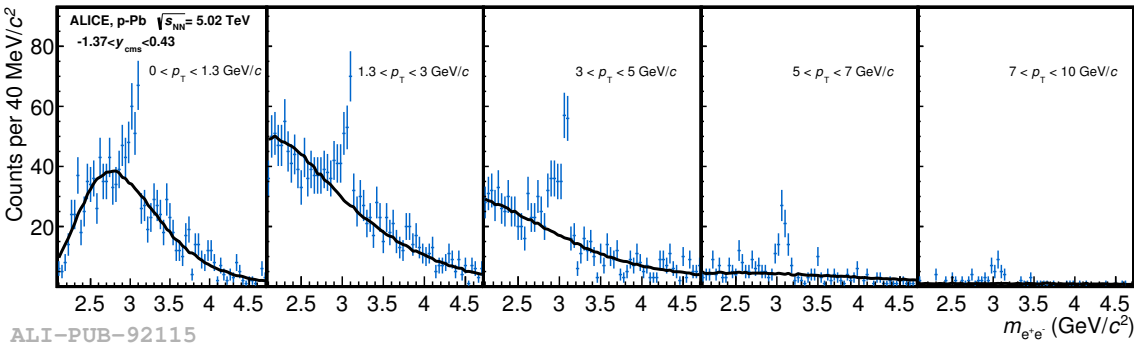

Figure 5.24.: The mixed-event signal extractions for the 5 considered p_{T} bins is shown as published in Ref. [201].

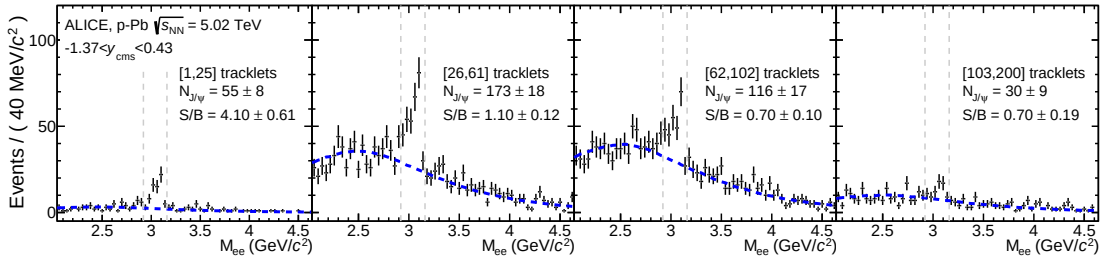

Figure 5.25.: The mixed-event signal extractions for the multiplicity dependent analysis is shown, which is prepared for publication [237].

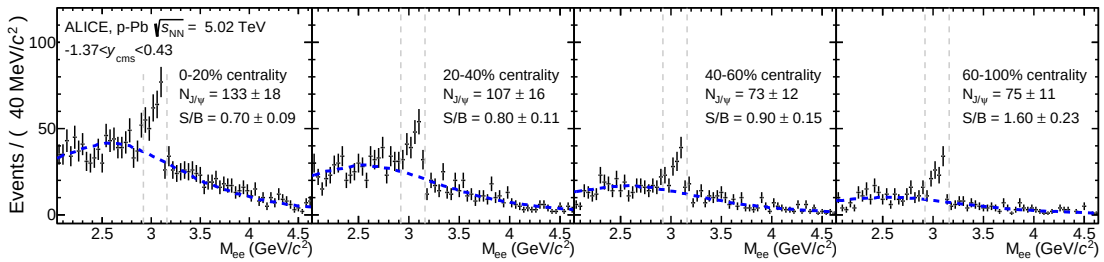

Figure 5.26.: The mixed-event signal extractions for the centrality dependence is shown as published in Ref. [183].

5.6. Determination of pp reference cross sections

5.6.1. pp reference for $\mathrm{d}\sigma/\mathrm{d}y|_{\mathrm{J}/\psi, y\approx 0}$ at $\sqrt{s} = 5.02$ TeV

In absence of a measurement in pp collisions at $\sqrt{s} = 5.02$ TeV, the pp reference J/ψ cross section was derived within ALICE based on the interpolation of inclusive J/ψ production measurements at mid-rapidity from ALICE in pp collisions at $\sqrt{s} = 2.76$ TeV [220], 7 TeV [151], from CDF in $\mathrm{p\overline{p}}$ collisions at $\sqrt{s} =$ 1.96 TeV [107] and from PHENIX in pp collisions at $\sqrt{s} = 0.2$ TeV [254]. Since the production of charmonium at TeV-scale collisions is strongly dominated by processes involving gluons in the initial state due to the small probed Bjorken-x, it is assumed that there is no difference between J/ψ production in $\mathrm{p\overline{p}}$ and pp collisions at $\sqrt{s} = 1.96$ TeV, which justifies the use of the most precise CDF data for the interpolation. lepton universality between the $\mu^+\mu^-$ and the $\mathrm{e^+e^-}$ decay channel is assumed for the derivation of the result.

The interpolation is derived as an average of different functional assumptions for the $\sqrt{s}$ dependence as illustrated in Fig. 5.27.

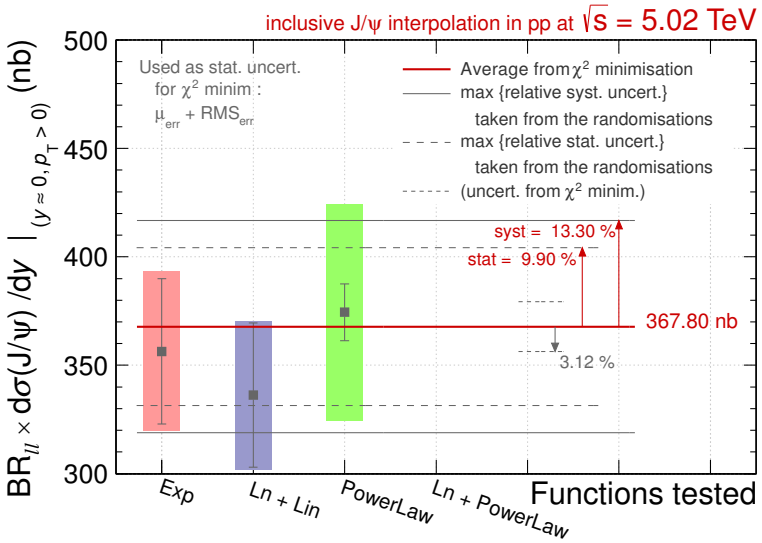

Figure 5.27.: The result of the interpolation procedure taken from [261] is shown. On the abscissa, different functional assumptions for the $\sqrt{s}$ dependence are depicted: exponential (Exp), the addition of a logarithmic and a linear function (Ln+Lin) and a power law dependence (PowerLaw). Details of the determination procedure can be found in the Refs. [201, 242].

The following value is derived:

$$BR_{ee} \cdot \mathrm{d}\sigma/\mathrm{d}y|_{y\approx 0,\sqrt{s}=5.02\ \mathrm{TeV}} = 367.80 \pm 36.4(\mathrm{stat.}) \pm 48.9(\mathrm{syst.})\ \mathrm{nb} \quad (5.17)$$

The statistical and the systematic uncertainties are added in quadrature in order to derive a single uncertainty on the pp reference for R_{pA}. This interpolation procedure was used for the results published in the Ref. [201, 242, 183].
The measurement in p–Pb collisions is not carried out in a rapidity range centred around $y = 0$. This does not have a significant impact compared to the uncertainties according to the rapidity shape provided in Ref. [262] describing the first attempt to provide a pp reference for J/ψ measurements at forward rapidity for the ALICE $\mu^+\mu^-$ measurements. Furthermore, the measurement of the rapidity dependence of Υ production by CMS shows no significant decrease of the Υ cross section in the rapidity ranges relevant for this analysis [246, 244].
After the publications of nuclear modification factors in p–Pb collisions at mid-rapidity [201, 183], a pp collision data sample at $\sqrt{s}$ =5.02 TeV was taken in Decembre 2015. The analysis on this data sample is ongoing and its potential impact in view of the nuclear modification factor will be shortly discussed in Appendix B.

5.6.2. p_{t}-differential pp reference

The p_{T}-differential pp reference is detailed in Ref. [263]. It is inspired by the approach described in Ref. [262]: the p_{T}-differential cross section approximately obeys a universal p_{T} dependence after appropriate rescaling by the $\langle p_{\mathrm{T}} \rangle$ and the total yield. A p_{T}-differential reference cross section can be therefore derived based on the knowledge of the $\langle p_{\mathrm{T}} \rangle$ of J/ψ production as a function of $\sqrt{s}$ and $BR(\mathrm{J}/\psi \rightarrow ee) \cdot \mathrm{d}\sigma/\mathrm{d}y|_{\mathrm{J}/\psi, y\approx 0,\sqrt{s}}$.
The negligibility of the rapidity shift of the experimental acceptance on the reference for $\mathrm{d}\sigma/\mathrm{d}y$ is explained in Section 5.6.1. In addition, the $\langle p_{\mathrm{T}} \rangle$ needed for the scaling might be affected by the different rapidity range. A fully double-differential J/ψ-cross section measurement down to $p_{\mathrm{T}} = 0$ was performed by LHCb [104]. A difference of 1.0% between the $\langle p_{\mathrm{T}} \rangle$ in the rapidity-ranges $y \in [2, 3.5]$ and $y \in [2.5, 4]$ is observed, whereas the difference between the ranges from $y \in [2.5, 4.0]$ and

$y \in [3.0, 4.5]$ is already 2.5%. We expect that the difference of the $\langle p_{\mathrm{T}} \rangle$ in pp collisions in the rapidity range $y \in [-0.9, 0.9]$ and $y \in [-1.37, 0.45]$ exhibits a smaller deviation. As a supplementary argument, the $\Upsilon(1S)$ measurement by the CMS collaboration in pp collisions at 7 TeV [246, 244] indicates no change as a function of p_{T} within the probed rapidity range of the measurement. Knowing that the interpolated $\langle p_{\mathrm{T}} \rangle$ value retrieved has already a systematic uncertainty of 2.4% and a statistical uncertainty of 2.8%, no correction is applied and no uncertainty is assigned for this effect. Figure 5.28 shows the scaled cross sections from the different experiments used for the derivation of the shape. Figure 5.29 shows the actual interpolated p_{T}-differential cross sections compared to measurements. The cross section values are listed in Table J.2 in Appendix J.3.

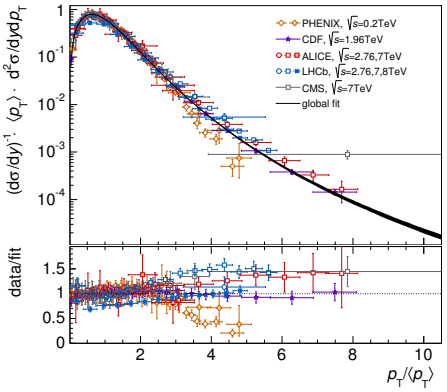

Figure 5.28.: Fit to rescaled data

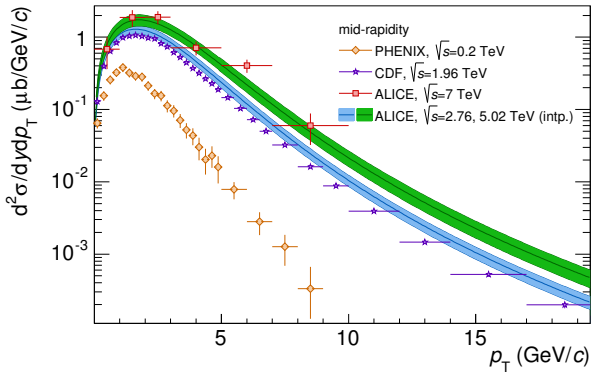

Figure 5.29.: Interpolation results

The phenomenological fit of the spectral shape of hadronic J/ψ production is shown on the left hand side together with the experimental data used for the derivation as shown in Ref. [263]. The result of the p_{T}-differential J/ψ cross section in pp collisions together with selected experimental results at mid-rapidity is shown on the right hand side [263].

5.7. Uncertainty estimation

In the following section, the sources and the sizes of the considered uncertainties are discussed.

5.7.1. Signal extraction

The uncertainty due to the signal extraction arise mainly from the statistically limited knowledge of the background shape. Two sources of signal extraction uncertainty were considered: the variation of the invariant mass region used for the matching of the background to the e^+e^- mass spectra and the variation of the signal extraction window. The uncertainties from both sources are added in quadrature and stated as systematic uncertainty due to signal extraction for the integrated and the p_T-differential cross sections.
The signal extraction scaling windows were varied independently away from the default background scaling regions $m \in [2.0, 2.5]$ GeV/c^2 and $m \in [3.2, 3.7]$ GeV/c^2 The lower edge of the first invariant mass range was varied between 2.0,1.4,1.6 GeV/c^2 and the upper edge of this range between $2.5, 2.2$ GeV/c^2. For the second invariant mass window, the matching was varied analogously among $3.2, 3.4$ GeV/c^2 for the lower bound and among 3.7, 4.0, 4.9 GeV/c^2 for the upper bound. This variation results in 36 different scaling choices. Further variations were done with the method for the scaling and the scaling regions, which lead to results within the variations obtained with the considered variations or which did not yield to similarly well matching of the background and the mixed-event distributions. The root mean square of the observed deviations is assigned as systematic uncertainty. The central data points are the arithmetic mean of these variations. It was checked that the different results yield to systematic deviations beyond allowed statistical variations due to the finite statistical uncertainty of the scaling factor itself. The uncertainty for the p_T-integrated yield amounts to 3.5%. For the p_T-differential result, the values range between 2.5% and 7.0%.
The tail of the J/ψ-lineshape depends on the detector and reconstruction simulation and most crucially on the precision of the material budget simulation. Therefore, it is necessary to estimate the uncertainty due to the fraction of the signal inside the signal extraction region. Since the statistics is finite and the matching of the

background shape assumptions cannot be tested up to high precision, the choice of the window is also sensitive to the precision of the background description.

The signal extraction window edges were varied independently for all considered cut choices but for a specific background scaling window ([2.0, 2.5] GeV/c^2 and [3.2, 3.7] GeV/c^2) away from the standard signal extraction choice of $m \in [2.92, 3.16]$ GeV/c^2. As lower edge of the signal extraction window, the mass values 2.80, 2.92, 3.00 GeV/c^2 were considered, whereas the upper edge was varied between 3.12, 3.16, 3.20 GeV/c^2. The efficiencies determined in simulations[16] for these signal extraction windows range between 53% and 83%, the default window cut choice ($m \in [2.92, 3.16]$ GeV/c^2) has an efficiency of about 69%. This fraction is slightly dependent on the specific single track cuts and also dependent on the pair p_{T} as shown in Fig. 5.6. Supplementary material can be found in Appendix F.

The root mean square of the retrieved variations of the raw counts corrected for the specific signal extraction window efficiency is taken as an estimate for the uncertainty. A value of 3.1% for p_{T}-integrated case was derived. For the p_{T} differential case, variations between 4.9-12.0% were observed with the largest deviations for two lowest p_{T} ranges $[0, 1.3]$ GeV/c and $[1.3, 3.0]$ GeV/c amounting to 7.0% and 13.0%, where the S/B is smaller than at high p_{T}. It was observed that the obtained deviations were statistically significant except for two highest evaluated p_{T}-ranges ($[5, 7], [7, 10]$ GeV/c). For those two ranges, the value from the range $p_{\mathrm{T}} \in [3, 5]$ GeV/c was taken.

For the multiplicity and the centrality dependent analysis, the signal extraction was not separated in the two subcomponents as in the previously discussed integrated and p_{T}-dependent analysis. The signal extraction choices were taken from the variation of the following criteria. The lower border of signal extraction mass window was varied between 2.8, 284, 2.88, 2.92, 2.96, 3.00 GeV/c^2, the upper one between 3.12, 3.16, 3.20, 3.24 GeV/c^2. Furthermore, the upper scaling window was varied between $[3.2, 3.7]$, $[3.2, 4.0]$, $[3.2, 4.9]$, $[3.4, 3.7]$, $[3.4, 4.0]$, $[3.4, 4.9]$ GeV/c^2 and the lower window between $[1.4, 2.2]$, $[1.4, 2.5]$, $[1.6, 2.2]$, $[1.6, 2.5]$, $[1.6, 2.5]$, $[2.0, 2.2]$, $[2.0, 2.5]$ GeV/c^2. Finally, 53 combinations, which avoid overlap of the scaling regions and the signal extraction, were considered. The selected choices are listed in Appendix F.6. The statistical uncertainty is obtained as an average of the statis-

[16] The term efficiency is defined as the ratio of the reconstructed J/ψ in the considered signal extraction mass range after all cuts and the number of reconstructed J/ψ after all cuts, but the invariant mass cut.

tical uncertainties of the different signal extractions. The systematic uncertainty corresponds to the root mean square of the obtained distribution. For the multiplicity dependent analysis, the root mean square of the considered signal ratio distribution was evaluated. The signal extraction uncertainties for the Q_{pPb} analysis range between 4.2% and 7.3%. In the multiplicity dependent analysis, the obtained uncertainties vary between 3.2% and 8.4%.

5.7.2. Particle identification

The detected systematic deviations between the efficiency of primary electrons in simulation and between electrons from γ-conversions in data and in simulations were not corrected for. Therefore, the observed deviations were used as a proxy for the related systematic uncertainty.

We consider the maximal relative deviation of the single track efficiencies of 2.0% in the pion rejection phase space from Fig. 5.16 and Fig. 5.19[17] for both tracks. Assuming that the difference between simulations and data is completely induced by an incorrect PID parameterisation of that order of magnitude, we retrieve a maximal systematic mismatch of the efficiency of 4%, i.e., 2× the single electron efficiency mismatch. The larger deviations in the single track efficiencies due to the proton rejection at low momenta induce a deviation of the same or smaller size at low $\mathrm{e}^+\mathrm{e}^-$-pair p_{T} due to the phase space arguments given in Section 5.4.4. In addition, they were probed by equalising the observed deviations in the data simulations by applying a different proton rejection. The induced differences in the $Acc. \times eff.$ on pair efficiency level were smaller than the 4% over the full pair p_{T} range. One could try to remove the discrepancy by proper weighting of the $Acc. \times eff.$ factors. However, this is not done due to a lack of precise understanding of the discrepancies. In view of the fact that the uncertainty on the uncertainty estimate is sizeable due to the statistical limitations to conduct data-driven multidimensional investigations, the 4% are assigned as an upper uncertainty estimate over the full phase space.

Additionally, cross checks with the p_{T}-integrated analysis, were made to ensure that the PID-uncertainty is not underestimated. The PID selection was varied by using a $n\sigma_{\mathrm{TPC,pion}}, \sigma_{\mathrm{TPC,proton}} > 2.5, 3.0, 4.0$ selection together with the variation of the p_{T}-daughter selection between $p_{\mathrm{T}} > 0.8, 1.0, 1.1$ GeV/c and the cross sections retrieved

[17] The deviation for the 3σ pion rejection applied at $\mathrm{e}^+\mathrm{e}^-$-pair p_{T} larger 5 GeV/c is of very similar size as shown in Appendix G.2.

with the corresponding $Acc. \times eff.$ factors from simulations. These cross checks are presented in Appendix F. In addition, the p_{T}-integrated analysis was conducted with an additional requirement of $N_{\mathrm{PIDcluster}} > 120$. All particle identification selection criteria were applied with the occupancy correction of the PID parameterisation disabled. The result was only shifted by about 1%. A cross check was performed with selection criteria exclusively cutting in the $n\sigma_{\mathrm{electron}}$ variable, but varying as a function of momentum, η and $N_{\mathrm{PIDcluster}}$. These selections were tuned to mimic the 3.5σ pion rejection and 3.0σ proton rejection with electrons from pair conversion. In contrast to the standard method, it was avoided to cut deeper in the electron $\mathrm{d}E/\mathrm{d}x$ band than up to $-0.5\ \sigma_{\mathrm{TPC,electron}}$. All cross checks lead to either compatible results or to deviations within the assumed uncertainty of 4%. For the centrality differential uncertainty, the PID uncertainty is fully correlated as a function of the centrality. In the multiplicity differential analysis, the related uncertainty cancels in the ratio.

A significant dependence of the PID-response as a function of the azimuthal angle was observed within the course of the QA of this analysis due to a sector-by-sector variation of the $\mathrm{d}E/\mathrm{d}x$ signal of the TPC. The correlation of the tracks due to the decay kinematics could give rise to an additional uncertainty not covered by looking at single track efficiencies, especially for high-p_{T} pairs. Since no correction for this dependence was applied, a simplified simulation study was performed in order to check whether this dependence can add additional systematic uncertainties to the measurement.

J/ψ mesons were generated isotropically in their rest-frame with a parameterisation of the p_{T}-spectrum at 7 TeV in pp collisions. Kinematical selections on pseudo-rapidity and transverse momentum were applied on the generated quantities. For each daughter track track a random $\mathrm{d}E/\mathrm{d}x$ signal was generated according to the momentum and the azimuthal angle of the track. For this purpose, the functional form employed in the TPC calibration was used, neglecting the dependence on $N_{\mathrm{PIDcluster}}$ in data and the dependence on η. The proton and pion veto criteria were applied using the nominal positions without and with the distortions in azimuthal angle. The applied φ-dependence of the resolution and the centre of the electron TPC signal distribution was extracted from $\mathrm{e}^+\mathrm{e}^-$ pair conversion electrons in data. Due to the lack of statistics, those φ-maps were only generated in φ dimension. In addition, the single track efficiency due to the ITS requirement efficiency was also applied as a substep in order to exclude any effect, which might be not present for a

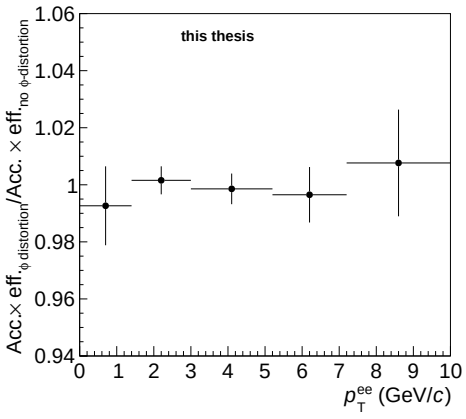

Figure 5.30.: The ratio of $Acc. \times eff.$ for with and without introduced φ-distortion as a function of e^+e^- pair p_T.

completely homogeneous efficiency as a function of azimuthal angle and one which is distorted weighted by the φ-distribution seen for a requirement of hits in layers of the SPD. This could be possible, since the missing SPD channels are caused by complete large subelements of the detector. Finally, the e^+e^- pair $Acc. \times eff.$ values with and without φ-dependence were compared.
No effect could be inferred from the simplified model studies: the derived $Acc. \times eff.$ values were the same within the statistical precision of the generated J/ψ. The ratio of the two $Acc. \times eff.$ factors as a function of e^+e^--pair-p_T is depicted in Fig. 5.30. No additional uncertainty was therefore considered due to this dependence.

5.7.3. Tracking

In particular for the TPC tracking efficiency related studies presented in Section 5.4.3, a separation of particle identification and tracking was not achieved and it is assumed that the related uncertainty is already taken into account by the PID-efficiency uncertainty. A second contribution to the tracking efficiency uncertainty could arise from the ITS-TPC prolongation efficiency. However, this efficiency is more than 95% and the maximal uncertainty for a two track uncertainty will be smaller than 2% on pair level for hadrons as explained in Section 5.4.3. Knowing that the total present uncertainties are at least a factor 6 larger in the J/ψ analyses, no uncertainty is assigned.

5.7.4. Simulation kinematics

Since the efficiency is a common factor applied to the raw number of counts, there is no kind of weighting directly on the pairs or the single electrons, the result depends on the knowlegde of the p_{T} and rapidity distributions of the input simulation for the efficiency determination. The reweighting according to the measurement itself is explained in Section 5.4.2.

The uncertainty derivation is based on the uncertainties, which are underlying the fit to the experimental p_{T}-differential result. The fit function can be found in Section 5.4.2. Different shape assumptions have been tested as well. The dependence on the functional shape was found to be negligible compared to the variation of the fit parameters allowed by the uncertainty of the measurement. The $Acc. \times eff.$ factors are calculated by varying the fit parameter p_0 introduced in Equation (5.14). The two dimensional variation of the parameters n and p_0 has been tested as well having negligible impact due to a strong correlation of the two parameters. The $Acc. \times eff.$ deviates from an increase of p_0-value by 1 σ from its nominal value by 3.0%. The deviation amounts to 1% for the decrease of p_0 by 1 σ. Finally, a symmetric uncertainty of 3.0% was assigned. This uncertainty is also used for the centrality differential analysis as an uncertainty, which is correlated as a function of centrality intervals.

Since it is not feasible to do a double differential measurement as a function of multiplicity/centrality due to the lack of statistics, it is necessary to account for the uncertainty due to variation of the p_{T}-differential shape of the cross section as a function of centrality/multiplicity.

For the Q_{pA} and the multiplicity dependence, the p_{T}-differential spectra measured by the ALICE muon arm as a function of centrality are used [183]. The p_{T} spectra as a function of the centrality in the $\mu^+\mu^-$-analysis at forward and backward rapidity are fitted with the same function and fitting options as in described in Section 5.4.2. The relative variation of the two shape parameters for every centrality bin with respect to the centrality integrated p_{T} spectrum is retrieved. The relative variation is used to deviate the default parameters of the default fit to the electron spectrum for every of the considered centrality bins. The fitted spectra are used to reweight a p_{T}-differential histogram with the $Acc. \times eff.$ of the J/ψ analysis at mid-rapidity. The relative deviation of this reweighted p_{T}-integrated $Acc. \times eff.$ is taken as orientation for the uncorrelated uncertainty for the unknown variation of

the p_{T}-shape at mid-rapidity.
The observed deviations from the forward (backward) rapidity data range between 98.6-100.01% (98.7-100.00%). We assign for this variation an uncertainty of 1.4% without further specification of correlation between the centrality ranges. Evidently, this uncertainty is of course not fully uncorrelated and also mainly contributing to the most peripheral centrality range, where the deviations are observed. Considering the fact that the deviations are 5 to 10 times smaller than the statistical uncertainty, we stay with this assumption for simplicity. For the multiplicity dependent result, we assume the same uncertainty as for the Q_{pA} in absence of a double differential result in other rapidity ranges.

5.7.5. Pile-up

For rate measurements with the used prescription integrated without a selection, which is not enhancing the amount of pile-up, the effects can be neglected in view of the size of other experimental uncertainties. For the multiplicity differential analysis, substantial systematic effects are possible both for the J/ψ measurement as well as for the multiplicity estimation. A simplified simulation was used to evaluate the effect also for the multiplicity dependent analysis. The effects were found negligible compared to the other systematic uncertainties. The details of the approach can be found in Appendix H.

5.7.6. Uncertainties on the J/ψ yield in the multiplicity dependent analysis induced by the multiplicity correction

As explained in Section 4.3.5, there is a non-negligible uncertainty related to the random character of the multiplicity correction. We take as a proxy for the uncertainty the root mean square of the distribution of 20 repetitive trials of the correction with new random seeds. The uncertainty ranges between 2.8% and 9.8% as a function of multiplicity.

5.7.7. Multiplicity estimate uncertainty

The uncertainty of the multiplicity measurement is dominated by the scale uncertainty to correct from the visible cross section to the total number of non-single diffractive (NSD) events, which amounts to 3.1%. This uncertainty is only attributed to the denominator, since the measurement of the multiplicity does not include events with no trigger and no vertex, which constitute the source of the normalisation uncertainty. Since the total uncertainty of the experimental value of $\mathrm{d}N_{ch}/\mathrm{d}\eta_{|\eta|<1.0}$ is dominated by the normalisation uncertainty, we assign the relative uncertainty on the denominator to the normalised multiplicity although some uncertainties might cancel partially.
In addition to this uncertainty, it is necessary to assign an uncertainty to the α factors described in Section 4.3.5, which parameterise the non-linear relationship between the multiplicity estimator variable and the charged-particle multiplicity. The uncertainty needs to take into account the uncertainty related to the particular event simulation generator. This was done in the parallelly ongoing muon analysis and applied in this analysis [236]. The related uncertainties amount to 4-5%.

5.7.8. Normalisation uncertainties

The luminosity uncertainty amounts to 3.7%, the normalisation from the visible number of events to the number of NSD events to 3.1%. For the cross section measurements, the uncertainty of the branching ratio for the dielectron decay of the J/ψ has to be taken into account, which amounts to 0.5% [21].

5.7.9. pp-reference

The pp reference uncertainties are derived with the interpolation procedure described in Section 5.6. The uncertainty for $\mathrm{d}\sigma/\mathrm{d}y|_{\mathrm{J}/\psi,y\approx0} \times BR(\mathrm{J}/\psi \rightarrow \mathrm{e}^+\mathrm{e}^-)$ amounts to 16.6% and is the dominating uncertainty for the integrated nuclear modification factor R_{pA} and the centrality dependent nuclear modification factor Q_{pA}. The uncertainties of the p_{T}-differential uncertainties are also among the largest in the p_{T}-dependent nuclear modification factor and are listed in Tab. 5.1.

5.7.10. Determination of the correlation within the statistical uncertainty of the relative multiplicity analysis

The analysis as a function of multiplicity is presented in the form of the ratio of the measured J/ψ yield in a given multiplicity bin over the integrated J/ψ yield as a function of multiplicity. Hence, the statistical uncertainties on the yield have to be propagated properly taking into account the correlation between the denominator and the numerator of the observable.

We follow two approaches: 1) calculating the uncertainty analytically via Gaussian uncertainty propagation, 2) calculating the uncertainty based on a pseudo-data generation. For the final result, the pseudo-data approach is chosen and is described in the following. The details about the calculations with analytical formulae are given in Appendix G.4. Both approaches give results which differ at maximum by 10% of the respective uncertainty size.

As starting point, we take the raw opposite-sign dielectron mass spectrum integrated as a function of multiplicity and in the multiplicity range in question. We consider the invariant mass distribution in a multiplicity range $N_{\mathrm{OS,\,j}}(m_i)$. The index i denotes here the invariant mass bin; the index j denotes the multiplicity range. In addition, we have to use the invariant mass distribution, which originates from the subtraction of the mass distribution in the multiplicity bin from the multiplicity integrated distribution. For every invariant mass bin of both distributions, a Poissonian random distribution is evaluated with the measured value as mean in every bin.

A signal extraction is performed on the randomly generated invariant mass counts in the multiplicity bin using the mixed-event distribution as background estimate as in the data. Both artificially generated invariant mass distributions are added together and a signal extraction is performed for this multiplicity integrated distribution. This procedure is repeated 1000 times for every multiplicity bin. For every newly generated distribution pair, the signal extraction in the multiplicity bin and in the multiplicity integrated case are performed and the ratio of the results is retrieved. The RMS of the distribution of the extracted ratios is used as an estimator of the statistical uncertainty. The reduction of the uncertainty compared to the assumption of independent statistical uncertainties between numerator and denominator ranges between 33% for the bin with the second lowest multiplicity and 1.1% for the bin with the highest multiplicity.

5.7.11. Determination of the J/ψ $\langle p_{\mathrm{t}} \rangle$

In the course of this analysis, the $\langle p_{\mathrm{T}} \rangle$ of the measured inclusive J/ψ p_{T} spectrum was determined. The strategy followed closely the parallelly done analysis in the $\mu^+\mu^-$ channel at forward and backward rapidity. The details are given in the Appendix I.

5.7.12. Combination of uncertainties

Table 5.1 shows all uncertainties, which are considered in this analysis for the integrated and the p_{T}-differential results. The uncertainties related to signal extraction and the efficiency correction of the yield are added in quadrature to derive the total systematic uncertainty on the efficiency and acceptance corrected signal counts. The following uncertainties are fully/partially correlated with respect to the muon result:

- the $\langle T_{\mathrm{pA}} \rangle$ uncertainty relevant for the centrality dependent measurement (3.4%), which is fully bin-by-bin correlated uncertainty, fully correlated with respect to the $\mu^+\mu^-$ analysis measusurements,
- the centrality differential $\langle T_{\mathrm{pA}} \rangle$ uncertainty, which is fully correlated between $\mu^+\mu^-$ and $\mathrm{e}^+\mathrm{e}^-$ result, but not correlated between centrality bins,
- the luminosity uncertainty (3.7%) for cross section measurement and integrated and p_{T}-differential nuclear modification factor measurement, which is fully correlated with respect to the muon results at forward rapidity, partially correlated with respect to the backward result muon-result. The details are given in Ref. [235].

All just mentioned uncertainties are fully correlated between the different bins for the p_{T}-differential result and the centrality dependence except of the centrality differential uncertainty.
The systematic uncertainty due to the pp-reference is not correlated between the $\mathrm{e}^+\mathrm{e}^-$-analysis and the muon-arm result. The uncertainties entering the p_{T}-integrated and the p_{T}-differential results published in Ref. [201] are listed in Table 5.1.
Table 5.2 shows all uncertainties, which are considered in the centrality dependent

relative uncertainties in %						
p_{T}-bins in GeV/c	p_{T}-int.	0-1.3	1.3-3.0	3.0-5.0	5.0-7.0	7.0-10.0
statistical	8.1	20.6	15.4	12	15	23
Signal extraction: scaling var.	3.5	7.0	3.7	2.5	4.6	7.0
Signal extraction: extr. window	3.1	7.0	12.0	4.9	4.9	4.9
Signal extraction: total	4.7	9.9	12.6	5.5	6.7	8.5
reconstr. eff. (PID-dominated)	4.0	4.0	4.0	4.0	4.0	4.0
kinematics	3.0	/	/	/	/	/
MC-statistics	0.4	0.6	0.4	0.5	0.9	1.5
Luminosity (cross sections/R_{pA})	3.7	3.7	3.7	3.7	3.7	3.7
BR(J/$\psi \rightarrow \mathrm{e}^+\mathrm{e}^-$) (not for R_{pA})	0.5	0.5	0.5	0.5	0.5	0.5
pp-reference, corr. (R_{pA})	16.6	16.6	16.6	16.6	16.6	16.6
pp-reference, uncorr. (R_{pA})	/	7.3	4.8	5.7	12.8	15.7

Table 5.1.: Overview of the uncertainties considered for the integrated and the p_{T}-differential results.

Q_{pA} published in Ref. [183]. It is indicated, which uncertainties are correlated bin-by-bin and for which no further correlation specification is given. Table 5.3 provides the corresponding quantities for the multiplicity differential analysis. The multiplicity variable uncertainties are given in Tab. 5.4. The draft of the multiplicity dependent analysis [237] is in the ALICE internal review process at the time of the thesis writing.

relative uncertainties in %				
event act. bins in %	0-20	20-40	40-60	60-100
statistical	11.0	11.4	12.2	12.2
Signal extraction (uncorr.):	7.3	4.2	4.7	6.1
reconstruction eff. (PID-dominated, corr.)	4.0	4.0	4.0	4.0
kinematics (corr.)	3.0	3.0	3.0	3.0
kinematics (uncorr.)	1.4	1.4	1.4	1.4
MC-statistics (corr.)	0.4	0.4	0.4	0.4
$\langle T_{\mathrm{pA}} \rangle$ (uncorr.)	5.6	1.9	4.8	5.6
$\langle T_{\mathrm{pA}} \rangle$ (corr.)	3.4	3.4	3.4	3.4
pp-reference (corr.)	16.6	16.6	16.6	16.6
Total systematic uncert. (corr.)	17.6	17.6	17.6	17.6
Total systematic uncert. (uncorr.)	9.4	4.4	6.8	7.9

Table 5.2.: Overview of the uncertainties considered for the Q_{pA} analysis.

relative uncertainties in %				
tracklets range	1-25	26-61	62-102	103-200
statistical	14.4	7.2	11.8	33.1
Signal extraction (corr. not specified):	4.4	3.2	3.4	8.4
kinematics (corr. not specified)	1.4	1.4	1.4	1.4
mult. 'fluctuations' (corr. not specified)	4.3	2.8	3.8	9.8
Total systematic uncert. (corr. not specified)	6.3	4.5	5.3	13.0

Table 5.3.: Overview of the uncertainties considered for the normalised J/ψ yields in the multiplicity dependent analysis.

$N^{\mathrm{corr}}_{\mathrm{tracklets}}$ bin	$\langle N^{\mathrm{corr}}_{\mathrm{tracklets}} \rangle$	$dN_{ch}/d\eta$	$\mathrm{d}N_{ch}/\mathrm{d}\eta/\langle dN_{ch}/d\eta \rangle$	σ/σ_{MB}
1 - 25	11.5	6.88 ± 0.22	0.39 ± 0.02	46.3%
26 - 61	39.7	22.9 ± 0.6	1.30 ± 0.05	38.9%
62 - 102	74.7	42.3 ± 1.1	2.40 ± 0.10	10.7%
103 - 200	116.1	64.4 ± 1.6	3.65 ± 0.15	1.0%

Table 5.4.: Multiplicity estimation and its uncertainties obtained from the $N^{\mathrm{corr}}_{\mathrm{tracklets}}$ quantity measured in $|\eta| < 1$. The values correspond to the data sample used for the mid-rapidity analysis. Only systematic uncertainties are shown since the statistical ones are negligible. The minimum bias cross section fractions in multiplicity bins are also shown.

6. Results

In the following, the results of this thesis are presented. They include the first published measurements of J/ψ production in p–A collisions at the TeV-scale at mid-rapidity [201]. Comparisons to the muon arm results of ALICE [200, 201, 183, 237] at forward ($y_{\mathrm{cms}} > 0$ on the proton-fragmentation side as defined in Section 5.1), and backward rapidity on the lead-fragmentation side ($y_{\mathrm{cms}} < 0$) and ATLAS [203] at mid-rapidity are shown. In addition, comparisons to phenomenological calculations are discussed. CMS data is not considered for comparisons, since the results are not finalised [204] and are in agreement with the ATLAS results [264].
There are no comparisons with the LHCb analysis results shown, since they are consistent within uncertainties with the forward and backward ALICE results for all considered observables [202, 193]. LHCb could also separate the prompt and the non-prompt component of the J/ψ cross section. This measurement confirmed the expectations based on pp collisions and is mentioned where it is relevant for the discussion. All results are shown in tabulated form in Appendix J.

6.1. Inclusive integrated and p_{t}-differential J/ψ cross sections

Figure 6.1 shows the comparison of the inclusive J/ψ cross section as a function of rapidity measured by ALICE at mid-rapidity [201], forward and backward rapidity [200]. The cross section $\mathrm{d}\sigma/\mathrm{d}y(\mathrm{J}/\psi, y \in [-1.37, 0.43])$ amounts to 909 ± 106 μb. It is clearly visible that the extracted cross sections are not symmetric around mid-rapidity, but suppressed at forward rapidity. This behaviour is expected in all available model calculations due to a suppression of the effective incoming gluon flux from the lead nucleus at low Bjorken-x or due to the coherent energy loss of

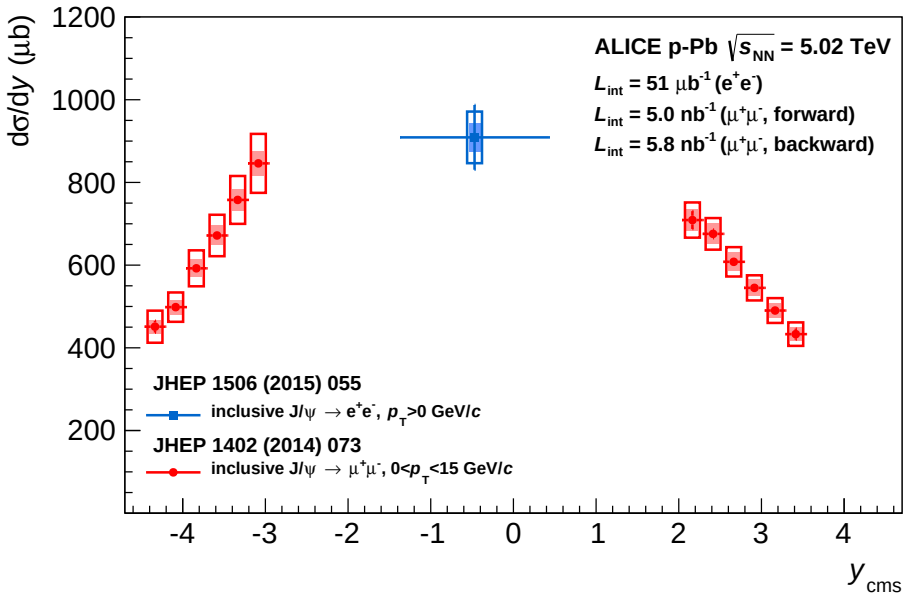

Figure 6.1.: $\mathrm{d}\sigma/\mathrm{d}y$ of inclusive J/ψ production as a function of rapidity as measured by ALICE [200, 201]. The bars represent the statistical uncertainties, the boxes the systematic uncertainties. The filled areas are cross section scale uncertainties. This uncertainty convention is kept for all following figures if not stated otherwise.

the coloured $c\bar{c}$ dipole propagating through the nucleus.

The experimental cross section measurements are more precise than the nuclear modification factors discussed in the following due to the large uncertainties of the interpolated pp reference cross sections. Most phenomenology calculations do not provide absolute cross sections, since the uncertainties on the absolute quantities are typically larger than on the nuclear modification factors. The nuclear modification factor does not suffer from the uncertainties of the absolute incoming proton gluon flux in pp collisions and is less sensitive to the variation of the charm-quark mass, the factorisation and renormalisation scale, which are usually used to estimate the theoretical uncertainty.

A calculation of the inclusive prompt J/ψ cross section with uncertainties is given in Ref. [253], where a Leading-Order (LO) Color Glass Condensate (CGC) approach is coupled to Long-Distance Matrix Elements (LDME) from Non-Relativistic QCD (NRQCD) fits in the collinear framework to high-p_{T} J/ψ-production data[1]. The comparison with the experimental data at forward and mid-rapidity is shown in Fig. 6.2. The uncertainty of the cross section at mid-rapidity is about 30% pre-

[1] Absolute cross sections are given in Ref. [175] also in a CGC framework, but only for rapidities $y > 1.5$.

suming symmetric uncertainties in the calculation. The uncertainty of the corresponding R_{pPb} is about a factor 2 smaller. Good agreement between the calculation and the measurement is observed within the sizeable uncertainties. The subtraction of the b feed-down from the inclusive J/ψ data will not change this statement based on the findings of the LHCb Collaboration [202] at forward rapidity[2]. No calculation in the CGC framework is provided for the backward rapidity region, since it is not clear that the used dilute-dense framework is applicable in this regime, where the Bjorken-x of the incoming proton might be too small to apply the dilute approximation. Hence, a full dense-dense regime calculation as for A–A collisions might be necessary in this picture. This type of calculation is much more involved and not yet done [265]. Figure 6.3 shows the

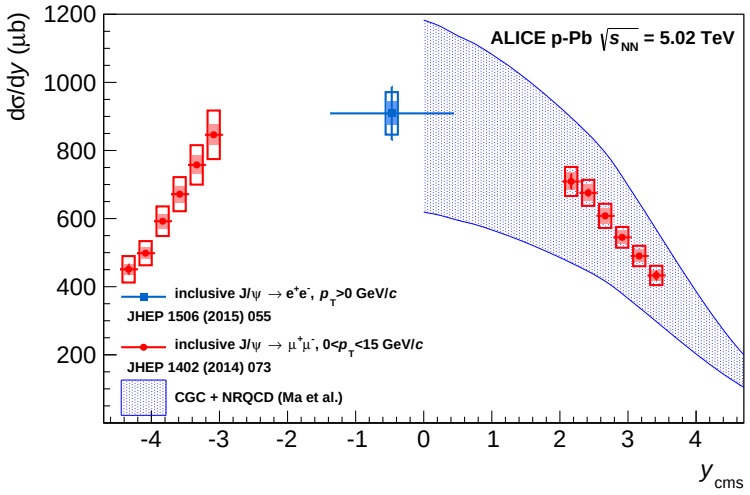

Figure 6.2.: Comparison of dσ/dy of inclusive J/ψ production with the phenomenology results presented in Ref. [253].

p_{T}-differential result in p–Pb collisions at mid-rapidity compared with the results by ALICE at forward and backward rapidity. The p_{T} spectrum at mid-rapidity is harder than the ones at forward and backward rapidity. The observed shape at mid-rapidity resembles the one expected in pp collisions at the same collision energy in first approximation: the extracted $\langle p_{\mathrm{T}} \rangle$ in the p_{T} range $[0, 10]$ GeV/c is 2.86 ± 0.149 (stat.)$\pm$0.103 (syst.) GeV/c. The $\langle p_{\mathrm{T}} \rangle$ value for pp collisions from the direct interpolation of the $\langle p_{\mathrm{T}} \rangle$ between PHENIX, CDF and ALICE data at mid-rapidity is for $p_{\mathrm{T}} \in [0, 10]$ GeV/c: 2.814 ± 0.089(stat.) ± 0.035(syst.) GeV/c [263],

[2]The b feed-down amounts to about 10-15% for the rapidity ranges closest to the acceptance of this analysis. The p_{T}-differential behaviour is similar to the one obtained in pp collisions shown in Fig 2.2.

which is still compatible within uncertainties. However, when looking not only at the first moment of the distribution, but at the p_{T}-differential nuclear modification factor, modifications become visible as described in Section 6.2. Fig. 6.4 shows the

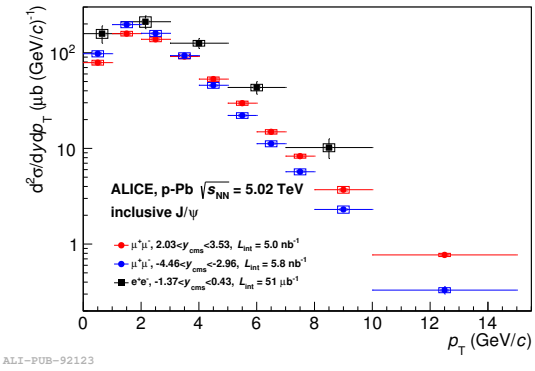

Figure 6.3.:
ALICE internal comparison

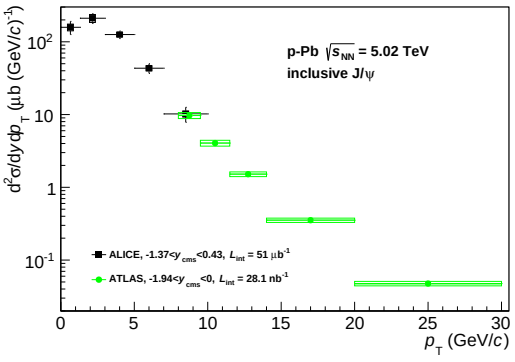

Figure 6.4.:
Comparison with ATLAS

Figures 6.3 and 6.4 show $\mathrm{d}^2\sigma/\mathrm{d}y\mathrm{d}p_{\mathrm{T}}$ of J/ψ in p–Pb at mid-rapidity [201] compared to results at forward and backward rapidity [201] and with ATLAS [203] from the addition of the prompt and non-prompt cross sections. The uncertainties on the inclusive ATLAS J/ψ results are only approximate assuming full correlation of the systematic uncertainty of the prompt and the non-prompt component according to the recommendation for the plotting from the ATLAS Collaboration [264].

comparison with ATLAS data, which has an overlap with the ALICE measurement as a function of p_{T}. The difference in the rapidity coverage is not expected to alter the comparison. The results agree within their uncertainties.

6.2. Integrated and p_{t}-differential nuclear modification factors

Figure 6.5 shows the comparison of the mid-rapidity result presented in this thesis with the ALICE results at forward and backward rapidity. The mid-rapidity value for R_{pPb} amounts to 0.71. The deviation from unity amounts to 2.1 standard deviations adding the systematic and the statistical uncertainty in quadrature. It is consistent with the strong suppression observed at forward rapidity and indicates a sizeable nuclear modification. This similar behaviour between mid-rapidity and forward rapidity is expected with the common shadowing parameterisations, since the relative reduction in the gluon flux is not expected to be very different for the

Bjorken-x probed with forward-rapidity and mid-rapidity production. In Fig. 6.6

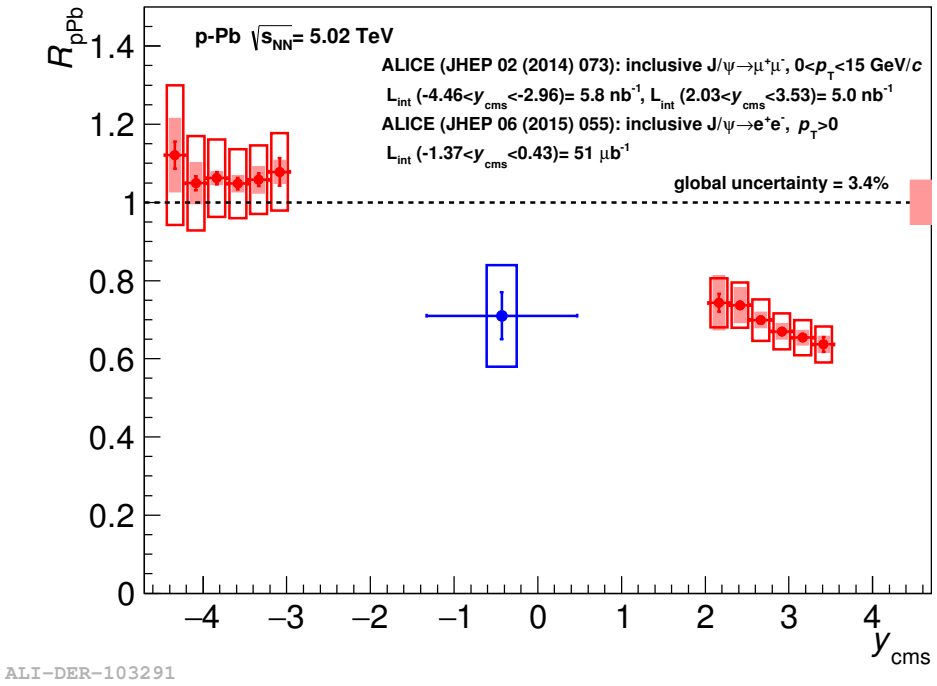

Figure 6.5.: R_{pPb} of J/ψ at mid-rapidity compared with the ALICE muon arm results.

and in Fig. 6.7, the experimental results from ALICE as a function of rapidity are compared with different phenomenological calculations. All shown calculations are done for prompt J/ψ production. However, the measurement of non-prompt J/ψ in p–Pb collisions at low p_{T} at forward rapidity [202] shows a result compatible with the one measured in pp collisions. Hence, the difference between the nuclear modification factor of inclusive and prompt J/ψ production is expected to be significantly smaller than the experimental uncertainties on the inclusive J/ψ nuclear modification factor. A detailed discussion of the magnitude of the effect can be found in the Refs. [200, 201, 183].

The models shown in Fig. 6.6 employ either collinear factorisation [266, 267] or the coherent-energy-loss model [136]. The latter model is based on a parameterisation of measurements in pp collisions and the nuclear modification of the J/ψ production due to the coherent energy loss. The energy-loss-hybrid calculation uses EPS09 [163] for the reduction of the produced $c\bar{c}$ cross section as input.

The nuclear modification is reasonably well described by both collinear-factorisation calculations [266, 267] employing EPS09 as nuclear parton description. The two cal-

culations are based on different assumptions on the production of the J/ψ and do not differ only by the order of the perturbative expansion in α_s. The NLO calculation [266] uses the CEM as hadronisation model, whereas the leading-order calculation [267] assumes $2 \rightarrow 2$ kinematics for the production of J/ψ in order to calculate the nuclear modification. The latter approach is inspired by the CSM, which predicts only $2 \rightarrow 2$ kinematics at leading order for direct J/ψ production, which is the dominating contribution to the inclusive cross section. The latter model is also supplemented by the effect of nuclear absorption for illustration. Nuclear absorption is commonly assumed to be negligible as discussed in Section 2.5.1.
The coherent-energy-loss model [136] is also able to describe the data without any shadowing or, alternatively, with a smaller energy loss of the colour dipole in the nuclear medium supplemented by a shadowing parametrisation based on EPS09. The parameter for the energy loss is derived for both calculations from fits to lower energy data with and without the addition of leading-twist shadowing effects based on EPS09.

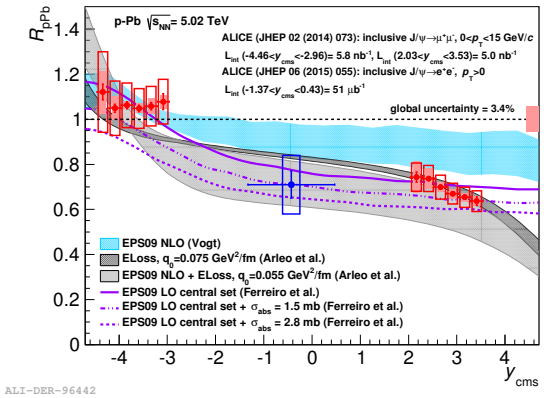

Figure 6.6.:
Collinear factorisation & coherent energy loss

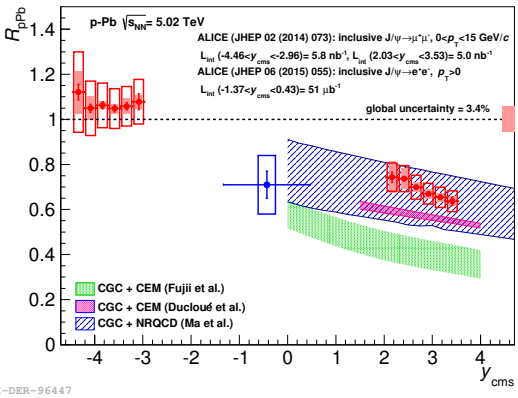

Figure 6.7.:
CGC models

R_{pPb} as a function of rapidity measured by ALICE compared to models. Fig. 6.6 shows models employing collinear factorisation [266, 267] and the energy loss model [136] as well as a combination of both approaches. Fig. 6.7 shows models employing the CGC framework [268, 253, 175].

Figure 6.7 shows the comparison with different CGC model calculations [268, 253, 175]. The early CGC calculation by Fujii et al. [268] using the CEM for the charmonium hadronisation underpredicts the experimental data clearly. In Ref. [175], it is argued that the failure of Ref. [268] is caused by an improper treatment of geo-

metrical effects in the calculation. More recent applications of the CGC framework employing the CEM [175] and the NRQCD approach [253] for the description of the transition of the perturbatively calculated $c\bar{c}$ state to the hadronic bound-state describe the data at forward rapidity and at mid-rapidity fairly well taking into account the uncertainty estimates. The CGC-NRQCD calculation is in agreement with the data. The CEM model calculation is less than 2 σ below the data assuming much smaller uncertainties than the NRQCD based approach. The CEM calculation provides the uncertainties related to scale uncertainties of the charm-quark mass variation in the range $[1.2, 1.5]$ GeV/c^2 and the variation of the factorisation and renormalisation scale from $m_T/2$ to $2 \cdot m_T$. The NRQCD approach uses the ratio of all cross sections from all considered short distance matrix elements taken individually. These ratios envelope all possible ratios of linear combinations of cross sections with specific short distance matrix elements. The latter approach hence gives an upper estimate on the uncertainty related to the model for the J/ψ hadronisation, whereas this is not varied for the calculation in Ref. [175] although there is certainly a sizeable uncertainty related to this part of the calculation. Both calculations agree well with the absolute cross section measurements in pp and in p–Pb collisions within their uncertainties.

Figure 6.8 shows the p_{T}-dependent R_{pPb} of J/ψ at mid-rapidity compared to the corresponding results at forward rapidity and backward rapidity and compared with models. As in the case of the p_{T} integrated result, the mid-rapidity data points suggest a similar behaviour of the J/ψ suppression as at forward rapidity. A strong suppression is indicated below 3 GeV/c and a result consistent with unity at high p_{T}. However, the uncertainties are sizeable. The largest contribution to the correlated uncertainties and the systematic uncertainties originates from the pp reference described in Section 5.6.2. The backward rapidity result shows a weak p_{T} dependence with no p_{T}-interval significantly suppressed below unity.

The early CGC calculation underpredicts the data as in case of the rapidity dependence. The collinear calculations at NLO in the CEM framework [269] is in agreement with the data. However, the uncertainties are sizeable and the lowest transverse momenta are not reached due to instabilities in the calculation. The pure coherent-energy-loss based calculation [174] reproduces the principle shape of the observed deviations from unity in all rapidity intervals. However, especially at forward rapidity, it exhibits a much steeper dependence as a function of p_{T} than the data suggests and is below the data at low transverse momentum and above

the data at high transverse momentum. The agreement is slightly improved when a hybrid approach with a shadowing correction is considered. Nevertheless, the disagreement at low p_{T} persists. At mid-rapidity, both model versions agree with the measurement considering also the scale uncertainty, which is dominated by the pp reference cross section. At backward rapidity, the pure energy loss model shows a too strong suppression at low p_{T}, whereas the combined model is in agreement with the data.

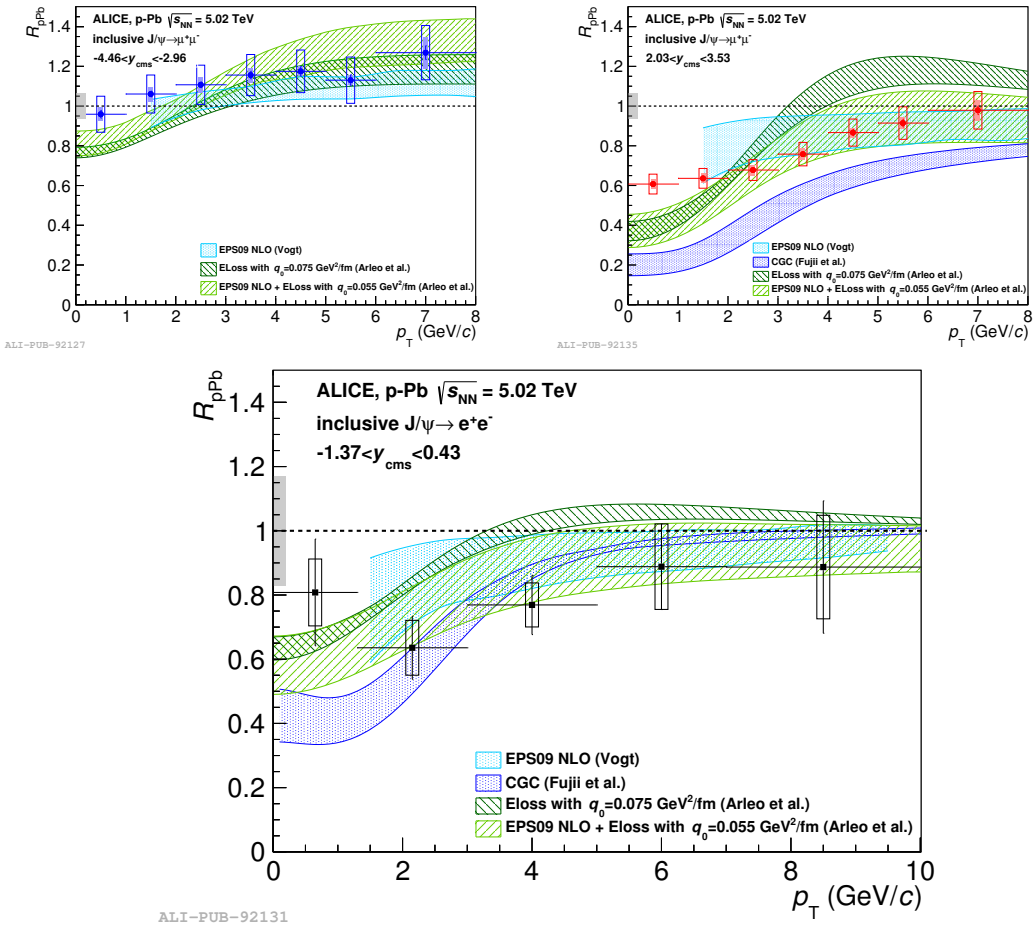

Figure 6.8.: $R_{\mathrm{pPb}}(p_{\mathrm{T}})$ of J/ψ measured by ALICE at backward and forward rapidity in the upper panels and at mid-rapidity in the lower panel. In addition to the uncertainties indicated in the previous figures, the grey bar at the y-axis indicates the bin-by-bin correlated uncertainty, which is dominated by the pp reference. This visualisation is also used for the following centrality-dependent measurements and the R^2_{pA} observable. The coherent-energy-loss model [174] also combined with leading-twist shadowing, calculations in the collinear factorisation at NLO using the CEM [269] and employing EPS09 and the early CGC framework calculation using the CEM [268] are shown.

6.3. Centrality dependence

The centrality-dependent nuclear modification factor is called Q_{pPb} by ALICE in p–Pb collisions due to the caveats in its determination discussed in Section 4.3.1. As an illustration of the biases mentioned in Section 4.3.1, the centrality-dependent nuclear modification factor Q_{pPb} of J/ψ production measured with different centrality estimators is shown compared to the Q_{pPb} of charged particles measured in the central barrel of ALICE as a function of transverse momentum taken from [233] in Fig. 6.9. A hint of the same behaviour as observed for the Q_{pPb} of charged particles averaged in the p_{T} range 10 GeV/c < p_{T} < 20 GeV/c is visible. The estimate of the geometric centrality classes causes an autocorrelation of the observables for centrality estimators overlapping with or close to the acceptance of the particle production involving a hard scale: Q_{pPb} exceeds the centrality-integrated R_{pPb} value by about 30-70%. In most 'peripheral' collisions, most prominently for 80-100%, the opposite effect is observed for the charged track analysis, whereas the statistics does not allow to probe this behaviour in case of the J/ψ measurement. In case of the charged hadrons, the measurement is shown with a *G-PYTHIA* calculation [233]: a simple superposition of nucleon-nucleon collisions by PYTHIA simulated according to a MC-Glauber model. This simple model captures the basic features of the correlation of the soft (centrality estimator) and hard particle production (single high-p_{T} hadron), which is encoded in the centrality-differential results. Details of the modelling and further explanations can be found in Ref. [233]. These effects lead to the choice of the neutral energy deposition on the lead fragmentation side for the slicing of the cross section in centrality quantiles. The simple particle production correlation effects demonstrated by the *G-PYTHIA* simulation dominate over the desired geometric information with estimators based on acceptances close to the observable in question and render the extraction of the latter more difficult.

As mentioned in Section 4.3.1, the ALICE approach for the centrality estimation is based on ad-hoc assumptions and does not give an estimate of the centrality resolution and the corresponding effects due to bin migration for the centrality determination in p–Pb collisions. Hence, the result as a function of centrality and its comparison to phenomenological calculations has to be regarded with care.

Fig. 6.10 shows the Q_{pPb} at forward rapidity, mid-rapidity and backward rapidity compared to models as a function of the number of colliding nucleons in the

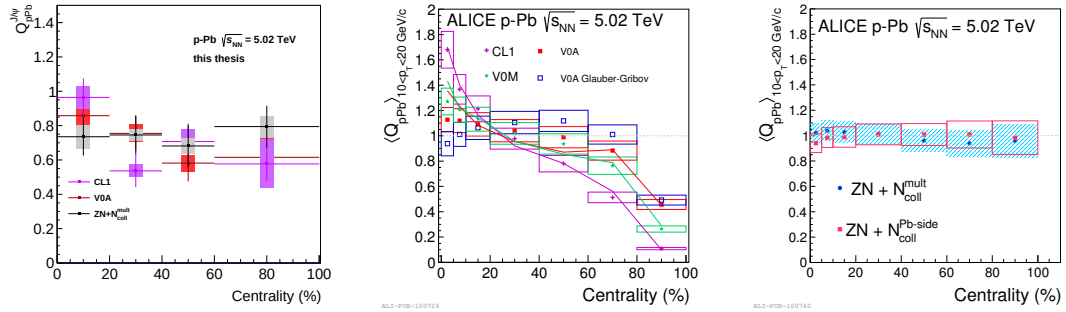

Figure 6.9.: The left panel shows the centrality dependence of the nuclear modification factor Q_{pPb} of inclusive J/ψ at mid-rapidity with centrality different estimators: CL1: mid-rapidity, V0A ($4.5 < \eta_{\mathrm{lab}} < 2$ on lead fragmentation side), ZN (zero degree calorimeter on lead fragmentation side) with $\langle T_{\mathrm{pA}} \rangle$ factors based on the hybrid model. The middle panel shows Q_{pPb} for charged particles as a function of centrality for the estimators based on the V0A and the CL1 estimators [233]. In addition, the V0M estimator is shown corresponding to the addition of the detector amplitudes of the VZERO detectors on both sides of the interaction point. The right panel shows the nuclear modification factor as a function of centrality for the high-p_{T} charged particles with the hybrid approach. The bin-by-bin correlated pp reference uncertainty for the J/ψ measurement is omitted for simplicity.

p–Pb collisions as extracted from the hybrid model introduced in Section 4.3.1. The uncertainty on the $\langle N_{\mathrm{coll}} \rangle$ variable is sizeable and fully correlated with the corresponding uncertainties of the $\langle T_{\mathrm{pA}} \rangle$ values as described in Section 4.3.4.

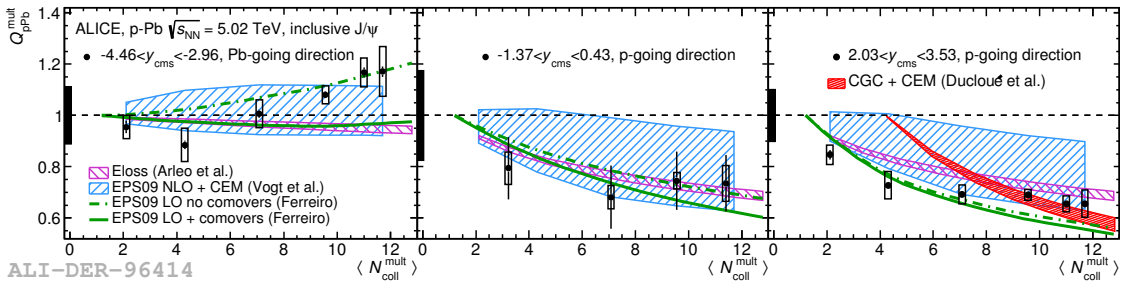

Figure 6.10.: Q_{pPb} of J/ψ at mid-rapidity presented in this work and at forward and backward rapidity compared with the models presented in the Refs. [266, 190, 174, 175].

A measurable variation of the nuclear modification can be observed. At backward rapidity an increase and at forward rapidity a decrease is seen, whereas the mid-rapidity Q_{pPb} shows a behaviour compatible with no centrality dependence. However, the uncertainties are sizeable and the behaviour could also be consistent with the forward-rapidity result. These results are complemented at forward and backward rapidity by double differential results as a function of p_{T} and centrality presented in Ref. [183].

A model comparison as a function of centrality is interesting. The suppression of

the gluon flux is expected to show a dependence on the impact parameter, since it is an effect depending on the gluon density and the energy loss model is expected to show a path-length dependence.
Different methods are employed to estimate the centrality dependence in the presented models. The calculation by R. Vogt based the impact parameter dependence of the EPS09 shadowing on a proportionality between the path length and the shadowing factor as explained in Ref. [266]. The centrality dependence of the shadowing in Ref. [190] is taken from the authors of EPS09, who provided an extension of the shadowing parameterisation as a function of the impact parameter based on fits to the atomic mass number dependence of the nuclear suppression measurements as detailed in Ref. [270]. In addition, the effect of the nuclear modification within the comover model is combined with a centrality-dependent formulation of nuclear shadowing [190]. The model using comovers does not catch the centrality dependence of the J/ψ measurement at backward rapidity, where it predicts a flat behaviour as a function of $\langle N_{\mathrm{coll}} \rangle$, whereas the data show a rising trend. The comover model was introduced to describe the stronger suppression of ψ(2S) detailed in the following section. The model will be commented on in Section 6.5.1.
The coherent-energy-loss model [174] describes the data at forward and mid-rapidity and misses the shape at backward rapidity. The CGC model in Ref. [175] was extended to provide a centrality dependence in Ref. [271]. It shows a stronger suppression in most central collisions as it is qualitatively observed in data. No quantitative agreement is however reached.
However, no centrality resolution is accounted for in the comparisons. Therefore, it is not possible to claim disagreement between the models and the data at the present stage. An experimental determination of the resolution is in preparation within the ALICE Collaboration [234].

6.4. Multiplicity dependence measurement and discussion

Figure 6.11 shows the multiplicity dependence of inclusive J/ψ production at mid-rapidity presented in this thesis. For this purpose, the J/ψ yield extracted in a given multiplicity range was divided by the integrated yield measured in non-single

diffractive events as explained in Section 5.1. In comparison, the forward and backward rapidity results by ALICE are shown as well. Furthermore, the mid-rapidity result is compared to the corresponding result in pp collisions at $\sqrt{s} = 7$ TeV. The result is not unfolded for bin migration effects due to the finite resolution in the multiplicity estimator as discussed in Section 4.3.5. The J/ψ yield shows an approximately linear dependence on the multiplicity in the measured acceptance. This pattern was already observed in pp collisions at $\sqrt{s} = 7$TeV [221] with the same slope as it can be seen in the comparison.

Since the acceptance of the multiplicity measurement and the J/ψ measurement overlaps completely in case of the mid-rapidity result, but not in case of the muons, where the separation in pseudorapidity between the multiplicity measurement and the J/ψ tracks amounts to at least 1.5 units, the comparison with the forward and backward rapidity results has to be done with care. The dependence measured at backward rapidity, $-4.46 > y_{\mathrm{cms}} > -2.96$, is consistent with the mid-rapidity result, $-1.37 > y_{\mathrm{cms}} > 0.43$, within the uncertainties over the entire multiplicity range. The rise of the relative J/ψ yield at forward rapidity, $3.53 > y_{\mathrm{cms}} > 2.03$, shows a different trend: the slope of the J/ψ yield as a function of multiplicity starts to decrease at about $1.5 \cdot \langle \mathrm{d}N_{\mathrm{ch}}/\mathrm{d}\eta \rangle (|\eta_{\mathrm{lab}}| < 1)$ reaching a flat behaviour as a function of multiplicity above $2.5 \cdot \langle \mathrm{d}N_{\mathrm{ch}}/\mathrm{d}\eta \rangle (|\eta_{\mathrm{lab}}| < 1)$ within uncertainties.

In pp collisions, the signal was also separated in the prompt and the non-prompt component and compared with D-meson measurements [222]. All mentioned measurements show a similar behaviour within the uncertainties in the probed multiplicity range. The comparison with the inclusive J/ψ measurement in pp collisions is shown in Fig. 6.11. In Fig. 6.12, the J/ψ result as a function of multiplicity in p–Pb collisions is compared with the corresponding D-meson result with similar acceptances for the measured quantities. Also here an agreement between the measurements is observed.

These results show a generic feature of the correlation between particle production involving a hard scale given by the $c\bar{c}$ bound-state or the open-heavy-flavour mesons and soft particle production in pp and p–Pb collisions. They provide therefore crucial input for the full modelling of hadronic collisions. This is of particular interest, since heavy-flavour production at low transverse momentum is typically not well modelled by standard event generators and the underlying mechanisms are not quantitatively understood as explained in the following.

In Ref. [272], it was shown that the production of J/ψ in pp collsisions as a function of

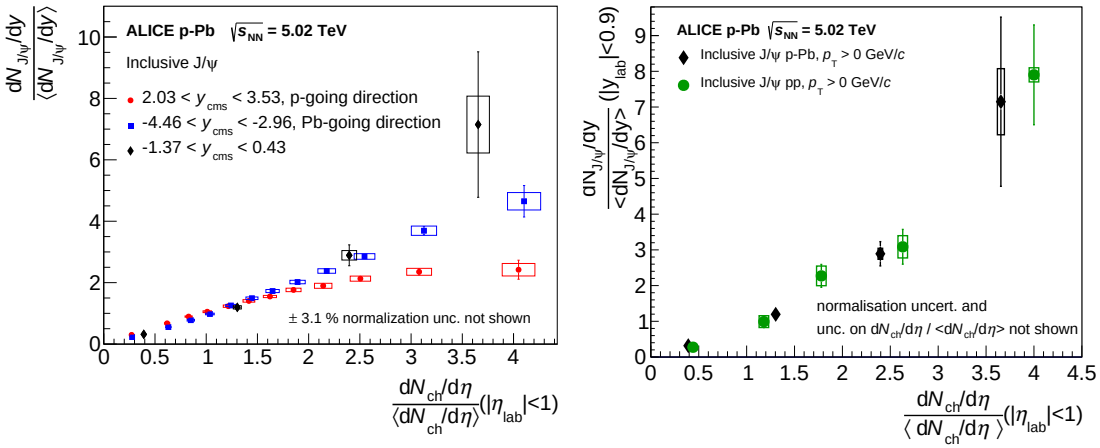

Figure 6.11.: The dependence of the normalised inclusive J/ψ yield on multiplicity as measured by ALICE in three rapidity ranges [237] in p–Pb collisions is shown on the left hand side. The bars represent the statistical uncertainty, the height of the boxes the systematic uncertainty of the relative J/ψ yield. The uncertainty related to the multiplicity are displayed as box width . The right hand side shows the comparison between the result in p–Pb collisions at $\sqrt{s_{\rm NN}} = 5.02$ TeV and the one in pp collisions at $\sqrt{s} = 7$ TeV [221]. In the latter visualisation, the box width does not correspond to the multiplicity related uncertainties.

multiplicity is not well controlled in the standard event generator PYTHIA 6.4, the most common event generator for the simulation of minimum bias and underlying-event-related observables in high-energy physics [227]. The observable was proposed in the same reference as a sensitive probe of the interaction implementation in PYTHIA or in similar event generators. The first experimental data by ALICE [221] showed that the pre-LHC Perugia tune of PYTHIA 6.4 [259] indeed showed a decrease of J/ψ production as a function of multiplicity opposite to the experimental data.

A further motivation for the multiplicity-differential measurement is the potential insight into the wave-function of the proton. In Ref. [273], it is argued that the qualitative features of the correlation of the J/ψ production or any particle production creation at a similar hard scale with the soft particle production up to the probed 3-4·$\langle N_{\rm ch}\rangle$ can be explained by a transverse structure of the proton wave-function as suggested in the Refs. [274, 275] and may contain further information on the proton structure. The proton has in this impact parameter picture a dense core, which is also responsible for hard particle production. In contrast to this static dense core geometry picture, it is argued in Ref. [276] that the proportionality is mainly caused by higher frozen Fock-state components of both protons. This spe-

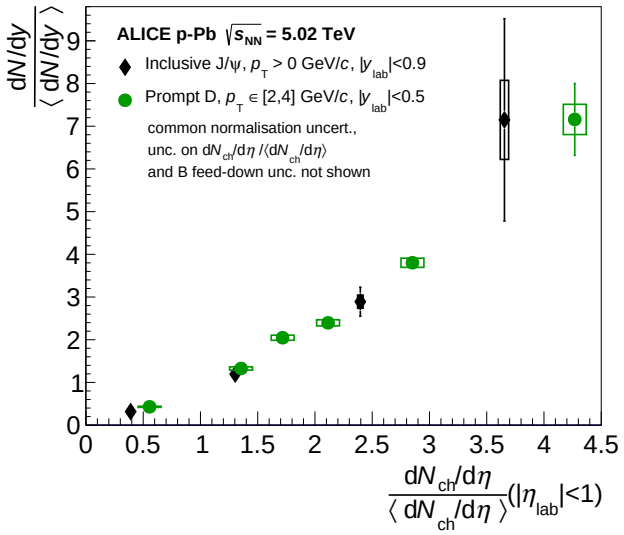

Figure 6.12.: The multiplicity dependence of J/ψ production in p–Pb collisions at mid-rapidity compared to respective D-meson result at mid-rapidity. The uncertainties related to the multiplicity scale are not shown.

cial configuration corresponds to a larger multiplicity and to a larger probability of hard particle production. These rare proton configurations are claimed to behave similarly as the average gluon configuration in the nucleus assuming a continuous description of high-multiplicity pp and p–Pb collisions. In Ref. [277], the measurements of J/ψ in pp collisions are described in a colour string picture, where the number of J/ψ was assumed to be proportional to the number of collisions of strings. The charged-particle multiplicity scales in this approach with the number of participating colour strings. This behaviour corresponds to a proportionality between J/ψ and multiplicity production at low multiplicities, whereas it leads to a quadratic multiplicity dependence at higher multiplicities and hence underlies also the picture in the Refs. [276, 273]. These dependencies are argued to be generic for any picture attributing the hard scale production and the multiplicity generation on collision of the same constituents, which could be also based on a multi-parton interaction description in a standard event generator.

More recent tunes of PYTHIA 8 for soft QCD observables were able to provide a reasonable description for open-heavy-flavour production at the LHC [222] as a function of multiplicity. However, the underlying dominating production mechanism by sea-c quarks seems unphysical based on pQCD calculations and questions the reliability of the current modelling. The event generator EPOS was also compared to the open-charm data by ALICE in pp collisions [222]. The model is based

on reggeized pomerons and containing a similar underlying picture as proposed in Ref. [277]. A reasonable agreement was observed.
The struggling of the standard event generators modelling pp collisions and the continuum of the correlation between soft- and hard-particle production between p–A and pp collisions, calls for a concerted phenomenology effort not only on tuning, but even more on a conceptual level to understand better the involved correlations. It appears to be evident that the large soft particle multiplicities and particle production involving a perturbative scale is caused by the same source terms. However, the exact relation to the particle production in p–A collisions is not clarified and it remains unclear to which extent geometrical effects or colour fluctuations are responsible for the variation of the number of sources in both systems. Extending the measurement up to higher multiplicities may give a better understanding of the importance of the different considered effects. A better understanding of these correlations in pp collisions might become beneficial for the energy frontier measurements as well as for even higher collision energies in hadronic collisions than at the LHC for the proper modelling of the backgrounds induced by the multiple occurrence of hard processes in one event. Experimental data of cross sections and of angular correlations between several charmed hadrons in the final state measured by LHCb [260] in pp collisions and charged particles as by ALICE [278] in pp as well as in p–Pb collisions will hopefully provide further constraining power in this context.

6.5. Discussion of the J/ψ nuclear modification factor

In general, the nuclear modification factor of J/ψ production at mid-rapidity as well as at forward and backward rapidity is within expectations of pQCD calculations based on collinear factorisation combined with different charmonium hadronisation mechanisms. However, these model calculations are not stable at low p_{T} at NLO in the Colour Evaporation Model (CEM) [269]. Hence, there is no prediction given by these models at the lowest p_{T}, although they provide p_{T}-integrated quantities as a function of rapidity[3]. It is argued that these calculations are stabilised by the large

[3]For the direct J/ψ production in the Colour Singlet Model (CSM), the leading-order calculations for the p_{T}-differential result are of the same order of α_s as the rapidity differential result, since,

phase-space integration: the variations causing the blow up of the uncertainties at low p_{T} in the variation of charm-quark mass and scale uncertainties are claimed to be cured in the integrated case.

It is argued in Ref. [279], that direct J/ψ production at leading order in the Colour Singlet Model (CSM) in pp collisions can be taken as estimate of the total cross section not considering the available NLO calculation due to the unphysical behaviour with, e.g., negative cross section contributions. This is questionable and it could be argued that the worse convergence behaviour at NLO compared to LO rather signals the break-down of the approach in the specific phase-space domain due to the violation of factorisation either with respect to the initial state, i.e., break-down of collinear factorisation, or with respect to the final state in the projections to the final state as discussed in Section 2.3.

It is claimed in Ref. [280] that the usual fixed-order NLO collinear-factorisation calculations combined with NRQCD fits to cross section and polarisation measurements are only applicable for $p_{\mathrm{T},\psi}/M_{\psi}$ >3-4 based on fit stability arguments without providing a theoretical reasoning for this ad-hoc value. It could be that either higher-order corrections are needed for a description at lower transverse momentum or other schemes for the treatment of the incoming gluon flux should be used. However, it has to be noted that ep collision data from the HERA collider on charmonium production [281] could be described down to lowest p_{T} in global fits within the collinear framework down to fairly low Bjorken-x. Hence, firm conclusions on the size of the mentioned effects breaking the collinear factorisation or the NRQCD factorisation scheme can only be done based on global analyses considering several collision systems and observables.

Due to all these caveats, it is questionable whether the description of charmonium within a collinear framework provides the best expansion strategy of the contributing graphs, even more in p–A collisions than in pp collisions. In addition, the description of shadowing within a leading-twist framework is a very strong assumption and might be conceptually not the correct one. This could lead to unreliable results in the nuclear modification of charmonium. Nevertheless, it is not disproven by data and represents by far the best known framework for perturbative calculations in hadronic collisions.

The coherent-energy-loss model [136] can provide a reasonable description for the

in contrast to W or Z boson production, the model has no contributions to the cross section from $2 \to 1$ processes.

rapidity dependence of J/ψ production without any consideration of shadowing. The transverse momentum dependence is not reproduced in detail, but it is improved, when shadowing is incorporated although the disagreement persists at forward rapidity at the lowest transverse momentum. The energy loss corrections are higher-twist corrections and are hence by definition not incorporated in leading-twist shadowing approaches. The fact that the rapidity dependence can be described by the consideration of disjunct effects illustrates prominently that it is not clear up to now what is the main effect causing nuclear modifications in p–Pb collisions at the LHC. The observation is made that the energy-loss approach could be disentangled from leading-twist shadowing by comparisons of charmonium production with Drell-Yan production in Ref. [282], since the coherent energy loss is caused by gluon emission of an object carrying colour charge. Although there exists a preliminary result in pp collisions down to comparatively low invariant masses of the dilepton pair, below the Υ mass, in pp collisions at the LHC [283], it is questionable whether such a measurement will be feasible with sufficient precision in the near future at the LHC in the vicinity of the J/ψ mass.

The already mentioned CGC effective-field-theory ansatz combined with the NRQCD formalism [253] as well as with the CEM [175] provides a decent description considering all uncertainties of the approaches. However, in order to validate the approach, it will be important to carry out calculations for polarisation in pp collisions as well as for the ψ(2S) nuclear modification discussed in Section 6.5.1. Furthermore, the mentioned open-charm comparison could be interesting as one can deduce from the comment in Ref. [279]: both calculations approximately reproduce the total J/ψ cross section in pp collisions although the projection probability of $c\bar{c}$ pair to J/ψ is different by a about factor 10. Consequently, the 'effective' gluon flux from both incoming hadrons in the CGC calculation of Ref. [253] is suppressed by a factor 10 compared to the collinear-framework calculation in Ref. [279]. Calculations of the total charm cross section in pp collisions or ratios of the open-heavy-flavour cross sections over the J/ψ cross section compared to data can provide discriminating power in order to falsify at least one of the compared calculations.

6.5.1. The nuclear modification of ψ(2S) production and its implications

Furthermore, for the interpretation of charmonium results in p–Pb collisions, it is important to put the J/ψ measurements in the context of the findings for the radially excited state of J/ψ, the $\psi(2S)$. This state has been found to be more strongly suppressed by about a factor two compared to the J/ψ [191]. This ALICE result was confirmed by LHCb [193], separating also the prompt and the non-prompt component of the ψ(2S) production. A hint of this behaviour was already observed in d–Au collisions by PHENIX [284]. The measurements by the ALICE and PHENIX Collaborations of inclusive ψ(2S) are shown in Fig. 6.13.

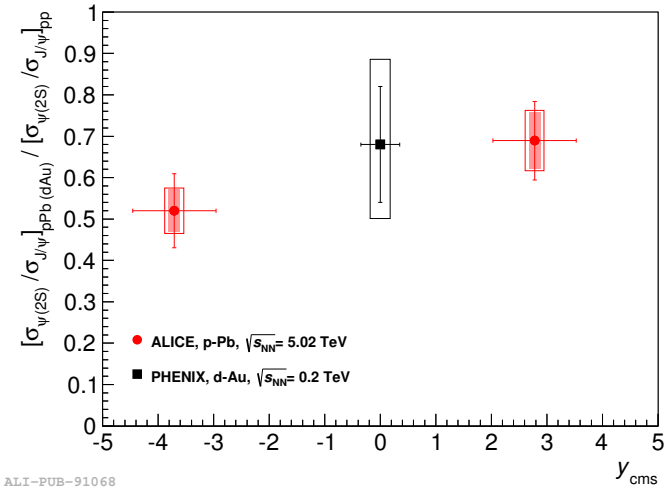

Figure 6.13.: The ALICE results on inclusive ψ(2S) to J/ψ production double ratio in p–Pb vs. pp collisions at forward and backward rapidity is compared to the result obtained by the PHENIX Collaboration at lower beam energy at mid-rapidity. The comparison is taken from Ref. [191].

This behaviour is not explained within the framework of standard leading-twist shadowing and also not in the coherent-energy-loss model. Both models do not modify the projection probability of the colour dipole to the given charmonium state. In case of standard shadowing, only the gluon distribution functions are modified which are acting on the production of both states on quite equal footing due to the similar mass of the two states. There can be effects caused by the structure of the ratio of the gluon parton distribution functions between the proton and the nucleus as a function of Bjorken-x, which is usually assumed to be similar than the ratio of the structure functions shown in Fig. 2.8. However, this ratio

of the gluon parton distribution functions does not show strong dependences on Bjorken-x for the parameter ranges probed by the ψ(2S) and J/ψ states at the LHC for all available nuclear PDF parameterisations. The latter effect was quantified in Ref. [285] for the RHIC case for different nuclear PDF parameterisations, where the largest deviation from unity observed for the observable shown in Fig. 6.13 as a function of rapidity amounted to about 7% with sign opposite to the experimental observation.

The comover model and related approaches [190] was the first calculation which was able to provide an explanation for the suppression pattern of ψ(2S). The comover model was originally introduced for the study of A–A collisions at the SPS and aims at incorporating the interaction of charmonium at a late stage with comoving hadrons, i.e., at the LHC mostly pions. The model is very compact, since it only works with a limited number of parameters. However, there are a number of ad-hoc assumptions. For instance, it is not clear what the particle composition and time evolution of the comovers are. The model parameters can be rather seen as a kind of time and space average and do not carry specific information about the exact degrees of freedom involved. The fact that an interaction of the already built charmonium states with other objects is part of the model, makes it possible to explain the stronger suppression of the ψ(2S) compared to the J/ψ state. A similar approach was followed in Ref. [131], where this late stage interaction was also considered as an explanation of the unexpected results by CMS on ψ(2S) production in Pb–Pb collisions [286].

Also in CGC models, it is imaginable that different nuclear modifications of ψ(2S) production compared to J/ψ production occur by enhanced multiple gluon interactions between the quark lines in the diagram in p–Pb compared to pp. This effect could lead to stronger modifications in case of ψ(2S), since it is very close to the open-charm threshold. In any case, this observation strongly violates collinear factorisation combined with standard approaches for the hadronisation of charmonium.

In summary, there is not yet a unique explanation for the additional suppression of the excited state $\psi(2S)$ and the ad-hoc considerations usually called final-state effects remain vague formulations at the moment. The fact that these results cannot be explained by the most-discussed modifications for the J/ψ state, puts also a question mark on the interpretation of J/ψ result as a sign of leading-twist gluon shadowing and/or energy loss. A comprehensive explanation in combination with other results sensitive to gluon shadowing like J/ψ and ψ(2S) production in ultra-

peripheral collisions as well as open-heavy-flavour production is necessary in order to provide firm interpretations of the available data.

6.6. Implications for the interpretation of J/ψ results in A–A collisions

Based on the experimental measurements, we attempted an extrapolation of nuclear effects from the p–A collision system to the A–A collision system under certain assumptions as published in Ref. [201].

The Bjorken-x of the Pb nucleus probed in the J/ψ measurements in p–Pb collisions at $\sqrt{s_{\mathrm{NN}}} = 5.02$ TeV is similar to the Bjorken-x probed in Pb–Pb collisions at $\sqrt{s_{\mathrm{NN}}} = 2.76$ TeV due to the rapidity shift of the centre-of-mass system. Assuming that J/ψ is dominantly produced by a $2 \to 1$ production mechanism, i.e., that the production cross section is dominated by contributions with no hard gluon in the outgoing state, we can derive a closed formula for the probed Bjorken-x of the lead ion at a given rapidity y_{cms} with the sign convention introduced in Equation (4.2) and p_{T} of the produced J/ψ:

$$x_{\mathrm{Pb}} = \frac{m_{\mathrm{T}}}{\sqrt{s_{\mathrm{NN}}}} \cdot e^{-y_{\mathrm{cms}}}, \tag{6.1}$$

where $m_{\mathrm{T}} = \sqrt{m^2 + p_{\mathrm{T}}^2}$ with $\hbar = c = 1$. For this production assumption, the Bjorken-x values for the measurements in both collision systems are shown in Fig. 6.14.

For a production mechanism, which is dominated by $2 \to 2$ production as it is the case for direct J/ψ production in the CSM at leading order, the formula cannot be given independent of the Bjorken-x of the second colliding gluon. The corresponding formula is given in Ref. [287].

If the $2 \to 1$ kinematics is valid, restricting the discussion to leading-order graphs; the modification of charmonium production in p–Pb collisions can be factorised in the parton distribution function as a function of Bjorken-x via $f_A(x_i, Q^2) = f_A^i(Q^2) = A \cdot f_p(x_i, Q^2) \cdot R_A(x_i, Q^2) = A \cdot f_p^i(Q^2) \cdot R_A^i(Q^2)$[4], the differential nu-

[4] In practice, any other factorisation into factors only depending on Bjorken-x is also a sufficient condition.

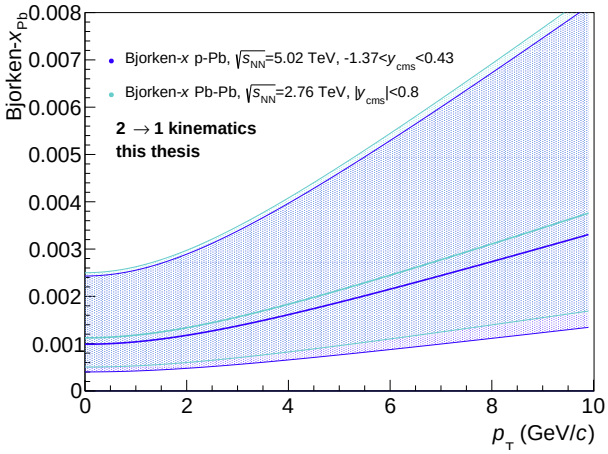

Figure 6.14.: Bjorken-x values probed in the lead nucleus as calculated from Equation (6.1) comparing the acceptances of the measurements in p–Pb collisions [201] and Pb–Pb collisions [242]. The central lines indicate the maximum of the $Acc. \times eff.$ for both J/ψ production measurements and the area covers the full rapidity range.

clear modification factor of direct J/ψ production can be factorised in the following way:

$$R_{\mathrm{pA}}^{\text{direct J/}\psi}(p_{\mathrm{T}}, y) = \frac{\sum_{\mathrm{j}} \hat{\sigma}_{\mathrm{gg}\to c\bar{c}_{\mathrm{j}}}(p_{\mathrm{T}}, y) \cdot F_{\mathrm{j}}(\mathrm{J}/\psi) \cdot A \cdot f_p^1 \cdot R_A^1 \cdot f_p^2}{A \cdot \sum_{\mathrm{j}} \hat{\sigma}_{\mathrm{gg}\to c\bar{c}_{\mathrm{j}}} \cdot F_{\mathrm{j}}(J/\psi) \cdot f_p^1 \cdot f_p^2} = R_A^1 \tag{6.2}$$

The gluon parton distribution function of the nucleus is denoted here with $f_A(x_i, Q^2)$ $= f_A^i(Q^2)$, where Q^2 denotes the factorisation scale usually taken to be m_{T} of the J/ψ, i is the index of the colliding hadron with the corresponding x_i, A the atomic mass number and $R_A^i(Q^2)$ the ratio of the parton distribution functions of the nucleus and the proton as extracted from PDF fits. $\hat{\sigma}_{\mathrm{gg}\to c\bar{c}_{\mathrm{j}}}$ is the partonic cross section for the gluon-gluon interaction going to $c\bar{c}$ with the quantum numbers summarised with the index j, $F_{\mathrm{j}}(\mathrm{J}/\psi)$ the non-perturbative matrix element for the transition of the $c\bar{c}_{\mathrm{j}}$ state to the J/ψ bound-state.

This factorisation assumption may be wrong as explained in Section 2.5.2, depending on the description of the nuclear modifications in p–Pb collisions. In addition, the factorisation is derived for infinitesimally small intervals in rapidity and p_{T}. With the same assumptions, R_{AA} can be expressed similarly:

$$R_{\mathrm{AA}}^{\text{direct J/}\psi}(p_{\mathrm{T}}, y) = \frac{\sum_{\mathrm{j}} \hat{\sigma}_{\mathrm{gg}\to c\bar{c}_{\mathrm{j}}}(p_{\mathrm{T}}, y) \cdot F_{\mathrm{j}}(\mathrm{J}/\psi) \cdot A^2 \cdot f_p^a \cdot R_A^a \cdot f_p^b \cdot R_A^b}{A^2 \cdot \sum_{\mathrm{j}} \hat{\sigma}_{\mathrm{gg}\to c\bar{c}_{\mathrm{j}}}(p_{\mathrm{T}}, y) \cdot F_{\mathrm{j}}(\mathrm{J}/\psi) \cdot f_p^b \cdot f_p^a} = R_A^a \cdot R_A^b \tag{6.3}$$

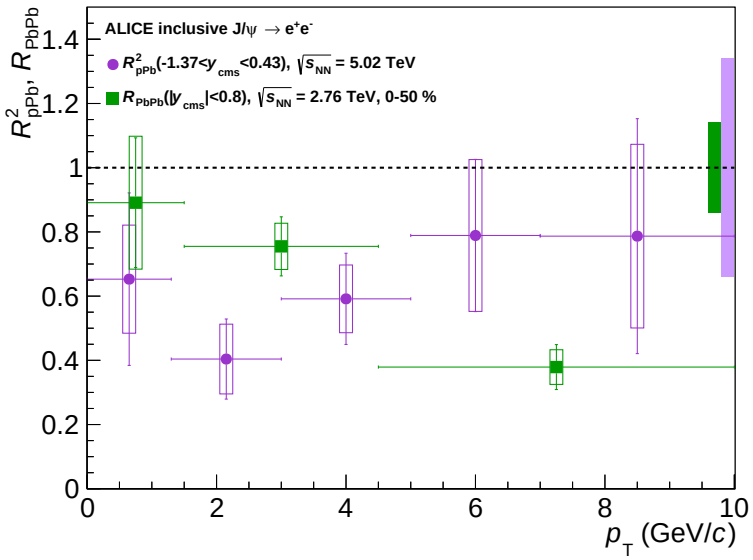

Figure 6.15.: R^2_{pA} compared to R_{AA} as a function of transverse momentum measured by ALICE at mid-rapidity. This result of this thesis was published in Ref. [201].

Under the given assumptions, we see that the squared nuclear modification factor R_{pA} can provide an estimate of R_{AA} assuming that only the nuclear modifications present in p–A collisions are acting also in A–A collisions, assuming that $x_a = x_1$ and $x_b = x_2$:

$$R_{\mathrm{AA}}^{\text{direct J}/\psi} = R_A^a \cdot R_A^b = R_A^1 \cdot R_A^2 = R_A^1 \cdot R_A^1 = R_{\mathrm{pA}}^{\text{direct J}/\psi} \cdot R_{\mathrm{pA}}^{\text{direct J}/\psi} \tag{6.4}$$

The square of R_{pA} was computed and compared with the measured R_{AA} as a function of transverse momentum [242]. The comparison is shown in Fig. 6.15.
The comparison under the given assumptions hints at a value of R_{AA} above unity after the correction of the nuclear effects based on the p–A result in the sketched way. Independent from the specific assumptions, the different kinematical dependence of R_{AA} and R_{pA} as a function of transverse momentum enforces the experimental evidence for the emergence of an additional J/ψ production component at low transverse momentum in A–A collisions, which is expected in transport models and the statistical hadronisation model as a sign of deconfinement acting on the $c\bar{c}$ bound-states as described in Section 2.4.3.

7. Conclusions and Outlook

In this thesis, the first measurements of J/ψ cross sections and nuclear modification factors and the charged-particle multiplicity dependence of J/ψ production in p–Pb collisions at mid-rapidity is presented. An indication of a strong nuclear suppression of integrated J/ψ production and of J/ψ production at low p_{T} is observed. The normalised J/ψ yield is proportional to the charged-particle multiplicity within uncertainties.

Given the precision of the results and the model calculations with different underlying assumptions leading to fairly similar results for the nuclear modification factor, it is not possible to identify the main mechanisms of nuclear modification in proton-nucleus collisions at the present stage. The production could be affected by a number of different nuclear modification mechanisms and their relative importance is not clear from the present theoretical understanding and the available p–A results on J/ψ production at the LHC at the moment. However, there is a large amount of experimental data on charmonium, open-heavy flavour production at the LHC in p–Pb and pp collisions and implications of ep data from HERA and ultra-peripheral collisions and from lower energy collision energies providing constraining power in their combination, which is not yet fully exploited.

In the case that the main modification of charmonium production is given by a leading twist nuclear modification of the parton distribution functions, the J/ψ result provides very useful input constraining the strength of shadowing. Under this assumption, the J/ψ result presented in this thesis can be used as an ingredient for the charmonium phenomenology calculations in A–A collisions, since shadowing impacts directly the production rate of the total amount of charm quark pairs in A–A collisions produced in the initial stage of the collision. Up to now, the total cross section of open-charm production both in p–Pb and in Pb–Pb, which test the total charm production directly, is not measured yet at the LHC. Measurements of open-charm hadrons with topological selections in fully reconstructed hadronic

channels as well as in leptonic channels become increasingly difficult going to low p_{T} due to the missing boost or large backgrounds. As an example, the measurement of D-mesons by ALICE are restricted to $p_{\mathrm{T}} > 1$ GeV/c in p–Pb [288] and in Pb–Pb collisions [289]. Large backgrounds prevent a measurement in Pb–Pb collisions down to zero p_{T} without topological selections at mid-rapidity. In p–Pb collisions, a measurement without topological selection is in preparation within ALICE at mid-rapidity [290]. Therefore, the charmonium measurement presented in this thesis gives the most stringent measurement of nuclear suppression of the initially produced $c\overline{c}$ pairs in A–A collisions by shadowing assuming that it is also the dominating effect for the nuclear modification of charmonium production in p–Pb collisions.

Consequently, following the interpretation that leading twist shadowing or at least that an effect, which scales as a function of Bjorken-x and which factorises accordingly, is the main effect to be considered, the square of the presented R_{pA} measurement enables a first extrapolation to the Pb–Pb collision system as discussed in Section 6.6. The result of this ansatz strengthens an interpretation of the A–A results as a sign of late stage charmonium production from the phase boundary or from the deconfined stage of the system evolution, since the R_{AA} at low p_{T} is even larger than the square of the R_{pA}. This comparison has at the present stage only qualitative nature due to all mentioned caveats and the sizeable uncertainties.

The experimental precision of the nuclear modification factor in p–Pb collisions is limited by the precision of the reference cross section in pp collisions, which is the largest contribution to the uncertainties. The measurement of the nuclear modification factor would therefore benefit from more precise J/ψ cross section measurements in pp collisions at the LHC, preferably at the same collision energy in order to avoid interpolations. Assuming no cancellation of uncertainties between the measurements in the two collision systems in the nuclear modification factor, ALICE would need to record about 100 million minimum-bias collisions to achieve the same precision in a direct measurement like in the present interpolation data sample as detailed in Appendix B. A data sample of this size was recorded in fall 2015 at $\sqrt{s} = 5$ TeV. However, a significant improvement of the precision of the nuclear modification factor R_{pA} would either require a substantial cancellation of uncertainties in the ratio or a much larger data sample in pp collisions. The statistics reach of ALICE for J/ψ measurements in pp collisions down to low p_{T} until 2018 with minimum-bias triggered data and with the TRD trigger is discussed in

Appendix B.

In addition, the measurement of the total open-charm cross section as well as the open- to hidden-charm ratio in p–Pb collisions compared to the one of pp collisions integrated as a function of transverse momentum, if extracted with sufficient precision, could be used to falsify proposed ansätze for heavy-flavour production as detailed in Section 6.5. The golden channel for the discrimination between leading twist shadowing and the energy loss model is evidently the measurement of Drell-Yan production at the same mass scale as the J/ψ as explained in Section 6.5.

The separation and description of geometric effects caused by the nucleus or the proton and colour fluctuations of the hadrons in the p–A measurements as a function of multiplicity and centrality prove to be difficult, both on the experimental side as well as on the theory side. However, a coherent understanding of the correlation of hard scattering products and soft particle production promises to provide information on the structure of hadrons as detailed in Section 6.4.

The ALICE measurement of J/ψ production in p–A collisions at mid-rapidity gives insight in the nuclear modification of charmonium. It provides guidance for the expectation for non-deconfinement effects in A–A collisions at the TeV-scale enforcing the interpretation of an additional low-p_{T} component to the measured production of charmonium in A–A collisions as a sign of deconfinement in the statistical hadronisation or in transport models. The dominant mechanisms for nuclear modification could not yet be singled out among the different proposals. The research field is working very actively and the LHC data promoted the understanding on the phenomenological side. Future measurements at the LHC will certainly help to constrain the production mechanisms, but there is a rich set of observables already available. Any closed theoretical explanation has to consider this ensemble of measurements at different energies and in various collision systems. A consistent description of J/ψ production in p–A and pp collisions within perturbative QCD seems feasible thanks to the hard scales in the process and the large amount of data despite the challenges in the formulation of valid factorisation schemes for the production of $c\bar{c}$ bound states. The latter would be a major achievement of perturbative QCD at the frontier of its applicability.

Bibliography

[1] H. Geiger and E. Marsden. On a Diffuse Reflection of the α-Particles. *Proc. Roy. Soc. A*, 82:495, 1909.

[2] E. Rutherford. The scattering of α and β particles by matter and the structure of the atom. *Phil. Mag.*, 21:669–688, 1911.

[3] J. Chadwick. Possible Existence of A Neutron. *Nature*, 192:312, 1932.

[4] H. Yukawa. On the Interaction of Elementary Particles I. *Proc. Phys. Math. Soc. Jap.*, 17:48–57, 1935. Prog. Theor. Phys. Suppl.1,1(1935).

[5] G. Occhialini and C. Powell. Nuclear disintegration produced by slow charged particles of small mass. *Nature*, 159:453–456, 1987.

[6] C. Lattes, G. Occhialini, and C. Powell. Observations on the Tracks of Slow Mesons in Photographic Emulsions. *Nature*, 160:453–456, 1947.

[7] M. Gell-Mann. The Eightfold Way: A Theory of Strong Interaction Symmetry. *CTSL-20(unpublished), reprinted in "The Eigthfold Way", op. cit, pp. 11-57*, 1961.

[8] Y. Ne'eman. Derivation of strong interactions from a gauge invariance. *Nuclear Physics*, 26(2):222 – 229, 1961.

[9] M. Breidenbach et al. Observed Behavior of Highly Inelastic Electron-Proton Scattering. *Phys. Rev. Lett.*, 23:935–939, 1969.

[10] G. Miller et al. Inelastic Electron–Proton Scattering at Large Momentum Transfers and the Inelastic Structure Functions of the Proton. *Phys. Rev. D*, 5:528–544, 1972.

[11] J. D. Bjorken. Asymptotic Sum Rules at Infinite Momentum. *Phys. Rev.*, 179:1547–1553, 1969.

[12] R. Feynman. The behaviour of hadron collisions at extreme energies. 1969. Proceedings, conference on high energy collisions* 237-258, IN *Stony Brook 1969.

[13] M. Gell-Mann. A schematic model of baryons and mesons. *Physics Letters*, 8(3):214 – 215, 1964.

[14] G. Zweig. An SU_3 model for strong interaction symmetry and its breaking; Version 2. CERN-TH-412:80 p, 1964. Version 1 is CERN preprint 8182/TH.401, 1964.

[15] H. Fritzsch and M. Gell-Mann. Current algebra: Quarks and what else? *eConf*, C720906V2:135–165, 1972.

[16] H. Fritzsch, M. Gell-Mann, and H. Leutwyler. Advantages of the Color Octet Gluon Picture. *Phys. Lett.*, B47:365–368, 1973.

[17] D. Gross and F. Wilczek. Ultraviolet Behavior of Non-Abelian Gauge Theories. *Phys. Rev. Lett.*, 30:1343–1346, 1973.

[18] H. Politzer. Reliable Perturbative Results for Strong Interactions? *Phys. Rev. Lett.*, 30:1346–1349, 1973.

[19] J. Aubert et al. Experimental Observation of a Heavy Particle J. *Phys. Rev. Lett.*, 33:1404–1406, 1974.

[20] J. Augustin et al. Discovery of a Narrow Resonance in e^+e^--Annihilation. *Phys. Rev. Lett.*, 33:1406–1408, 1974. [Adv. Exp. Phys.5,141(1976)].

[21] K. Olive et al. Review of Particle Physics. *Chin. Phys.*, C38:090001, 2014.

[22] R. Ellis, W. Stirling, and B. Webber. QCD and collider physics. *Camb. Monogr. Part. Phys. Nucl. Phys. Cosmol.*, 8:1–435, 1996.

[23] T. Matsui and H. Satz. J/ψ suppression by quark-gluon plasma formation. *Phys.Lett.B*, 178:416–422, 1986.

[24] I. Pomeranchuk. On the theory of multiple particle production in a single collision. *Dokl. Akad. Nauk Ser. Fiz.*, 78:889–891, 1951.

[25] R. Hagedorn. Statistical thermodynamics of strong interactions at high-energies. *Nuovo Cim. Suppl.*, 3:147–186, 1965.

[26] R. Hagedorn. Hadronic matter near the boiling point. *Nuovo Cim.*, A56:1027–1057, 1968.

[27] N. Cabibbo and G. Parisi. Exponential hadronic spectrum and quark liberation. *Phys.Lett.B*, 59(1):67 – 69, 1975.

[28] A. Chodos, R. Jaffe, K. Johnson, Charles B. Thorn, and V. Weisskopf. A New Extended Model of Hadrons. *Phys. Rev.*, D9:3471–3495, 1974.

[29] J. C. Collins and M. J. Perry. Superdense Matter: Neutrons or Asymptotically Free Quarks? *Phys. Rev. Lett.*, 34:1353–1356, 1975.

[30] D. Rischke. The Quark gluon plasma in equilibrium. *Prog. Part. Nucl. Phys.*, 52:197–296, 2004.

[31] V. Koch. Aspects of chiral symmetry. *Int. J. Mod. Phys.*, E6:203–250, 1997.

[32] S. Borsanyi et al. Full result for the QCD equation of state with flavors. *Phys. Lett. B*, 730:99 – 104, 2014.

[33] A. Bazavov et al. Equation of state in $(2 + 1)$-flavor QCD. *Phys. Rev. D*, 90:094503, 2014.

[34] K. Fukushima and T. Hatsuda. The phase diagram of dense QCD. *Rept. Prog. Phys.*, 74:014001, 2011.

[35] H.-T. Ding, F. Karsch, and S. Mukherjee. Thermodynamics of strong-interaction matter from Lattice QCD. *Int. J. Mod. Phys.*, E24(10):1530007, 2015.

[36] K. Wilson. Confinement of Quarks. *Phys. Rev.*, D10:2445–2459, 1974.

[37] E. Shuryak. Theory of Hadronic Plasma. *Sov. Phys. JETP*, 47:212–219, 1978. [Zh. Eksp. Teor. Fiz.74,408(1978)].

[38] E. Shuryak. Quark-Gluon Plasma and Hadronic Production of Leptons, Photons and Psions. *Phys. Lett.*, B78:150, 1978. [Yad. Fiz.28,796(1978)].

[39] P. Braun-Munzinger and J. Wambach. The Phase Diagram of Strongly-Interacting Matter. *Rev. Mod. Phys.*, 81:1031–1050, 2009.

[40] E. Fermi. High Energy Nuclear Events. *Progress of Theoretical Physics*, 5(4):570–583, 1950.

[41] E. Feinberg. Multiple production of hadrons at cosmic ray energies (experimental results and theoretical concepts). *Physics Reports*, 5(5):237 – 350, 1972.

[42] E. Shuryak. Quantum Chromodynamics and the Theory of Superdense Matter. *Phys. Rept.*, 61:71–158, 1980.

[43] J. D. Bjorken. Highly Relativistic Nucleus-Nucleus Collisions: The Central Rapidity Region. *Phys. Rev.*, D27:140–151, 1983.

[44] C. Gale, S. Jeon, B. Schenke, P. Tribedy, and R. Venugopalan. Event-by-event anisotropic flow in heavy-ion collisions from combined Yang-Mills and viscous fluid dynamics. *Phys. Rev. Lett.*, 110(1):012302, 2013.

[45] P. Braun-Munzinger, V. Koch, T. Schäfer, and J. Stachel. Properties of hot and dense matter from relativistic heavy ion collisions. 2015. arXiv:1510.00442.

[46] P. Braun-Munzinger and J. Stachel. The quest for the quark-gluon plasma. *Nature*, 448:302–309, 2007.

[47] C. Shen, U. Heinz, J. Paquet, and C. Gale. Thermal photons as a quark-gluon plasma thermometer reexamined. *Phys. Rev.*, C89(4):044910, 2014.

[48] C. Gale, S. Jeon, and B. Schenke. Hydrodynamic Modeling of Heavy-Ion Collisions. *Int. J. Mod. Phys.*, A28:1340011, 2013.

[49] M. Lisa, S. Pratt, R. Soltz, and U. Wiedemann. Femtoscopy in relativistic heavy ion collisions. *Ann. Rev. Nucl. Part. Sci.*, 55:357–402, 2005.

[50] K. Aamodt et al. (ALICE Collaboration). Two-pion Bose–Einstein correlations in central Pb–Pb collisions at $\sqrt{s_{\rm NN}}$ =2.76 TeV. *Phys. Lett. B*, 696(4):328 – 337, 2011.

[51] P. Braun-Munzinger, A. Kalweit, K. Redlich, and J. Stachel. Confronting fluctuations of conserved charges in central nuclear collisions at the LHC with predictions from Lattice QCD. *Phys. Lett.*, B747:292–298, 2015.

[52] P. Braun-Munzinger, K. Redlich, and J. Stachel. Particle production in heavy-ion collisions. *Hwa, R.C. (ed.) et al.: Quark gluon plasma 491-599*, 2003.

[53] P. Braun-Munzinger, J. Stachel, and C. Wetterich. Chemical freezeout and the QCD phase transition temperature. *Phys. Lett.*, B596:61–69, 2004.

[54] C. Blume. Is there Life after Hadronization? An Experimental Overview. *Acta Phys. Polon.*, B43:577–586, 2012.

[55] J. Adam et al. (ALICE Collaboration). Production of light nuclei and anti-nuclei in pp and Pb-Pb collisions at LHC energies. 2015. arXiv:1506.08951.

[56] R. Lea for the ALICE Collaboration. (Anti-)deuteron production and anisotropic flow measured with ALICE at the LHC. *Presentation at the Quark Matter conference 2015*, 2015.

[57] P. Huovinen and H. Petersen. Particlization in hybrid models. *Eur. Phys. J.*, A48:171, 2012.

[58] M. Strickland. Anisotropic Hydrodynamics: Three lectures. *Acta Phys. Polon.*, B45(12):2355–2394, 2014.

[59] J. Berges, K. Boguslavski, S. Schlichting, and R. Venugopalan. Turbulent thermalization process in heavy-ion collisions at ultrarelativistic energies. *Phys. Rev.*, D89(7):074011, 2014.

[60] A. Kurkela. Initial state of Heavy-Ion Collisions: Isotropization and thermalization. In *25th International Conference on Ultra-Relativistic Nucleus-Nucleus Collisions (Quark Matter 2015) Kobe, Japan, 2015*, 2016.

[61] V. Khachatryan (CMS Collaboration). Observation of Long-Range Near-Side Angular Correlations in Proton-Proton Collisions at the LHC. *JHEP*, 09:091, 2010.

[62] B. Abelev (ALICE Collaboration). Long-range angular correlations on the near and away side in p–Pb collisions at $\sqrt{s_{NN}} = 5.02$ TeV. *Phys. Lett.*, B719:29–41, 2013.

[63] G. Aad (ATLAS Collaboration). Observation of Associated Near-Side and Away-Side Long-Range Correlations in $\sqrt{s_{\rm NN}}$=5.02TeV Proton-Lead Collisions with the ATLAS Detector. *Phys. Rev. Lett.*, 110(18):182302, 2013.

[64] S. Chatrchyan (CMS Collaboration). Observation of long-range near-side angular correlations in proton-lead collisions at the LHC. *Phys. Lett.*, B718:795–814, 2013.

[65] P. Bozek and W. Broniowski. Correlations from hydrodynamic flow in p–Pb collisions. *Phys. Lett.*, B718:1557–1561, 2013.

[66] B. Schenke and R. Venugopalan. Eccentric protons? Sensitivity of flow to system size and shape in p+p, p+Pb and Pb+Pb collisions. *Phys. Rev. Lett.*, 113:102301, 2014.

[67] H. Niemi and G. Denicol. How large is the Knudsen number reached in fluid dynamical simulations of ultrarelativistic heavy ion collisions? 2014. arXiv:1404.7327.

[68] J. Bjorken. Energy loss of Energetic Partons in Quark-Gluon Plasma: Possible Extinction of High $p_{\rm T}$ Jets in Hadron-Hadron Collisions. *unpublished*, 1982.

[69] A. Drees. First hints of jet quenching at RHIC. *Nucl. Phys.*, A698:331–340, 2002.

[70] G.-Y. Qin and X.-N. Wang. Jet quenching in high-energy heavy-ion collisions. *Int. Journal of Modern Physics E*, 24(11):1530014, 2015.

[71] A. Adare et al. (PHENIX Collaboration). Enhanced production of direct photons in Au+Au collisions at $\sqrt{s_{NN}}$ = 200 GeV and implications for the initial temperature. *Phys. Rev. Lett.*, 104:132301, 2010.

[72] A. Adare et al. (PHENIX Collaboration). Centrality dependence of low-momentum direct-photon production in Au+Au collisions at $\sqrt{s_{_{NN}}}$ = 200 GeV. *Phys. Rev.*, C91(6):064904, 2015.

[73] J. Adam et al. (ALICE Collaboration). Direct photon production in Pb–Pb collisions at $\sqrt{s_{\rm NN}}$=2.76 TeV. *Phys. Lett. B*, 754:235 – 248, 2016.

[74] A. Adare et al. (PHENIX Collaboration). Azimuthally anisotropic emission of low-momentum direct photons in Au+Au collisions at $\sqrt{s_{\rm NN}}$ = 200 GeV. 2015. arXiv:1509.07758.

[75] D. Lohner for the ALICE collaboration. Measurement of Direct-Photon Elliptic Flow in Pb-Pb Collisions at $\sqrt{s_{NN}}$ = 2.76 TeV. *J. Phys. Conf. Ser.*, 446:012028, 2013.

[76] G. Agakichiev et al. (CERES Collaboration). e^+e^- pair production in Pb–Au collisions at 158-GeV per nucleon. *Eur. Phys. J.*, C41:475–513, 2005.

[77] R. Arnaldi et al. (NA60 Collaboration). First Measurement of the ρ Spectral Function in High-Energy Nuclear Collisions. *Phys. Rev. Lett.*, 96:162302, 2006.

[78] D. Adamova et al. (CERES Collaboration). Modification of the ρ-meson detected by low-mass electron-positron pairs in central Pb–Au collisions at 158-A-GeV/c. *Phys. Lett.*, B666:425–429, 2008.

[79] R. Rapp, J. Wambach, and H. van Hees. The Chiral Restoration Transition of QCD and Low Mass Dileptons. *Landolt-Bornstein*, 23:134, 2010.

[80] L. Adamczyk et al. (STAR Collaboration). Dielectron Mass Spectra from Au+Au Collisions at $\sqrt{s_{\rm NN}}$=200 GeV. *Phys. Rev. Lett.*, 113(2):022301, 2014. [Addendum: Phys. Rev. Lett.113,no.4,049903(2014)].

[81] A. Adare et al. (PHENIX Collaboration). Dielectron production in Au+Au collisions at $\sqrt{s_{NN}}$=200 GeV. *Phys. Rev.*, C93(1):014904, 2016.

[82] T. Appelquist and H. Politzer. Orthocharmonium and e^+e^-Annihilation. *Phys. Rev. Lett.*, 34:43, 1975.

[83] A. De Rújula and S. Glashow. Is Bound Charm Found? *Phys. Rev. Lett.*, 34:46–49, 1975.

[84] G. Abrams et al. The Discovery of a Second Narrow Resonance in e^+e^-Annihilation. *Phys. Rev. Lett.*, 33:1453–1455, 1974. [Adv. Exp. Phys.5,150(1976)].

[85] E. Eichten, K. Gottfried, T. Kinoshita, J. B. Kogut, K. D. Lane, and T.-M. Yan. The Spectrum of Charmonium. *Phys. Rev. Lett.*, 34:369–372, 1975. [Erratum: Phys. Rev. Lett.36,1276(1976)].

[86] L. Kluberg and H. Satz. Color Deconfinement and Charmonium Production in Nuclear Collisions. 2009. arXiv:hep-ph/0901.3831.

[87] G. Bali. QCD forces and heavy quark bound states. *Phys. Rept.*, 343:1–136, 2001.

[88] F. Abe et al. (CDF Collaboration). Measurement of the average lifetime of B hadrons produced in $p\overline{p}$ collisions at $\sqrt{s} = 1.8$ TeV. *Phys. Rev. Lett.*, 71:3421–3426, 1993.

[89] R. Jesik et al. (E672 and E706 Collaborations). Bottom Production in π^-–Be Collisions at 515 GeV/c. *Phys. Rev. Lett.*, 74:495–498, 1995.

[90] D. Jansen et al. Measurement of the Bottom-Quark Production Cross Section in 800 GeV/c Proton–Gold Collisions. *Phys. Rev. Lett.*, 74:3118–3121, 1995.

[91] F. Abe et al. (CDF Collaboration). J/ψ and ψ(2S) production in $p\overline{p}$ collisions at $\sqrt{s} = 1.8$ TeV. *Phys. Rev. Lett.*, 79:572–577, 1997.

[92] C. Albajar et al. (UA1 Collaboration). High transverse momentum J/ψ production at the CERN proton-antiproton collider. *Physics Letters B*, 200(3):380 – 390, 1988.

[93] C. Albajar et al. (UA1 Collaboration). J/ψ and ψ' production at the CERN $p\overline{p}$ collider. *Phys.Lett.*, B256:112–120, 1991.

[94] F. Abe et al. (CDF Collaboration). Inclusive J/ψ, $\psi(2S)$, and b-quark production in $p\overline{p}$ collisions at $\sqrt{s} = 1.8$ TeV. *Phys. Rev. Lett.*, 69:3704–3708, 1992.

[95] S. Abachi et al. (DØ Collaboration). J/ψ production in $p\overline{p}$ collisions at $\sqrt{s} =$ 1.8 TeV. *Phys. Lett. B*, 370(1–2):239 – 248, 1996.

[96] G. Aad et al. (ATLAS Collaboration). Measurement of the differential cross-sections of inclusive, prompt and non-prompt J/ψ production in proton-proton collisions at $\sqrt{s} = 7$ TeV. *Nucl. Phys.*, B850:387–444, 2011.

[97] G. Aad et al. (ATLAS Collaboration). Measurement of the differential cross-sections of inclusive, prompt and non-prompt J/ψ production in proton-proton collisions at $\sqrt{s} = 7$ TeV. *Nucl. Phys.*, B850:387–444, 2011.

[98] G. Aad et al. (ATLAS Collaboration). Measurement of the differential cross-sections of prompt and non-prompt production of J/ψ and J/ψ in pp collisions at $\sqrt{s} = 7$ and 8 TeV with the ATLAS detector. 2015. arXiv:1512.03657.

[99] B. Abelev et al. (ALICE Collaboration). Measurement of prompt J/ψ and beauty hadron production production cross sections at mid-rapidity in pp collisions $\sqrt{s} = 7$ TeV. *JHEP*, 1211:065, 2012.

[100] V. Khachatryan et al. (CMS Collaboration). Prompt and non-prompt J/ψ production in pp collisions at $\sqrt{s} = 7$ TeV. *Eur. Phys. J.*, C71:1575, 2011.

[101] S. Chatrchyan et al. (CMS Collaboration). J/ψ and ψ_{2S} production in *pp* collisions at $\sqrt{s} = 7$ TeV. *JHEP*, 02:011, 2012.

[102] V. Khachatryan et al. (CMS Collaboration). Measurement of J/ψ and ψ(2S) prompt double-differential cross sections in pp collisions at $\sqrt{s}$=7 TeV. *Phys. Rev. Lett.*, 114(19):191802, 2015.

[103] R. Aaij et al. (LHCb Collaboration). Measurement of J/ψ production in pp collisions at $\sqrt{s} = 2.76$ TeV. *JHEP*, 02:041, 2013.

[104] R. Aaij et al. (LHC Collaboration). Measurement of J/ψ production in pp collisions at $\sqrt{s} = 7$ TeV. *Eur. Phys. J.*, C71:1645, 2011.

[105] R. Aaij et al. (LHCb Collaboration). Production of J/ψ and Υ mesons in pp collisions at $\sqrt{s}$= 8 TeV. *JHEP*, 06:064, 2013.

[106] R. Aaij et al. (LHCb Collaboration). Measurement of forward J/ψ production cross-sections in pp collisions at $\sqrt{s} = 13$ TeV. *JHEP*, 10:172, 2015.

[107] D. Acosta et al. (CDF Collaboration). Measurement of the J/ψ meson and *b*-hadron production cross sections in $p\overline{p}$ collisions at $\sqrt{s} = 1960$ GeV. *Phys. Rev. D*, 71:032001, 2005.

[108] F. Abe et al. (CDF Collaboration). Production of J/ψ mesons from χ_c meson decays in $p\overline{p}$ collisions at $\sqrt{s} = 1.8$ TeV. *Phys. Rev. Lett.*, 79:578–583, 1997.

[109] R. Aaij et al. (LHCb Collaboration). Measurement of the ratio of prompt χ_c to J/ψ production in pp collisions at $\sqrt{s} = 7$ TeV. *Phys. Lett.*, B718:431–440, 2013.

[110] T. Aaltonen et al. (CDF Collaboration). ψ(2S) mesons in $p\overline{p}$ collisions at 1.96 TeV. *Phys. Rev. D*, 80:031103, 2009.

[111] R. Aaij et al. (LHCb Collaboration). Measurement of ψ(2S) meson production in pp collisions at $\sqrt{s}$=7 TeV. *Eur. Phys. J.*, C72:2100, 2012.

[112] B. Abelev et al. (ALICE Collaboration). Measurement of quarkonium production at forward rapidity in pp collisions at $\sqrt{s} = 7$ TeV. *Eur. Phys. J.*, C74(8):2974, 2014.

[113] R. Ball et al. Parton distributions with LHC data. *Nuclear Physics B*, 867(2):244 – 289, 2013.

[114] F. Gelis, E. Iancu, J. Jalilian-Marian, and R. Venugopalan. The Color Glass Condensate. *Ann. Rev. Nucl. Part. Sci.*, 60:463–489, 2010.

[115] G. Bodwin. Theory of Charmonium Production. In *Proceedings, 5th International Workshop on Charm Physics (Charm 2012)*, 2012.

[116] G. Bodwin, E. Braaten, and G. Lepage. Rigorous QCD analysis of inclusive annihilation and production of heavy quarkonium. *Phys. Rev.*, D51:1125–1171, 1995. [Erratum: Phys. Rev.D55,5853(1997)].

[117] G. Nayak. Proof of NRQCD Factorization at All Order in Coupling Constant in Heavy Quarkonium Production. 2015. arXiv:1506.02593.

[118] A. Andronic et al. Heavy-flavour and quarkonium production in the LHC era: from proton–proton to heavy-ion collisions. 2015. arXiv:1506.03981.

[119] Y.-Q. Ma and R. Venugopalan. Comprehensive Description of J/ψ Production in Proton-Proton Collisions at Collider Energies. *Phys. Rev. Lett.*, 113(19):192301, 2014.

[120] P. Sun, C.-P. Yuan, and F. Yuan. Heavy Quarkonium Production at Low p_{T} in NRQCD with Soft Gluon Resummation. *Phys. Rev.*, D88:054008, 2013.

[121] P. Arnold. Quark-Gluon Plasmas and Thermalization. *Int. J. Mod. Phys.*, E16:2555–2594, 2007.

[122] A. Mocsy, P. Petreczky, and M. Strickland. Quarkonia in the Quark Gluon Plasma. *Int. J. Mod. Phys.*, A28:1340012, 2013.

[123] Y. Burnier, O. Kaczmarek, and A. Rothkopf. Quarkonium at finite temperature: Towards realistic phenomenology from first principles. *JHEP*, 12:101, 2015.

[124] A. Rothkopf. A first look at Bottomonium melting via a stochastic potential. *JHEP*, 04:085, 2014.

[125] P. Braun-Munzinger and K. Redlich. Charmonium production from the secondary collisions at LHC energy. *Eur. Phys. J.*, C16:519–525, 2000.

[126] J. Uphoff, O. Fochler, Z. Xu, and C. Greiner. Heavy-quark production in ultrarelativistic heavy-ion collisions within a partonic transport model. *Phys. Rev. C*, 82:044906, 2010.

[127] A. Andronic, P. Braun-Munzinger, K. Redlich, and J. Stachel. Statistical hadronization of heavy quarks in ultra-relativistic nucleus–nucleus collisions. *Nucl.Phys.A*, 789:334–356, 2007.

[128] R. Aaij et al. (LHCb Collaboration). Prompt charm production in pp collisions at $\sqrt{s} = 7$ TeV. *Nucl. Phys.*, B871:1–20, 2013.

[129] M. Miller, K. Reygers, S. Sanders, and P. Steinberg. Glauber modeling in high energy nuclear collisions. *Ann. Rev. Nucl. Part. Sci.*, 57:205–243, 2007.

[130] F. Karsch and H. Satz. The Spectral analysis of strongly interacting matter. *Z. Phys.*, C51:209–224, 1991.

[131] X. Du and R. Rapp. Sequential regeneration of charmonia in heavy-ion collisions. *Nucl. Phys.*, A943:147–158, 2015.

[132] S. Brodsky and A. Mueller. Using nuclei to probe hadronization in QCD. *Phys. Lett. B*, 206(4):685 – 690, 1988.

[133] B. Kopeliovich and B. Zakharov. Quantum effects and color transparency in charmonium photoproduction on nuclei. *Phys. Rev.*, D44:3466–3472, 1991.

[134] D. Kharzeev and R. Thews. Quarkonium formation time in a model independent approach. *Phys. Rev.*, C60:041901, 1999.

[135] T. Song, C. M. Ko, and S. H. Lee. Quarkonium formation time in relativistic heavy-ion collisions. *Phys. Rev.*, C91(4):044909, 2015.

[136] F. Arleo and S. Peigné. Heavy-quarkonium suppression in p–A collisions from parton energy loss in cold QCD matter. *JHEP*, 03:122, 2013.

[137] R. Baier, Y. Dokshitzer, A. Mueller, S. Peigné, and D. Schiff. Radiative energy loss and p_{T}-broadening of high-energy partons in nuclei. *Nucl. Phys.*, B484:265–282, 1997.

[138] K. Burke et al. Extracting the jet transport coefficient from jet quenching in high-energy heavy-ion collisions. *Phys. Rev.*, C90(1):014909, 2014.

[139] P. Braun-Munzinger and J. Stachel. (Non)thermal aspects of charmonium production and a new look at J/ψ suppression. *Phys.Lett.B*, 490:196–202, 2000.

[140] R. Thews, M. Schroedter, and J. Rafelski. Enhanced J/ψ production in deconfined quark matter. *Phys.Rev.C*, 63:054905, 2001.

[141] A. Andronic, P. Braun-Munzinger, K. Redlich, and J. Stachel. Evidence for charmonium generation at the phase boundary in ultra-relativistic nuclear collisions. *Phys.Lett.B*, 652:259–261, 2007.

[142] A. Andronic, P. Braun-Munzinger, K. Redlich, and J. Stachel. The thermal model on the verge of the ultimate test: particle production in Pb–Pb collisions at the LHC. *J. Phys.*, G38:124081, 2011.

[143] Y. Liu, Z. Qu, N. Xu, and P. Zhuang. J/ψ transverse momentum distribution in high energy nuclear collisions. *Phys. Lett.*, B678:72–76, 2009.

[144] K. Zhou, N. Xu, Z. Xu, and P. Zhuang. Medium effects on charmonium production at ultrarelativistic energies available at the CERN Large Hadron Collider. *Phys. Rev.*, C89(5):054911, 2014.

[145] X. Zhao and R. Rapp. Charmonium in Medium: From Correlators to Experiment. *Phys. Rev.*, C82:064905, 2010.

[146] X. Zhao and R. Rapp. Medium Modifications and Production of Charmonia at LHC. *Nucl.Phys.A*, 859:114–125, 2011.

[147] E. Ferreiro. Charmonium dissociation and recombination at LHC: Revisiting comovers. *Phys. Lett.*, B731:57–63, 2014.

[148] J. Uphoff, O. Fochler, Z. Xu, and C. Greiner. Open heavy flavor and J/ψ at RHIC and LHC. *Nucl. Phys.*, A910-911:401–404, 2013.

[149] V. Kumar, P. Shukla, and R. Vogt. Quarkonia suppression in PbPb collisions at $\sqrt{s_{NN}} = 2.76$ TeV. *Phys. Rev.*, C92(2):024908, 2015.

[150] A. Andronic. Experimental results and phenomenology of quarkonium production in relativistic nuclear collisions. *Nucl. Phys.*, A931:135–144, 2014.

[151] K. Aamodt et al. (ALICE Collaboration). Rapidity and transverse momentum dependence of inclusive J/ψ production in pp collisions at $\sqrt{s} = 7$ TeV. *Phys.Lett.B*, 704:442–455, 2011.

[152] X.-L. Zhu, P. Zhuang, and N. Xu. J/ψ transport in QGP and $p_{\rm T}$ distribution at SPS and RHIC. *Phys.Lett.B*, 607:107–114, 2005.

[153] L. Yan, P. Zhuang, and N. Xu. Competition between J/ψ suppression and regeneration in quark-gluon plasma. *Phys.Rev.Lett.*, 97:232301, 2006.

[154] B. Alessandro et al. (NA50 Collaboration). A New measurement of J/ψ suppression in Pb–Pb collisions at 158-GeV per nucleon. *Eur. Phys. J.*, C39:335–345, 2005.

[155] R. Arnaldi et al. (NA60 Collaboration). J/ψ production in Indium–Indium collisions at 158-GeV/nucleon. *Phys. Rev. Lett.*, 99:132302, 2007.

[156] B. Kopeliovich, I. Potashnikova, H. Pirner, and I. Schmidt. Heavy quarkonium production: Nontrivial transition from pA to AA collisions. *Phys. Rev.*, C83:014912, 2011.

[157] B. Kopeliovich, I. Potashnikova, and I. Schmidt. J/ψ production off nuclei: a detour from SPS to LHC. *EPJ Web Conf.*, 70:00067, 2014.

[158] A. Capella and E. Ferreiro. J/ψ suppression and the decrease of nuclear absorption with increasing energy. *Phys. Rev.*, C76:064906, 2007.

[159] K. Tywoniuk, I. Arsene, L. V. Bravina, A. B. Kaidalov, and E. E. Zabrodin. Nuclear suppression at RHIC and LHC in Glauber-Gribov approach. *J. Phys.*, G35:044039, 2008.

[160] N. Armesto. Nuclear shadowing. *J. Phys.*, G32:R367–R394, 2006.

[161] D. de Florian and R. Sassot. Nuclear parton distributions at next-to-leading order. *Phys.Rev.D*, 69:074028, 2004.

[162] M. Hirai, S. Kumano, and T.-H. Nagai. Determination of nuclear parton distribution functions and their uncertainties in next-to-leading order. *Phys. Rev.*, C76:065207, 2007.

[163] K. J. Eskola, H. Paukkunen, and C. Salgado. EPS09: A New generation of NLO and LO nuclear parton distribution functions. *JHEP*, 04:065, 2009.

[164] D. de Florian, R. Sassot, P. Zurita, and M. Stratmann. Global analysis of nuclear parton distributions. *Phys. Rev.*, D85:074028, 2012.

[165] K. Kovarik, T. Jezo, A. Kusina, F.I. Olness, I. Schienbein, et al. CTEQ nuclear parton distribution functions. *PoS*, DIS2013, 2013.

[166] K. Kovarik et al. nCTEQ15 - Global analysis of nuclear parton distributions with uncertainties in the CTEQ framework. 2015. arXiv:1509.00792.

[167] B. Kopeliovich. Puzzles of J/ψ production off nuclei. *Nucl.Phys.A*, 854(1):187 – 197, 2011.

[168] A. Baltz. The physics of ultraperipheral collisions at the LHC. *Phys. Rept.*, 458:1–171, 2008.

[169] E. Abbas et al. (ALICE Collaboration). Charmonium and e^+e^- pair photoproduction at mid-rapidity in ultra-peripheral Pb–Pb collisions at $\sqrt{s_{\rm NN}}$=2.76 TeV. *Eur. Phys. J.*, C73(11):2617, 2013.

[170] J. Nystrand. Photonuclear vector meson production in ultra-peripheral Pb–Pb collisions studied by the ALICE experiment at the LHC. 2013. [PoSConfinementX,199(2012)].

[171] H. Fujii, F. Gelis, and R. Venugopalan. Quark pair production in high energy pA collisions: General features. *Nucl. Phys.*, A780:146–174, 2006.

[172] B. Kopeliovich, I. Potashnikova, and I. Schmidt. Nuclear suppression of J/ψ: from RHIC to the LHC. *Nucl. Phys.*, A864:203–212, 2011.

[173] R. Sharma and I. Vitev. High transverse momentum quarkonium production and dissociation in heavy ion collisions. *Phys. Rev.*, C87(4):044905, 2013.

[174] F. Arleo, R. Kolevatov, S. Peigné, and M. Rustamova. Centrality and $p_{\rm T}$ dependence of J/ψ suppression in proton–nucleus collisions from parton energy loss. *JHEP*, 05:155, 2013.

[175] B. Ducloué, T. Lappi, and H. Mäntysaari. Forward J/ψ production in proton–nucleus collisions at high energy. *Phys. Rev. D*, 91:114005, 2015.

[176] D. Antreasyan, J. Cronin, H. Frisch, M. Shochet, L. Kluberg, P. Piroué, and R. Sumner. Production of hadrons at large transverse momentum in 200-, 300-, and 400-GeV pp and p–nucleus collisions. *Phys.Rev.D*, 19:764–778, 1979.

[177] A. Accardi. Cronin effect in proton nucleus collisions: A Survey of theoretical models. 2002. arXiv:hep-ph/0212148.

[178] J. Hüfner, Y. Kurihara, and H. Pirner. Gluon multiple scattering and the transverse momentum dependence of J/ψ production in nucleus–nucleus collisions. *Phys.Lett.B*, 215(2):218 – 222, 1988.

[179] B. Kopeliovich, I. Potashnikova, and I. Schmidt. J/ψ production in nuclear collisions: Theoretical approach to measuring the transport coefficient. *Phys. Rev.*, C82:024901, 2010.

[180] B. Kopeliovich, J. Nemchik, A. Schäfer, and A. Tarasov. Cronin effect in hadron production off nuclei. *Phys.Rev.Lett.*, 88:232303, 2002.

[181] B. Abelev et al. (ALICE Collaboration). Transverse momentum distribution and nuclear modification factor of charged particles in p–Pb collisions at $\sqrt{s_{\rm NN}} = 5.02$ TeV. *Phys. Rev. Lett.*, 110(8):082302, 2013.

[182] Z.-B. Kang and J.-W. Qiu. Nuclear modification of vector boson production in proton–lead collisions at the LHC. *Phys. Lett.*, B721:277–283, 2013.

[183] J. Adam et al. (ALICE Collaboration). Centrality dependence of inclusive J/ψ production in p–Pb collisions at $\sqrt{s_{\rm NN}} = 5.02$ TeV. *JHEP*, 11:127, 2015.

[184] J. Jalilian-Marian, Y. Nara, and R. Venugopalan. The Cronin effect, quantum evolution and the color glass condensate. *Phys.Lett.B*, 577:54–60, 2003.

[185] J. Adam et al. (ALICE Collaboration). Multiplicity dependence of pion, kaon and proton production at large transverse momentum in p–Pb collisions at $\sqrt{s_{\rm NN}} = 5.02$ TeV. *in preparation*, 2015.

[186] C. Bierlich, G. Gustafson, L. Lönnblad, and A. Tarasov. Effects of Overlapping Strings in pp Collisions. *JHEP*, 03:148, 2015.

[187] K. Aamodt et al. (ALICE Collaboration). Centrality Dependence of the Charged-Particle Multiplicity Density at Midrapidity in Pb–Pb Collisions at $\sqrt{s_{\rm NN}} = 2.76$ TeV. *Phys. Rev. Lett.*, 106:032301, 2011.

[188] E. Pereira de Oliveira Filho for the ALICE Collaboration. Measurements of electrons from heavy-flavour hadron decays in pp, p–Pb and Pb–Pb collisions with ALICE at the LHC. *Nuclear Physics A*, 932:258 – 263, 2014.

[189] Y. Liu, C. Ko, and T. Song. Hot medium effects on J/ψ production in p+Pb collisions at $\sqrt{s_{\rm NN}} = 5.02$ TeV. *Phys. Lett.*, B728:437–442, 2014.

[190] E. Ferreiro. Excited charmonium suppression in proton–nucleus collisions as a consequence of comovers. *Phys. Lett.*, B749:98–103, 2015.

[191] B. Abelev et al. (ALICE Collaboration). Suppression of ψ(2S) production in p–Pb collisions at $\sqrt{s_{\rm NN}}$=5.02 TeV. *JHEP*, 12:073, 2014.

[192] R. Arnaldi for the ALICE Collaboration. Inclusive ψ(2S) production in p-Pb collisions with ALICE. *Nucl. Phys.*, A931:628–632, 2014.

[193] R. Aaij et al. (LHCb Collaboration). Study of $\psi(2S)$ production and cold nuclear matter effects in pPb collisions at $\sqrt{s_{\rm NN}} = 5$ TeV. 2016. arXiv:1601.07878.

[194] L. Evans and P. Bryant. LHC Machine. *JINST*, 3:S08001, 2008.

[195] G. Aad et al. (ATLAS Collaboration). The ATLAS Experiment at the CERN Large Hadron Collider. *JINST*, 3:S08003, 2008.

[196] S. Chatrchyan et al. (CMS Collaboration). The CMS experiment at the CERN LHC. *JINST*, 3:S08004, 2008.

[197] A. Alves et al. (LHCb Collaboration). The LHCb Detector at the LHC. *JINST*, 3:S08005, 2008.

[198] K. Aamodt et al. (ALICE Collaboration). The ALICE experiment at the CERN LHC. *JINST*, 3:S08002, 2008.

[199] F. Marcastel. CERN's Accelerator Complex. La chaîne des accélérateurs du CERN. 2013. https://cds.cern.ch/record/1621583.

[200] B. Abelev et al. (ALICE Collaboration). J/ψ production and nuclear effects in p–Pb collisions at $\sqrt{s_{\rm NN}}$=5.02 TeV. *JHEP*, 02:073, 2014.

[201] J. Adam et al. (ALICE Collaboration). Rapidity and transverse-momentum dependence of the inclusive J/ψ nuclear modification factor in p–Pb collisions at $\sqrt{s_{\rm NN}}$ =5.02 TeV. *JHEP*, 06:055, 2015.

[202] R. Aaij et al. (LHCb Collaboration). Study of J/ψ production and cold nuclear matter effects in *pPb* collisions at $\sqrt{s_{\rm NN}} = 5$ TeV. *JHEP*, 02:072, 2014.

[203] G. Aad et al. (ATLAS Collaboration). Measurement of differential J/ψ production cross sections and forward-backward ratios in p+Pb collisions with the ATLAS detector. *Phys. Rev.*, C92(3):034904, 2015.

[204] V. Khachatryan et al. (CMS Collaboration). J/ψ production in pPb collisions. Technical Report CMS-PAS-HIN-14-009, CERN, Geneva, 2015.

[205] R. Aaij et al. (LHCb Collaboration). Measurement of the $\eta_c(1S)$ production cross-section in proton-proton collisions via the decay $\eta_c(1S) \to {\rm p}\overline{\rm p}$. *Eur. Phys. J.*, C75(7):311, 2015.

[206] B. Abelev et al. (ALICE Collaboration). Performance of the ALICE Experiment at the CERN LHC. *Int. J. Mod. Phys.*, A29:1430044, 2014.

[207] T. Kollegger for the ALICE Collaboration. The ALICE high level trigger: The 2011 run experience. In *Proceedings, 18th Real-Time Conference (RT2012)*, 2012.

[208] L. Betev et al. (ALICE Collaboration). Definition of the ALICE coordinate system and basic rules for sub-detector components numbering. *ALICE-INT-2003-028*, 2003.

[209] J. Wiechula. *Commissioning and Calibration of the ALICE-TPC*. PhD thesis, Johann-Wolfgang Goethe Unversität, Frankfurt, 2008.

[210] D. Lange. The EvtGen particle decay simulation package. *Nucl. Instrum. Meth.*, A462:152–155, 2001.

[211] E. Barberio, B. van Eijk, and Z. Was. PHOTOS – a universal Monte Carlo for QED radiative corrections in decays. *Computer Physics Communications*, 66(1):115 – 128, 1991.

[212] E. Barberio and Z. Was. PHOTOS – a universal Monte Carlo for QED radiative corrections: version 2.0. *Computer Physics Communications*, 79(2):291 – 308, 1994.

[213] A. Kalweit. *Production of light flavor hadrons and anti-nuclei at the LHC*. PhD thesis, TU Darmstadt Fachbereich Physik, Darmstadt, 2012.

[214] J. Alme et al. (ALICE TPC Collaboration). The ALICE TPC, a large 3-dimensional tracking device with fast readout for ultra-high multiplicity events. *Nuclear Instruments and Methods in Physics Research Section A: Accelerators, Spectrometers, Detectors and Associated Equipment*, 622(1):316 – 367, 2010.

[215] A. Maire and C. Kuhn. *Production des baryons multi-étranges au LHC dans les collisions proton-proton avec l'expérience ALICE*. PhD thesis, Strasbourg U., 2011.

[216] J. Adam et al. (ALICE collaboration). The ALICE Transition Radiation Detector: construction, operation, and performance in LHC Run 1. *in preparation*, 2016.

[217] A. Akindinov et al. Performance of the ALICE Time-Of-Flight detector at the LHC. *Eur. Phys. J. Plus*, 128:44, 2013.

[218] E. Abbas et al. (ALICE Collaboration). Performance of the ALICE VZERO system. *JINST*, 8:P10016, 2013.

[219] Y. Belikov, M. Ivanov, K. Safarik, and J. Bracinik. TPC tracking and particle identification in high density environment. *eConf*, C0303241:TULT011, 2003.

[220] B. Abelev et al. (ALICE Collaboration). Inclusive J/ψ production in pp collisions at $\sqrt{s} = 2.76$ TeV. *Phys.Lett.B*, 718:295–306, 2012.

[221] B. Abelev et al. (ALICE Collaboration). J/ψ production as a function of charged particle multiplicity in pp collisions at $\sqrt{s} = 7$ TeV. *Phys.Lett.B*, 712(3):165 – 175, 2012.

[222] J. Adam et al. (ALICE Collaboration). Measurement of charm and beauty production at central rapidity versus charged-particle multiplicity in proton–proton collisions at $\sqrt{s} = 7$ TeV. *JHEP*, 09:148, 2015.

[223] C. Lippmann. Particle identification. *Nucl. Instrum. Meth.*, A666:148–172, 2012.

[224] J. Wansch. Analysis of J/ψ production with the ALICE TRD trigger. Bachelor thesis, 2015.

[225] S. Weber. *ALICE internal presentations and private commnunication.* PhD thesis, TU Darmstadt Fachbereich Physik, 2015.

[226] M. Gyulassy and X.-N. Wang. HIJING 1.0: A Monte Carlo program for parton and particle production in high-energy hadronic and nuclear collisions. *Comput. Phys. Commun.*, 83:307, 1994.

[227] T. Sjöstrand, Stephen M., and P. Skands. PYTHIA 6.4 Physics and Manual. *JHEP*, 05:026, 2006.

[228] G. Trombetta and G. Bruno. Private communication. 2015.

[229] R. Brun et al. CERN Program Library Long Write-up, W5013, GEANT Detector Description and Simulation Tool. 1994.

[230] S. Roesler, R. Engel, and J. Ranft. The Monte Carlo event generator DPMJET-III. *Proceedings, Conference, MC2000, Lisbon, Portugal, 2000*, pages 1033–1038, 2000.

[231] B. Abelev et al. (ALICE Collaboration). Centrality determination of Pb–Pb collisions at $\sqrt{s_{NN}}$=2.76 TeV with ALICE. *Phys. Rev.*, C88(4):044909, 2013.

[232] B. Abelev et al. (ALICE Collaboration). Pseudorapidity density of charged particles in p–Pb collisions at $\sqrt{s_{\rm NN}}$ = 5.02 TeV. *Phys. Rev. Lett.*, 110(3):032301, 2013.

[233] J. Adam et al. (ALICE Collaboration). Centrality dependence of particle production in p–Pb collisions at $\sqrt{s_{\rm NN}}$=5.02 TeV. *Phys. Rev.*, C91(6):064905, 2015.

[234] C. Oppedisano and A. Toia. Centrality resolution in p–A collisions. *Private communication, work in progress*, 2016.

[235] B. Abelev et al. (ALICE Collaboration). Measurement of visible cross sections in proton–lead collisions at $\sqrt{s_{\rm NN}}$= 5.02 TeV in van der Meer scans with the ALICE detector. *JINST*, 9(11):P11003, 2014.

[236] J. Blanco. *Study of* J/ψ *production dependence with the charged particle multiplicity in p–Pb collisions at* $\sqrt{s_{NN}} = 5.02$ *TeV and* pp *collisions at* $\sqrt{s} = 8$ *TeV with the ALICE experiment at the LHC*. PhD thesis, Matiere, Molecules, Materiaux en Pays de la Loire, 2015.

[237] J. Adam et al. (ALICE Collaboration). Multiplicity dependence of the inclusive J/ψ production in p–Pb collisions at $\sqrt{s_{\rm NN}}$ = 5.02 TeV. *in preparation*, 2016.

[238] B. Abelev et al. (ALICE Collaboration). Transverse momentum dependence of inclusive primary charged-particle production in p-Pb collisions at $\sqrt{s_{\rm NN}}$ = 5.02 TeV. *Eur. Phys. J.*, C74(9):3054, 2014.

[239] M. Knichel. *Transverse momentum distributions of primary charged particles in pp, p–Pb and Pb–Pb collisions measured with ALICE at the LHC*. PhD thesis, TU Darmstadt Fachbereich Physik, Darmstadt, 2015.

[240] J. Adam et al. (ALICE Collaboration). Measurement of electrons from heavy-flavour hadron decays in p–Pb collisions at $\sqrt{s_{\rm NN}}$ = 5.02 TeV. *accepted by PLB*, 2015.

[241] B. Hess, H. Schmidt, and W. Vogelsang. *Particle Identification in Jets and High-Multiplicity* pp *Events with the ALICE TPC*. PhD thesis, Tübingen U., 2015.

[242] J. Adam et al. (ALICE Collaboration). Inclusive, prompt and non-prompt J/ψ production at mid-rapidity in Pb–Pb collisions at $\sqrt{s_{\rm NN}}$=2.76 TeV. *JHEP*, 07:051, 2015.

[243] G. Aad et al. (ATLAS Collaboration). Measurement of the inclusive $W^{\pm}$ and Z/γ cross sections in the electron and muon decay channels in pp collisions at $\sqrt{s} = 7$ TeV with the ATLAS detector. *Phys. Rev.*, D85:072004, 2012.

[244] S. Chatrchyan et al. (CMS Collaboration). Measurement of the Υ(1S), Υ(2S), and Υ(3S) cross sections in pp collisions at $\sqrt{s} = 7$ TeV. *Phys. Lett.*, B727:101–125, 2013.

[245] G. Aad et al. (ATLAS Collaboration). Measurement of Υ production in 7 TeV pp collisions at ATLAS. *Phys. Rev.*, D87(5):052004, 2013.

[246] V. Khachatryan et al. (CMS Collaboration). Υ Production Cross-Section in pp Collisions at $\sqrt{s} = 7$ TeV. *Phys. Rev.*, D83:112004, 2011.

[247] S. Chatrchyan et al. (CMS Collaboration). Measurement of the $\Upsilon(1S)$, $\Upsilon(2S)$, and $\Upsilon(3S)$ Polarizations in *pp* Collisions at $\sqrt{s} = 7$ TeV. *Phys. Rev. Lett.*, 110:081802, 2013.

[248] S. Chatrchyan et al. (CMS Collaboration). Measurement of the prompt J/ψ and ψ(2S) polarizations in pp collisions at $\sqrt{s} = 7$ TeV. *Phys. Lett.*, B727:381–402, 2013.

[249] B. Abelev et al. (ALICE Collaboration). J/ψ polarization in pp collisions at $\sqrt{s} = 7$ TeV. *Phys. Rev. Lett.*, 108:082001, 2012.

[250] T. Affolder et al. (CDF Collaboration). Measurement of J/ψ and $\psi(2S)$ polarization in $\mathrm{p\overline{p}}$ collisions at $\sqrt{s} = 1.8$ TeV. *Phys. Rev. Lett.*, 85:2886–2891, 2000.

[251] A. Abulencia et al. (CDF Collaboration). Polarization of J/ψ and ψ_{2S} mesons produced in $\mathrm{p\overline{p}}$ collisions at $\sqrt{s} = 1.96$ TeV. *Phys. Rev. Lett.*, 99:132001, 2007.

[252] R. Aaij et al. (LHCb Collaboration). Measurement of J/ψ polarization in pp collisions at $\sqrt{s} = 7$ TeV. *Eur. Phys. J.*, C73(11):2631, 2013.

[253] Y.-Q. Ma, R. Venugopalan, and H.-F. Zhang. J/ψ production and suppression in high energy proton-nucleus collisions. *Phys. Rev.*, D92:071901, 2015.

[254] A. Adare et al. (PHENIX Collaboration). J/ψ production versus transverse momentum and rapidity in pp collisions at $\sqrt{s} = 200$ GeV. *Phys. Rev. Lett.*, 98:232002, 2007.

[255] M. Ivanov. Private communication. 2015.

[256] B. Abelev et al. (ALICE Collaboration). Multiplicity Dependence of Pion, Kaon, Proton and Lambda Production in p–Pb Collisions at $\sqrt{s_{\rm NN}} = 5.02$ TeV. *Phys. Lett.*, B728:25–38, 2014.

[257] J. Adam et al. (ALICE Collaboration). Multi-strange baryon production in p-Pb collisions at $\sqrt{s_{\rm NN}} = 5.02$. 2015. arXiv:1512.07227.

[258] B. Abelev et al. (ALICE Collaboration). Centrality, rapidity and transverse momentum dependence of J/ψ suppression in Pb–Pb collisions at $\sqrt{s_{NN}} =$ 2.76 TeV. *Phys. Lett.*, B734:314–327, 2014.

[259] P. Skands. Tuning Monte Carlo Generators: The Perugia Tunes. *Phys. Rev.*, D82:074018, 2010.

[260] R. Aaij et al. (LHCb Collaboration). Observation of double charm production involving open charm in pp collisions at $\sqrt{s} = 7$ TeV. *JHEP*, 06:141, 2012. [Addendum: JHEP03,108(2014)].

[261] A. Maire. Interpolation of J/ψ production cross-sections at $y \approx 0$ in pp collisions at $\sqrt{s} = 2.76$ TeV and 5.02 TeV. *unpublished internal note*, 2014.

[262] F. Bossu et al. Phenomenological interpolation of the inclusive J/ψ cross section to proton–proton collisions at 2.76 TeV and 5.5 TeV. 2011. arXiv:1103.2394.

[263] J. Book. J/ψ *Production in Pb–Pb Collisions with ALICE at the LHC*. PhD thesis, Johann Wolfgang Goethe Unversität, Frankfurt am Main, 2014.

[264] M. Arratia Munoz (ATLAS Collaboration). Private communication. 2016.

[265] R. Venugopalan. Private communication. 2015.

[266] R. Vogt. Cold Nuclear Matter Effects on J/ψ and Υ Production at the LHC. *Phys.Rev.C*, 81:044903, 2010.

[267] E. Ferreiro, F. Fleuret, J.-P. Lansberg, and A. Rakotozafindrabe. Impact of the Nuclear Modification of the Gluon Densities on J/ψ production in p–Pb collisions at $\sqrt{s_{\rm NN}} = 5$ TeV. *Phys. Rev.*, C88(4):047901, 2013.

[268] H. Fujii and K. Watanabe. Heavy quark pair production in high energy pA collisions: Quarkonium. *Nucl. Phys.*, A915:1–23, 2013.

[269] R. Vogt. Shadowing effects on J/ψ and Υ production at energies available at the CERN Large Hadron Collider. *Phys. Rev. C*, 92:034909, 2015.

[270] I. Helenius, K. Eskola, H. Honkanen, and C. Salgado. Modeling the Impact Parameter Dependence of the nPDFs With EKS98 and EPS09 Global Fits. *Nucl. Phys.*, A910-911:510–513, 2013.

[271] B. Ducloué, T. Lappi, and H. Mäntysaari. Centrality dependence of forward J/ψ suppression in high energy proton-nucleus collisions. In *25th International Conference on Ultra-Relativistic Nucleus-Nucleus Collisions (Quark Matter 2015) Kobe, Japan, 2015*, 2015.

[272] S. Porteboeuf and R. Granier de Cassagnac. J/ψ yield vs. multiplicity in proton–proton collisions at the LHC. *Nucl. Phys. Proc. Suppl.*, 214:181–184, 2011.

[273] M. Azarkin, I. Dremin, and M. Strikman. Jets in multiparticle production in and beyond geometry of proton–proton collisions at the LHC. *Phys. Lett.*, B735:244–249, 2014.

[274] T. Sjöstrand and M. van Zijl. A Multiple Interaction Model for the Event Structure in Hadron Collisions. *Phys. Rev.*, D36:2019, 1987.

[275] L. Frankfurt, M. Strikman, and C. Weiss. Transverse nucleon structure and diagnostics of hard parton-parton processes at LHC. *Phys. Rev.*, D83:054012, 2011.

[276] B. Kopeliovich, H. Pirner, I. Potashnikova, K. Reygers, and I. Schmidt. J/ψ in high-multiplicity pp collisions: lessons from pA. *Phys. Rev.*, D88(11):116002, 2013.

[277] E. Ferreiro and C. Pajares. High multiplicity *pp* events and J/ψ production at LHC. *Phys. Rev.*, C86:034903, 2012.

[278] F. Colamaria. *Measurements of D-hadron azimuthal correlations with ALICE at the LHC*. PhD thesis, U. Bari, 2014.

[279] Y. Feng, J.-P. Lansberg, and J.-X. Wang. Energy dependence of direct-quarkonium production in pp collisions from fixed-target to LHC energies: complete one-loop analysis. *Eur. Phys. J.*, C75(7):313, 2015.

[280] P. Faccioli, V. Knünz, C. Lourenco, J. Seixas, and H. Wöhri. Quarkonium production in the LHC era: a polarized perspective. *Phys. Lett.*, B736:98–109, 2014.

[281] M. Butenschön and B. Kniehl. Reconciling J/ψ production at HERA, RHIC, Tevatron, and LHC with NRQCD factorization at next-to-leading order. *Phys. Rev. Lett.*, 106:022003, 2011.

[282] F. Arleo and S. Peigné. Disentangling Shadowing from Coherent Energy Loss using the Drell-Yan Process. 2015. arXiv:1512.01794.

[283] R. Aaji et al. (LHCb Collaboration). Inclusive low mass Drell-Yan production in the forward region at $\sqrt{s} = 7$ TeV. *Public analysis note*, 2012. Linked to LHCb-ANA-2012-029.

[284] A. Adare et al. (PHENIX Collaboration). Nuclear modification of ψ', χ_c and J/ψ production in d+Au collisions at $\sqrt{s_{\rm NN}} = 200$ GeV. *Phys. Rev. Lett.*, 111(20):202301, 2013.

[285] E. Ferreiro, F. Fleuret, J. P. Lansberg, and A. Rakotozafindrabe. J/ψ and ψ' production in proton(deuteron)–nucleus collisions: lessons from RHIC for the proton-lead LHC run. 2012. [J. Phys. Conf. Ser.422,012018(2013)].

[286] V. Khachatryan et al. (CMS Collaboration). Measurement of Prompt $\psi(2S)$ to J/ψ Yield Ratios in Pb–Pb and pp Collisions at $\sqrt{s_{NN}} = 2.76$ TeV. *Phys. Rev. Lett.*, 113(26):262301, 2014.

[287] E. Ferreiro, F. Fleuret, J.-P. Lansberg, and A. Rakotozafindrabe. Cold nuclear matter effects on J/ψ production: Intrinsic and extrinsic transverse momentum effects. *Phys.Lett.B*, 680:50–55, 2009.

[288] B. Abelev et al. (ALICE Collaboration). Measurement of prompt D-meson production in p–Pb collisions at $\sqrt{s_{\rm NN}} = 5.02$ TeV. *Phys. Rev. Lett.*, 113(23):232301, 2014.

[289] J. Adam et al. (ALICE Collaboration). Transverse momentum dependence of D-meson production in Pb–Pb collisions at $\sqrt{s_{\rm NN}} = 2.76$ TeV. 2015. arXiv:1509.06888.

[290] J. Adam et al. (ALICE Collaboration). D-meson production in p–Pb collisions at $\sqrt{s_{\rm NN}}$ =5.02 TeV and in pp collisions at $\sqrt{s}$ =7 TeV. *in preparation*, 2007.

[291] A. Andronic and J. Wessels. Transition radiation detectors. *Nuclear Instruments and Methods in Physics Research Section A: Accelerators, Spectrometers, Detectors and Associated Equipment*, 666:130 – 147, 2012. Advanced Instrumentation.

[292] N. Pitz. *Gas system, gas quality monitor and detector control of the ALICE Transition Radiation Detector and studies for a pre-trigger data read-out system.* PhD thesis, Goethe Universität Frankfurt am Main,Insitut für Kernphysik, Frankfurt, 2012.

[293] R. Achenbach et al. (ALICE Collaboration). *ALICE transition-radiation detector: Technical Design Report.* Technical Design Report ALICE. CERN, Geneva, 2001.

[294] R. Achenbach et al. (ALICE Collaboration). *ALICE time projection chamber: Technical Design Report.* Technical Design Report ALICE. CERN, Geneva, 2000.

[295] A. Andronic, S. Biagi, P. Braun-Munzinger, C. Garabatos, and G. Tsiledakis. Drift velocity and gain in argon- and xenon-based mixtures. *Nuclear Instruments and Methods in Physics Research A*, 523:302–308, 2004.

[296] M. Fleck. *Commissioning a gas chromatograph for automatic measurements of gas compositions in the ALICE TPC and TRD and Measurement of electrons from semi-leptonic heavy-flavour hadron decays in p–Pb collisions at* $\sqrt{s_{NN}} =$ 5.02 *TeV with the ALICE TRD.* Master thesis, 2014.

[297] E. Bich, J. Millat, and E. Vogel. The viscosity and thermal conductivity of pure monatomic gases from their normal boiling point up to 5000 K in the limit of zero density and at 0.101325 MPa. *J. Phys. Chem. Ref. Data*, 19, 1990.

[298] A. Fenghour, W. A. Wakeham, and V. Vesovic. The viscosity of carbon dioxide. *J. Phys. Chem. Ref. Data*, 27, 1998.

[299] J. Stiller. Gain Calibration of the ALICE TRD using the Decay of ^{83m}Kr and Alignment of the ALICE TRD, 2011. Diploma thesis.

[300] B. Abelev et al. (ALICE Collaboration). Measurement of inelastic, single- and double-diffraction cross sections in proton–proton collisions at the LHC with ALICE. *Eur.Phys.J.C*, 2012.

[301] M. Figueredo. *Estudo da produço de* J/ψ *com o experimento ALICE utilizando o calorimetro electromagnético.* PhD thesis, Instituto de Fisica, So Paulo, 2013.

[302] J. Klein. Triggering with the ALICE TRD. *Nucl. Instrum. Meth.*, A706:23–28, 2013.

[303] J. Klein. *Jet Physics with A Large Ion Collider Experiment at the Large Hadron Collider.* PhD thesis, University of Heidelberg, 2014.

[304] O. Schmidt. *Simulation and Commissioning of the rejection of late conversions in the TRD triggers of ALICE.* Master thesis, 2016.

[305] U. Westerhoff. *Title unknown.* PhD thesis, University of Münster, 2016.

[306] M. Cacciari, S. Frixione, N. Houdeau, M. Mangano, P. Nason, and G. Ridolfi. Theoretical predictions for charm and bottom production at the LHC. *JHEP*, 10:137, 2012.

[307] M. Cacciari, M. Mangano, and P. Nason. Gluon PDF constraints from the ratio of forward heavy-quark production at the LHC at $\sqrt{S} = 7$ and 13 TeV. *Eur. Phys. J.*, C75(12):610, 2015.

[308] T. Plehn. Lectures on LHC Physics. *Lect. Notes Phys.*, 844:1–193, 2012.

[309] K.. Golec-Biernat and M. Wusthoff. Saturation effects in deep inelastic scattering at low Q^2 and its implications on diffraction. *Phys. Rev.*, D59:014017, 1998.

[310] S. Baranov, A. Lipatov, and N. Zotov. Prompt J/ψ production at LHC: new evidence for the k_{T}-factorization. *Phys. Rev.*, D85:014034, 2012.

[311] V. Saleev, M. Nefedov, and A. Shipilova. Prompt J/ψ production in the Regge limit of QCD: From Tevatron to LHC. *Phys. Rev.*, D85:074013, 2012.

[312] H. Fritzsch. Producing heavy quark flavors in hadronic collisions—A test of quantum chromodynamics. *Phys. Lett. B*, 67(2):217 – 221, 1977.

[313] F. Halzen. CVC for gluons and hadroproduction of quark flavours. *Phys. Lett. B*, 69(1):105 – 108, 1977.

[314] J.-P. Lansberg. *Quarkonium production at high-energy hadron colliders: A Systematic gauge-invariant approach to relativistic effects of* J/ψ, ψ' *and* Υ *production*. PhD thesis, Liege U., 2005.

[315] J.-P. Lansberg. J/ψ production at sqrt(s)=1.96 and 7 TeV: Color-Singlet Model, NNLO* and polarisation. *J. Phys.*, G38:124110, 2011.

[316] J.-P. Lansberg. Total J/ψ production cross section at the LHC. 2010. arXiv:1006.2750.

[317] M. Butenschoen, Z.-G. He, and B. Kniehl. η_c production at the LHC challenges nonrelativistic-QCD factorization. *Phys. Rev. Lett.*, 114(9):092004, 2015.

[318] H. Han, Y.-Q. Ma, C. Meng, H.-S. Shao, and K.-T. Chao. η_c production at LHC and indications on the understanding of J/ψ production. *Phys. Rev. Lett.*, 114(9):092005, 2015.

[319] H.-F. Zhang, Z. Sun, W.-L. Sang, and R. Li. Impact of η_c hadroproduction data on charmonium production and polarization within NRQCD framework. *Phys. Rev. Lett.*, 114(9):092006, 2015.

[320] S. Chatrchyan et al. (CMS Collaboration). Suppression of non-prompt J/ψ, prompt J/ψ, and Υ(1S) in PbPb collisions at $\sqrt{s_{\mathrm{NN}}} = 2.76$ TeV. *JHEP*, 05:063, 2012.

[321] R. Shahoyan. Private communication. 2015.

[322] S. Gorbunov. *On-line reconstruction algorithms for the CBM and ALICE experiments*. PhD thesis, Universität Frankfurt, 2013.

[323] T. Dahms. *Dilepton spectra in p+p and Au+Au collisions at RHIC*. PhD thesis, SUNY, Stony Brook, 2008.

Acknowledgements

I thank Johanna Stachel that I could work on very interesting topics in her working group with excellent physicists in Heidelberg and at GSI and in a very independent manner, since my time as a bachelor student. Furthermore, I would like to thank her for her strong support, her credit and for interesting discussions. I thank Hans-Christian Schultz Coulon to be available as second referee.

I thank Anton Andronic who I worked with since my time as a bachelor student. He has been open for discussions on any topic at nearly any time. I profited from his enthusiasm, his advice and broad experience. I am grateful that I worked with Ionut Arsene as my convenor. He has been able to provide motivation, ideas and to help with analysis problems and software.

I learned from Chilo Garabatos a lot about the operation of gaseous detectors and how to keep focused and efficient under extreme pressure. I thank him for his credit in dealing with critical things in the detector operation. I want to thank in this context Albin Wasem and Martin Fleck for a constructive cooperation concerning the TRD gas system operation.

Antonin Maire has been a help on various levels. His style of attacking problems helped often to isolate problems and distil their solution. I owe him thanks for his steady support. Felix Reidt helped me a lot with software issues when I already lost the patience and provided support in stressful moments as a listener. I am grateful to Alexander Kalweit for interesting and educative conversations on detector calibration, QGP physics and other topics. I thank Martin Völkl for many discussions about systematic uncertainty determination and physics as well as for standing me as an office mate. I thank Yvonne Pachmayer for being always available to talk and for providing advice. Jens Wiechula and Silvia Masciocchi had a lot of patience with me concerning computing. I had with both of them open, friendly and motivating discussions on various topics. I thank Benjamin Hess for his formidable work on the TPC-PID calibration in the p–Pb minimum bias data sample and his support on computing issues and insights about PID. I would like to thank Peter Glässel, who I know since my first semester and who brought me into contact to heavy-ion physics, for his comments and his support.

I thank Kai Schweda, Lucia Leardini, Klaus Reygers, Michael Knichel, Jorge Mercado, Jochen Klein, Rainer Schicker, Johannes Stiller, Goran Simatovic, Ralf Aver-

beck and Hans Beck for their help or advice and their listenership and appreciation of my comments. I want to thank Peter Braun-Munzinger for his capability to share his broad knowledge and to provide constructive criticism at various occasions. Furthermore, I would like to express my gratitude to Marian Ivanov in giving me insights in his understanding of the TPC tracking and its particle identification. I would like to mention the very prompt support and help from Christoph Blume as PAG convenor. Giuseppe Bruno has also been very supportive in the PAG and in the PWG. Julian Book and Fiorella Fionda helped me promptly with the dielectron framework at various occasions. Thanks to Annalisa Mastroserio and Francesco Prino for their help with the MC event simulations. Furthermore, I appreciated the work with Enrico Scomparin, Roberta Arnaldi and Chiara Oppedisano from Torino, Cynthia Hadjidakis and Christophe Suire from Orsay as well as Javier Martin Blanco and Laurent Aphecetche from Nantes. They listened to me in different functions in terms of analysis problems and physics interpretations most notably also in case of dissent.

I thank Boris Kopeliovich, Raju Venugopalan and Michael Klasen for enlightening discussions about the theory of charmonium production in pp and p–Pb collisions and Alexander Rothkopf for discussions about in-medium properties of charmonium.

I would like to thank Yvonne Pachmayer, Anton Andronic, Ionut Arsene, Chilo Garabatos, Klaus Reygers, Peter Glässel and Antonin Maire for proof-reading this thesis.

Vielen Dank für Ihre Unterstützung geht an meine Freunde in Heidelberg Simon Mayer, Oliver Breitwieser, Markus Als und Kristijan Cule auch und gerade in den stressigen Momenten.

Ich danke meinen Eltern vielmals für Ihre Unterstützung während meines Studiums und während der Doktorarbeit. Sie waren beide ein nicht zu erschütternder Ruhepol mit gutem Rat.

A. The Gas System of the ALICE TRD

The Transition Radiation Detector (TRD) of ALICE is designed for the identification of electrons and positrons via the measurement of their higher energy loss via ionisation and the transition radiation emitted in the radiator material in front of the Multi-Wire Proportional Chambers (MWPCs) of the detector. In addition, it improves the p_{T} resolution of the central barrel at high track p_{T} and provides trigger capabilities based on p_{T} and particle identification on track level. Electrons and positrons can be separated from hadrons by Transition Radiation (TR), since it sets in for particles with relativistic $\gamma \gtrsim 1000$, which is already reached by electrons and positrons for track momenta of about 0.5 GeV/c, whereas it becomes only relevant for the next heavy charged particles, the muons[1], for $p > 100$ GeV/c. A detailed description of TR, its application to particle identification and an introduction to the ALICE TRD can be found in Ref. [291]. The construction, installation, maintenance and performance of the ALICE TRD is described in detail in Ref. [216]. A detailed description of the TRD gas system and its maintenance between 2009–2012 is given in Ref. [292]. In the following, the TRD design in view of its gas system and the gas system installation, upgrades and operation in the time period 2013–2015 are summarised.

A.1. Design considerations

It is necessary to choose a gas with a large photon absorption cross section for the exploitation of Transition Radiation (TR) in gaseous detectors for particle identi-

[1] In practice, the separation with respect to pions with similar mass than muons is much more important due to their larger abundance.

fication. Xenon provides, thanks to its high charge number Z, the highest cross section among all stable noble gases as shown in Fig. A.1. In addition, it has the largest difference of ionisation energy loss for charged particles between the Fermi-plateau and a minimum ionising particle. Therefore, Xenon is chosen as counting gas component of all constructed gaseous TRDs. The requirement of an inert and non-flammable gas leaves only CO_2 as quenching gas. The gas of the ALICE TRD consists of a Xe-CO_2 (85:15) mixture. The ALICE TRD with its about 27 m^3 gas

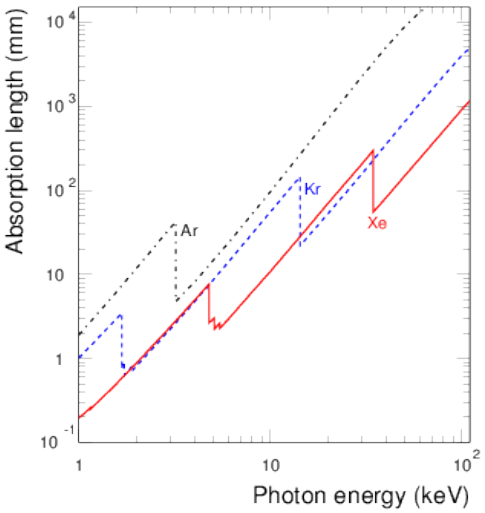

Figure A.1.: Photon absorption length for noble gases as a function of the photon energy. The TR photon energy for typical radiator dimensions ranges between 3 and 15 keV [291]. Figure taken from Ref. [291].

volume is in terms of volume the largest of its type ever built. The large volume is necessary due its large active detector surface of 716 m^2, since it is placed at outer radii than the TPC in order to guarantee low material budget for hadron tracking and the requirement of several detector layers, in practice 6 layers, to provide sufficient separation power on track level. In addition, the gas volume of the MWPCs in radial direction amounts to 3.4 cm in order to exploit the late arrival of the electrons produced by the absorption of TR photons in the counting gas for additional discrimination power.

Xenon is an expensive gas due to its rareness in the atmosphere. It is about a factor 3000 (50) more expensive than Argon (Neon) costing about 10 Euro per litre gas at standard conditions. Consequently, the gas system has to fulfill strict tightness conditions in order to keep the Xenon consumption as low as possible. Due to the multilayer ALICE TRD design, necessary to profit from TR emission in every layer,

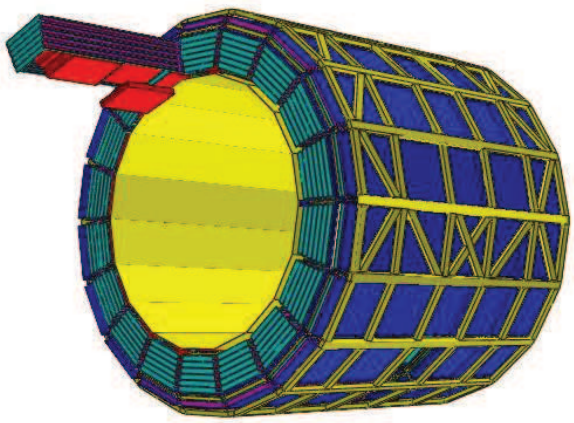

Figure A.2.: TRD layout

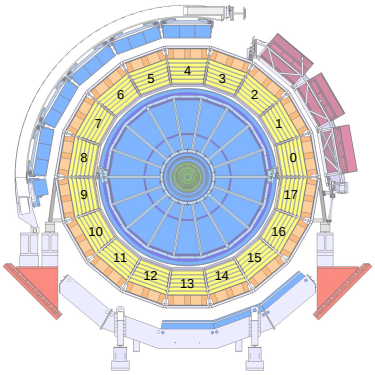

Figure A.3.: SM numbering

The TRD layout is shown on the right hand side. The azimuthal structure in 18 SMs is shown with its 6 MWPC layers. One SM is pulled out of the nominal position to illustrate the segmentation in stacks in z-direction. The figure is the courtesy of D. Miskowicz and is taken from [216]. On the left hand side, a cross section view of the central barrel is shown. The z-axis is pointing towards the viewer. The TRD is indicated in yellow and the SM numbering scheme is indicated.

the volume-to-surface ratio of 0.017 m [293] is unfavourable for good tightness. As comparison, the ALICE TPC has a volume to surface ratio of about 0.7 m [294]. It is clear that a recirculation of the gas is necessary to avoid venting it out apart from the unavoidable leaks. Furthermore, in order to limit the mechanical stress on the MWPCs with areas of up to 1 m^2, there is the need for an active pressure regulation in the whole system providing a constant small overpressure in the detector volume relative to the atmospheric pressure.

A.2. TRD gas system layout

Figure A.2 shows the spatial segmentation of the TRD. It consists of 6 concentric chamber layers at a radius of about 3.5 m. It is subdivided in the azimuthal direction into 18 sectors, called SuperModules (SMs) following the TPC sector boundaries. The naming convention in arabic numbers according to the SM position and the surrounding detectors is depicted in Fig. A.3. Each SM is divided into 5 stacks each equipped with 6 chambers along the beam-axis direction. The middle stack is missing in the sectors 13 to 15 in front of the PHOS calorimeter. A schematical

view of the gas system layout is shown in Fig. A.4. The system is arranged in separate modules, each fulfilling a particular task. The modules are distributed in the surface, in an area about half down the shaft to the detector, this being located about 60 m underground. The gas system compressor maintaining the flow of the system and the return regulation as well as the inlet distribution to the detector is placed in the shaft. The system components for fresh gas supply, gas cleaning and gas separation are at the surface. The gas system has two buffers, one in front of the compressor operated at small negative pressure with respect to atmospheric pressure as part of the return regulation and one high pressure buffer directly downstream of the compressor.
The large density of the Xenon, 4.6 times the density of air at standard temperature and pressure, requires special care in the design considerations, since the hydrostatic pressure difference between the top and the bottom amounts to 2.8 mbar. This value is uncomfortably large, since the chambers are known to hold an (over)underpressure of about 5 mbar with respect to their ambiance. In order to avoid this uncomfortable situation, the SMs are supplied by individual supply and pressure reducers situated in the gas system room in the shaft. The connection from the pressure reducer to the SMs is done by pipes of small inner diameter, 4 mm, such that the pressure drop within the line is substantially larger than the difference in the hydrostatic pressure among the SMs. The latter design feature enables not only the delivery of the same overpressure to all SMs, but also similar flows at the same operating overpressure.
In the following, the different components of the gas system are described.

A.2.1. Gas system components

The TRD gas system follows a modular construction common to all LHC detectors enabling the standardisation of common hardware components and a common software support, which are both customised according to the needs of each individual system.
The software follows the modular construction of the hardware system subcomponents allowing to steer Programmable Logical Controllers (PLCs). The setting of the PLCs can be moved to 'stop' or 'start' or the running mode can be changed from 'run' or 'purge' etc. Furthermore, individual elements of a subcomponent

can be operated as specific valves, flow-meter settings or Proportional Integration Differential (PID) regulation parameters. A given software command results in the execution of a sequence of commands sent to the PLC to operate and regulate all concerned hardware subelements, in order to ensure the desired working set-point of gas flow, pressure or other parameters. The parameters of the regulation can be tuned by the user in the 'recipes', which are part of the software interface.

Gas connections and equipment of a supermodule

The gas supply connections from the gas system to the detector are placed on the A-side of the detector[2]. They consist of three 4-6 mm lines supplying each SM from the shaft. The chambers in one layer are interconnected through short PEEK tubes, and each two layers are connected through stainless steel bellows at the C-side of the SMs[3]. Thus gas flows through one layer and back through a neighbouring layer. Three layers, usually the innermost, the third and the fifth layer are supplied by incoming gas from the gas system from the A-side.
The three outlet connections of the SM are connected to a manifold mounted on the SM hull at the A-side. The manifold also houses a two-way bubbler and pressure sensors. The manifold arrangement is shown in Fig. A.5. The bubbler protects the MWPCs from under and overpressure exceeding about 1.3 mbar with respect to the atmospheric pressure in case of active pressure regulation failure. The outlet of the bubbler is connected to a back-up line through which a permanent flow of N_2 is maintained. Hence, in case of underpressure in the detector, N_2 is sucked in the detector. In case of overpressure in the detector, the detector gas mixture falls down the back-up line. Two pressure sensors measure the pressure difference of the detector gas with respect to the atmospheric pressure and with respect to the back-up system. One of them is chosen to drive the active pressure regulation mechanism controlled by the system's PLC. All connections of the Xe-CO_2 gas mixture from the manifold to the SM and from the SM to the gas system are equipped with ISO quick release flanges of various diameters. They employ elastomeric O-rings placed on metal centering rings and clamps allowing for tight closure and quick opening

[2]The A-side of the central barrel is indicated in Fig. 3.5, where the global coordinate system of ALICE is introduced.
[3]The C-side is also shown in Fig. 3.5.

without further tooling.
The SM triplets in the sectors 3-4-5 and 12-13-14, which have similar hydrostatic pressures, share a pressure sensor, since they have common supplies and common regulation points. A detailed description of the bubbler and back-up system specifications can be found in Ref. [216].

Distribution

The distribution modules, located in the shaft, contain the regulation of the small overpressure of about 0.1 mbar at the outlet of the SMs and displays both measured pressures. The regulation of the measured pressure, by default the pressure with respect to the back-up system is used, is achieved by a variable opening of the valve downstream with respect to the pressure measurements. Every SM inlet is equipped with separate CO_2 lines external to the gas loop entering at the distribution inlet modules. They enable the purging of the SMs at a flow of about 50 l/h per double layer in order to remove the air from newly installed SMs. Since during this operation, the loop's return is closed, the purging gas is exhausted through the SM bubbler.
The measured overpressure in front of the small pipes going to the SMs is also monitored remotely. It is regulated manually by pressure reducers half-way down to the experiment. At sufficient high pressure buffer pressures of more than about 0.6 bar, its overpressure is approximately constant and tuned to 60–90 mbar during Xe-CO_2 running. this results in a sufficiently uniform flow in all SMs of about 300 l/h.

Mixer

The mixer is placed at the surface and is used for the injection of fresh gas. During regular running, it replaces the gas losses by leaks via two flowmeters, one for Xenon and one for CO_2, which inject Xe-CO_2 gas mixture according to an adjustable mixing ratio. The standard flow for the leak compensation is about 11 l/h Xenon-CO_2 mixture. The duration and the frequency of the injections are further explained in Section A.9.
In addition, the mixer has another set of flowmeters appropriate for a flow of up to

480 l/h for Xenon and up to 1320 l/h for CO_2. They can be used for the injection of pure CO_2 or pure Xe, in conjunction with the membrane system (see below) for the recuperation and filling processes.

Pump

The continuous gas flow of about 5 m^3/h for the complete detector is guaranteed by a pressure gradient between the low pressure buffer directly downstream to the SMs and the high pressure buffer produced by two pumps, which run at a constant frequency. The variation of the pressure gradient between the detector and the high-pressure part is necessary to accommodate the atmospheric pressure variations at a constant overpressure of the MWPCs. It is achieved by a bypass line with regulated throughput. The pressurised gas continues to flow through the modules at the surface and back to the inlet distribution modules in the shaft.
The high buffer pressure serves as gas reservoir, when gas from the detector needs to be absorbed (distributed) due to decreasing (increasing) atmospheric pressure. It has a volume of 930 l and is operated at pressures between 0.6 bar and 1.6 bar overpressure with respect to atmospheric pressure. Thus, in the ideal case of a completely gas-tight system, as the gas flows through the loop, it is moved from the detector to the high pressure buffer and back, following the atmospheric pressure changes.
The low pressure buffer in front of the compressor damps possible pressure oscillations due to the coupling between the regulation of the individual SM flows guaranteeing the constant small overpressure with respect to atmospheric pressure and the regulation of the pump, which is set to keep the pressure in the low buffer buffer at -34 mbar half way up the cavern shaft. This value is chosen to match the expected pressure drop in the return lines from the detector to the buffer.

Exhaust

No gas is vented out of the system in this part of the system. The exhaust module is used for the gas recirculation at sufficient high pressure to serve the distribution in the shaft of the experimental cavern. In addition, it contains provisions for connecting containers like a Krypton calibration source.

Membranes

The membranes module is needed for the exchange of the gas mixture during filling or emptying of the detector with the nominal gas mixture or large composition changes without a large waste of precious Xenon.
The core of the system consists of two cartridges. They allow the gas separation via bundles of capillary polyimide tubes, which are contained themselves inside the cartridges. The tube walls have a much smaller permeability for Xenon than for the smaller CO_2 molecule enabling the separation of the two gases. Part of the gas flow can be sent through the two stage membrane system. The Xenon richer effluent of the first membrane can be either sent back to the gas system or to the cryogenic plant for a N_2 removal explained in Section A.6. The CO_2 rich gas is sent to a second membrane. The Xe rich outlet of the second membrane is sent back to the first membrane, whereas the CO_2 rich part is exhausted to the atmosphere. A bypass pressure regulator is used to adjust the fraction of the recirculating gas flowing through the membrane system, in order to guarantee that the mixer can provide sufficient gas to compensate what is removed by the membranes. As the gas composition changes, the bypass regulation is manually adjusted.

Purifier

Since the gas is permanently recirculated, the unavoidable leaks lead to intakes of atmospheric gas as most notably N_2 and O_2. N_2 has very little impact on the drift velocity [295] at a constant Xe to CO_2 concentration ratio. However, a larger fraction of N_2 contamination corresponds to a lower Xenon concentration and, hence, a degraded TR detection performance. Therefore, the removal of N_2 from the mixture is necessary and is achieved every 1-3 years by the procedure described in Section A.6. In addition, the intake of the electronegative O_2 has to be actively limited during running, since its presence yields to attachment of electrons from the primary ionisation by charged tracks or transition radiation. Due to the comparatively small maximal drift length of $2.8/\cos(\Theta_{\text{Lorentz}})$ cm[4], the requirements are not as tight as for a TPC. In addition, a considerable intake of H_2O is observed from the detector, which has to be removed actively. The H_2O intake is attributed to

[4]The Lorentz angle for the nominal gas composition and the nominal magnetic field amounts to 8°.

diffusion of water molecules through the aluminised mylar, which serves as the drift electrode of the read-out chambers [216].
The O_2 contamination as well as the H_2O contamination is actively removed by the purifier module positioned in the high pressure part of the system. It consists of two columns of about 6 l volume. The gas flow is sent to one of the two columns, where the other is either regenerated or in standby. The columns are filled with porous pellets covered with dispersed metallic copper, a catalyst. This copper oxides to form CuO und thus removes oxygen from the gas stream. The water is mechanically removed by adsorption in the porous material. The purifier columns are swapped about every 4 days when the filtering of the H_2O gets ineffective and the H_2O content reaches about 400 ppm. The O_2 contamination of the detector stays always below 10 ppm.
The regeneration of the inactive purifier column is achieved by the flushing with a H_2 rich Argon based gas mixture at 200°C.

Analysis

The analysis module measures the CO_2, the O_2 and the H_2O content of the TRD gas permanently. It has the ability to sample the return gas from each individual SM loop, and also the common return gas from the low pressure buffer. The analysis line pumps the gas back into the main loop because no gas should be vented away. In order to avoid contamination of the gas, the analysis devices must be free of chemicals, and have been validated for ageing. Details about the employed analysis techniques can be found in Ref. [292].
A switch between the channels happens every 4 min in standard running mode. This is set by the operation in the recipes.

Gas chromatograph

A gas chromatograph shared with the ALICE TPC is used for the precise analysis of the gas composition. In 2013 and 2014, a new gas chromatograph was commissioned and integrated in the detector control system of the TPC and the TRD. A detailed description of the commissioning and the calibration of this device can be found in Ref. [296]. The main TRD gas components Xenon and CO_2 as well as the N_2 content

are automatically measured with the gas chromatograph about every 4 hours. The gas, which flows through the gas chromatograph is vented out and corresponds to a leak rate of about a few centilitres/4 h.

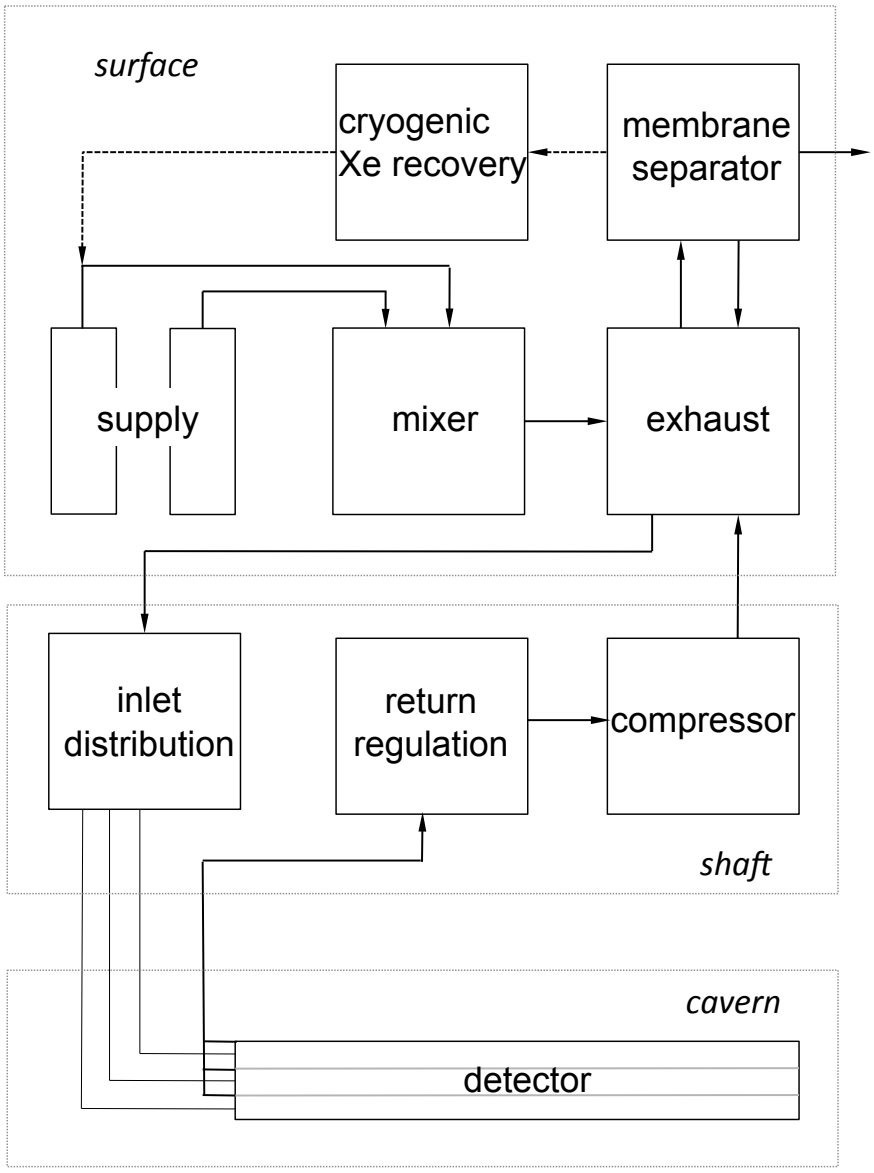

Figure A.4.: A schematical view of the main components of the TRD gas system is shown. The figure is taken from Ref. [216].

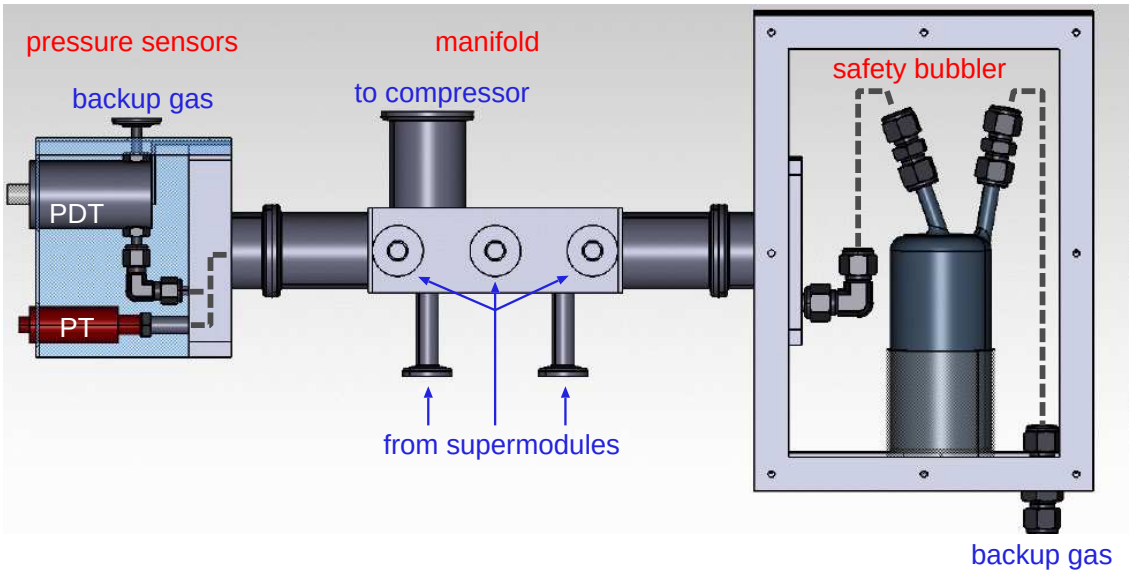

Figure A.5.: The layout of the fully equipped manifold of a SM is shown. The figure is taken from Ref. [216].

A.3. Super-Module gas system commissioning

At the end of Run 1, 13 out of 18 SMs were installed. In the course of the data taking break between 2013 and 2015, the TRD construction and installation was completed. The SM in sector 17 was completely reworked. In addition, the SMs in the sectors 7, 8, 10, 11, 15 and 16 were removed from their position and reworks of low voltage connections were done before the reinsertion into the support structure and the reconnection of the services.

A.3.1. Tests at the surface

The newly built SM were fully assembled in Münster and brought to CERN via truck. During the transport of the SMs, the gas volume of the detector was allowed to equilibrate its pressure with the atmosphere via appropriate paper filters installed at the gas inlets.

In order to test the full functionality of the SM after the transport prior to the installation, tests of the low voltage, the high voltage, the cooling and the gas system were performed in building 2252 within the interaction point 2 area of the LHC ring, where ALICE is situated. We shortly describe the tests involving the gas system.

Firstly, the bubblers were filled with paraffine to define a gas-bubbling threshold at about ± 1.3 mbar. As a first test, all parts connected to the manifold in the cavern were tested together as shown in Fig. A.5 pressurising them with Argon or with an Ar-CO_2 mixture at about 1 mbar. The liquid level of the bubbler was observed for about 30 minutes. This test was done to exclude large leaks in these parts external to the MWPCs and their interconnections within the SM.

As a second test, the SM was connected to a rack with 3 flow meters supplied with Ar or with an Ar-CO_2 mixture providing a gas flow operated between 15 and 50 l/h per double layer. The connection arrangements were connected as in the cavern except of the back-up system connections, which were simply left open to the atmosphere. A static test was performed at overpressure to check that the SM and its equipment hold the pressure. After this test of the manual connections, the SM was flushed first at overpressure and then at underpressure with Ar or Ar-CO_2 while the the O_2 content of the exhausted gas was measured by an Orbisphere

oxygen meter, down to the ppm level. The underpressure was achieved by a vacuum pump, which was connected to the outlets of the SM. A detailed description of the test set-up can be found in Ref. [292]. The leak conductivity L was measured by the oxygen content of the gas in the underpressure running mode using the following relation:

$$\begin{aligned} L &= \frac{\mathrm{d}(PV)/\mathrm{d}t}{\Delta P} \approx \frac{P \cdot \mathrm{d}V/\mathrm{d}t}{\Delta P} \\ &= \frac{P \cdot \mathrm{fl}}{\Delta P} = \frac{f_{\mathrm{atm}}}{F_{\mathrm{O2}}} \cdot \frac{p \cdot \mathrm{fl}_{\ \mathrm{input}}}{\Delta P} \end{aligned} \tag{A.1}$$

with the volume of the SM V, the absolute pressure P of the detector, the pressure gradient between the detector and the ambiance ΔP, the measured O_2 content at the detector outlet F_{O2}, the fraction of O_2 in the atmosphere $f_{\mathrm{atm}} = 0.21$, the flow provided to the detector $\mathrm{fl}_{\mathrm{input}}$ and the gas flow into the detector $\mathrm{fl} = \mathrm{d}V/\mathrm{d}t = \mathrm{fl}_{\mathrm{input}} \cdot f_{\mathrm{atm}}/F_{\mathrm{O2}}$. This underpressure procedure was necessary, since a sensitivity to viscous leaks was required due to their occurrance at an early stage of the production, which had to be fixed with additional glueing, as explained in Ref. [216]. The largest measured leak conductivity at underpressure amounted to 48 l/h.

After the gas and high voltage tests, the SMs were disconnected from the gas supply and its connections were closed as for the transport from Münster during the installation or, in case of storage exceeding a few days in the building prior to the installation, they were continuously flushed at low flow with Argon or Argon based mixtures protected from too large overpressure by the bubblers.

A.3.2. Installation

After moving the SM in its final position, the manifold fixation and the bubbler and the pressure sensor fixation were done on the A-side of the ALICE set-up. Finally, the various gas pipes were connected to the system. The work was conducted by two persons with climbing equipment. Due to the low voltage reworks, in total 12 out of 18 SMs were (re)connected to the gas system in 2013–2014.

The tightness was tested by pressurising the SM via the mentioned separate CO_2 supply directly to the SM to approximately 1 mbar overpressure being sensitive to non-tight connections during the installation. Several times, it was necessary to perform a leak search after this initial test, since the connections were not always

tight due to their partially difficult accessibility without intervisibility. For the leak search, the SM was pressurised to an overpressure maximally hold by the bubbler and the sector connections were checked with a sniffer.
If the overpressure at the SM was constant relative to the ambient pressure over several hours, it was considered tight. Next, it was flushed with a CO_2 flow of about 150 l/h (50 l/h per double layer) for about 3 days to ensure a sufficient number of volume exchanges with pure CO_2 prior to its connection to the gas loop.
The pressure sensors for the pressure monitoring were calibrated by reading off their value at a liquid column of 1 cm corresponding to approximately 1 mbar overpressure in the detector. The displayed value $p_{\mathrm{dis,1mbar}}$ varies up to 0.3 mbar from the expected 1 mbar with respect to the back-up system. The operational point of the detector corresponding to 0.1 mbar overpressure in the software control was defined assuming a simple off-set between the measurement and actual pressure value.

A.4. Gas mixture change

The density of CO_2 is lower by a factor 3 and its dynamic viscosity lower by a factor 1.5 than the ones of pure Xenon [297, 298]. Gas mixture changes from the nominal detector mixture to pure CO_2 therefore require significant changes of the operational set-points.
The flow is reduced manually in several steps during the gas exchange from the mixture to CO_2 by changing the pressure value in front of the SMs from about 65 mbar to about 30 mbar. This lower set-point is also used for the flushing of the SMs prior to their connection to the gas loop. In addition, the pressure set-point of the low-pressure buffer is set to -6 mbar in order to ensure stable running of the system allowing for similar pressures in the SMs as for Xe-CO_2 running. the latter change takes into account the reduced pressure gradient of pure CO_2 compared to the Xe-based mixture from the detector to the low pressure buffer in the shaft.

A.5. System performance

The system runs with a very high efficiency and stable pressure conditions as it is documented by the pressure sensor measurement of a SM shown in Fig. A.6.

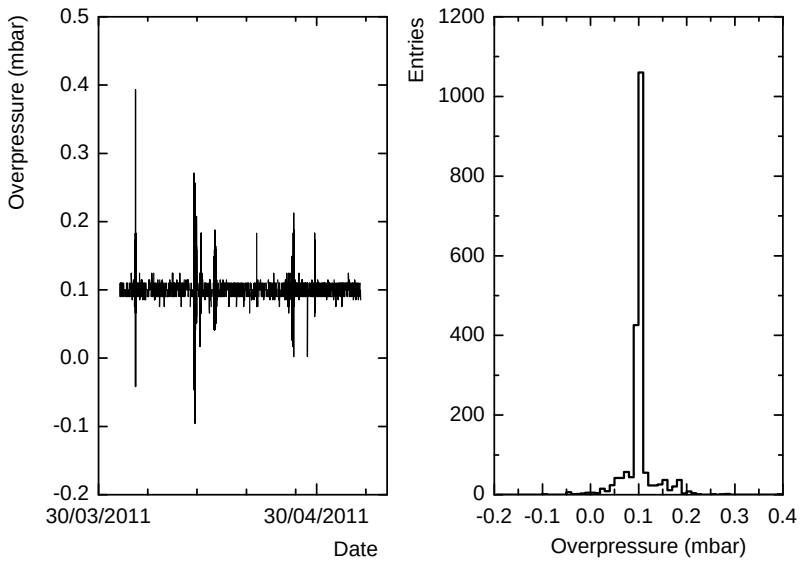

Figure A.6.: The measured variations of the overpressure relative to atmospheric of a SM during active regulation by the gas system are shown. The figure is taken from Ref. [216].

The stops of the gas system or of single SMs in 2015 during regular running are listed below:

1. A system circulation stop occurred on the 11th of February after a detector temperature change during the switch-on of the TRD front-end electronics. Such a temperature change results in a rapid change of the gas density, and a quick relocation of gas between detector and high pressure buffer takes place. In the latter case, the system was not able to cope with this variation and stopped the circulation.

2. Three system circulation stops were caused at the 30th of March by stormy weather.

3. SM 17 was isolated from the gas system due to a faulty pressure transmitter at the 17th of April.

4. A system circulation stop happened at the 15th of June due to a power cut of the PLCs.

In all cases except of the PLC power cut, the gas system circulation could be resumed within less than one hour by remote intervention. No beam data taking was concerned by the system stops. The pressure transmitter at the pressure reducer for SM17 in the experimental shaft had to be replaced. The first alarm occured at around 9 AM, stable circulation for this sector was reestablished after the replacement in the evening of the same day. This incident happened during regular data taking.
The system stop related to the temperature change and the relation of the cooling temperature, the front end electronics status and the gas system are detailed in Section A.10.3. The stormy weather can lead to problems, since wind blows can cause pressure waves leading to pressure oscillations in the ambient pressure in the shaft, where the pressure for the low pressure buffer regulation is measured. Hence, the system can start to develop fluctuations in the regulation of the compressor module, which can trigger a system stop, when a threshold difference between measured pressure and its set-point in the low pressure buffer is exceeded. No easy mitigation has been found for this known problem.
The consequences of the power cut of the PLCs is detailed in Section A.8.2.
In addition, a small leak lead to wrong measurement values of O_2 and H_2O from the analysis loop. This leak could be found ensuring standard monitoring of the gas system.

A.6. Cryogenic gas filtering

In order to guarantee a good electron identification, the N_2 content of the gas mixture is required to be as low as possible. Since there is a small but continuous leak induced N_2 intake, there is the need for a removal of this contamination. The gas system itself has no possibility to separate Xenon from nitrogen as easily as it is the case for the separation between Xenon and CO_2. Hence, for this purpose, a cryogenic plant inherited from the ALEPH collaboration is used every 1-3 years. During the procedure the Xenon is filled in bottles and the gas system is filled with CO_2 until the bottles are refeeded into the system.

Evidently, permanent running of the gas system with the Xe-based mixture during long periods without data taking as between February 2013 and January 2015 would yield to a considerable loss of Xenon and would require tight supervision of the system as during regular running. Hence, it is advantageous to remove Xenon from the detector via the cryogenic plant before long shutdowns and store it in bottles, which are used for the refill after the shut down. A cryogenic purification of the TRD gas was done in April 2013 including the commissioning of a new control rack for the steering of the different sub-steps. The process is subdivided in 3 parts: transport of Xenon from the detector to the cryogenic plant and freezing of Xenon in the plant, phase 1, removal of impurities, phase 2, warm up and compression of Xenon to storage, phase 3.

During the first phase, the gas system is supplied by a high flow of CO_2 and the two-step membranes system are configured such that the Xe-rich gas extracted from them is directed to the cryogenic plant, which is cooled by liquid nitrogen (LN_2) to a temperature below 163 K and above 77 K, such that Xenon freezes to a solid mass and N_2 remains in the gaseous phase. Argon as a potential impurity is also still gaseous for Temperatures above 84 K. The LN_2 cooling is automatically regulated by electrovalves that allow to start or stop the LN_2 through the cryogenic plant depending on the reading of temperature probes installed in the walls of the column. The daily LN_2 consumption during the cool down amounted to about one third of the LN_2 dewar at ALICE's site. After the cool down of the pipes and the plant, it still amounted to about 25% requiring regular refill of the reservoir. This consumption will be reduced for the next cryogenic campaign, since the piping from the reservoir to the cryogenic plant was upgraded in January 2016 with a vacuum

isolated cryogenic pipe, which was not in place in 2013.

For the second phase, the membranes are stopped and the valves to the detector are closed. The system circulates now practically pure CO_2 through the detector. The cryogenic plant is decoupled from the gas system. In the cryogenic plant, the gas, mainly N_2, is pumped out of the plant at low temperature. In that way, the impurities are removed and the Xenon remains in the cryogenic plant[5].

During the last stage, the cryogenic tank is heated and the Xenon is compressed by vaccum pumping towards storage bottles. The temperature of the plant is still regulated by LN_2 to prevent that the pressure in the column increases beyond the limit that it can hold.

In should be noted that when in phase 1 the mixture left in the detector has little Xe content, the osmotic pressure at the membranes is too large to prevent CO_2 to flow into the cryogenic plant. Therefore the dominant fraction of the gas tranported to the cryogenic plant is CO_2 at this stage. The Xenon content of the detector follows approximately an exponential decay. Hence, there is a trade-off between the duration of the recovery and the Xenon remaining in the detector[6].

In order to increase the speed of the first phase, which is still coupled to the gas system operation, the high flow meter of the Xenon supply was bypassed and used for CO_2. In addition, at a later stage, the CO_2 high flow meter was exchanged to support flows of up to 1320 l/h instead of the initial 84 l/h. Finally, after these modifications, the speed of the operation was limited by the gas flow, which could be pushed through the membrane bypass by reducing the flow in the main line. This value is limited, since the flow impedance is strongly enlarged and eventually the circulation flow through the membranes decreases at some point. During the first phase, the settings of the gas system itself had to be changed due to the changing density and viscosity of the mixture. The system has to be permanently supervised to guarantee that the amount of gas removed via the membranes is as close as possible to the amount of gas which is injected. It was checked by gas chromatograph measurements that the usage of one membrane column would result in a 5% Xe concentration of the exhausted gas in the beginning of the process. After the use of the two stage approach, the Xenon content in the exhaust gas was below 0.2%. The

[5]Traces of Xenon will be also removed due to the finite vapor pressure, which amounts to 5 mbar at 116 K, which is a typical running temperature.

[6]This fraction of gas is largely lost, if the recovery takes place at the beginning of a very long period of no data taking after that the system is flushed with CO_2 in order to remove the accumulated N_2 efficiently.

freezing stage was stopped, when the Xenon content in the detector was at about 2%, which corresponded to about 400 l Xenon left in the system with 13 SM.
This phase took 6 days. It was necessary to stop this phase 3 times in order to pump out N_2 in order to keep the plant pressure low enough for the gas transport.
The most critical step of the operation is the heating phase, since the maximal pressure of the cryogenic plant must stay below the maximal plant pressure of 40 bar to ensure that no Xenon is vented out to the atmosphere. This was achieved by the active restart of the LN_2 cooling, regulated by the newly commissioned control rack, when the pressure measured inside the cryogenic plant exceeds 5 bar. In 2013, this phase took seven days.
The cryogenic procedure inevitably leads to losses of Xenon via the membranes, the Xenon remaining in the detector if no immediate refill is done and the gas lost during the regeneration. In 2013, the Xenon lost amounted to about 0.7 m^3 estimated by the bottle weights, gas chromatograph measurements and the estimate of the total system volume of about 20.75 m^3 with 13 SM corresponding to about 16.6 m^3 Xe. Therefore, the efficiency of the process is about 96%. The N_2 concentration in the detector was about 6%, the measured N_2 concentration in the gas bottles filled during the cryogenic procedure was less than 1%. The Xe volume concentration of the bottles amounts to 57%. The rest of the gas in the bottle was CO_2.

A.7. Krypton calibration

A relative pad-by-pad gain calibration of the TRD was done in February 2015 by releasing the radioactive Krypton isotope ^{83m}Kr prior to the start of collision data taking with the nominal gas mixture Xe-CO_2. A detailed account of the technique and its application to the ALICE TRD calibration can be found in Ref. [299].
The radiation source is a foil where ^{83}Rb deposited at the ISOLDE facility at CERN, introduced inside a small volume shielded by a massive brass container, with provisions for gas inlet and outlet and corresponding valves. It was connected to a bypass of the gas system, such that the gas flow through the source set-up carries the gaseous Krypton isotope through the gas loop. A pulser trigger to the readout of the detector is used to collect clusters due to those isotopes which decay inside the volume of the detector.

In order to accumulate enough decay statistics for every TRD read-out pad, it was necessary to change the gas flow settings of the gas system despite an available source activity of about 3.8 MBq. In particular, the MWPCs at the end of the two layer gas flow arrangement within a SM would have not been sufficiently exposed to radioactive decays in order to perform a pad-by-pad calibration. This limitation could be overcome by an increase of the default gas flow of about 60-70 l/h per double layer for groups of SMs by about 40% and decreased in the other sectors by about 40%. After the record of a statistically sufficient data sample, the arrangement was modified to achieve sufficiently large samples for all pads. It was not possible to increase the flow for all SMs at the same time, since the compressors of the system cannot deliver such high flows and maintain the pressure gradient stably.
The gas system saw the lowest observed atmospheric pressure of 931 mbar and large variations to more common values above 950 mbar during the Krypton calibration. This complicated the stable operation in the special flow mode significantly. One complete system stop was triggered, when the sign of the atmospheric pressure variation changed. The problem could be solved by manual intervention within one hour after the stop of the system.

A.8. System running and incidences 2013–2015

A.8.1. Regular system leak rate

The Xenon loss of the full system has two components: the permanent reduction of gas molecules in the system and the amount of nominal mixture, which is replaced via intakes of N_2. The first component can be estimated from the injection into the gas system by the mixer, the second component is derived from the N_2 content increase measured by the gas chromatograph.
The system leak rate, which had to be replaced by gas injections, amounted at the end of data taking in 2013 with 13 SMs to about 0.8 l/h. The N_2 intake was approximately 0.09 l/h.
This loss exceeded the target value of a replacement of 10% or less of the total gas volume per year translating to a leak rate of 0.24 l/h for 13 SMs.

After the (re)connection of 9 SMs with 15 installed SMs[7] in fall 2014, all SM were set at an overpressure of about 1 mbar and isolated from the system for 1 day in order to find large leaks. By this procedure and subsequent sniffing, a leak at the outlet of the outermost layer of the SM in sector 6 was found. Sector 6 was not concerned by the reworks, hence the leak must have contributed to the leak rate in the past. The estimated leak rate at nominal overpressure amounted to about 0.05 l/h. This accounts for about 10% of the leak rate in 2012/2013.
It turned out that the largest leak after the completion and recommissioning of the TRD is caused by the purifier, where a permanent loss is introduced by the necessity of changing from one purifier column to the other. The issue and its mitigation is explained in detail in Section A.10.2. Without partially recovering the gas lost via the purifier, the injection of Xe-CO_2 mixture that are necessary to maintain the operation of the gas system amounts to 0.23 l/h for the full system in fall 2015. The effective system gas loss due to exchange with N_2 amounts to 0.06 l/h. The system gas lost via the purifier can be partially recovered reducing the required injection rate to 0.07 l/h. These rates are well below the maximal target leak rate of 0.3 l/h corresponding to a volume exchange of about 10% during one full year of running.
However, the leak rate was dominated in 2015 by two large leaks detailed in the following section.

A.8.2. Leak incidences in 2015

A leak occured in February 2015 directly downstream of two pressure reducers regulating the flow in front of the SMs. The reason for the leak were faulty safety valves, which protect the MWPCs from overpressure at the inlet in case of very large pressure fluctuations, where the protection of the SM at the outlet via the bubbler might be not sufficient. These valves are mechanical based on a spring, so no electrical power is needed, and are supposed to open, when a gas pressure of about 0.2 bar is exceeded at this point. The usual operating pressure ranges between 30 and 90 mbar. When the safety valve opens once, it may happen that it does not close gas tightly again. Hence, the valve must have opened due to unknown stress and did not close properly again. The leak could not be detected by static standard

[7] The remaining 3 SMs were connected later and the test was repeated in 2015 after the installation of all SMs, when no problem was found.

tests. The SMs are put during this test at an overpressure of about 1 mbar, which is also the approximate overpressure at the safety valve in absence of flow in contrast to about 65 mbar during regular running. The leaky valves were found by direct sniffing. All SMs were tested in this way, 2 out of 13 safety valves were found leaky. The concerned safety valves were closed by plugs. The leak rate amounted to about 10 l/h during the incident. Hence, the system was just able to maintain circulation by permanent gas injections via the standard flow meter for gas replacement from leaks. In total, about 4 m^3 Xe were lost to the atmosphere by this leak. Due to the large amount of gas lost, several measures were taken and further modifications are discussed, which are described in the following section about leak monitoring.
The same type of leak occured a second time in Novembre 2015. The leak rate amounted again to about 10 l/h. The total amount of lost gas was about 710 l. It was not necessary to stop the system during data taking, since the safety valve problem was suspected and the exhaust of the safety valve is reachable by a sniffing device. In this case, the safety valve of one SM failed and was closed by a plug. In addition, a smaller leak in a similar safety valve in the purifier was found at this occasion, which was also closed.

A.8.3. PLC power cut

In June 2015, a power cut affected the PLCs of the TRD gas system. The power cut resulted in the closing of all remotely steerable pneumatic connection valves and hence an isolation of all SMs. Unfortunately, it happened directly after the switch-off of the TRD front-end electronics. The SMs were isolated during the temperature decrease of the detector. Consequently, the volume of the detector gas shrinked and N_2 was sucked in from the back-up system. Since the detector DCS was switched off just after the front-end electronics state movement for maintenance, the temperature in the TRD could not be restored by ramping up again the front-end electronics. During this incidence, 85 l N_2 were sucked into the system.

A.9. Leak gas replacement and monitoring

After the first incident related to the safety valves, the leak monitoring was reevaluated and largely automatised.

During the data taking in 2013 and earlier, the injection of additional gas for gas leak replacements was activated when the high pressure buffer decreased below a fixed threshold. Since the high-pressure buffer serves as reservoir for gas absorption and delivery to the detector in case of changing atmospheric pressure, the injection rate of the detector cannot be directly used for fast gas leak monitoring in this running mode. After the leak in February 2015, the set-point of the buffer pressure was chosen to be dynamical following the expected behaviour from the atmospheric pressure according to the following formula:

$$P_{\text{buffer set-point}} = \frac{-P_{\text{atm}} \cdot V_{\text{detector}} + (P_{\text{max atm}} \cdot V_{\text{detector}} + P_{\text{min buffer}} \cdot V_{\text{buffer}})}{V_{\text{buffer}}} \quad \text{(A.2)}$$

where $P_{\text{buffer set-point}}$ denotes the high buffer pressure set-point, P_{atm} the atmospheric pressure, V_{detector} the part of the gas system, which is adjusted relative to the atmospheric pressure[8] and dominated by the volume of the SMs, $P_{\text{max atm}}$ the maximal atmospheric pressure for which the buffer pressure set-point is calculated by this formula, $P_{\text{min buffer}}$ the minimal buffer pressure, which is reached at the maximal atmospheric pressure $P_{\text{max atm}}$ and the effective volume of the high pressure part of the detector V_{buffer}, which is dominated by the buffer volume. The maximal buffer pressure is set to $P_{\text{max atm}} = 997$ mbar. If this atmospheric pressure is exceeded, the system starts to inject gas to keep the minimal buffer pressure $P_{\text{min buffer}}$, which is usually set to 0.65 bar. The formula does not take into account temperature changes, which occur during the switching on and off of the front-end electronics of the TRD. The gas in the detector is adjusted for the front-end electronics in on-mode. The issues related to the temperature variations are detailed in Section A.10.3.

Gas injection start when the set-point and the actual measured buffer pressure differ by about 0.04 bar in the high pressure buffer, which corresponds approximately to 40 l gas volume at ambient pressure. The injection stops when the set-point is reached again via injections. This dead band for the gas injection is in place in

[8] Constant off-sets with respect to the atmosphere cancel in this formulation and do not matter for the set-point calculation.

order to avoid frequent switching off and switching on of the mixer unit, since the granularity of the buffer set-point is only 0.01 bar. However, this procedure would result in 4 hours long injections, which is unfortunate, since automatic leak alarms based on the injection rate would only be possible after significantly injection durations. However, when a freshly regenerated purifier column is reconnected to the system, it is evacuated prior to the connection as explained in Section A.10.2. This evacuation results in a drop in the flow of the system at the position of the purifier and, hence, a drop of the pressure of about 0.1 bar in the high pressure part for about 4 s. This drop triggers the start of the injection that remains active although the pressure deficit is much smaller than 0.04 bar under equilibrium conditions. In this way, injections typically occur with the frequency of the purifier swapping and take typically about 1 to 2 hours. Therefore, several purifier swappings are necessary to estimate the leak rate despite the regular injections. However, in this operational mode, an alarm is put in place in the detector control system of ALICE, if the injection duration of the flow meter exceeds the usual duration. In this way, a potential leak is detected already after the loss of only a few tens of litres, which has to be compared with the total system volume at ambient pressure of more than 27 m^3.

Furthermore, the possibility to remove or to replace the safety valves with less error prone devices to protect the SMs is in discussion with the gas group of CERN.

In order to improve the Xenon supply reservoir measurement in addition to the information of the input flow, the Xenon supply bottle is permanently weighed since Octobre 2015 and the measured value is published in the gas system control system. Previously, only the bottle pressure was available, which provided only an estimate of the available Xenon in absence of a precise temperature measurement, since highly compressed Xenon is at ambient temperature close to its critical temperature showing a very shallow dependence of the density on the pressure according to the Van-der-Waals equation of state. In addition, the Xenon bottle was moved within the gas supply building in direct vicinity of the mixer in order to avoid additional pipe length of about 30 m.

A.10. Design modifications and upgrades

A.10.1. Gas connections

In the design for the SM triplets in the sectors 12-13-14 as well as 3-4-5, only one pressure sensor is foreseen for the supervision of the pressure of the three SMs together. In order to guarantee a low flow impedance and hence a low pressure gradient between the outlets of the three SMs, it was decided to add connection pipes (bellows) with an inner diameter of 40 mm between the manifolds of the concerned SMs. It was verified by eye inspection of the three bubblers and the electronic measurement available with the pressure sensor that the observed overpressure during the flushing with CO_2 with a flow of 50 l/h per double layer prior to the installation did not exceed about 1.7 mbar. Fig. A.7 shows the usual bellow arrangement in a single SM and Fig. A.8 shows the design choice for the triplet SM arrangement. The small lines at the pressure sensors and the bubblers indicate the connection to the back-up system, the arrows the gas flow in standard operation mode.

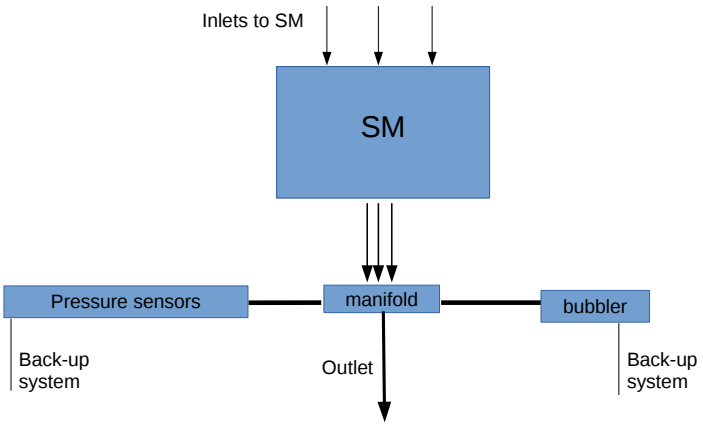

Figure A.7.: Default layout

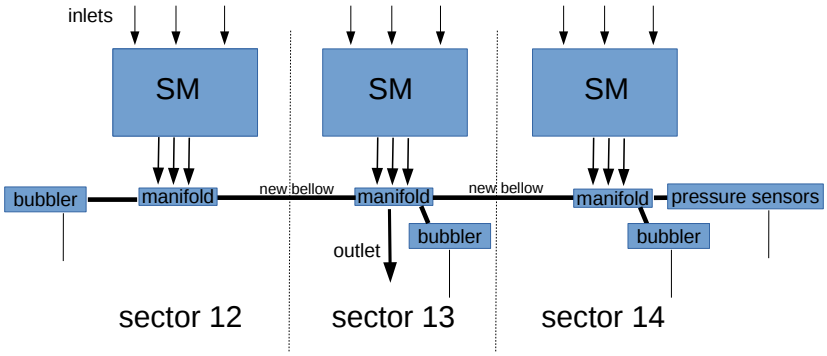

Figure A.8.: Modified triplet layout

The schematic view of the piping on the A-side connecting the SM with the gas system is shown. The left hand side shows the default set-up and the right hand side shows the set-up for the triple SMs 12-13-14 and 03-04-05.

A.10.2. Purifier

As mentioned, the purifier is the largest leak source for regular system running. At the beginning of the running in 2015, the purifier column was after the end of its service period closed by pneumatic valves from the system and flushed with CO_2. Hence, the detector Xe-CO_2 gas mixture, which was within the column at the time of the column operation was lost. In addition, the purifier column was after its regeneration with H_2 rich Argon again flushed with CO_2. The column was connected to the gas loop at the approximate overpressure of the system in this position, which is around 1 bar. Hence, since the Xe-CO_2, which was previously inside the column was effectively replaced by pure CO_2 yielding not only to a loss precious Xenon, but effectively to a gas exchange between the detector mixture and pure CO_2. This exchange of gas happening at every purifier swapping could be observed in the gas chromatograph measurement, which took place about every 4 hours. The gas exchange amounted to about 35 l Xenon loss per swapping corresponding to a decrease of the Xenon concentration of the gas mixture of roughly 0.14% at every swapping. As an immediate measure, the purifier cycling time was enlarged from initially around 2 to 4.2 days. A further prolongation was not done to keep the H_2O content of the detector below 400 ppm. The longer swapping frequency resulted in a Xenon loss rate via purifier induced gas exchange of about 0.37 l/h.
As a second measure, the CERN gas group changed the software such that the column is evacuated after its connection and prior to the connection to the loop. By this change, no Xenon should be saved, but the mixture should stay stable in contrast to the previous situation. This goal was achieved. Furthermore, the additional leak rate in the gas injection was only 0.19 l/h, although the mixture stayed now constant at the swappings. The latter leak rate corresponds also roughly to the expectation of a purely volume exchange based leak rate as naively expected. The fact that the leak rate and the gas exchange rate differ seems to indicate that the gas exchange was not only induced by a pure gas volume exchange, but maybe to an additional absorption process, which was absent with the new software setting. However, no such mechanism could be identified.
Finally, the gas, which was pumped out of the purifier after the isolation from the system could be recovered by a hardware modification, which transfers the recovered gas from the purifier from a small bottle of 20 l and further to a storage bottle. The composition of the retrieved gas mixture measured by the gas chromatograph gave

an approximately doubled content of CO_2 compared to the gas system mixture. It is planned to reinject the gas recovered at every purifier swapping back into the system in order to limit the total fresh gas injection of the system.

A.10.3. Cooling compensation of temperature changes

As explained in the section on the regular running, it was found out that the volume of the gas of the TRD increased (decreases) by about 400 l, when the front electronics (FEE) are switched on, implying a change of the average gas temperature by more than 3 K. The time constant for this approximately exponential temperature change amounts to about 1 h, which is a rather rapid change of the gas system running conditions, which does not happen due to atmospheric pressure changes. This change of gas volume lead during the 2015 running to a full system stop. Therefore, any ramp-down or ramp-up of the FEE requires close monitoring. Since the gas volume is changing strongly, a stop of the gas system circulation during a FEE ramp-up or ramp-down can lead to significant N_2 intake or waste of detector gas in a much smaller time window than gas losses or intakes during circulation stops from usual atmospheric pressure changes. it was therefore decided to do intentional ramp-up or ramp-down of the FEE with only 1/3 of the detector at a time.
In addition to the impact on the gas system of the TRD, it is clear that such strong temperature variations can also affect the temperature stability of neighbouring detectors despite the thermal screens in place. In particular, the TPC running with an unsaturated drift gas requires a temperature stability of 0.1 K to reach its nominal performance. Therefore, it was decided to evaluate the possibility to equilibrate the average effect of the FEE on/off action by changing the cooling temperature of the TRD. This was successfully tested in Decembre 2015. However, to achieve the necessary change of around 3 K gas temperature, the cooling temperature has to be changed by about 6 K. The exact running conditions for the automatic cooling temperature adjustments will be defined in early 2016.

B. J/ψ measurements in pp and p–Pb collisions with ALICE at mid-rapidity in 2015-2018

A main limitation of the measurement of the J/ψ nuclear modification factors in Pb–Pb collisions and in p–Pb collisions with the central barrel of ALICE is the lack of appropriate pp reference measurements at the same collision energy. Hence, it is instrumental to explore the potential of future data taking during Run 2 of the LHC until 2018. The contribution of the recorded minimum-bias events and TRD triggered data to an improvement of the situation are detailed in the following.

B.1. Minimum-bias collisions

The potential of future minimum-bias data taking with the central barrel is investigated for the p_{T}-integrated and the p_{T}-differential cross sections at $\sqrt{s} = 5$ TeV. The following assumptions were used:

1. The J/ψ cross section is used from the interpolation ($\mathrm{d}\sigma/\mathrm{d}y \times \mathrm{BR}(\mathrm{J}/\psi \rightarrow \mathrm{e}^{+}\mathrm{e}^{-}) = 365$ nb) as introduced in Section 5.6.2.

2. The minimum-bias trigger cross section amounts to about 49 mbarn assuming the same efficiency for the minimum-bias trigger for inelastic hadronic collisions as at $\sqrt{s} = 7$ TeV and a scaling of the inelastic cross section as shown in Ref. [300].

3. The $Acc. \times eff.$ factor is assumed to be same as in p–Pb collisions in 2013.

4. The S/B for the signal extraction of the J/ψ counts as in pp data at $\sqrt{s} = 7$ TeV as measured in Ref. [151] for a requirement of a hit in either of the first two layers of the SPD for both J/ψ daughter tracks.

For the systematic uncertainty, for simplicity, a constant uncertainty of 8% for the p_{T}-differential uncertainty except of the uncertainty due to the luminosity and branching ratio was assumed. This is in line with the precision achieved in p–Pb collisions for S/B background values achieved in pp collisions as shown in Table J.1. For the p_{T} integrated result, a systematic uncertainty except of the branching and the luminosity contribution of 6% was used for the estimate by assuming that the signal extraction uncertainty can be substantially decreased to 3% thanks to a better $S/B = 1.5$ in pp collisions than in p–Pb collisions. The results are given in Tab. B.1. The estimates illustrate that a similar precision as the currently available p_{T}-integrated interpolated reference cross section requires about 100 million minimum-bias triggered events. However, a substantial improvement of the pp reference cross section requires either a much larger data sample or the cancellation of systematic uncertainties in the nuclear modification factors. The cancellation of systematic uncertainties due to the signal extraction appears to be difficult due to different background conditions. A cancellation of uncertainties due to PID is complicated by the change of the TPC gas from a Neon to an Argon-based mixture after the data taking period in 2013. A reduction of the uncertainty for the p_{T}-differential nuclear modification factors appears to be out of reach for conceivable number of recorded minimum-bias collision data samples.

A data sample of about 100 million minimum-bias collisions was recorded by ALICE in 2015 at $\sqrt{s} = 5$ TeV and can be hence used to check independently the size of the interpolated reference cross section, but it will be difficult to improve the precision compared to the interpolation procedure.

The central barrel detectors without the SDD can be read-out with about 2 kHz in pp collisions at low interaction rates ($O(30)$ kHz) corresponding to low pile-up in the TPC. As example, a data sample of 500 million collisions corresponds therefore roughly to a pure recording time of about 70 h after subtraction of all inefficiencies and without consideration efficiency losses on the level of the event selection. The estimated uncertainties for such a data sample are given in the Tab. B.1. The integrated pp reference cross section precision could be substantially improved with this data sample. A data sample of this size would probably also allow for a further

reduction of the systematic uncertainties thanks to a better control of the signal extraction and the particle identification.

p_{T}-bins in GeV/c	p_{T}-int.	0-1.3	1.3-3.0	3.0-5.0	5.0-7.0	7.0-10.0
$\mathrm{d}\sigma/\mathrm{d}y$ (μb)	6.19	1.22	2.71	1.54	0.47	0.166
BR $\times\ \sigma|_{y\in[-0.9,0.9]}$ nb	661	131	290	164	50	18
$N_{\mathrm{J}/\psi} \in [-0.9, 0.9]$ per triggered event	$1.35 \cdot 10^{-5}$	$2.7 \cdot 10^{-6}$	$5.9 \cdot 10^{-6}$	$3.4 \cdot 10^{-6}$	$1.0 \cdot 10^{-6}$	$3.6 \cdot 10^{-7}$
$Acc. \times eff.$	0.092	0.085	0.06	0.092	0.14	0.15
Detected J/$\psi \in [-0.9, 0.9]$ per triggered event	$1.2 \cdot 10^{-6}$	$2.3 \cdot 10^{-7}$	$3.5 \cdot 10^{-7}$	$3.1 \cdot 10^{-7}$	$1.4 \cdot 10^{-7}$	$5.4 \cdot 10^{-8}$
expected S/B	1.5	1	2	3	5	10
syst. uncert. except lum./BR.	6%	8%	8%	8%	8%	8%
luminosity uncertainty	3.7%	3.7%	3.7%	3.7%	3.7%	3.7%
Detected J/$\psi \in [-0.9, 0.9]$ for 10^6 events	124	23	36	31	14	5
stat. uncertainty for 10^6 events	12%	30%	21%	21%	29%	45%
total uncertainty for 10^6 events	15%	31%	22%	23%	30%	46%
Detected J/$\psi \in [-0.9, 0.9]$ for $5 \cdot 10^6$ events	621	114	178	154	72	27
stat. uncertainty for $5 \cdot 10^6$ events	5%	13%	9%	9%	13%	20%
total uncertainty for $5 \cdot 10^6$ events	10%	16%	13%	13%	16%	22%
current pp reference unc. (corr. or p_{T}-integrated)	16.6%	16.6%	16.6%	16.6%	16.6%	16.6%
current pp reference unc. (uncorr.)	/	7.3%	4.8%	5.7%	12.8%	15.7%

Table B.1.: Estimated statistics and uncertainties for potential future pp reference measurements with minimum-bias collisions compared with the current pp reference uncertainties.

B.2. TRD triggered collisions

From the previous considerations, it is clear that minimum-bias collision based analyses in pp and/or in p–Pb with the current read-out capabilities of ALICE have clear statistical limitations. It is evident that a suitable trigger could improve the situation significantly. However, high precision measurements at high p_{T} are provided by the CMS and ATLAS at mid-rapidity. ALICE cannot compete at high p_{T} due to the absolute collision rate limitations of the central barrel detectors of about 700 (200) kHz in pp (p–Pb) collisions. Therefore, the focus of ALICE quarkonia measurements in pp and p–Pb collisions is the low-p_{T} regime, where it has unique capabilities and which is most important as a reference for the understanding of charm thermalisation in Pb–Pb collisions.

The use of calorimeter triggers was already exploited in a exploratory study [301]. The transverse momentum reach down to low p_{T} was very close to the one, which is already accessible by CMS and ATLAS.

The Transition Radiation Detector, being fully installed for the data taking in 2015, is able to provide electron triggers [302]. The trigger contributes to the ALICE trigger system at Level 1 and uses the stand-alone tracking capabilities of the TRD. The transverse momentum of the track crossing the 6 layers of the TRD is estimated by the offset of a straight line fit of the track points in the TRD with respect to the beam-line position. The ionisation signal of the the track is used as online information for the separation of electrons from hadrons. The TRD trigger system is detailed in Ref. [303].

In 2013 p–Pb data taking, two TRD electron triggers were used in p–Pb collisions to select electrons with an online p_{T} threshold of 2 GeV/c respectively 3 GeV/c. A first exploratory J/ψ measurement based on the TRD triggered data was presented in Ref. [224] and will be pursuit further [225]. A broader use of the electron trigger capabilities in the data taking in 2013 and earlier was prevented by the yet uncomplete azimuthal acceptance and by the background from $\mathrm{e}^{+}\mathrm{e}^{-}$ pair creation in the material between the TPC active volume and the TRD. Low p_{T} non-primary electrons from this source can fulfill the p_{T} condition of the TRD trigger due to their secondary vertex. This background source will be substantially reduced in the coming data taking by the exploitation of the curvature of the track within the TRD length in 2016. The sagitta of the track within the six layers of the TRD can be

measured and compared for consistency with the result of the straight line fit. This method rejects efficiently the electron and positrons from e^+e^- pair conversions at outer radii than the TPC with low transverse momentum. Basic considerations for the performance of these trigger after the inclusion of the late conversion rejection for future data taking in pp as well in p–Pb collisions were done in 2014. In this context, the performance of single electron triggers was investigated for pp collisions at 13 TeV. The result will be presented in the following. However, the considerations hold also at lower beam energies. In the mean time, the sagitta information is available at the online level without increase of the latency of the trigger decision and will be used in 2016 for electron triggering with the TRD [304].
For the calculation of the statistical reach of the trigger, the following ingredients are needed:

1. the online tracking efficiency relative to the ITS-TPC tracking efficiency,
2. single electron track efficiencies for the online particle identification and the sagitta selection for a given achieved event rejection factor,
3. the inspected rate of events for a rate assessment,
4. the cross sections of the observable,
5. and a simulation to translate the single track efficiencies into J/ψ efficiencies.

The online tracking and online PID as well sagitta selection efficiencies were provided by the TRD trigger group based on investigations in real data [305]. In order to accommodate the read-out of the trigger in the available band-width, a rejection of at least 1000 had to be required with respect to the number of inspected events. The rejection was also determined in data and was scaled up according to the increase in acceptance for the completed TRD. For the study in this thesis, a minimum-bias trigger condition was assumed as input trigger for the inspected events.
Due to stack and sector boundaries[1] and inactive chambers, not for all available trigger tracks information from all 6 TRD layers is available[2]. Since the resolution on the sagitta and particle identification information depends strongly on the number of available track layers and, for the sagitta determination, their position in

[1] A short overview of the TRD geometry is given in Appendix A.
[2] In fact, the online tracking requires at least 4 layers in order to build an online track.

radial direction, all possible track pattern had to be checked to identify the maximal possible single track efficiency still leading to an event rejection of 1000.

It turned out that for an online-p_{T} threshold of 2 GeV/c (3 GeV/c), an efficiency of the particle identification and sagitta selection of about 25% (33%) seemed achievable in pp collisions for a event level rejection of 1000. In fact, similar values for the single track efficiency could be reached in the final set-up [304][3]. In addition, the tracking efficiency of the TRD online system with respect to the default TPC-ITS analysis had to be estimated. On single track level for tracks with $|\eta| < 0.9$, $p_{\mathrm{T}} > 3.5$ GeV/c, the efficiency saturates at a level of 68% taking into account the not instrumented region in front of the PHOS calorimeter. The tracking efficiency drops by about 10% at $p_{\mathrm{T}} = 2$ GeV/c for positive tracks and for negative tracks on average[4]. For this first study, the tracking efficiency was taken to be constant above 2 GeV/c for simplicity.

The $Acc. \times eff.$ of the J/ψ decays was estimated based on a fast simulation and was estimated relative to the performance expected in minimum-bias collisions. First, the standard kinematic restrictions on both daughter tracks were imposed ($|\eta| < 0.9$ and $p_{\mathrm{T}} > 1$ GeV/c) and the trigger p_{T} condition on one of both decay daughters was required as in data by the trigger. This acceptance of the fast simulation was divided by the acceptance resulting from the standard offline acceptance ($|\eta| < 0.9$ and $p_{\mathrm{T}} > 1$ GeV/c). This ratio was used to compare the TRD trigger for a given inspected luminosity with the corresponding minimum-bias collision scenario. This procedure is only a first estimation, since the TPC PID requirements on the trigger electron can be softer than in the standard analysis thanks to the hadron rejection by the TRD. In addition, this estimate can deviate due to effects due to correlations of inactive detector channels in the SPD and the TRD, which are not taking into account with this simple set-up.

In order to translate the estimates in absolute numbers, the raw counts observed at $\sqrt{s} = 7$ TeV by ALICE in minimum-bias collisions were used, i.e., the same $Acc. \times eff.$ as in 2010 pp data taking was implicitly assumed. The cross section of J/ψ production was scaled up to the expected J/ψ cross section at $\sqrt{s}$ =13 TeV according to the $c\bar{c}$ cross section ratio expected by the FONLL set-up in Ref. [306, 307]. Since a minimum-bias trigger is used as precondition and in the minimum-bias trig-

[3] For a study in p–Pb collisions in 2014, the efficiency had to be decreased by a factor 2.4 (1.3) for the 2 GeV/c (3 GeV/c) threshold due to the lower rejection induced by the larger track multiplicity.

[4] The efficiency has a charge dependence in the on-set curve.

ger scenario, the corresponding change of the minimum-bias collision trigger had to be estimated as well. Assuming the same trigger efficiency for inelastic hadronic collisions as at $\sqrt{s} = 7$ TeV, the cross section for the firing of both VZERO scintillator arrays was taken to be 60 mb according to the parameterisation of the energy dependence of the inelastic pp cross section provided in Fig. 10 of Ref. [300].
The results of the approach are shown in Table B.2 in steps of e^+e^- pair p_T. At $p_T = 0$ GeV/c, the TRD trigger has practically no acceptance as expected due to the p_T requirement on one of the daughter p_T. The relative acceptance reaches already plateau for a e^+e^--pair $p_T > 3$ GeV/c. For $p_T = 3$ GeV/c, the plateau is reached for e^+e^--pair $p_T > 5$ GeV/c.
At $\sqrt{s}$ =13 TeV, the integrated luminosity was estimated to be 2.8 pb^{-1} in the data taking period from 2015-2017. This estimate was based on an inspection rate of minimum-bias collisions by the TRD of 30 kHz. These numbers would correspond to 5600 J/ψ counts in the p_T range $5-7$ GeV/c with the trigger with the p_T threshold at 2 GeV/c. In the same data taking period, it was assumed that a minimum-bias collision sample smaller by a factor 35 would be recorded in 2015-2017. The option of a dielectron trigger was also investigated, but not further pursued due to the strong acceptance and track efficiency losses compared to the single electron trigger rendering the trigger not more attractive than the single track trigger for realistic scenarios.
Since the minimum-bias collision based analysis at $\sqrt{s} = 13$ TeV is assumed to be already systematically limited for the p_T-integrated and the p_T-differential results up to 7 GeV/c, where the ALICE experiment has unique capabilities, the TRD trigger will very like not contribute to an improvement of these results, since the trigger will introduce additional systematic uncertainties which are not present in the minimum-bias collision analysis. However, statistics hungry analyses as the polarisation measurement, J/ψ-hadron correlations, the ψ(2S) cross section will certainly profit from the enhanced statistics. In addition, the measurement of the fraction of b feed-down, which does not require an absolute efficiency correction can also profit from these triggers. For the polarisation measurements, it has to be noted that at the lowest available e^+e^--pair p_T with the trigger, where the acceptance ratio has not reached yet a plateau, the acceptance is not independent of the emission angles of the electron and the positron in the rest-frame of the J/ψ and the efficiency as function of the emission angle is more sensitive to the onset behaviour of the p_T trigger threshold. Hence, polarisation measurements will be difficult in this corner of

phase space.

The collected statistics reach in pp collisions at $\sqrt{s}$ =5 TeV with the TRD trigger compared to minimum-bias collision data samples will strongly depend on the time sharing between minimum-bias triggers and the rare triggering with higher interaction rate and the inspection rate, which will be available for the TRD trigger. The efficiency ratios with respect to the minimum-bias collisions are the same as for the estimates at 13 TeV assuming no strong change of the achieved rejection.

For the ψ(2S), estimates indicate that a cross section measurement should be feasible with the total integrated TRD trigger statistics at $\sqrt{s} = 13$ TeV compared to a likely not feasible measurement with the minimum-bias trigger in the full data sample in 2015-2017.

p_{T}-bins in GeV/c	0-1	2-1	2-3	3-4	4-5	5-6	6-7	7-10
$Acc._{\cdot\text{trigger 2GeV}/c}/Acc._{\cdot\text{MB}}$	0.02	0	0	0.36	0.71	1.0	1.0	1.0
$Acc._{\cdot\text{trigger 3GeV}/c}/Acc._{\cdot\text{MB}}$	0	0.5	0.9	1.0	1.0	1.0	1.0	1.0
$N_{\mathrm{J}/\psi,\text{trigger 2GeV}/c}/N_{\mathrm{J}/\psi,\text{MB}}$	0.3	3	5.8	6.0	6.0	6.0	6.0	6.0
$N_{\mathrm{J}/\psi,\text{trigger 3GeV}/c}/N_{\mathrm{J}/\psi,\text{MB}}$	0	0	0.25	2.8	5.6	7.4	7.8	7.8

Table B.2.: Estimated J/ψ statistics comparison between minimum-bias (MB) trigger and TRD trigger assuming a ratio of the inspected luminosity of 35 in pp collisions.

C. Theory of charmonium production in pp and in p(d)–A collisions

In the following, a more extended introduction to the production of charmonium in hadronic collisions is given.

C.1. Treatment of incoming gluon flux

As explained in Section 2.3, there are different possibilities how to get from the non-perturbative bound states as the proton or the nuclei to an incoming partonic flux as input for the perturbative calculations. The main strategies in the description of charmonium will be introduced in the following.

C.1.1. Collinear factorisation

In the collinear factorisation framework, the prototypical Drell-Yan production cross section can be calculated in pp collisions according to the following formula:

$$\sigma_{\mathrm{tot}}(\mu_{\mathrm{F}},\mu_{\mathrm{R}}) = \int_0^1 \mathrm{d}x_1 \int_0^1 \mathrm{d}x_2 \sum_{\mathrm{ij}} f_{\mathrm{i}}(x_1,\mu_{\mathrm{F}}) f_{\mathrm{j}}(x_2,\mu_{\mathrm{F}}) \hat{\sigma}_{\mathrm{ij}}(x_1 x_2 S, \alpha_s(\mu_{\mathrm{R}}^2), \mu_{\mathrm{F}}, \mu_{\mathrm{R}}), \tag{C.1}$$

where μ_{F} denotes the factorisation scale, μ_{R} the renormalisation scale, x_1 and x_2 the Bjorken-x values of the two colliding partons, f_{i} and f_{j} the parton distribution functions of the parton types i and j, $\hat{\sigma}_{\mathrm{ij}}$ the partonic cross section (the hard

process matrix element calculable in perturbative QCD), S the square of the collision energy of the two protons in the rest frame. The dependence scale $\mu_{\mathrm{F}}(\mu_{\mathrm{R}})$ represents an artefact of the finite order of perturbative expansion remaining after the removal of the infrared/collinear (ultraviolet) divergences via factorisation (renormalisation). A pedagogic introduction to renormalisation and factorisation is given in Ref. [308] including a discussion of the practical applications of Equation C.1.

The Parton Distribution Functions (PDFs) are themselves non-perturbative input describing the incoming hadron wave function, but their evolution as a function of Q^2 can be described with the perturbative DGLAP evolution equation. The PDFs are process independent for a large class of applications, i.e., parton distribution functions can be extracted from the experimentally and theoretically clean deep inelastic scattering results and the extracted PDFs can be applied to calculate hadron-hadron collider observables. High precision data is provided by Deeply Inelatic Scattering (DIS) experiments, most notably for the low Bjorken-x regime by ZEUS and H1, which took data at HERA, the only ep collider ever built. Therefore, the parton distribution function are well constrained over a large parameter space in Bjorken-x and Q^2 as it is shown in Fig. 2.4. At the LHC, the collinear factorisation is applied successfully to a large variety of hard processes as jet-production, weak-gauge boson and Higgs-boson production. However, its application to charmonium production, in particular at low transverse momenta, might be limited: it is clear that at very low x and not too large Q^2, the picture of linear differential equations as the DGLAP evolution equations has to break down, since the system of partons, at low x dominantly gluons, cannot be handled as a dilute system of partons due to the steep increase of the phase occupancy. At some point, the possibility of gluon fusion and not only radiation of gluons has to be considered. In fact, to be more precise, the collinear factorisation is designed in the so-called Bjorken limit $Q^2, s \to \infty, x_{Bj} \approx Q^2/s = \text{const}$. Parametrically, the relevant scale, the so-called saturation scale, where the approximation should break down at latest can be estimated from HERA data. In the Golec-Biernat-Wusthoff dipole model [309], for $x = 10^{-3}$ probed by J/ψ production at mid-rapidity at low p_{T}, the saturation scale amounts to about 0.8 GeV in pp collisions. In the lead nucleus, the saturation scale can be estimated to be about 2.0 GeV due to the $A^{1/3}$-proportionality of the squared saturation scale. Both values are close to the rest mass of the J/ψ. In addition, at low x, there is a large phase space between the beam rapidity and the involved

parton rapidity for gluon emission, which has to be accounted for in a fixed order collinear factorisation approach by cumbersome calculations at higher order in α_s.

Other factorisation schemes might therefore provide better convergence behaviour, since there are suited for the limit $s/Q^2 \to \infty$. They may provide a better approximation at the LHC for the calculation of charmonium cross sections than the Bjorken limit. They will be discussed in the following. In this context, the different existing evolution equation for non-perturbative descriptions of the parton content of hadrons and their direction as well as the validity boundaries for their application in the $1/x$-Q^2 plane are depicted in Fig. C.1.

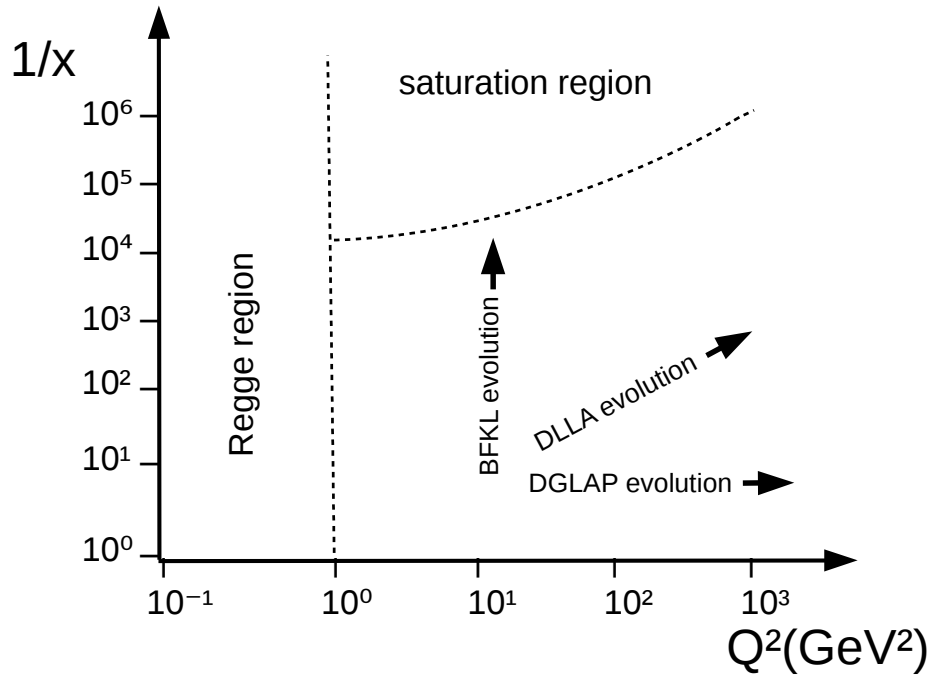

Figure C.1.: The direction of the different perturbative evolution equations for the non-perturbative parton distribution functions in the $1/x$-Q^2 plane as well as the boundary towards the non-perturbative regime as well as the one to the saturation regime, which will be discussed in more details in the following. The figure is adapted from Ref. [22].

C.1.2. k_{T}-factorisation

In collinear factorisation, the transverse dynamics of the partons are neglected. However, charmonium production takes place at the LHC at low Bjorken-x and the smallness of small transverse momenta of the gluon compared to the longitudinal momentum might not be justified any longer due to substantial gluon emissions prior to the hard partonic collision. The so-called k_{T}-factorisation formalism might therefore provide a better convergence behaviour at low Bjorken-x. Since the hard scale of charmonium production, especially at low p_{T} is about three orders of magnitude lower than the collision energy at the LHC, it might be relevant for LHC applications.
The used parton distribution function in this context are not the same as the ones used in the collinear framework. The underlying factorisation uses so-called unintegrated gluon parton distribution functions for the non-perturbative initial state, which describe 'reggeized' off-shell gluons. Although charmonium production at the LHC has been taken by some authors as a strong indication for the validity of the approach in the given kinematic regime of low x at the LHC in the colour singlet model [310] as well as in the NRQCD approach [311] at leading order, most publications on charmonium production at the LHC rely on collinear factorisation. No calculations for p–Pb collisions in this framework have been published so far.

C.1.3. Gluon saturation and color glass condensate

Finally, in the very small-x regime, due to the Froizart boundary, the parton distribution function densities need to stop growing at very small x. As already discussed, the gluon densities are that large that not only radiation, but also fusion of gluons needs to be taken into account and hence the differential equations governing the evolution need to become non-linear. Finally, a regime has to be reached where the density of gluons in phase space can no longer grow. In the limit of low x can be treated effectively as a system of classical gluon fields as dynamic degrees of freedom and static colour sources on the light cone. The described state has been named Colour Glass Condensate. A detailed introduction into the subject

is given in Ref. [114]. The non-perturbative description of the hadron gluon distribution is a kind of 'super'-PDF, a density matrix encoding not only the gluon densities, but also multi-gluon correlations in the hadron. The evolution equation for this object is the JIMWLK equation. However, it is not established at which Q^2 and x in which collision system, the corresponding formalism provides a better approximation than the collinear factorisation and whether even an overlap with the applicability of collinear factorisation is achievable despite the contrasting underlying physical pictures. This overlap was claimed to be observed for charmonium production in Ref. [119], which is at least surprising considering the different underlying physical pictures. The formalism has been applied to charmonium production for one of the two colliding hadrons (dilute-dense approximation) combined with different hadronisation models both in pp as well as in p–Pb collisions as discussed in depth in Section 6.

C.2. Transition from heavy quarks to the bound state: hadronisation models for charmonium

In order to calculate the production cross sections for charmonium states, it is necessary to provide the probability for the transition from the $c\bar{c}$ pair, the final state of the perturbative cross section calculation, to the different charmonium states. Conceptually different proposals were made and no consensus could be found up to now within the community which underlying physical picture is the correct one.

C.2.1. Colour evaporation model

The Colour Evaporation Model (CEM), first introduced in 1977 [312, 313], calculates the $c\bar{c}$ cross section below the open-charm threshold and redistributes this cross section between different charmonium states. These fractions are supposed to be collision energy independent and independent of the collision system and of kinematic variables. Hence, it contains only one free parameter per state for direct production and offers therefore good predictivity. The model does not implement a direct connection between the quantum numbers of the produced $c\bar{c}$ pair and the

bound charmonium state although rules can be put in by hand between the different states according to their degeneracies in the discrete quantum numbers. The procedure is justified by assuming that soft gluon emission will 'adjust' the colour, spin, parity and charge conjugation properties accordingly. These soft gluons are assumed to neither influence the kinematics nor to produce suppressions due to higher orders in α_s.

Despite the underlying picture is quite intuitive, the factorisation scheme is ad-hoc and it has not been justified based on QCD, although the non-perturbative factors can be partially matched to the non-perturbative parts within other models and constraints can be built in accordingly. The CEM is often seen rather as a tool for cross section estimates than as a rigorous approach to charmonium production. In principle, polarisation observables can be computed as well, but seeing the character of the model, it is questionable whether the calculation provides reasonable results. This model contains at leading order of α_s only contributions to the total cross section or the rapidity differential distribution in hadronic collisions with vanishing p_{T} when it is combined with collinear factorisation. This behaviour is similar to the calculation of inclusive W or Z gauge boson production at leading order. This kinematic behaviour is often referred to as $2 \to 1$ kinematics or 'intrinsic' transverse momentum scheme. For direct J/ψ production, this is in contrast to other models imposing the same quantum numbers for the $c\overline{c}$ pair as for the bound state, since the quantum numbers of the J/ψ require that a third gluon is attached to the quark line in order to build a colour neutral state with the same quantum numbers as J/ψ. In case that the leading order in CEM is dominating the rapidity differential cross section or the integrated cross section, the direct production is dominated by the $2 \to 1$ production scheme, the Bjorken-x of the contributing parton distribution functions can be uniquely identified based on the rapidity of the measured charmonium state by the following equation:

$$x_1 = \frac{m_{\mathrm{T}}}{\sqrt{s}} e^{-y_1} \tag{C.2}$$

In this formulae, x_1 denotes the Bjorken x of one of the two protons, y_1 the rapidity of the produced meson, the transverse mass $m_{\mathrm{T}} = \sqrt{m^2 + p_{\mathrm{T}}^2}$ with the transverse momentum p_{T} and the mass m of the produced particle and $\sqrt{s}$ the collision energy in the centre-of-mass frame ($\hbar = c = 1$).

C.2.2. Colour singlet model

The Colour Singlet Model (CSM) calculates the cross section of the $c\bar{c}$ pair in the proper quantum numbers corresponding to the ones of the charmonium state in question including colour neutrality with a vanishing relative velocity of the two heavy quarks for the s-wave states. The non-perturbative input for the transition of the $c\bar{c}$ pair to the charmonium states can be extracted from the experimentally known leptonic decay width of the corresponding states. Hence, this model has a strong predictivity. Conceptually, the production of P-wave production in the CSM is not consistent due to the appearance of an infrared divergence. The problem was solved within the framework of NRQCD. The leading-order diagrams for the direct production of J/ψ production are shown in Fig. C.2. A pedagogical introduction to the differences with respect to other approaches including a detailed explanation of the P-wave production problem and related references as well as the successes and failures of the CSM in the nineties and early 2000s is given in Ref. [314].
CSM leading-order calculations underpredicted the cross section of ψ(2S) at the Tevatron measured by CDF by a factor 50 [91][1]. Higher order corrections have shown to provide higher cross sections. At high transverse momentum, where the calculations as well as the experimental data is most precise, the production cross section has not been able to fully account for the experimentally measured higher cross section values up to now, when including the full NLO calculation at fixed order and real correction at NNLO [315]. However, it was argued that the colour singlet contributions could be sufficient to account for the dominant contribution to the total cross section at low transverse momentum [316]. Such a behaviour was also observed in k_{T} factorisation framework [311], whereas the calculation in the CGC framework [119] suggest a dominance of colour octet channels down to low p_{T}. Hence, it is still not settled whether the contribution of the hard production of $c\bar{c}$ pairs in a non-colour neutral state is contributing significantly to the charmonium cross section at low transverse momentum, which is a conceptually interesting question on its own.

[1] Similar problems were seen for the J/ψ, but the unknown contribution from χ_c-production prohibited the conclusion based only on prompt but not on direct J/ψ production data.

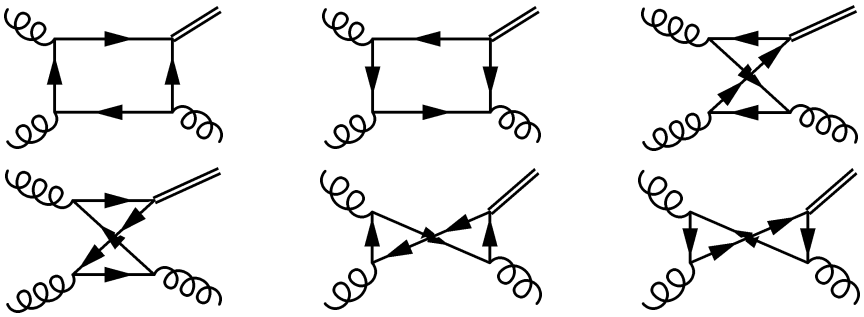

Figure C.2.: The leading-order diagrams contribution to direct J/ψ production in the CSM are shown.

C.2.3. Non-Relativistic QCD

The fact that charmonium can be treated as a non-relativistic system, i.e., $\beta = v/c$ significantly smaller than 1, enables to identify different momentum scales and hence a decoupling of steps in the production process:

1. perturbative hard production scale: the size of the transverse mass $m_T = \sqrt{(2 \cdot m_c)^2 + p_{\mathrm{T}}^2} \lesssim 3.0$ GeV as the relevant scale, justifies the use of perturbative QCD.

2. The quark momenta: the approximately non-relativistic nature of deeply bound charmonia enables to seperate the typical scale of the quark momenta $m_c \cdot \beta$ from the production energy scale.

3. The binding energy: the binding energy, i.e., the energy difference between the bound state mass and the open charm threshold, can be related with the virial theorem to $m_c \cdot \beta^2$.

This hierarchisation enables the application of non-relativistic effective field theory, which facilitates numerical calculations of bound state properties compared to calculations in full QCD.
The non-relativistic quantum chromodynamics approach, which was pioneered in Ref. [116], aims at a systematic incorporation of the colour singlet as well as colour octet amplitudes in one formalism. It 'integrates out' the modes related to the hard mass scale and keeps the dynamic degrees of freedom at the lower scales. The hierarchy between the mass scale and the lower scales, enables to derive an effective non-relativistic Lagrangian based on the QCD Lagrangian. The approach

provides universal non-perturbative long-distance matrix elements, if factorisation holds. The formalism was introduced for the calculations of decay amplitudes and production cross sections and provides a rough estimate of the order of magnitude of the non-perturbative transition amplitudes, often referred as Long-Distance Matrix Elements (LDME). The estimate of the size of the LDMEs proceeds via the involved powers of the relative momenta of the charm quarks. The in principle infinite number of non-perturbative factors can be therefore truncated at a given order of the relative quark velocity. At the LHC, amplitudes up to $O(v^4)$ are used to describe the cross section.

In principle, this procedure provides the most sound theoretical framework for the calculation of inclusive charmonium production. Nevertheless, it is unclear whether the scale separation for the charmonium is large enough to provide a reasonable expansion in velocity for the given system and it is not clear to which extent the underlying factorisation assumptions hold at comparatively low p_T. There are several fits to global data in different collision systems or only in a given data sample combined with the collinear factorisation approach. A summary of the different approaches and the differences between them is given in Ref. [115]. In the current form of fixed order perturbation calculations and of collinear factorisation, the formalism could not be applied successfully to low-p_T data. It has been argued that this might be solved by resummation of large logs [120], which is not done in the standard fixed order calculations. There is no agreement between the analyses although there is an agreement in the perturbative matrix elements, which are used. This fact is caused by different p_{T} ranges and data samples for the fit extraction of the LDMEs. In addition, polarisation observables are generally not well reproduced compared to the cross sections, which are usually used for the fitting. However, it has been argued that these discrepancies can be lifted, if only data at very high-p_T, $p_{\mathrm{T}}/M_\psi > 3$, are considered [280]. It is in this context unclear whether the break-down of the description at low p_{T} is related to the break-down of NRQCD as framework or rather to the break-down of collinear factorisation or the potentially missing of the resummation of kinematically enhanced factors, which are not taking into account in a fixed order calculation.

Furthermore, the measurement of η_c by LHCb [205] was seen as a strong argument of the break-down of this approach, since the calculations in [317] show explicitly that their calculation based on a global fit to charmonium world data in different collision systems is off with respect to the measurement by about a factor 2. Two

other groups disagree on this conclusion [318, 319].
Most recently, NRQCD factorisation has been combined with the combined collinear factorisation at low transverse momentum and a CGC approach at high transverse momentum in pp [119] as well as p–Pbcollisions [253]. The provided description of inclusive prompt J/ψ is very promising. It will be interesting to see whether the approach can also describe the polarisation observables and the η_c measurement. It was pointed out in Ref. [279] that the description provided by this approach points to a reduction of the gluon flux by about a factor 10. If this was true, the reduction of the corresponding cross sections would be also visible in other observables sensitive to such low Bjorken-x and which are perturbatively accessible, as for example to open charm production, which has been already measured both at mid- as well as at forward rapidity.

In summary, the quest is open for a conclusive description of charmonium hadroproduction within NRQCD.

D. Multiplicity correction impact on J/ψ yield determination

In the following appendix, the impact of the random character of the multiplicity correction on the number of extracted J/ψ candidates in this analysis is presented. In order to estimate the introduced fluctuations, the multiplicity correction was repeated 20 times with new random seeds for all events entering the analysis. The invariant mass distributions were obtained for all $N_{\text{tracklets}}$ bins separately. Finally, a signal extraction was performed for all multiplicity bins and trials with the standard signal extraction via mixed events. The root mean square of the distribution of retrieved raw J/ψ counts was evaluated to quantify the observed fluctuation.

The whole procedure was repeated for different reference tracklet numbers $N_{\text{reference}}$ and different event selections on the z coordinate of the reconstructed vertex z_{vtx}. For $N_{\text{reference}}$, the minimum, the average and the maximum of the distributions shown in Fig. 4.4 were selected.

Each figure presented in the following shows the root mean squares over the average numbers of retrieved signal counts in one multiplicity range for the different reference tracklet $N_{\text{reference}}$ and different z_{vtx} selections. The size of the fluctuations tend to be largest for the minimum as reference, which is easily explained by the largest size of the additional dispersion by the Poissonian correction. Figure D.1 shows the multiplicity range corresponding to about 47% of the inelastic cross section in terms of tracklet counts at the lowest multiplicities, Fig. D.2 the tracklets selection corresponding to the next 40% of the cross section and Fig. D.3 to the next 11%. The Figure corresponding to the largest multiplicities is shown in Section 4.3.5.

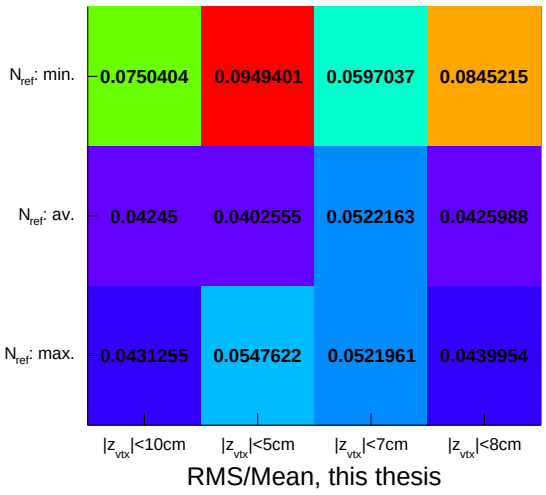

Figure D.1.: The root mean square of the extracted J/ψ signal from 20 repetitions of the Poissonian smearing divided by the corresponding average for different choices of the reference SPD tracklet number $N_{\text{reference}}$ and z_{vtx} selections is shown for the $N_{\text{tracklets}}$ bin with the lowest average multiplicity.

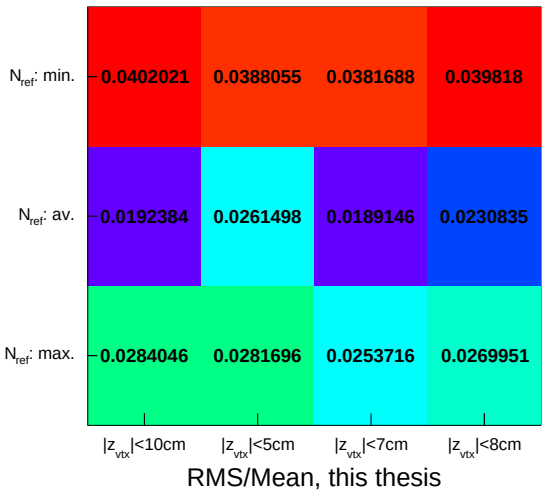

Figure D.2.: The root mean square of the extracted J/ψ signal from 20 repetitions of the Poissonian smearing divided by the corresponding average for different choices of the reference SPD tracklet number $N_{\text{reference}}$ and z_{vtx} selections is shown for the $N_{\text{tracklets}}$ bin with the second lowest average multiplicity.

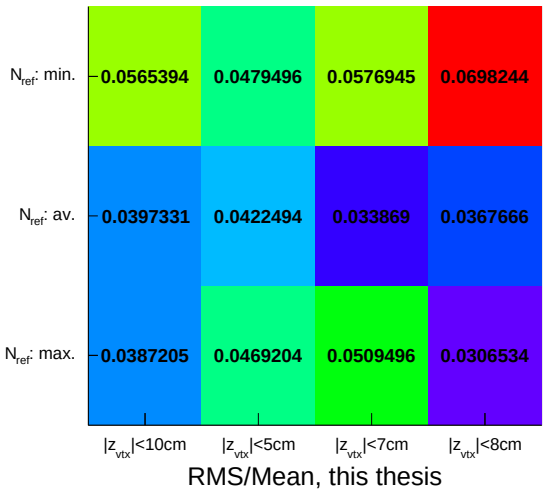

Figure D.3.: The root mean square of the extracted J/ψ signal from 20 repetitions of the Poissonian smearing divided by the corresponding average for different choices of the reference SPD tracklet number $N_{\text{reference}}$ and z_{vtx} selections is shown for the $N_{\text{tracklets}}$ bin with the second largest average multiplicity.

As discussed in Section 4.3.5, it is possible that events classified in bins of the corrected number of $N_{\text{tracklets}}$ exhibit much different charged-particle multiplicities. Although the additional dispersion by the Poissonian removes the dependence of the average number of tracklets as function of z_{vtx} integrated as function of multiplicity, the very different size of the dispersion as function of z_{vtx} could lead to very different distributions of true multiplicities contributing to a given bin of $N_{\text{tracklets}}$ after the correction as function of z_{vtx}.

In order to probe this possible problem, a check was done in simulations with the large minimum bias collision sample with the event generator DPMJET introduced in Section 4.2. The average number of generated charged-particle multiplicity correction as function of z_{vtx} was retrieved in the $N_{\text{tracklets}}$ slices, where the tracklet observable was corrected as in data. The charged-particle multiplicity on generator level includes all stable particles as well as weakly decaying light flavour hadrons and muons.

Figure D.4 shows the average charged-particle multiplicity on generator level on the y-axis as function of z_{vtx} for the bin with the lowest average multiplicity. The error bars correspond to the root mean square of the true multiplicity in the corresponding z_{vtx} bin. Figure D.5 shows the same quantity for the tracklets range with second lowest multiplicity. Figures D.6 and D.7 correspond to the two largest multiplicity ranges. Differences as function of z_{vtx} both for the mean and the root mean square values are clearly visible[1]. However, the variations of average charged-particle multiplicity are in the range of 4% or below except of very few exceptions and the dispersions as function of z_{vtx} are of similar magnitude. Given the precision of the overall measurements including the statistical limitations of the J/ψ yield measurement, the variations are acceptable. Evidently, for larger statistics, analysis changes should be employed to reduce these effects by either tighter selection criteria or by better strategies for the multiplicity correction.

[1] The bin corresponding to the largest average multiplicities is affected for large z_{vtx} by statistical limitations of the simulation.

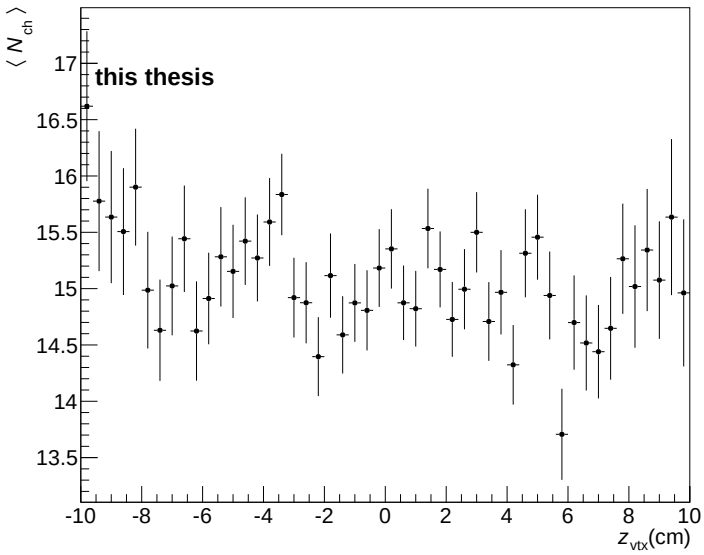

Figure D.4.: y-axis: true multiplicity in first bin analysis for maximum as reference multiplicity, x-axis: z-vertex position. Bin borders are taken to correspond to the same fraction of the MB cross section for both methods.

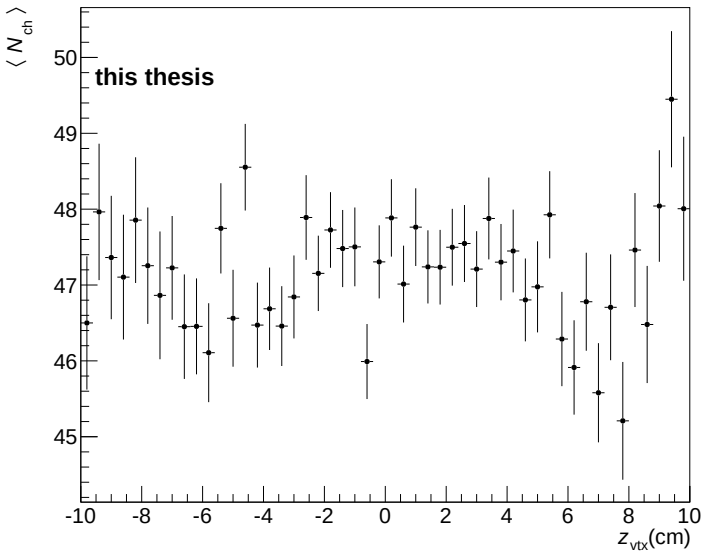

Figure D.5.: y-axis: true multiplicity in second bin analysis for maximum as reference multiplicity, x-axis: z-vertex position. Bin borders are taken to correspond to the same fraction of the MB cross section for both methods.

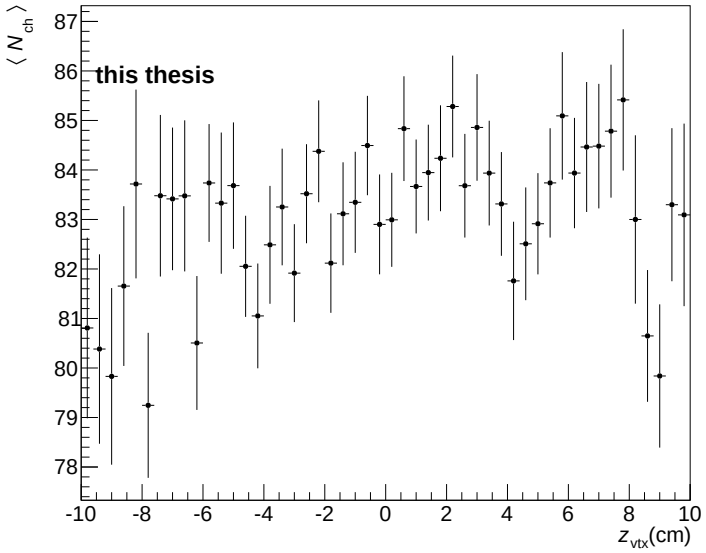

Figure D.6.: y-axis: true multiplicity in third bin analysis for maximum as reference multiplicity, x-axis: z-vertex position. Bin borders are taken to correspond to the same fraction of the MB cross section for both methods.

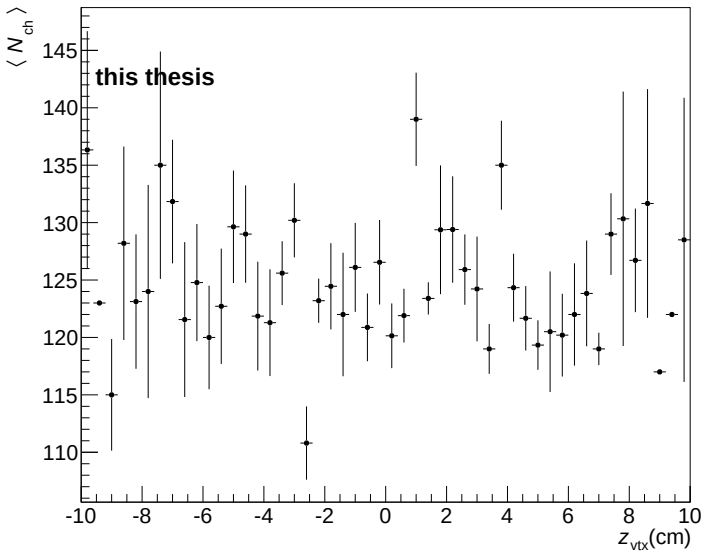

Figure D.7.: y-axis: true multiplicity in fourth bin analysis for maximum as reference multiplicity, x-axis: z-vertex position. Bin borders are taken to correspond to the same fraction of the MB cross section for both methods.

E. Correlation of multiplicity estimator with charged-particle multiplicity from simulation

It was mentioned in Section 4.3.5 that the multiplicity dependent measurement is not corrected for bin migration from one to the other multiplicity bin. Figure E.1 shows the correlation between the finally chosen multiplicity estimator ranges and the intervals in the primary charged-particle multiplicity on generator level based on the minimum bias collision simulation introduced in Section 4.2. The charged-particle multiplicity ranges are defined by choosing as borders the maximum in the distribution of charged-particle multiplicity in the $N_{\mathrm{tracklets}}$ bins for $25, 61, 102$. In absence of enough the statistics in the simulation, the uppermost bin was scaled according to the expectation from the α-factors introduced in Section 4.3.5. The statistics of the simulation does not allow to exploit the bin flow to non-measured bins at higher multiplicities.

This correlation matrix can be used to translate phenomenological calculations as function of charged-particle multiplicity into the estimator in this analysis. The off-diagonal elements are not negligible in particular for the bin migration between the two last multiplicity ranges, where they amount to about 20%. Hence, a folding of the theoretical calculations should be done for the comparison with the experimental data.

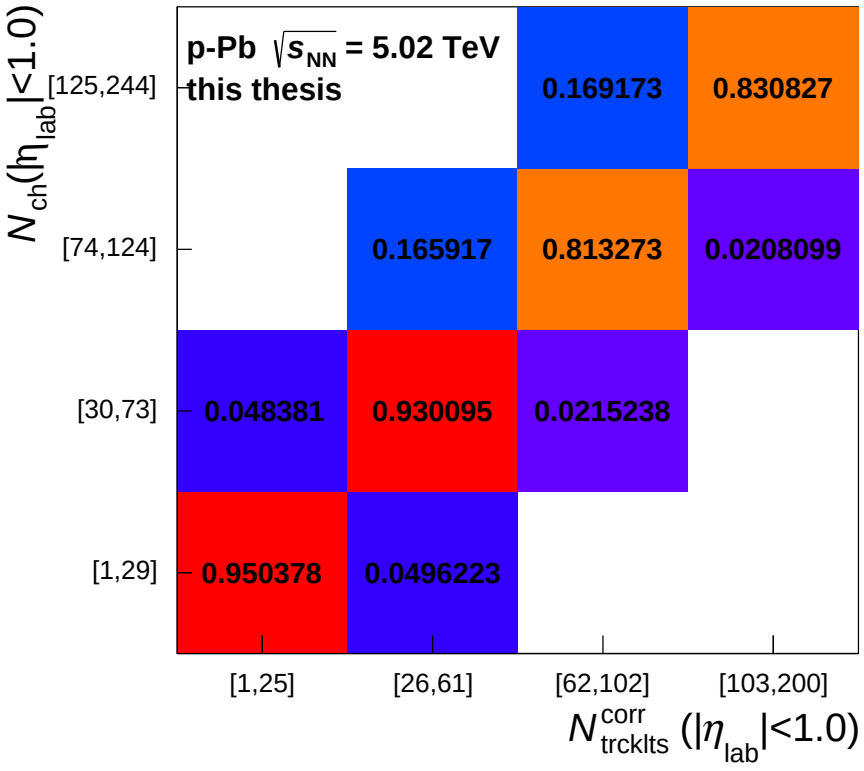

Figure E.1.: Probability of primary charged-particle multiplicity ranges $N_{ch}(|\eta| < 1.0)$ to result in measurements of $N^{\text{corr}}_{\text{trcklts}}$ in the measurement ranges according to event simulations.

F. Signal extraction and results from selection criteria variations

In the following, supplementary material concerning the signal extraction of the J/ψ counts in the analysis is given. First, alternative approaches to the followed mixed-event signal extraction will be detailed. Furthermore, additional mixed-event distribution ratios are shown the the variations of the selection criteria in the multiplicity and the centrality dependent analysis are listed.

F.1. Like-sign signal extraction

Instead of collecting pairs of electron and positron with opposite charges and compute the corresponding invariant mass, the pairs can be built from same charge pairs of electrons and positrons, like-sign pairs. All background sources listed in Section 5.5 except of the HFE background are expected to produce same charge pairs in close to same amounts as opposite charge pairs disregarding detector effects as, most notably, di-track acceptance differences. The HFE-HFE would not produce same-sign contribution neglecting potential contributions from double $c\bar{c}$-pair production in p–A collisions, if there was no neutral state mixing. For the B^0- and B_s^0-systems, the neutral state mixing is a well measured and large effect. For the D^0 system, the effect is very small [21] and negligible for the purpose of this work. Hence, the like-sign approach does not include the background from dileptons from charm and only parts of the $b\bar{b}$ background.
The di-track $Acc. \times eff.$ as a function of invariant mass is not the same for opposite-sign track pairs and like-sign pairs. The main effect of the symmetry breaking is the fact that the track $Acc. \times eff.$ for a given charge sign in a TPC sector is not symmetric around the middle of a given sector in azimuth.

In order to account for this difference in acceptance between like-sign and the opposite-sign pairs, which has an influence on the invariant mass shape, the like-sign distributions were scaled with the ratio of the mixed-event distributions[1] of like-sign and opposite charge pairs, which is the standard procedure for this kind of background approach.

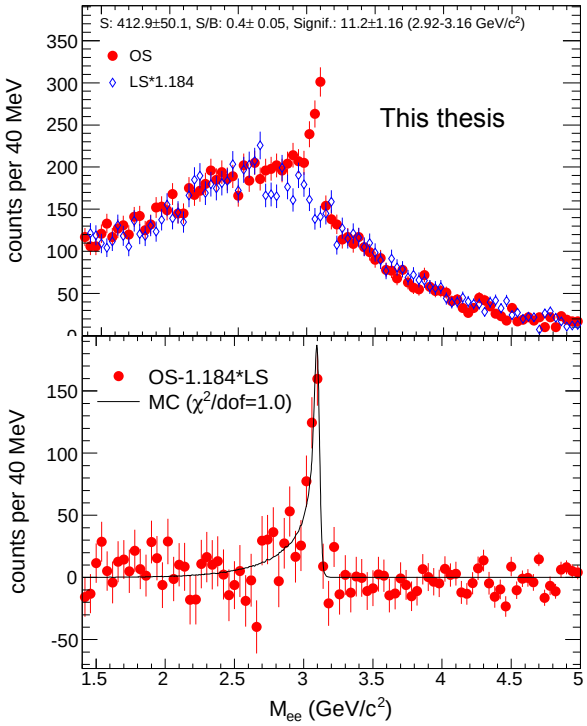

Figure F.1.: Like-sign signal extraction example for the standard selection criteria. The lower panel shows the comparison of the scaled arithmetic like-sign subtracted invariant mass distribution compared with the signal shape derived from the full detector simulation.

The unscaled invariant mass distribution of like-sign pairs as a background estimate is not sufficient in this analysis to account for the background, due to the HFE-HFE background, especially the $c\bar{c}$-pairs. Therefore, a scaling factor larger than unity is applied to the like-sign distribution to account empirically for this correlated background. The scaling factor is taken from the ratio of the integrals of the like-sign and the opposite-sign dielectron pairs in the invariant mass region from $[2.0, 2.5]$ GeV/c^2 and $[3.2, 3.7]$ GeV/c^2 and variations of these windows as in the mixed-event signal extraction.

The scaling factor is about 1.18 for the default cut choice case as shown in Fig. F.1

[1] The notion mixed-event is detailed in Section 5.5.2.

for the integrated signal extraction. The factor is larger, when a hit in the first layer of the SPD is requested for both daughter tracks and amounts to about 1.4. The scaling factor is an estimate of the $c\bar{c}$-pair background contribution. The signal counts were retrieved in the same invariant mass range as in the mixed-event signal extraction ($[2.92, 3.16]$ GeV/c^2).

It is not clear that the scaled like-sign method can provide a conceptually correct description: it assumes that the charm background, which dominates the difference between the two invariant mass distributions exhibits the same shape as the like-sign invariant mass distribution.

In order to probe the background description, the integral scaling regions used to match the distributions were varied as in the case of the mixed-event signal extraction. At the present stage of statistical precision, the matching of the background is good, e.g. the $\chi^2/n.d.f$ in the mass region $[1.4, 5.0]$ GeV/c^2 is 1.0 for the p_{T}-integrated case shown in Fig. F.1. With the given statistics, it is difficult to judge, if potential systematic deviations of the background shape appear with more candidate pairs as in the present analysis.

For this analysis, the geometrical mean approach as well as the arithmetic mean of the e^+e^+- and e^-e^--pair distributions were used to derive the like-sign invariant mass distribution for the p_{T}-integrated yield. The difference of the extracted signal between the two like-sign approaches amounts to 8 per mille for the default selection criteria. For the p_{T}-differential result, the arithmetic mean was only used.

The scaling approach of the like-sign was also validated in the integrated analysis by the comparison with the number of extracted signal counts by a subtraction of the unscaled like-sign distribution and a consecutive simultaneous fit of the background and the signal, which assumed a first or a second order polynomial for the background and the signal shape from simulations. The signal counts were retrieved by bin counting. The observed difference is below 1 per mille for the considered cut choice. However, for the p_{T}-differential results, the latter combined like-sign and fit approach was not enough constrained by the data points in order to give stable results due to the large statistical uncertainties for the two lowest bins in p_{T}.

Example signal extractions for the p_{T}-differential analysis in all bins are given in Fig. F.2, F.3, F.4, F.5, F.6.

The disadvantage of the like-sign approach in case of small statistics is the non-negligible amount of statistical uncertainty of the background itself, which influences the statistical precision of the finally extracted signal counts significantly. There-

fore, this method was only used for systematic checks throughout the measurement and not for the determination of the final results.

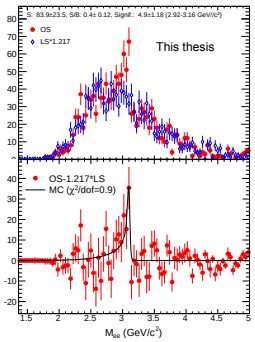

Figure F.2.:
$p_{\mathrm{T}} \in [0, 1.3]$ GeV/c

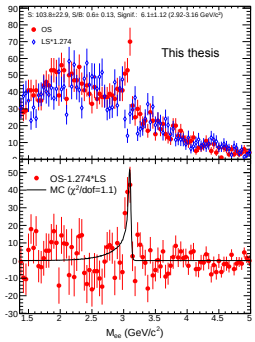

Figure F.3.:
$p_{\mathrm{T}} \in [1.3, 3]$ GeV/c

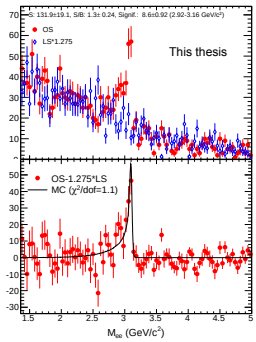

Figure F.4.:
$p_{\mathrm{T}} \in [3, 5]$ GeV/c

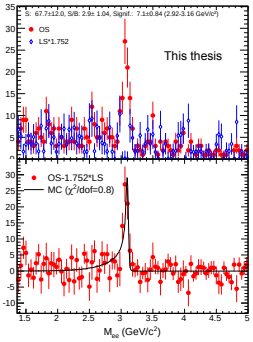

Figure F.5.:
$p_{\mathrm{T}} \in [5, 7]$ GeV/c

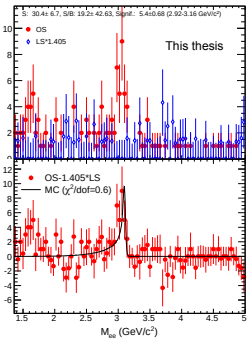

Figure F.6.:
$p_{\mathrm{T}} \in [7, 10]$ GeV/c

Like-sign signal extractions for the default selection criteria for the 5 considered p_{T} ranges. The lower plot shows the comparison of the scaled arithmetic like-sign subtracted invariant mass distribution compared with the signal shape derived from the full detector simulation.

F.2. Fit signal extraction

The background shape can be also modelled with a fit approach for the p_{T}-integrated yield and yields to results very close to the results obtained with the mixed-event method with the following procedure:

- a simultaneous fit of background and signal shape functions,
- a subtraction of the background function,

- and a raw signal determination by bin counting in the considered mass range for signal extraction $[2.92, 3.16]$ GeV/c^2.

As background function, the following shape was assumed $f_{bkg}(m_{ee}) = \frac{a+b\cdot m_{ee}^2}{c+d\cdot m_{ee}+e\cdot m_{ee}^2}$, where a, b, c, e were left as free parameters. Less complicated background descriptions as the one employed in the Υ analysis of CMS in Pb–Pb collisions [320], which deals with a similar background shape, or simple polynomials were not able to describe the background shape sufficiently well due to the peculiar shape introduced by the acceptance and particle identification choice.

The signal shape is taken from reconstructed simulation in order to account for the radiative decay and for bremsstrahlung. This function has only one free parameter, the absolute scale of the peak.

An example of this method for the p_{T}-integrated yield can be found in Fig. F.7 yielding to a difference with respect to the mixed event distribution of about 1.7% for the retrieved raw yield. Unfortunately, the functional shape is not able to describe properly the background shape in the lowest p_{T}-bin due to the steep dependence on mass and the low statistics. No stable fits could be obtained also after seeding the fit parameters of the background function with a fit to the like-sign mass distribution distribution. This is in particular because the chosen functional description allows for a divergence as a function of invariant mass. Therefore, the fit signal extraction is only used as cross check for the p_{T}-integrated yield.

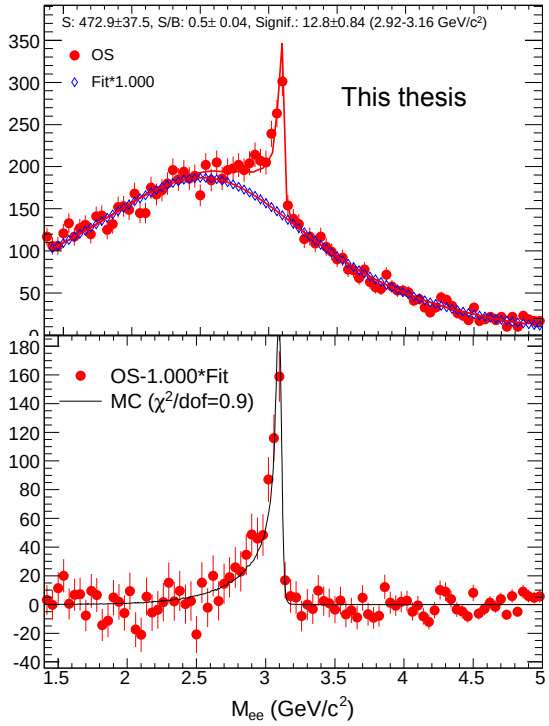

Figure F.7.: Fit signal extraction example for the p_{T} and multiplicity integrated result. The lower plot shows the comparison of the background fit subtracted invariant mass distribution compared with the signal shape derived from the full detector simulation.

F.3. Cut variations

In order to test the particle identification efficiency as well as the stability of the signal extraction by large variations of the hadron rejection, the integrated and p_{T}-differential result were also obtained with the like-sign and the mixed-event signal extraction for strong variations of the particle identification criteria as mentioned in Section 5.5.2 and in Section 5.7.2. We present the variation of the track p_{T} acceptance selection between $0.8, 1.0, 1.1$ GeV/c, the pion and proton rejection between $3.0, 3.5, 4.0\,\sigma$ and the requirement on the SPD, either requiring a hit in the first layer or in either of the two layers for both daughter candidate tracks. We will restrict the discussion here to the integrated results, which are less limited by statistics. For the like-sign signal extractions, the arithmetic mean was used. However, the geometric mean gives very similar results as detailed in Appendix F.1. For the following comparisons, the default matching procedure and signal extraction window

was used, which is introduced in Section 5.5.
The following overviews are based on an ordering of the selection criteria with the following index assignment:

- The index runs from 0 to 53.
- All odd cut indices correspond to a hit requirement in either of the two SPD layers for both decay daughter tracks, all even indices to a requirement in the first layer of the SPD.
- The $n\sigma_{\mathrm{TPC,pion}}$ criterion is always changed after two consecutive choices starting with the most open and ending with the most restrictive selection ($n\sigma_{\mathrm{pion}} >$ 3.0, 3.5, 4.0).
- The $n\sigma_{\mathrm{TPC,proton}}$ selection is always changed after six consecutive cases starting with the most open and ending with the most restrictive selection ($n\sigma_{\mathrm{proton}} >$ 3.0, 3.5, 4.0).
- After 18 consecutive indices, the track-p_{T} acceptance selection is changed in the following order: $p_{\mathrm{T}} > 0.8$, 1.0, 1.1 GeV/c.

Except of the pattern induced by the SPD requirement, the S/B increases monotonically, whereas the $Acc. \times eff.$ decreases with increasing index number.

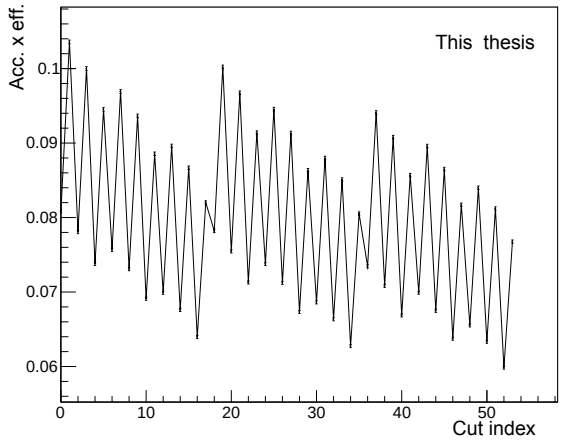

Figure F.8.: The $Acc. \times eff.$ factor as a function of the cut choice. The cut numbering scheme is explained in the beginning of chapter F.3.

These selections represent strong variations, since the raw signal counts and the

$Acc. \times eff.$ vary by about a factor two between the different cuts. The $Acc. \times eff.$ for the integrated case is shown in Fig. F.8[2]. Despite these large variations, the signal extractions has a similar statistical precision due to the variation of the S/B. We observe in Fig. F.9 that the matching of the background is non-optimal for the p_{T}-cut on the daughter track at 0.8 GeV/c (cut index 0-17) and for $p_{\mathrm{T}} > 1.0$ GeV/c and loose proton rejection of 3.0 σ (cut index 18-24). This empirical observation motivates to avoid these cut selection for the determination of the final result.
Additionally, we see in Fig. F.10 that the relative deviations between like-sign and mixed-event signal extraction for the signal yield are non-negligible significant, being dependent on the specific cut. For the default cut choice (cut index 27), the difference amounts to 10.5% for the p_{T}-integrated yield. The fact that the statistical uncertainty on the extracted signal yield is reduced compared to the like-sign signal extraction, has to be taken into account for such comparisons. The signal yields differ between 0.7 and 2.4σ with the signal yield extracted with the like-sign method within the non-shared statistical uncertainty as shown in Fig. F.11. The difference amounts to 1.3σ for the default cut choice. There are also statistically significant deviations between the different signal cut selections in both cases. The weighting of $Acc. \times eff.$ as function of p_{T} reduced significantly the spread of the derived results and is important to be taken into account. The root mean square of the distributions of the cut variations amount to 6.6% in case of the like-sign distribution and to 3.4% in case of the mixed event signal extractions. No obvious pattern independent of the signal extraction method indicating a dependence of the retrieved cross section due to a specific particle identification selection, p_{T} daughter tracks or SPD selection requirement could be found in detailed comparison of these selection criteria variations. The fact that the dependence on the selection criteria differ for the different signal extraction methods indicate that the variations probe mostly the signal extraction uncertainty and not the particle identification uncertainties.

An additional cross check with 2.5 σ hadron rejection track requirement on the daughter tracks was done for the p_{T}-integrated result with the like-sign signal extraction showing statistically consistent results with the stronger hadron rejections.

[2]No reweighting of the $Acc. \times eff.$ for the different p_{T}-distribution of the measured p_{T}-spectrum and the simulation p_{T}-spectrum has been done in this figure.

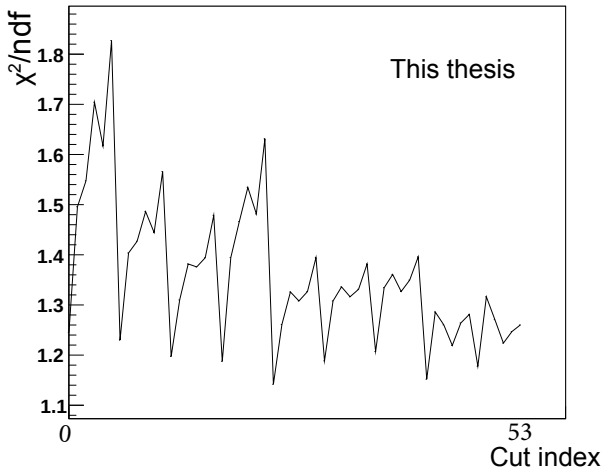

Figure F.9.: The χ^2/NDF (NDF=89) between the mixed-event background subtracted opposite-sign dielectron invariant mass distribution and the signal shape from MC-simulation for the invariant mass window $[1.4-5.0]$ GeV/c^2 for the p_{T}-integrated case. For the explanation of the cut index, see the beginning of chapter F.3.

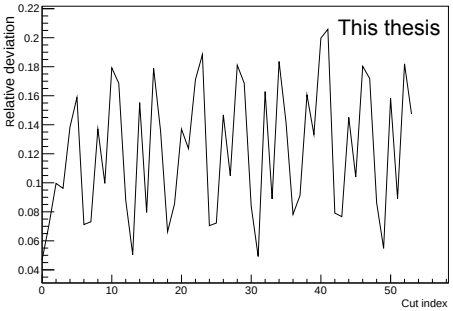

Figure F.10.: The relative difference of the efficiency corrected result for the like-sign and the event-mixing signal extraction scheme is shown. The cut numbering scheme is explained in the beginning of chapter F.3. The default cut is number 27.

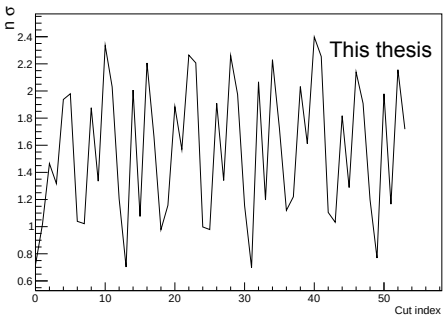

Figure F.11.: The difference of the efficiency corrected result for the like-sign and the event-mixing signal extraction scheme normalised by the non-shared statistical uncertainty ($\sqrt{|\sigma^2_{\mathrm{stat,LS}} - \sigma^2_{\mathrm{stat,ME}}|}$). The cut numbering scheme is explained in the beginning of chapter F.3. The default cut is number 27.

F.4. Mixed-event distribution ratio

In addition to the Fig. 5.22 for mixing categories based on multiplicity shown in Section 5.5.2, two additional examples of ratios of mixed-event invariant mass distributions are shown. As in the example, the deviations from unity in Fig. F.12 are at the level of 1% or below.

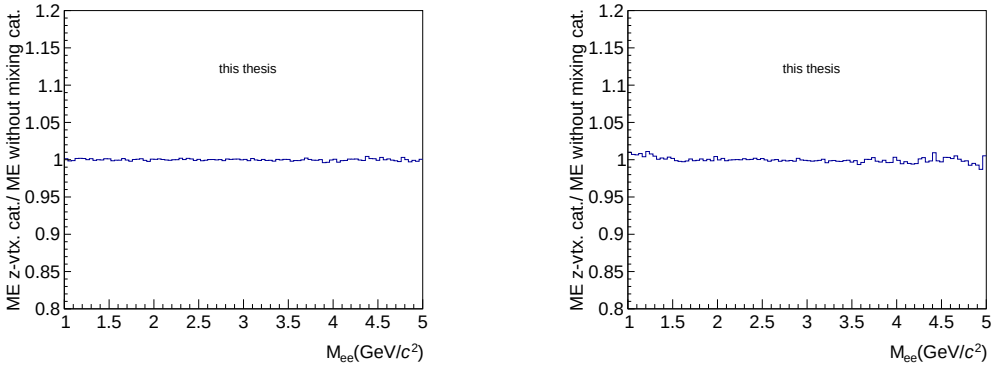

Figure F.12.: The ratios of normalised invariant mass distributions from mixed-event integrated over p_{T} are shown. The numerator is based on event mixing in categories of the z-coordinate of the event vertex, the denominator on event mixing without mixing categories. The left plot is for a requirement of a hit in either of two SPD layers for the contributing tracks whereas the right hand side plot is for a requirement of a hit in the first layer of the SPD and same cuts otherwise.

F.5. Signal extraction window variations

The variations for the signal extraction window used for the bin counting correspond to variations of the efficiency for this cut between 67% and 70.5% in the simulation, which is used for the correction.

F.6. List of signal extraction choices for the multiplicity and the centrality differential analysis

For the multiplicity and the centrality dependent analysis, the following combinations of background scaling ranges and signal extraction windows were used for the evaluation of the root mean square and the determination of the average value:

- signal extraction window: $m \in [2.8, 3.12]$ GeV/c^2, scaling window 1: $m \in [3.2, 4.9]$ GeV/c^2, scaling window 2: $m \in [1.4, 2.5]$ GeV/c^2
- signal extraction window: $m \in [2.8, 3.16]$ GeV/c^2, scaling window 1: $m \in [3.2, 4.9]$ GeV/c^2, scaling window 2: $m \in [1.4, 2.5]$ GeV/c^2
- signal extraction window: $m \in [2.8, 3.2]$ GeV/c^2, scaling window 1: $m \in [3.2, 4.9]$ GeV/c^2, scaling window 2: $m \in [1.4, 2.5]$ GeV/c^2
- signal extraction window: $m \in [2.84, 3.12]$ GeV/c^2, scaling window 1: $m \in [3.2, 4.9]$ GeV/c^2, scaling window 2: $m \in [1.4, 2.5]$ GeV/c^2
- signal extraction window: $m \in [2.84, 3.16]$ GeV/c^2, scaling window 1: $m \in [3.2, 4.9]$ GeV/c^2, scaling window 2: $m \in [1.4, 2.5]$ GeV/c^2
- signal extraction window: $m \in [2.84, 3.2]$ GeV/c^2, scaling window 1: $m \in [3.2, 4.9]$ GeV/c^2, scaling window 2: $m \in [1.4, 2.5]$ GeV/c^2
- signal extraction window: $m \in [2.88, 3.16]$ GeV/c^2, scaling window 1: $m \in [3.2, 4.9]$ GeV/c^2, scaling window 2: $m \in [1.4, 2.5]$ GeV/c^2
- signal extraction window: $m \in [2.88, 3.16]$ GeV/c^2, scaling window 1: $m \in [3.2, 4.9]$ GeV/c^2, scaling window 2: $m \in [1.4, 2.5]$ GeV/c^2
- signal extraction window: $m \in [2.88, 3.2]$ GeV/c^2, scaling window 1: $m \in [3.2, 4.9]$ GeV/c^2, scaling window 2: $m \in [1.4, 2.5]$ GeV/c^2
- signal extraction window: $m \in [2.92, 3.12]$ GeV/c^2, scaling window 1: $m \in [3.2, 4.9]$ GeV/c^2, scaling window 2: $m \in [1.4, 2.5]$ GeV/c^2

- signal extraction window: $m \in [2.92, 3.16]$ GeV/c^2, scaling window 1: $m \in [3.2, 3.7]$ GeV/c^2, scaling window 2: $m \in [1.4, 2.2]$ GeV/c^2
- signal extraction window: $m \in [2.92, 3.16]$ GeV/c^2, scaling window 1: $m \in [3.2, 3.7]$ GeV/c^2, scaling window 2: $m \in [1.4, 2.5]$ GeV/c^2
- signal extraction window: $m \in [2.92, 3.16]$ GeV/c^2, scaling window 1: $m \in [3.2, 3.7]$ GeV/c^2, scaling window 2: $m \in [1.6, 2.2]$ GeV/c^2
- signal extraction window: $m \in [2.92, 3.16]$ GeV/c^2, scaling window 1: $m \in [3.2, 3.7]$ GeV/c^2, scaling window 2: $m \in [1.6, 2.5]$ GeV/c^2
- signal extraction window: $m \in [2.92, 3.16]$ GeV/c^2, scaling window 1: $m \in [3.2, 3.7]$ GeV/c^2, scaling window 2: $m \in [2.0, 2.2]$ GeV/c^2
- signal extraction window: $m \in [2.92, 3.16]$ GeV/c^2, scaling window 1: $m \in [3.2, 3.7]$ GeV/c^2, scaling window 2: $m \in [2.0, 2.5]$ GeV/c^2
- signal extraction window: $m \in [2.92, 3.16]$ GeV/c^2, scaling window 1: $m \in [3.2, 4.04]$ GeV/c^2, scaling window 2: $m \in [1.4, 2.2]$ GeV/c^2
- signal extraction window: $m \in [2.92, 3.16]$ GeV/c^2, scaling window 1: $m \in [3.2, 4.04]$ GeV/c^2, scaling window 2: $m \in [1.4, 2.5]$ GeV/c^2
- signal extraction window: $m \in [2.92, 3.16]$ GeV/c^2, scaling window 1: $m \in [3.2, 4.04]$ GeV/c^2, scaling window 2: $m \in [1.6, 2.2]$ GeV/c^2
- signal extraction window: $m \in [2.92, 3.16]$ GeV/c^2, scaling window 1: $m \in [3.2, 4.04]$ GeV/c^2, scaling window 2: $m \in [1.6, 2.5]$ GeV/c^2
- signal extraction window: $m \in [2.92, 3.16]$ GeV/c^2, scaling window 1: $m \in [3.2, 4.04]$ GeV/c^2, scaling window 2: $m \in [2.0, 2.2]$ GeV/c^2
- signal extraction window: $m \in [2.92, 3.16]$ GeV/c^2, scaling window 1: $m \in [3.2, 4.04]$ GeV/c^2, scaling window 2: $m \in [2.0, 2.5]$ GeV/c^2
- signal extraction window: $m \in [2.92, 3.16]$ GeV/c^2, scaling window 1: $m \in [3.2, 4.9]$ GeV/c^2, scaling window 2: $m \in [1.4, 2.2]$ GeV/c^2
- signal extraction window: $m \in [2.92, 3.16]$ GeV/c^2, scaling window 1: $m \in [3.2, 4.9]$ GeV/c^2, scaling window 2: $m \in [1.4, 2.5]$ GeV/c^2

- signal extraction window: $m \in [2.92, 3.16]$ GeV/c^2, scaling window 1: $m \in [3.2, 4.9]$ GeV/c^2, scaling window 2: $m \in [1.6, 2.2]$ GeV/c^2
- signal extraction window: $m \in [2.92, 3.16]$ GeV/c^2, scaling window 1: $m \in [3.2, 4.9]$ GeV/c^2, scaling window 2: $m \in [1.6, 2.5]$ GeV/c^2
- signal extraction window: $m \in [2.92, 3.16]$ GeV/c^2, scaling window 1: $m \in [3.2, 4.9]$ GeV/c^2, scaling window 2: $m \in [2.0, 2.2]$ GeV/c^2
- signal extraction window: $m \in [2.92, 3.16]$ GeV/c^2, scaling window 1: $m \in [3.2, 4.9]$ GeV/c^2, scaling window 2: $m \in [2.0, 2.5]$ GeV/c^2
- signal extraction window: $m \in [2.92, 3.16]$ GeV/c^2, scaling window 1: $m \in [3.4, 3.7]$ GeV/c^2, scaling window 2: $m \in [1.4, 2.2]$ GeV/c^2
- signal extraction window: $m \in [2.92, 3.16]$ GeV/c^2, scaling window 1: $m \in [3.4, 3.7]$ GeV/c^2, scaling window 2: $m \in [1.4, 2.5]$ GeV/c^2
- signal extraction window: $m \in [2.92, 3.16]$ GeV/c^2, scaling window 1: $m \in [3.4, 3.7]$ GeV/c^2, scaling window 2: $m \in [1.6, 2.2]$ GeV/c^2
- signal extraction window: $m \in [2.92, 3.16]$ GeV/c^2, scaling window 1: $m \in [3.4, 3.7]$ GeV/c^2, scaling window 2: $m \in [1.6, 2.5]$ GeV/c^2
- signal extraction window: $m \in [2.92, 3.16]$ GeV/c^2, scaling window 1: $m \in [3.4, 3.7]$ GeV/c^2, scaling window 2: $m \in [2.0, 2.2]$ GeV/c^2
- signal extraction window: $m \in [2.92, 3.16]$ GeV/c^2, scaling window 1: $m \in [3.4, 3.7]$ GeV/c^2, scaling window 2: $m \in [2.0, 2.5]$ GeV/c^2
- signal extraction window: $m \in [2.92, 3.16]$ GeV/c^2, scaling window 1: $m \in [3.4, 4.04]$ GeV/c^2, scaling window 2: $m \in [1.4, 2.2]$ GeV/c^2
- signal extraction window: $m \in [2.92, 3.16]$ GeV/c^2, scaling window 1: $m \in [3.4, 4.04]$ GeV/c^2, scaling window 2: $m \in [1.4, 2.5]$ GeV/c^2
- signal extraction window: $m \in [2.92, 3.16]$ GeV/c^2, scaling window 1: $m \in [3.4, 4.04]$ GeV/c^2, scaling window 2: $m \in [1.6, 2.2]$ GeV/c^2
- signal extraction window: $m \in [2.92, 3.16]$ GeV/c^2, scaling window 1: $m \in [3.4, 4.04]$ GeV/c^2, scaling window 2: $m \in [1.6, 2.5]$ GeV/c^2

- signal extraction window: $m \in [2.92, 3.16]$ GeV/c^2, scaling window 1: $m \in [3.4, 4.0]$ GeV/c^2, scaling window 2: $m \in [2.0, 2.2]$ GeV/c^2
- signal extraction window: $m \in [2.92, 3.16]$ GeV/c^2, scaling window 1: $m \in [3.4, 4.0]$ GeV/c^2, scaling window 2: $m \in [2.0, 2.5]$ GeV/c^2
- signal extraction window: $m \in [2.92, 3.16]$ GeV/c^2, scaling window 1: $m \in [3.4, 4.9]$ GeV/c^2, scaling window 2: $m \in [1.4, 2.2]$ GeV/c^2
- signal extraction window: $m \in [2.92, 3.16]$ GeV/c^2, scaling window 1: $m \in [3.4, 4.9]$ GeV/c^2, scaling window 2: $m \in [1.4, 2.5]$ GeV/c^2
- signal extraction window: $m \in [2.92, 3.16]$ GeV/c^2, scaling window 1: $m \in [3.4, 4.9]$ GeV/c^2, scaling window 2: $m \in [1.6, 2.2]$ GeV/c^2
- signal extraction window: $m \in [2.92, 3.16]$ GeV/c^2, scaling window 1: $m \in [3.4, 4.9]$ GeV/c^2, scaling window 2: $m \in [1.6, 2.5]$ GeV/c^2
- signal extraction window: $m \in [2.92, 3.16]$ GeV/c^2, scaling window 1: $m \in [3.4, 4.9]$ GeV/c^2, scaling window 2: $m \in [2.0, 2.2]$ GeV/c^2
- signal extraction window: $m \in [2.92, 3.16]$ GeV/c^2, scaling window 1: $m \in [3.4, 4.9]$ GeV/c^2, scaling window 2: $m \in [2.0, 2.5]$ GeV/c^2
- signal extraction window: $m \in [2.92, 3.2]$ GeV/c^2, scaling window 1: $m \in [3.2, 4.9]$ GeV/c^2, scaling window 2: $m \in [1.4, 2.5]$ GeV/c^2
- signal extraction window: $m \in [2.96, 3.12]$ GeV/c^2, scaling window 1: $m \in [3.2, 4.9]$ GeV/c^2, scaling window 2: $m \in [1.4, 2.5]$ GeV/c^2
- signal extraction window: $m \in [2.96, 3.16]$ GeV/c^2, scaling window 1: $m \in [3.2, 4.9]$ GeV/c^2, scaling window 2: $m \in [1.4, 2.5]$ GeV/c^2
- signal extraction window: $m \in [2.96, 3.2]$ GeV/c^2, scaling window 1: $m \in [3.2, 4.9]$ GeV/c^2, scaling window 2: $m \in [1.4, 2.5]$ GeV/c^2
- signal extraction window: $m \in [3.0, 3.12]$ GeV/c^2, scaling window 1: $m \in [3.2, 4.9]$ GeV/c^2, scaling window 2: $m \in [1.4, 3.5]$ GeV/c^2
- signal extraction window: $m \in [3.0, 3.16]$ GeV/c^2, scaling window 1: $m \in [3.2, 4.9]$ GeV/c^2, scaling window 2: $m \in [1.4, 2.5]$ GeV/c^2

- signal extraction window: $m \in [3.0, 3.2]$ GeV/c^2, scaling window 1: $m \in [3.2, 4.9]$ GeV/c^2, scaling window 2: $m \in [1.4, 2.5]$ GeV/c^2

G. Acceptance and efficiency

G.1. Acceptance comparison between the Υ measurements with CMS and the J/ψ measurements with ALICE

Figure G.2 shows the CMS acceptance for Υ production with track selection choices of $p_{\mathrm{T}} > 3.5$ GeV/c for $|\eta_{\mathrm{lab}}| < 1.6$ and $p_{\mathrm{T}} > 2.5$ GeV/c for $1.6 < |\eta_{\mathrm{lab}}| < 2.4$.

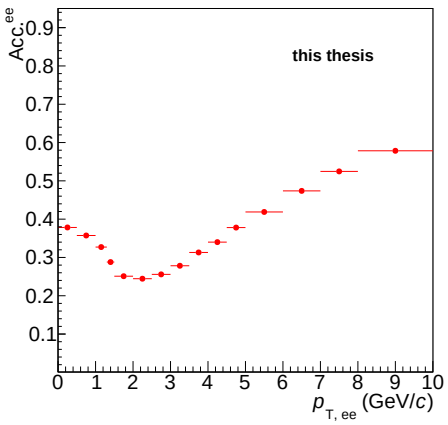

Figure G.1.:
ALICE $J/\psi \to e^+e^-$ acceptance

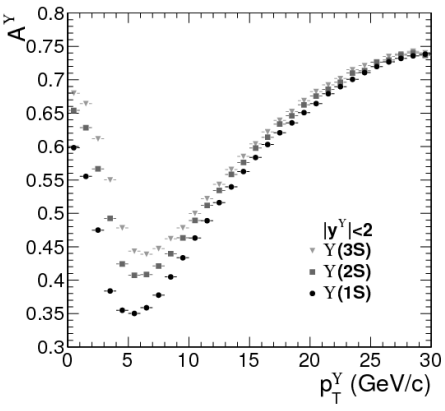

Figure G.2.:
CMS $\Upsilon \to \mu^+\mu^-$-acceptance

The comparison of J/ψ acceptance on the right hand side and Υ acceptances in CMS from Ref. [246] as a function of transverse momentum is shown. The acceptance definition for the ALICE case is given in Equation (5.12). The CMS definition can be found in Ref. [246].

G.2. Particle identification

Figure G.3 shows the comparison between data and simulation observables in the same way as in Fig. 5.16 for the selection criteria for e^+e^--pair $p_T > 5$ GeV/c. The Figs. G.4 and G.5 correspond to the Figs. 5.17 and 5.19. The Figures extend to higher momenta, since there are becoming more relevant for the e^+e^- pairs with p_T above 5 GeV/c as shown in Fig. 5.20.

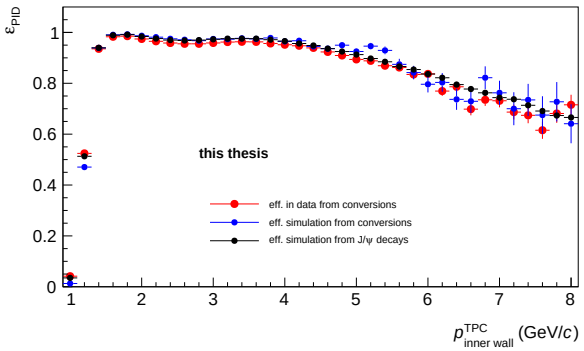

Figure G.3.: The single track PID-efficiency for electrons and positrons derived from conversions in data and in simulations and from J/ψ decays in simulation for the PID selection used for pair p_T above 5 GeV/c. Further details are explained in Section 5.4.4.

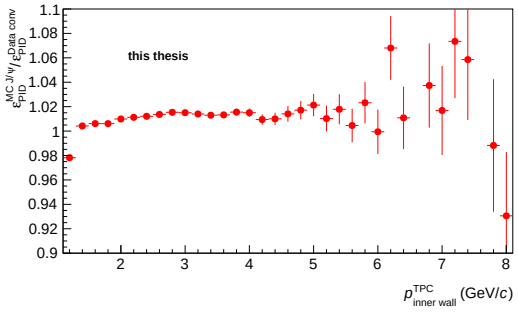

Figure G.4.:
J/ψ simulation vs. conversion data

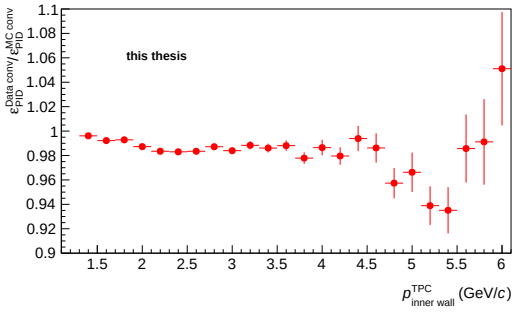

Figure G.5.:
conversions data vs. simulation

The ratio of single track PID-efficiencies derived from conversions in simulations and in data, and between conversions in data and from simulation of J/ψ decay daughters for the cut selection used for e^+e^--pair $p_T > 5$ GeV/c in the p_T-differential analysis. Further details are explained in the beginning of Section 5.4.4.

G.2.0.1. Cross check via alternative particle identification approach

Instead of applying directly $n\sigma_{\mathrm{TPC,pion}}/n\sigma_{\mathrm{TPC,proton}}$ rejection cuts, the position of the cut line as a function of 3 dimensions, momentum at the inner TPC wall, the pseudorapidity and the number of PID-cluster was translated in terms of a $n\sigma_{\mathrm{TPC,electron}}$ inclusion selection criterion. The retrieved cut histogram was then applied on data and on MC. This approach does not rely on the precision of the relative position of the different particle species, but only on the precision of the determination of the PID-parameters for electrons in data as well as in MC. Therefore, the standard MC PID-response can be used in this case to derive efficiencies from MC.

Since the number of tracks, which can be used to determine the position of the exclusion cuts, is finite, the method is limited by statistics, which determines the possible dimensionality and granularity. At higher momenta, where the number of tracks is decreasing, the lack of statistics does not allow for the determination of the cut position, therefore the lower limit of the inclusion cut is forced to be not larger than a given saturated level, $-0.5\sigma_{\mathrm{TPC,electron}}$. This has the drawback of higher pion contamination at high pair-p_{T} and the advantage of less problematic cuts deep in the electron distribution, where an imprecise knowledge of the position and width of the distribution translate in a increasingly large uncertainty of the efficiency.

Due to the statistical limitation in the granularity of the method and the related larger hadron contamination at the same efficiency, this method is not as performant as the standard strategy. The option was hence only used as a cross check. It provided consistent results with the standard veto cut approach based on MC tuned-on-data.

G.2.0.2. Further cross checks

The particle identification was tested by varying independently the pion and proton rejection between $2.5, 3, 3.5, 4$ σ and the track p_{T} acceptance cuts between $0.8, 1.0, 1.1$ GeV/c. These variations correspond to an efficiency change by a 25%

and 50% depending on pair p_{T}. No systematic effect could be seen beyond the statistically expected deviations or effects related to signal extractions for these very strong variation of the background conditions.

G.3. Tracking

The distribution of the variables used for the track quality criteria listed in Section 5.2.1 were compared in simulations and in data. The comparisons are shown on the level of unidentified tracks and tracks passing the electron selection of the analysis. Differences between electron and pion tracks are expected, since the average number of TPC clusters is higher for electrons than for pions thanks to the higher $\mathrm{d}E/\mathrm{d}x$ in the relevant momentum range. However, a comparison of the unidentified tracks should be considered as well, since the hadron rejection in the TPC can act as an implicit track quality cut.

First, we discuss the distributions of the unidentified tracks. The simulation results are based on the large minimum-bias collision data sample. The fraction of tracks in the acceptance ($p_{\mathrm{T}}>$ 1.0 GeV/c and $|\eta| < 0.9$), which are excluded by the quality cuts is both in simulations and in data below 1% for DCA-variables as shown in Figs. G.6 and G.7[1]. The same observation holds for the applied TPC cluster cut as shown in Figs. G.10 and G.11 as well as for the $\chi^2/N_{\mathrm{TPCcluster}}$ variable provided in Figs. G.9, G.8 under the condition of all other cuts including the requirements on the ITS and the TPC-PID. No information on the generator level was required for the simulation distributions.

The tests are also done for the number of cluster in a few p_{T}-intervals for the analysis in order to exclude that problematic corners in phase space are overseen by the integrated distributions. These comparisons are shown in Fig. G.12, G.13, G.14 and G.15 for two different p_{T} intervals. Although the fraction of excluded tracks reaches up to 4% in the simulation at higher p_{T}, the differences between the simulation and the data are well below 1%.

The same comparisons were also done for the signal enhanced data sample used for the acceptance and efficiency corrections. They are shown in Figs.G.16,G.17, G.18,

[1]In this comparison, the large source of conversion electrons in the tracks samples is visible.

G.19, G.20, G.21, G.22, G.23, G.25, G.24. This signal enhanced simulation data exhibits different properties due to different p_{T} distributions of the selected tracks due to added signals and a larger abundance of electrons. If we do the same comparison without applying the TPC-PID cuts, we get qualitatively a similar picture as can be seen in the Figs. G.28, G.29, G.27, G.26, G.32, G.33 for the p_{T}-integrated plots and for the p_{T}-selections G.35 G.34, G.36, G.37.

In practice, it is not possible to disentangle the improvement due to the fact that we the tracks are electrons or due to the fact that we use the TPC-PID based on primary tracks in the ITS-TPC system only with these comparisons. A bias free external detector or identification would be necessary. The usage of conversion would require in-depth investigation, what biases are already created on the secondary vertexing finding stage and whether this has an impact on the significant impact on the tracking variables. However, since only at most $O(1\%)$ of the hadronic tracks fall outside of the cut range in the distribution, we can neglect the related uncertainties safely. The uncertainties due to the difference in the cluster distribution thus mainly indirectly enter into the PID description, since the resolution is a function of the number of PID clusters which is strongly correlated with the number of tracking clusters shown in these comparisons.

The variation of the requirement of either a hit in the first layer of the SPD or in either of the two SPD layers does not alter the retrieved J/ψ result significantly taking into account that the signal extraction has also a significant uncertainty and the background shape is changing. Furthermore, the active channel map from data is well reproduced in simulation, the run-by-run weighting for MC events are reproducing the event fractions with a given SPD configuration from data and the variations over time are relevant, but little in the p-Pb data sample, see Fig. 5.5. The sensitivity of the $Acc. \times eff.$ to the cuts in transverse momentum[2] is implicitly tested by the sensitivity to the variation of the track-p_{T} acceptance selection. There is no statistical significant effect found as explained in Appendix F.

[2]Here, especially the proper simulation of the bremsstrahlung and hence of the material budget inside the detector is crucial.

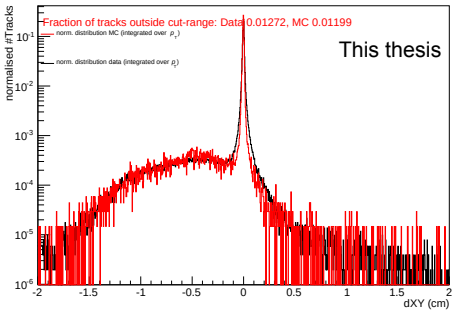

Figure G.6.: The normalised distributions of the *dca* in the transverse plane for the MB MC sample and data with TPC-PID-cuts (3σ pion exclusion, 3.5σ proton exclusion) for negatively charged tracks. The cut value in the analysis is 1 *cm*. All other tracking cuts are already applied.

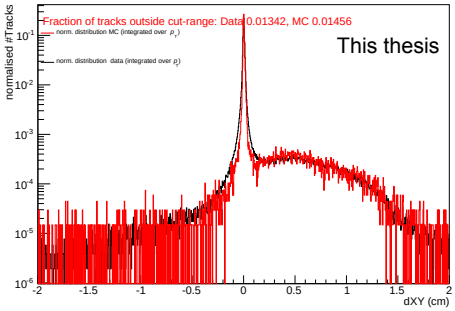

Figure G.7.: The normalised distributions of the *dca* in the transverse plane for the MB MC sample and data with TPC-PID-cuts (3σ pion exclusion, 3.5σ proton exclusion) for positively charged tracks. The cut value in the analysis is 1 *cm*. All other tracking cuts are already applied.

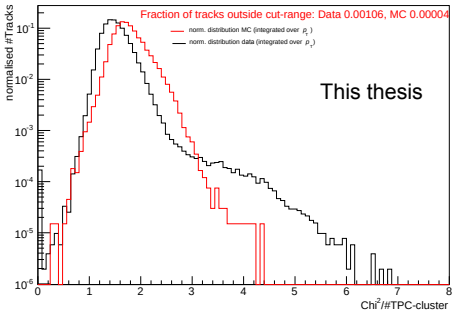

Figure G.8.: The normalised distributions of the χ^2/N_{TPCcl} for the MB MC sample and data with TPC-PID-cuts (3σ pion exclusion, 3.5σ proton exclusion) for positively charged tracks. The cut value in the analysis is 4.0. All other tracking cuts are already applied.

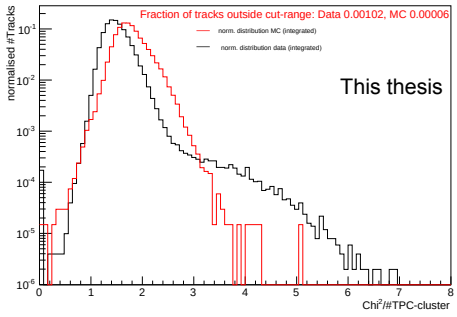

Figure G.9.: The normalised distributions of the χ^2/N_{TPCcl} for the MB MC sample and data with TPC-PID-cuts (3σ pion exclusion, 3.5σ proton exclusion) for negatively charged tracks. The cut value in the analysis is 4.0.

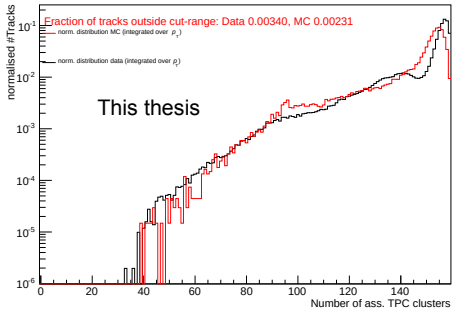

Figure G.10.: The normalised distributions of the number of associated TPC-cluster for the MB MC sample and data with TPC-PID-cuts (3σ pion exclusion, 3.5σ proton exclusion) for negatively charged tracks. The cut value in the analysis is 70.

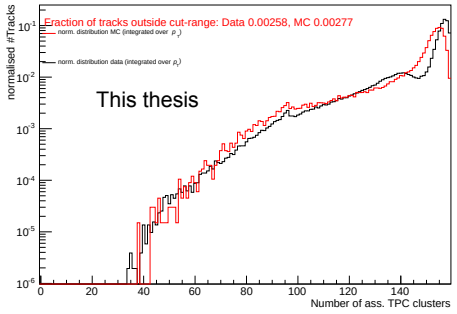

Figure G.11.: The normalised distributions of the number of associated TPC-cluster for the MB MC sample and data with TPC-PID-cuts (3σ pion exclusion, 3.5σ proton exclusion) for positively charged tracks. The cut value in the analysis is 70.

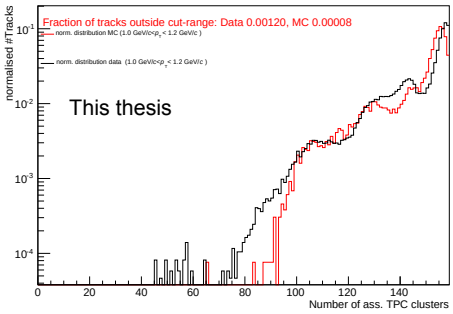

Figure G.12.: The normalised distributions of the number of associated TPC-cluster in the p_{T}-range $[1, 1.2]$ GeV/c for the MB MC sample and data with TPC-PID-cuts (3σ pion exclusion, 3.5σ proton exclusion) for negatively charged tracks. The cut value in the analysis is 70.

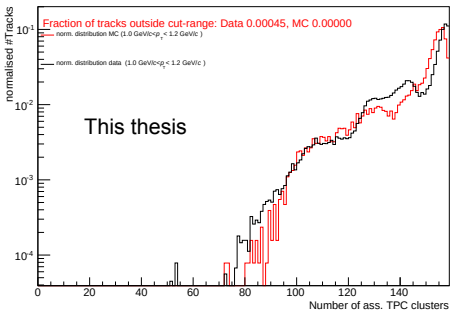

Figure G.13.: The normalised distributions of the number of associated TPC-cluster in the p_{T}-range $[1, 1.2]$ GeV/c for the MB MC sample and data with TPC-PID-cuts (3σ pion exclusion, 3.5σ proton exclusion) for positively charged tracks. The cut value in the analysis is 70.

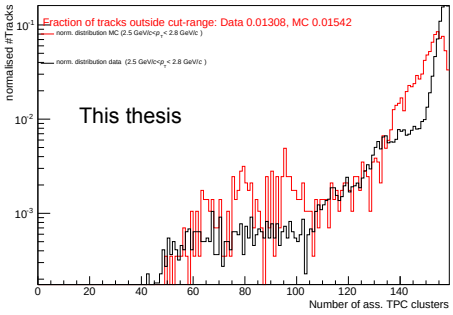

Figure G.14.: The normalised distributions of the number of associated TPC-cluster in the p_{T}-range $[2.5, 2.8]$ GeV/c for the MB MC sample and data with TPC-PID-cuts (3σ pion exclusion, 3.5σ proton exclusion) for negatively charged tracks. The cut value in the analysis is 70.

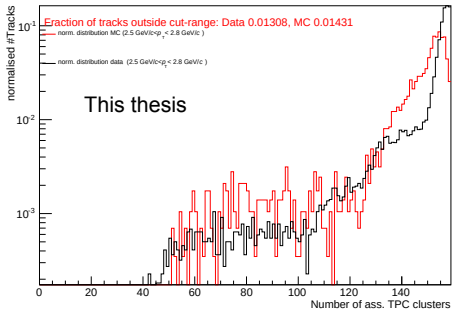

Figure G.15.: The normalised distributions of the number of associated TPC-cluster in the p_{T}-range $[2.5, 2.8]$ GeV/c for the MB MC sample and data with TPC-PID-cuts (3σ pion exclusion, 3.5σ proton exclusion) for positively charged tracks. The cut value in the analysis is 70.

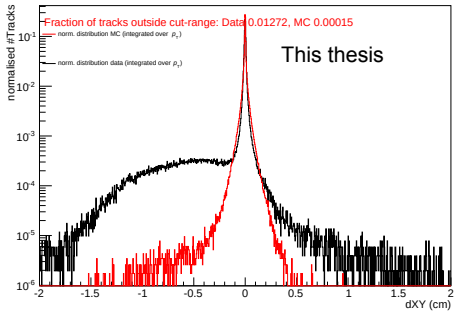

Figure G.16.: The normalised distributions of the *dca* in the transverse plane for the added signal MC sample and data with TPC-PID-cuts (3σ pion exclusion, 3.5σ proton exclusion) for negatively charged tracks. The cut value in the analysis is 1 *cm*. All other tracking cuts are already applied.

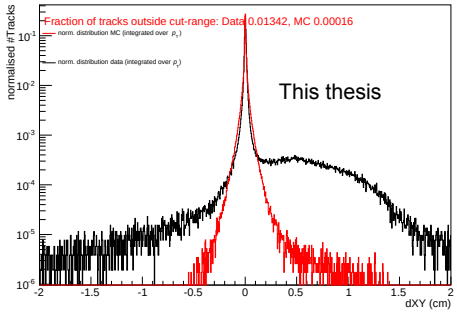

Figure G.17.: The normalised distributions of the *dca* in the transverse plane for the added signal MC sample and data with TPC-PID-cuts (3σ pion exclusion, 3.5σ proton exclusion) for positively charged tracks. The cut value in the analysis is 1 *cm*. All other tracking cuts are already applied.

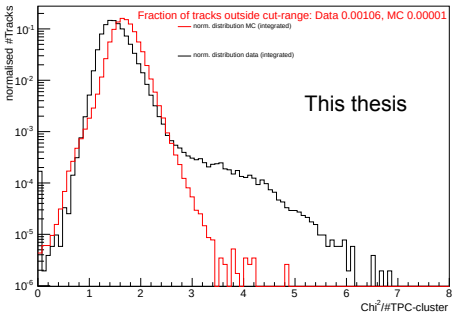

Figure G.18.: The normalised distributions of the χ^2/N_{TPCcl} for the added signal MC sample and data with TPC-PID-cuts (3σ pion exclusion, 3.5σ proton exclusion) for positively charged tracks. The cut value in the analysis is 4.0. All other tracking cuts are already applied.

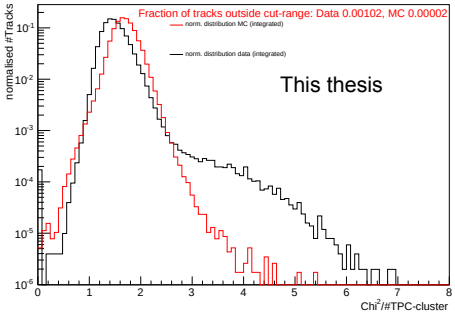

Figure G.19.: The normalised distributions of the χ^2/N_{TPCcl} for the added signal MC sample and data with TPC-PID-cuts (3σ pion exclusion, 3.5σ proton exclusion) for negatively charged tracks. The cut value in the analysis is 4.0.

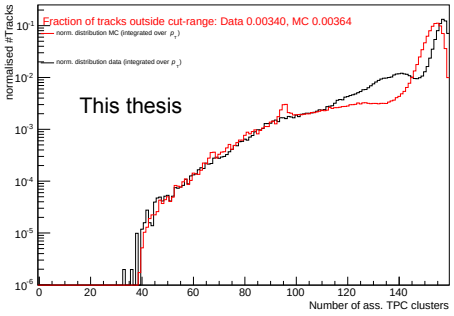

Figure G.20.: The normalised distributions of the number of associated TPC-cluster for the added signal MC sample and data with TPC-PID-cuts (3σ pion exclusion, 3.5σ proton exclusion) for negatively charged tracks. The cut value in the analysis is 70.

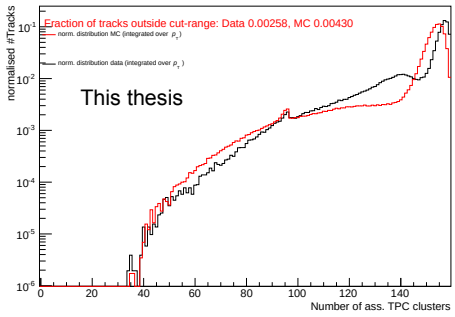

Figure G.21.: The normalised distributions of the number of associated TPC-cluster for the added signal MC sample and data with TPC-PID-cuts (3σ pion exclusion, 3.5σ proton exclusion) for positively charged tracks. The cut value in the analysis is 70.

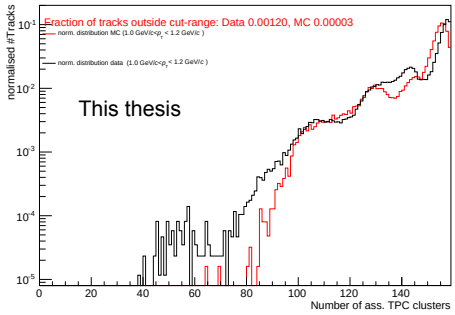

Figure G.22.: The normalised distributions of the number of associated TPC-cluster in the p_{T}-range $[1, 1.2]$ GeV/c for the added signal MC sample and data with TPC-PID-cuts (3σ pion exclusion, 3.5σ proton exclusion) for negatively charged tracks. The cut value in the analysis is 70.

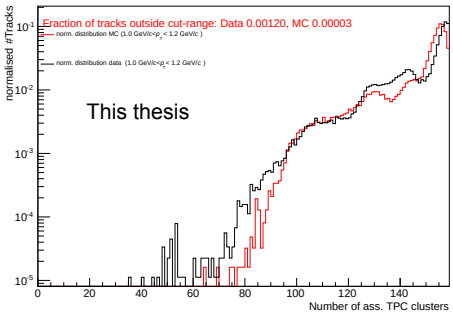

Figure G.23.: The normalised distributions of the number of associated TPC-cluster in the p_{T}-range $[1, 1.2]$ GeV/c for the added signal MC sample and data with TPC-PID-cuts (3σ pion exclusion, 3.5σ proton exclusion) for positively charged tracks. The cut value in the analysis is 70.

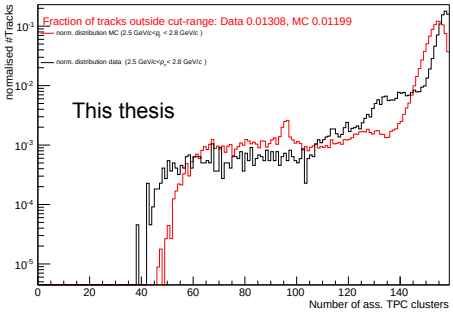

Figure G.24.: The normalised distributions of the number of associated TPC-cluster in the p_{T}-range $[2.5, 2.8]$ GeV/c for the added signal MC sample and data with TPC-PID-cuts (3σ pion exclusion, 3.5σ proton exclusion) for negatively charged tracks. The cut value in the analysis is 70.

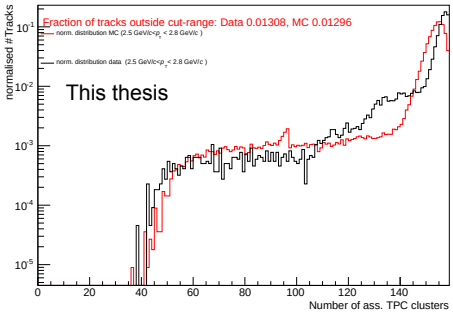

Figure G.25.: The normalised distributions of the number of associated TPC-cluster in the p_{T}-range $[2.5, 2.8]$ GeV/c for the added signal MC sample and data with TPC-PID-cuts (3σ pion exclusion, 3.5σ proton exclusion) for positively charged tracks. The cut value in the analysis is 70.

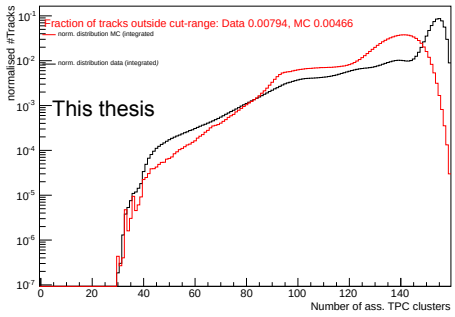

Figure G.26.: The normalised distributions of the number of associated TPC-cluster for the MB MC sample and data without any PID-cuts for negatively charged tracks. The cut value in the analysis is 70.

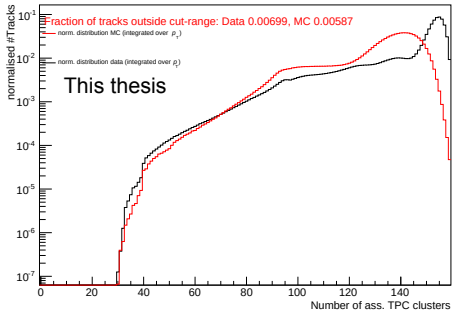

Figure G.27.: The normalised distributions of the number of associated TPC-cluster for the MB MC sample and data without any PID-cuts for positively charged tracks. The cut value in the analysis is 70.

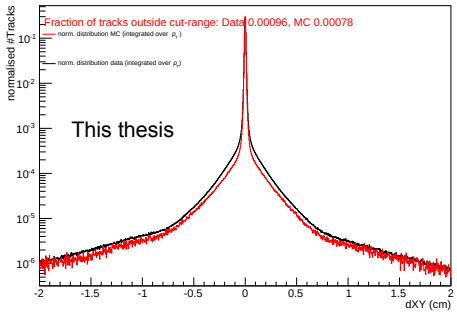

Figure G.28.: The normalised distributions of the *dca* in the transverse plane for the MB MC sample and data without any PID-cuts for negatively charged tracks. The cut value in the analysis is 1 *cm*. All other tracking cuts are already applied.

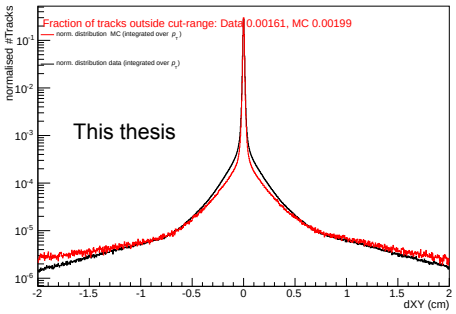

Figure G.29.: The normalised distributions of the *dca* in the transverse plane for the MB MC sample and data without any PID-cuts for positively charged tracks. The cut value in the analysis is 1 *cm*. All other tracking cuts are already applied.

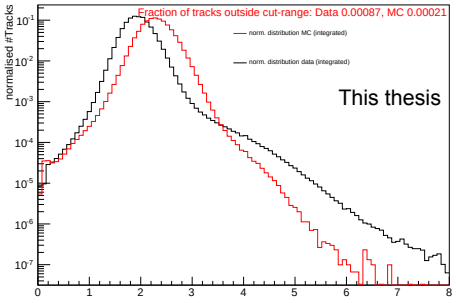

Figure G.30.: The normalised distributions of the χ^2/N_{TPCcl} for the MB MC sample and data without any PID-cuts for positively charged tracks. The cut value in the analysis is 4.0. All other tracking cuts are already applied.

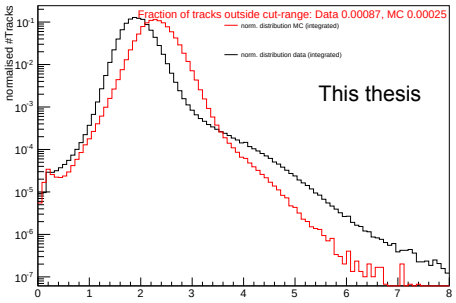

Figure G.31.: The normalised distributions of the χ^2/N_{TPCcl} for the MB MC sample and data without any PID-cuts for negatively charged tracks. The cut value in the analysis is 4.0.

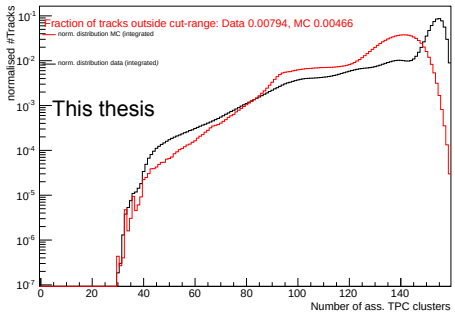

Figure G.32.: The normalised distributions of the number of associated TPC-cluster for the MB MC sample and data without any PID-cuts for negatively charged tracks. The cut value in the analysis is 70.

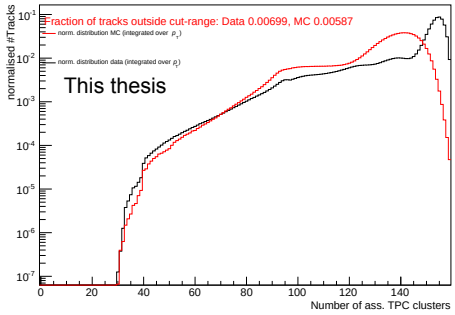

Figure G.33.: The normalised distributions of the number of associated TPC-cluster for the MB MC sample and data without any PID-cuts for negatively charged tracks. The cut value in the analysis is 70.

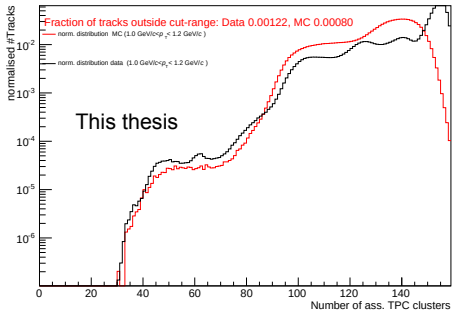

Figure G.34.: The normalised distributions of the number of associated TPC-cluster in the p_{T}-range $[1, 1.2]$ GeV/c for the MB MC sample and data without any PID-cuts for negatively charged tracks. The cut value in the analysis is 70.

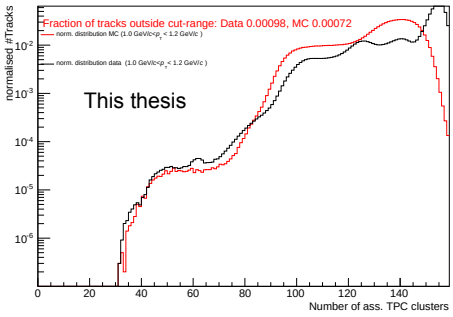

Figure G.35.: The normalised distributions of the number of associated TPC-cluster in the p_{T}-range $[1, 1.2]$ GeV/c for the MB MC sample and data without any PID-cuts for positively charged tracks. The cut value in the analysis is 70.

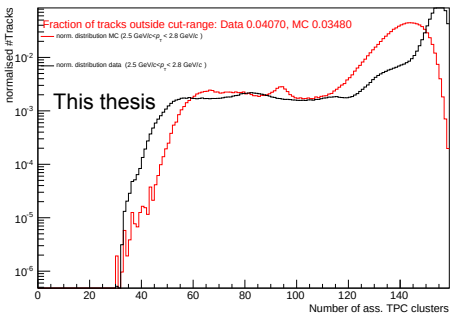

Figure G.36.: The normalised distributions of the number of associated TPC-cluster in the p_{T}-range $[2.5, 2.8]$ GeV/c for the MB MC sample and data without any PID-cuts for negatively charged tracks. The cut value in the analysis is 70.

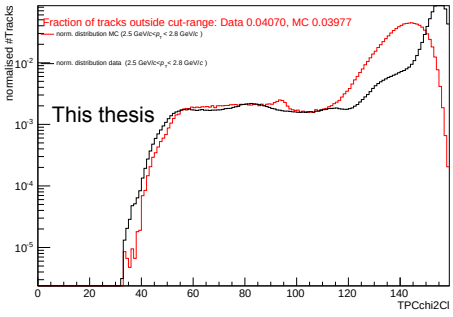

Figure G.37.: The normalised distributions of the number of associated TPC-cluster in the p_{T}-range $[2.5, 2.8]$ GeV/c for the MB MC sample and data without any PID-cuts for positively charged tracks. The cut value in the analysis is 70.

As detailed in Section 5.4.3, the reliability of the tracking efficiency correction was tested by the additional 'in-active-volume-cut'. The double ratios between the efficiency ratios in simulation and in data are shown in the Figs. G.40 for unidentified tracks and G.43 for tracks passing the PID selection employed in this analysis. They correspond to the simple ratios shown in Fig. 5.9, Fig. 5.10 for unidentified tracks and in Fig. 5.11 and Fig. 5.12 for tracks passing the PID selection used in this analysis. A discussion of these findings can be found in Section 5.4.3.

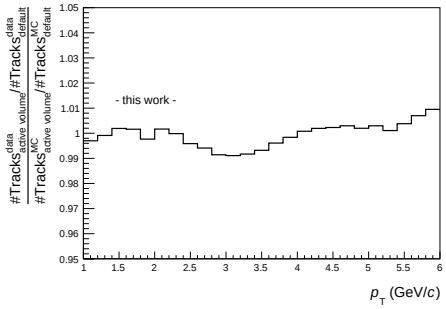

Figure G.38.: negatively charged

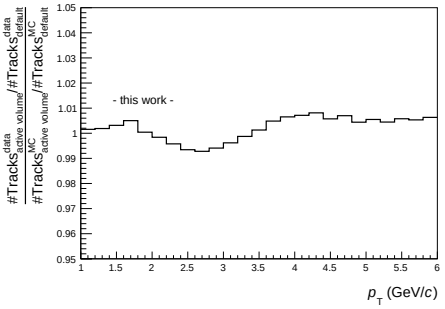

Figure G.39.: positively charged

Figure G.40.: Double ratios of the single ratios with the additional 'in-active-volume-cut' for non-identified tracks presented in Fig. 5.9 and in Fig. 5.10.

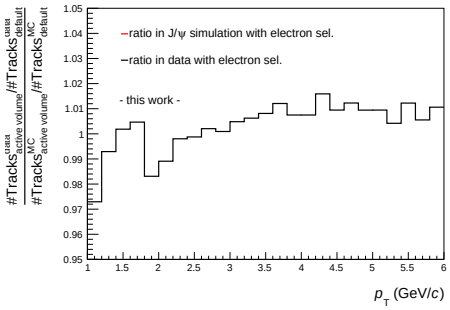

Figure G.41.: negatively charged

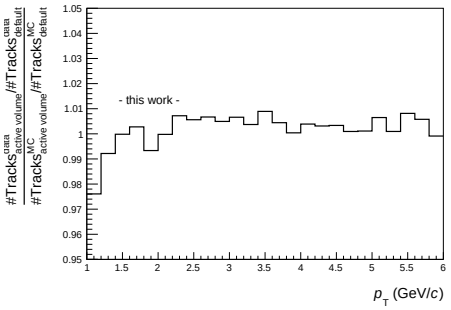

Figure G.42.: positively charged

Figure G.43.: Double ratios of the single ratios with the additional 'in-active-volume-cut' for tracks passing the electron selection presented in Fig. 5.11 and in Fig. 5.12.

G.4. Alternative evaluation of the statistical uncertainties in the multiplicity dependent analysis

In this appendix, the alternative calculation of the statistical uncertainty in the self-normalised yield is presented, which is not relying on pseudo-data generation.

In case of a background free measurement, in the limit that every bin has a sizeable contribution to the overall yield, but is still not dominating the whole sample, the statistical uncertainty can be computed by the binomial uncertainty, which is often used for the evaluation of the uncertainty of acceptance or efficiency factors. The J/ψ signal extraction presented here is not background free and this procedure is not applicable.

In the limit of small uncertainties for denominator and numerator, the statistical uncertainty can be also retained from a Gaussian error propagation by properly taking into account which signal counts vary independently from each other.

We define the following quantities:

1. N_{bin}: number of signal counts in the considered multiplicity range
2. N_{tot}: number of signal counts integrated as a function of multiplicity
3. $N_{notbin} = N_{tot} - N_{bin}$: number of all signal counts not in the considered multiplicity range
4. $\Delta_{stat}\,(X)$: statistical uncertainty of the variable X

We are interested in the determination of the quantity: $\Delta_{stat}\left(\frac{N_{bin}}{N_{tot}}\right)$. For the background free case, the statistical uncertainty is simply the binomial uncertainty in the mentioned limits:

$$\Delta_{stat}\left(\frac{N_{bin}}{N_{tot}}\right) = \sqrt{\frac{N_{bin}\cdot(N_{tot}-N_{bin})}{N_{tot}^3}} \tag{G.1}$$

In the case of a non-vanishing background, we consider the following calculation:

$$\begin{aligned}
\Delta_{stat}\left(\frac{N_{bin}}{N_{tot}}\right) &= \Delta_{stat}\left(\frac{N_{bin}}{N_{bin}+N_{notbin}}\right) \\
&= \sqrt{\left(\Delta_{stat}N_{bin}\cdot\left(\frac{N_{notbin}}{N_{tot}^2}\right)\right)^2+\left(\Delta_{stat}N_{notbin}\left(\frac{N_{bin}}{N_{tot}^2}\right)\right)^2} \\
\text{use: } (\Delta_{stat}N_{notbin})^2 &= (\Delta_{stat}N_{tot})^2-(\Delta_{stat}N_{bin})^2 \\
\Delta_{stat}\left(\frac{N_{bin}}{N_{tot}}\right) &= \\
&\sqrt{\left(\Delta_{stat}N_{bin}\left(\frac{N_{notbin}}{N_{tot}^2}\right)\right)^2+\left(\frac{N_{bin}}{N_{tot}^2}\right)^2((\Delta_{stat}N_{tot})^2-(\Delta_{stat}N_{bin})^2)} \\
\text{use: } N_{notbin} &= N_{tot}-N_{bin} \\
&= \sqrt{\frac{(\Delta_{stat}N_{bin})^2}{N_{tot}^4}(N_{tot}^2-2N_{tot}N_{bin})+\frac{(\Delta_{stat}N_{tot})^2}{N_{tot}^4}N_{bin}^2}
\end{aligned}$$

With this formulation, we retrieve the correct behaviour of the uncertainty for $B \to 0$ (binomial uncertainty), $N_{bin} \to N_{tot}$ (uncertainty to zero), $N_{tot} \to \infty$ (only numerator uncertainty matters). The deviations with respect to the default pseudo-data approach amount to maximally 10% of the uncertainty.

G.5. Supplementary $Acc. \times eff.$ figures

The $Acc. \times eff.$ correction factors as function of transverse momentum for the selection criteria used in the first two bins of the p_{T}-differential analysis, the multiplicity and centrality analysis are shown in Fig. G.44. Figure G.45 shows the corresponding quantities for the selections used for the p_{T}-differential results above $\mathrm{e}^{+}\mathrm{e}^{-}$ pair p_{T} above 5 GeV/c.

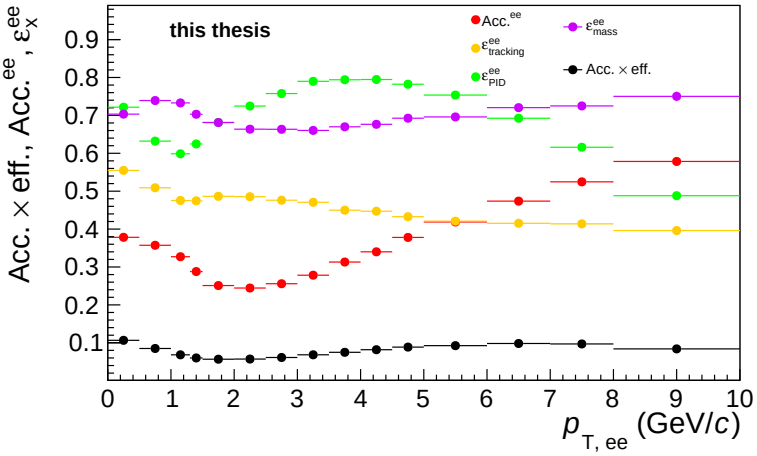

Figure G.44.: The transverse momentum dependence of the $Acc. \times eff.$-factor separated in several steps for the selection criteria in the p_{T}-differential analysis for pair p_{T} below 3 GeV/c and in the centrality and multiplicity differential analysis. The only difference with respect to Fig. 5.6 is the requirement of a hit in the first layer of the SPD instead of a hit in either of the two SPD layers. The invariant mass window for the signal extraction is $[2.92, 3.16]$ GeV/c^2.

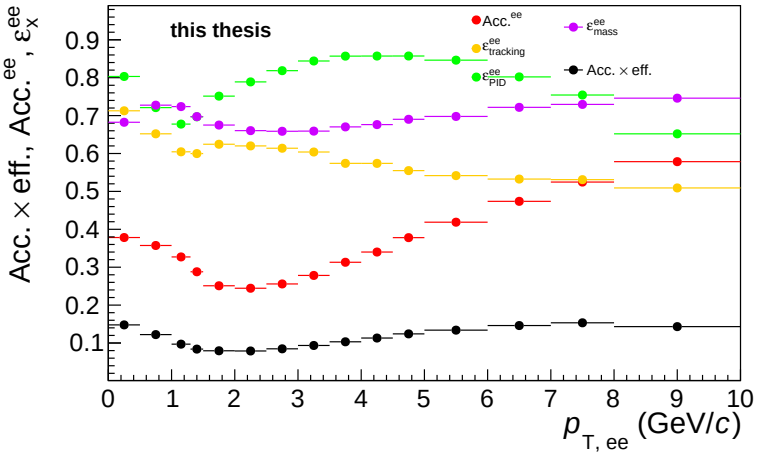

Figure G.45.: The transverse momentum dependence of the $Acc. \times eff.$-factor separated in several steps for the selection criteria in the p_{T}-differential analysis for pair p_{T} above 5 GeV/c with weaker pion and proton rejection. The invariant mass window for the signal extraction is $[2.92, 3.16]$ GeV/c^2.

H. Simplified model for pile-up impact evaluation

In order to estimate the impact of the in-bunch pile-up events on the multiplicity dependent analysis, a simplified model is used:

- The number of collisions is simulated with a random number generator according to a Poissonian with average value μ derived from the data.
- The z-coordinate position of the vertex of every collision is generated according to the measured Gaussian shape shown in Fig. 4.2.
- The z-vertex position selection is applied ($|z_{\mathrm{vtx}}| < 10$ cm).
- Selection criteria acting effectively as pile-up rejection detailed below are applied.
- For each collision of the bunch crossing, the number of corrected $N_{\mathrm{tracklets}}$ according to the measured distribution in data using a random number generator is generated.
- The distribution of corrected tracklets for every event passing the event selection and for the cumulative distribution of all events passing the selection in one bunch crossing are retained and compared with each other.

This procedure has a conceptual flaw: the measured distribution is used, which is already affected by pile-up as input for the distribution. Nevertheless, as long as the correction of our observable is small, we can use the output as an estimate of the effect, i.e. you can think of an expansion around the already slightly modified result instead of an expansion around the true value.

Since, as it will turn out, the number of J/ψ is proportional to the average multiplicity within the uncertainties in the probed multiplicity range, the relative impact on the average multiplicity in a given multiplicity range is taken as an estimator for the impact on the J/ψ measurement.

However, the mentioned selection criteria suppressing pile-up for the J/ψ observable and the multiplicity measurement are different. In case of the J/ψ yield measurement, pile-up is rejected by the requirement on the distance of closest approach cut in beam direction $|\mathrm{DCA}_z| < 3$ cm to the primary vertex of the daughter tracks. In case of the multiplicity measurement, only tracklets are counted, which are attached to the vertex with the largest multiplicity in the bunch crossing. The vertex separation power in the first step of the event reconstruction can be estimated to be about 1 cm in p–Pb collisions [321].

In summary, the impact of pile-up is negligible compared to other uncertainties, since the largest observed effect is 0.2 per mille for the multiplicity and 0.6 per mille for the J/ψ.

Since the centrality differential analysis deals with event classes composed of at least 20% of the visible cross section compared to about 1% in the multiplicity differential analysis, the effect is negligible for the centrality analysis.

I. Determination of the J/ψ $\langle p_{\mathrm{t}} \rangle$

The $\langle p_{\mathrm{T}} \rangle$ of the inclusive J/ψ p_{T} spectrum is determined based on a fit to the p_{T} differential result.

The following fit function is used:

$$f(p_{\mathrm{T}}) = C_0 \cdot \frac{p_{\mathrm{T}}}{(1 + (p_{\mathrm{T}}/p_0)^2)^n} \tag{I.1}$$

The fit parameters are the normalisation C_0 and the constants p_0 and n. As a first step, the p_{T}-differential spectrum is fitted with a χ^2-minimisation routine which takes into the uncertainties and which compares the integral of the fit function and of the measured cross section. The statistical and the systematic uncertainties without further correlation specification are added in quadrature as uncertainty in order to determine the central point. The fit is shown in Fig. I.1. The fit is repeated two times: once with statistical and once with systematic uncertainties only. The 1-σ 2 dimensional uncertainty ellipse for the parameters p_0 and n is extracted for the fit taking into account only the statistical uncertainty as shown in Fig. I.2 for the determination of the statistical uncertainty. The same procedure is applied for the determination of the systematic uncertainty as shown in Fig. I.3. Since the $\langle p_{\mathrm{T}} \rangle$ is not diagonal in the p_0 and n space and not independent of one of the two parameters, 2000 random points are generated along the two ellipse contours as shown in Fig. I.4 and Fig. I.5. The $\langle p_{\mathrm{T}} \rangle$ is evaluated for every parameter pair on the ellipses as shown in Fig. I.6 and Fig. I.7. The maximal deviation in one direction from the central value is taken as a symmetric uncertainty around the central value extracted with the fit.
It was verified that the use of all different functions, which are used in light flavour analyses in ALICE for the systematic uncertainty estimation of yields and $\langle p_{\mathrm{T}} \rangle$, does not contribute to the $\langle p_{\mathrm{T}} \rangle$ uncertainty evaluation. This was tested with the muon forward data, which has a much higher precision than the mid-rapidity data

points. The central value only moved by 3.8 per mille and the size of the statistical uncertainties derived with the same methodology changed by 20% and the systematic uncertainty by 1%.

The code used for the $\langle p_{\mathrm{T}} \rangle$ extraction in the dielectron analysis was validated by reproducing the results of the muon arm. The $\langle p_{\mathrm{T}} \rangle$ value was extracted using different p_{T}-ranges for the evaluation: $0 - 10\mathrm{GeV}/c$, $0 - 15\mathrm{GeV}/c$ (muon p_{T}-range) and $0 - 1000\mathrm{GeV}/c$. The results are given in Appendix J.2.

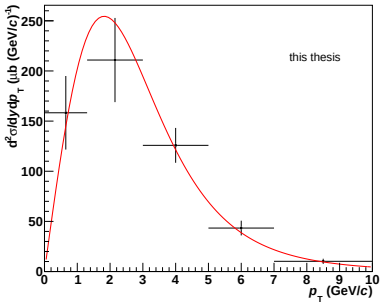

Figure I.1.: The fit for the determination of the $\langle p_{\mathrm{T}} \rangle$. The uncertainty bars correspond to the addition in quadrature of the statistical and the systematic uncertainty.

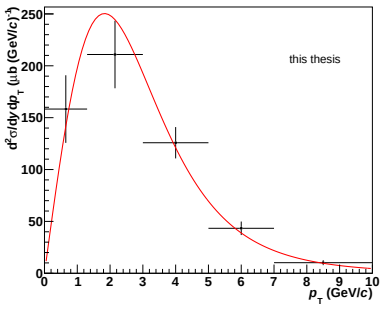

Figure I.2.: The fit for the determination for the retrieval of the uncertainty ellipse for the statistical uncertainty of $\langle p_{\mathrm{T}} \rangle$. The uncertainty bars correspond to the statistical uncertainties.

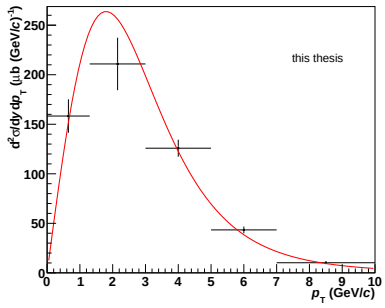

Figure I.3.: The fit for the determination for the retrieval of the uncertainty ellipse for the systematic uncertainty of $\langle p_{\mathrm{T}} \rangle$. The uncertainty bars correspond to the statistical uncertainties.

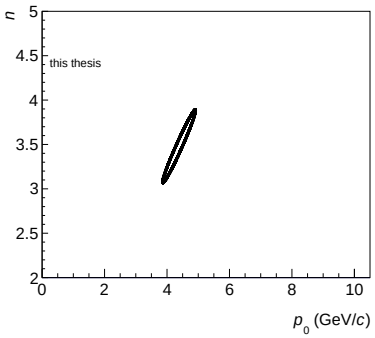

Figure I.4.: The 1-σ ellipse for the systematic uncertainty in the relevant n-p_0 phase space.

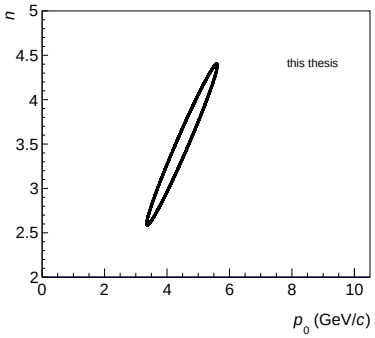

Figure I.5.: The 1-σ ellipse for the statistical uncertainty in the relevant n-p_0 phase space.

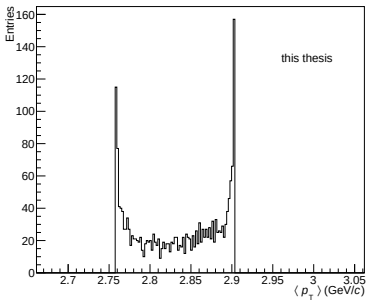

Figure I.6.: Retrieved values for the $\langle p_{\mathrm{T}} \rangle$ for the 2000 random points on the ellipse for the systematic uncertainty determination.

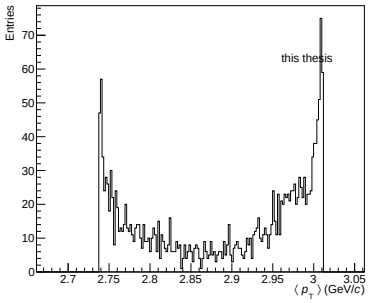

Figure I.7.: Retrieved values for the $\langle p_{\mathrm{T}} \rangle$ for the 2000 random points on the ellipse for the statistical uncertainty determination.

J. Result tables

J.1. Inclusive integrated and p_{t}-differential J/ψ cross sections

The result of the integrated cross section of J/ψ production amounts to:

$$\begin{aligned}\mathrm{d}\sigma/\mathrm{d}y(\mathrm{J}/\psi, y \in [-1.37, 0.43]) = (909.0 \pm 78.3\ &(\text{stat.}) \\ \pm 62\ &(\text{uncorr. syst. w.r.t. muons}) \\ \pm 35\ &(\text{corr. syst. w.r.t. forward muons}))\ \mu\mathrm{b}\end{aligned}$$

p_{T} bins in GeV/c	0-1.3	1.3-3.0	3.0-5.0	5.0-7.0	7.0-10.0
statistical uncertainties in %	20.578	15.44	12.01	15.02	23.3
statistical uncertainties (abs.)	32	32	15	6.5	2.3
uncorr. syst. uncertainty in %	10.7	14.1	6.8	7.9	9.5
uncorr. syst. uncertainty (abs.)	16.9	29.8	8.6	3.4	0.97
corr. syst. uncertainty in %	3.8	3.8	3.8	3.8	3.8
corr. syst. uncertainty (abs.)	6.0	8.018	4.8	1.6	3.9
$\mathrm{d}^2\sigma/\mathrm{d}y\mathrm{d}p_{\mathrm{T}}(\mu\mathrm{b}/(\mathrm{GeV}/c))$	158	211	126	43	10.2

Table J.1.: $\mathrm{d}^2\sigma/\mathrm{d}y\mathrm{d}p_{\mathrm{T}}$ of J/ψ for $y \in [-1.37, 0.43]$ at $\sqrt{s_{NN}} =$ 5.02 TeV and its uncertainties.

J.2. $\langle p_{\mathrm{t}} \rangle$ of inclusive J/ψ production

The extracted values ares the following by fitting the spectrum in the p_{T} range 0-10 GeV/c:

1. $\langle p_{\mathrm{T}} \rangle$ in $0-10$ GeV/c: 2.86 ± 0.149(stat.)$\pm$0.103(syst.) GeV/c
2. $\langle p_{\mathrm{T}} \rangle$ in $0-15$ GeV/c: 2.945 ± 0.161(stat.)$\pm$(0.107)(syst.) GeV/c
3. $\langle p_{\mathrm{T}} \rangle$ in $0-1000$ GeV/c: 2.978 ± 0.26(stat.)$\pm$0.11 (syst.) GeV/c

The $\langle p_{\mathrm{T}} \rangle$ value for pp collisions from the direct interpolation of the $\langle p_{\mathrm{T}} \rangle$ $0-10$ GeV/c within between PHENIX, CDF and ALICE data at mid-rapidity is: 2.814 $\pm$0.089 (stat.) $\pm$0.035 (syst.) GeV/c in the p_{T} range $0-10$ GeV/c [263].
If one evaluates the universal functional shape after being fed with the $\langle p_{\mathrm{T}} \rangle$ of the interpolation between the different experiments, ones retrieves a slightly different value, but which is still compatible within the uncertainties of the approach: 2.689 ± 0.094(stat.) $\pm$ 0.021(syst.)GeV/c evaluated with the function also within $0-10$ GeV/c.
The first $\langle p_{\mathrm{T}} \rangle$ value in pp collisions is recommended as comparison value because it is more directly extracted from the experimental data and more transparent without long explanations.

J.3. Integrated and p_{t}-differential pp reference cross sections

p_{T} bins in GeV/c	0-1.3	1.3-3.0	3.0-5.0	5.0-7.0	7.0-10.0
$\mathrm{d}^2\sigma/\mathrm{d}y\mathrm{d}p_{\mathrm{T}}\vert_{\mathrm{pp},J/\psi}$ (μb/(GeV/c))	0.9423	1.595	0.7865	0.2345	0.0553
corr. syst. uncert. in %	16.6	16.6	16.6	16.6	16.6
corr. syst. uncertainty (abs.)	0.1564	0.26477	0.1306	0.038927	0.00918
uncorr. syst. uncert. in %	7.3	4.8	5.7	12.8	15.7
uncorr. syst. uncert. (abs.)	0.069	0.077	0.0483	0.030	0.0087

Table J.2.: Reference $\mathrm{d}^2\sigma/\mathrm{d}y\mathrm{d}p_{\mathrm{T}}(\mathrm{pp}, J/\psi)$ at mid-rapidity in pp collisions for $\sqrt{s} =$ 5.02 TeV from interpolation and its uncertainties.

J.4. Integrated and p_{t}-dependent nuclear modification factors

The result for the integrated nuclear modification factor of J/ψ at mid-rapidity amounts to:

$$\begin{aligned} R_{\mathrm{pPb}}(\mathrm{J}/\psi, y \in [-1.37, 0.43]) = 0.708 &\pm 0.061 \text{ (stat.)} \\ &\pm 0.124 \text{ (uncorr. syst. w.r.t. muons)} \\ &\pm 0.024 \text{ (corr. syst. w.r.t. forward muons)} \end{aligned}$$

p_{T} bins in GeV/c	0-1.3	1.3-3.0	3.0-5.0	5.0-7.0	7.0-10.0
statistical uncertainties(in %)	21	15	12	15	23
statistical uncertainties(abs.)	0.17	0.098	0.092	0.13	0.21
uncorr. syst. uncertainty(in %)	12.5	13.3	9.0	14.9	18.0
uncorr. syst. uncertainty(abs.)	0.10	0.085	0.069	0.133	0.16
corr. syst. uncertainty(in %)	17.0	17.0	17.0	17.0	17.0
corr. syst. uncertainty(abs.)	0.138	0.109	0.131	0.152	0.151
R_{pPb}	0.80	0.64	0.77	0.89	0.89

Table J.3.: The R_{pPb} of J/ψ as a function of transverse momentum for $y \in [-1.37, 0.43]$ at $\sqrt{s_{NN}} =$ 5.02 TeV and its uncertainties are shown.

J.5. Centrality dependence

event act. bins in %	0-20	20-40	40-60	60-100
statistical unc. (in %)	14.9	15.3	18.0	15.3
statistical unc. (abs.)	0.110	0.114	0.122	0.122
Systematic uncert. (corr.) (in %)	17.6	17.6	17.6	17.6
Systematic uncert. (corr) (abs.)	0.130	0.131	0.120	0.140
Systematic uncert. (uncorr.) (in %)	9.4	4.4	6.8	7.9
Systematic uncert. (uncorr.) (abs.)	0.069	0.0326	0.0465	0.063
Q_{pPb}absolute value	0.735	0.745	0.681	0.794

Table J.4.: The overview of values and uncertainties considered for the Q_{pPb} analysis via the ALICE hybrid approach is shown.

J.6. Multiplicity dependence

corrected tracklets range	1-25	26-61	62-102	103-200
statistical unc. (in %)	14.4	7.2	11.8	33.1
statistical unc. (abs.)	0.0447	0.0845	0.333	2.32
Systematic uncert. (corr.) (in %)	3.1	3.1	3.1	3.1
Systematic uncert. (corr) (abs.)	0.0096	0.363	0.878	2.2 0
Systematic uncert. (corr. not specified) (in %)	6.3	4.5	5.3	13.0
Systematic uncert. (corr. not specified) (abs.)	0.0196	0.0525	0.1511	0.907
self-norm. yield values	0.310	1.17	2.83	7.00

Table J.5.: The overview of the values and uncertainties considered for the multiplicity dependent measurement is given.

K. Selection of electrons from e^+e^--pair conversions

In the following, the selection criteria for the electrons and positrons from pair conversions are listed:

- $|n\sigma_{electron,TPC}| < 10$,
- $|n\sigma_{electron,TOF}| < 3$ if available,
- $\Theta_{\text{pointing,e}^+\text{e}^-\text{-}pair} < 0.02$: pointing of track pair to primary vertex,
- $\chi^2/\text{NDF} < 10.0$: compatibility variable for both tracks coming from a common vertex implemented in the KF-package [322],
- $TrackDist < 0.25$ cm: small three dimensional distance between both tracks,
- $\psi_{\text{pair}} < 0.05$, the variable was introduced in Ref. [323] where it is explained in detail,
- the production radius between 3 cm and 90 cm,
- an invariant pair mass with the electron mass assumption below 50 MeV/c^2,
- an Armenteros-Podolanski $p_{\text{T}} < 50$ MeV/c for daughters
- and ITSrefit for PID comparisons: minimising effects due to different geometrical path with respect to primary tracks and possible cluster sharing effects.